



HAL
open science

Wave-based numerical approaches for non-destructive testing of structural assemblies involving straight waveguides and curved joints

Diego Salam Claro

► **To cite this version:**

Diego Salam Claro. Wave-based numerical approaches for non-destructive testing of structural assemblies involving straight waveguides and curved joints. Mechanical engineering [physics.class-ph]. INSA CVL - Institut National des Sciences Appliquées - Centre Val de Loire, 2024. English. NNT : 2024ISAB0003 . tel-04620188

HAL Id: tel-04620188

<https://hal.science/tel-04620188v1>

Submitted on 21 Jun 2024

HAL is a multi-disciplinary open access archive for the deposit and dissemination of scientific research documents, whether they are published or not. The documents may come from teaching and research institutions in France or abroad, or from public or private research centers.

L'archive ouverte pluridisciplinaire **HAL**, est destinée au dépôt et à la diffusion de documents scientifiques de niveau recherche, publiés ou non, émanant des établissements d'enseignement et de recherche français ou étrangers, des laboratoires publics ou privés.

INSA Centre Val de Loire

*ÉCOLE DOCTORALE ÉNERGIE,
MATÉRIAUX, SCIENCES DE LA TERRE ET DE L'UNIVERS*

Laboratoire de Mécanique Gabriel LaMé, UR 7494

THÈSE présentée par :

Diego SALAM CLARO

soutenue le : 07 mai 2024

pour obtenir le grade de : **Docteur de l'INSA Centre Val de Loire**

Discipline/ Spécialité : Génie Mécanique

Approches numériques basées sur les ondes pour le contrôle non destructif des assemblages composés de guides d'ondes élastiques rectilignes connectés par des jonctions coudées

THÈSE dirigée par :

M. MENCİK Jean-Mathieu

Professeur des Universités, INSA Centre Val de Loire

THÈSE co-encadrée par :

M. DENIS Vivien

Maître de Conférences, INSA Centre Val de Loire

RAPPORTEURS :

M. BALMÈS Etienne

Professeur des Universités, ENSAM Paris

M. TREYSSÈDE Fabien

Professeur des Universités, Université Gustave Eiffel

JURY :

M. BALMÈS Etienne

Professeur des Universités, ENSAM Paris

M. DENIS Vivien

Maître de Conférences, INSA Centre Val de Loire

M. DROZ Christophe

Chercheur, INRIA

M. DUHAMEL Denis (Président du jury)

Professeur, École des Ponts ParisTech

Mme. FUNFSCHILLING Christine

Docteur, Ingénieur, SNCF

M. MENCİK Jean-Mathieu

Professeur des Universités, INSA Centre Val de Loire

M. TREYSSÈDE Fabien

Professeur des Universités, Université Gustave Eiffel

Acknowledgments

I would like to express my gratitude to my supervisors, Dr. Jean-Mathieu MENCİK and Dr. Vivien DENIS, for their unwavering support throughout this thesis. Not only for their patience, corrections, and suggestions over the past three years but also for passing on invaluable knowledge and broadening my understanding of wave propagation phenomena. For that, I thank them heartily!

I would also like to extend my appreciation in advance to the jury members: Dr. BALMÈS Etienne and Dr. TREYSSÈDE Fabien for agreeing to be "*rapporteurs*" for this thesis, and also to Dr. DUHAMEL Denis, Dr. DROZ Christophe, and Dr. FUNFSCHILLING Christine for accepting to be part of the PhD defense jury.

A heartfelt thanks goes out to everyone who accompanied me, whether from a distance or in person, throughout my PhD journey in France. I am grateful to all my friends worldwide, to my family in Brazil, and to my new family in France. Their support has been crucial in overcoming the challenges along the way. Afraid of forgetting any names, I reserve the right not to mention anyone in particular; you know that you were important to me.

Lastly, I would like to express my gratitude to INSA-Centre Val de Loire, to the *Laboratoire de Mécanique Gabriel Lamé*, and to the *Région Centre Val de Loire* for welcoming me and providing the infrastructure and financial support that made this work possible.

“O correr da vida embrulha tudo, a vida é assim: esquenta e esfria, aperta e daí afrouxa, sossega e depois desinquieta. O que ela quer da gente é coragem.”

João Guimarães Rosa — Grande sertão: veredas.

“Le cours de la vie embrouille tout - la vie est ainsi : elle réchauffe et refroidit, elle contraint puis libère, rassérène et ensuite inquiète. Ce qu'elle réclame de nous c'est le courage.”

João Guimarães Rosa — Diadorim.

“The flow of life envelopes everything. Life is like this: it heats up and cools down, it squeezes and then loosens, it becomes calm and then restless. What it wants from us is courage.”

João Guimarães Rosa — The Devil to Pay in the Backlands

Résumé

Cette thèse étudie la détection et la localisation des défauts dans les assemblages de guides d'ondes, en explorant l'interaction entre les ondes se propageant dans des assemblages de guides d'ondes droits contenant des jonctions coudées et des défauts. A cet effet, la méthode Wave Finite Element (WFE) est utilisée. Des expériences numériques valident la robustesse et la précision de la méthode WFE à partir de comparaisons avec des solutions analytiques et éléments finis, en se concentrant particulièrement sur les courbes de dispersion et les réponses forcées. En élargissant l'étude aux assemblages comportant des éléments de couplage, tels que des joints et des défauts, l'étude met en évidence l'efficacité de la méthode WFE dans des scénarios impliquant de tels assemblages.

Une nouvelle stratégie utilisant un formalisme en matrices de diffusion est proposée pour la localisation des défauts, qui met l'accent sur les structures contenant des jonctions coudées. L'approche repose sur le calcul du temps de vol de paquets d'ondes transmis ou réfléchis au niveau d'un élément de couplage. La stratégie est validée par des simulations numériques, démontrant la précision de la localisation des défauts pour divers scénarios, notamment des poutres 2D en contraintes planes et des tuyaux avec une jonction coudée et un défaut.

Les structures élasto-acoustiques sont également traitées. Une stratégie de réduction basée sur la méthode de Craig-Bampton avec des vecteurs d'enrichissement est proposée pour améliorer le coût de calcul de la modélisation des éléments de couplage. L'analyse des coefficients de transmission et de réflexion en puissance des ondes dans des structures présentant des défauts

et des jonctions met en évidence la pertinence du mode de torsion dans les contrôles non destructifs par ondes guidées dans ce type de système.

Ces travaux de recherche contribuent non seulement à la compréhension de la propagation des ondes dans les assemblages de guides d'ondes, mais proposent également des stratégies pratiques pour une détection et une localisation précise des défauts, avec des applications potentielles dans divers contextes d'ingénierie.

Mots clés: méthode Wave Finite Element, propagation d'onde, jonctions coudées, détection de défauts, temps de vol

Abstract

This thesis investigates defect detection and localization within waveguide assemblies, exploring the interaction between waves in straight waveguides with curved joints and defects. For this purpose, the Wave Finite Element (WFE) method is used. Numerical experiments validate the robustness and accuracy of the WFE method through comparisons with analytical and Finite Element solutions, particularly focusing on dispersion curves and forced responses. Extending the investigation to assemblies with coupling elements, such as joints and defects, the study highlights the efficiency of the WFE method in scenarios involving waveguides.

A novel strategy is proposed within the scattering matrix formalism for defect localization, with a specific emphasis on structures containing curved joints. The approach relies on computing the time of flight of narrow wavepackets transmitted or reflected at a coupling element. The strategy is validated through numerical simulations, showcasing precision in defect localization for diverse scenarios, including 2D plane-stress beams and pipes, with a curved joint and a defect.

Elasto-acoustic structures are also treated. A reduction strategy based on Craig-Bampton reduction with enrichment vectors is proposed for computational efficiency to model coupling elements. Analysis of power transmission and reflection of waves in structures with defects and joints highlights the significance of the torsional mode in guided wave-based non-destructive testing in this type of system.

This research work contributes not only to the understanding of wave propagation

in waveguide assemblies but also offers practical strategies for accurate defect detection and localization, with potential applications in diverse engineering contexts.

Keywords: Wave finite element method, wave propagation, curved joints, defect detection, time of flight

Contents

Résumé	v
Abstract	vii
List of symbols	xiii
Résumé long (in French)	1
Introduction	17
1 Guided waves and non-destructive testing	21
1.1 Overview	21
1.2 Wave propagation	22
1.3 Guided waves	24
1.4 Non-destructive testing using guided waves	27
1.5 Interaction of waves with defects and curved joints	30
1.6 Numerical methods	33
1.6.1 SAFE method	33
1.6.2 WFE method	35
1.7 Conclusions	36
2 The Wave Finite Element (WFE) method	37

2.1	Overview	37
2.2	Wave mode computation	39
2.2.1	(\mathbf{N}, \mathbf{L}) transformation	43
2.2.2	($\mathbf{S} + \mathbf{S}^{-1}$) transformation	44
2.2.3	Tracking criteria	46
2.3	Forced response	46
2.4	Time response	48
2.5	Group velocity	49
2.6	Numerical results and discussion	51
2.6.1	Timoshenko beam	51
2.6.2	2D plane-stress beam	55
2.7	Coupling elements	61
2.7.1	Scattering matrix	62
2.7.2	CB method	65
2.7.3	Forced response	67
2.7.4	Numerical example	68
2.8	Conclusions	73
3	Defect localization in waveguide assemblies with curved joints	75
3.1	Overview	75
3.2	Problem description	77
3.3	Scattering matrices for coupling elements	79
3.4	Times of flight	81
3.4.1	Group velocities in waveguides	81
3.4.2	Times of flight in transmission	82
3.4.3	Times of flight in reflection	83
3.4.4	Discussion	84
3.5	Defect localization	86

3.6	Numerical results	88
3.6.1	2D plane-stress beam	88
3.6.1.1	Defect localization in a waveguide assembly without joint	91
3.6.1.2	Defect localization in a waveguide assembly with a joint	97
3.6.2	Pipeline with an elastic foundation	108
3.7	Conclusions	116
4	Elasto-acoustic waveguides	119
4.1	Overview	119
4.2	WFE modeling	121
4.2.1	Forced response	125
4.2.2	Group velocity	127
4.2.3	Numerical results	128
4.3	Elasto-acoustic coupling element	133
4.3.1	CB reduction	135
4.3.2	Power scattering coefficients	140
4.4	Numerical results	141
4.4.1	Reduced modeling of the coupling element	141
4.4.2	Influence of the size of the enrichment basis	145
4.4.3	Defect localization	146
4.5	Conclusions	155
5	Conclusions and perspectives	157
	Bibliography	173
	List of figures	182
	List of tables	184

List of symbols

Matrices and vectors

D	Dynamic stiffness matrix
q	Vector of nodal displacements
F	Vector of nodal forces
M	Mass matrix
C	Damping matrix
K	Stiffness matrix
G	Coupling matrix between solid and acoustic domains
S	Transfer matrix
J	Unit symplectic matrix
I	Identity matrix
u	State vector
N, L	Matrices involved in the (\mathbf{N}, \mathbf{L}) transformation
N', L'	Matrices involved in the $(\mathbf{S} + \mathbf{S}^{-1})$ transformation
μ	Diagonal matrix of the eigenvalues of S
Φ_q	Matrix of right-going wave mode (displacement components)
Φ_q^*	Matrix of left-going wave mode (displacement components)
Φ_F	Matrix of right-going wave mode (force components)
Φ_F^*	Matrix of left-going wave mode (force components)

\mathbf{Q}, \mathbf{Q}^*	Vector of right and left-going wave amplitudes
\mathbf{F}_0	Vector of right-going wave amplitudes
\mathbf{q}_0	Vector of left-going wave amplitudes
\mathbb{C}	Scattering matrix
\mathbf{X}_{st}	Matrix of static modes
\mathbf{X}_{e1}	Matrix of fixed-interface modes
\mathbf{T}_{CB}	Transformation matrix involved in Craig-Bampton reduction

Notation

B	Boundary degrees of freedom
L	Left degrees of freedom
I	Internal degrees of freedom
R	Right degrees of freedom
n	Number of boundary degrees-of-freedom in the WFE
f	Frequency
ω	Angular frequency
β_j	Wavenumber (mode j)
c_{pj}	Phase velocity (mode j)
c_{gj}	Group velocity (mode j)

Acronyms

DSM	Dynamic Stiffness Matrix
NDT	Non-destructive testing
FE	Finite Element
WFE	Wave Finite Element
SAFE	Semi-Analytical Finite Element

CB	Craig-Brampton
DoF	Degree of freedom
DFT	Discrete Fourier Transform
IDFT	Inverse Discrete Fourier Transform

Résumé long (in French)

Introduction

Les pipelines sont essentiels pour transporter les biens de production dans l'industrie énergétique, jouant un rôle vital dans le système économique mondial. Ils relient les points d'extraction, les raffineries, les usines et les résidences. Selon Wang et al. [1], il y avait $201,9 \times 10^3$ km de pipelines en service à la fin de l'année 2020, y compris ceux pour le gaz naturel, le pétrole brut et le produit pétrolier, ce qui entraîne d'importants défis en matière de gestion et de surveillance.

La maintenance et la surveillance de ce vaste réseau de pipelines impliquent différentes techniques et procédures. Kraidi et al. [2] ont identifié plusieurs facteurs de risque, tels que l'inspection et la maintenance inadéquates ainsi que la corrosion, qui ont un impact direct sur les pipelines. Les contrôle non destructifs (CND) tels que la diffraction des rayons X, la contrainte magnétique et les techniques d'ondes guidées sont couramment utilisés pour atténuer ces risques. Plus spécifiquement, les tests par ondes guidées reposent sur la propagation des ondes dans le milieu, et sont largement utilisés pour détecter et surveiller les fissures et la corrosion. Récemment, des algorithmes d'IA ont été introduits pour améliorer la détection des défauts et gérer les risques de manière plus efficace [3, 4].

Lorsqu'il s'agit de pipelines étendus, le test par ondes guidées est la méthode préférée pour la détection de défauts. Cette approche implique de générer des ondes guidées et de mesurer leur réflexion pour identifier la présence, le type et l'emplacement des défauts. Cependant,

l'interprétation du signal réfléchi peut être considérablement modifiée par les jonctions coudées qui relient les guides d'ondes, en raison des phénomènes de diffusion. De plus, la nature multimodale et dispersée de ces ondes ajoute de la complexité au processus. Néanmoins, le cas d'un défaut après une jonction est encore plus complexe et mérite une meilleure compréhension [5].

Dans ce sens, l'étude de la propagation des ondes et de son interaction avec les défauts est essentielle pour interpréter les signaux collectés. Ainsi, le développement d'outils numériques appropriés décrivant avec précision ce phénomène est vital. Les méthodes classiques, telles que la méthode des éléments finis (EF), peuvent entraîner des coûts de calcul élevés, en particulier pour des structures longues. Pour surmonter ces limitations, des méthodes basées sur les ondes ont été utilisées, par exemple, la méthode des éléments finis à ondes (WFE) et la méthode semi-analytique des éléments finis (SAFE).

Cette thèse applique la méthode WFE pour modéliser la propagation des ondes et la diffusion des ondes dans des structures composées de guides d'ondes liés par des éléments de couplage. Dans ce cadre, les jonctions coudées et les défauts sont modélisés via EF, ce qui permet le calcul des coefficients de transmission et de réflexion. La première partie développe une stratégie pour localiser un défaut après une jonction en se basant sur les matrices de diffusion. Dans la deuxième partie, un modèle de réduction des éléments de couplage élasto-acoustique dans le cadre de la méthode WFE est présenté, permettant une réduction du temps de calcul dans le calcul des matrices de diffusion.

Organisation du manuscrit

Le chapitre 1 présente les concepts impliqués dans la technique de CND pour la localisation des défauts. Une introduction de base à la propagation des ondes dans des milieux infinis et finis est brièvement présentée. Ensuite, l'interaction des ondes guidées avec les défauts/jonctions coudées est décrite sur la base de la littérature publiée. Ces études mettent en évidence l'importance des simulations et des expériences pour améliorer les techniques d'ondes guidées.

Le chapitre 2 présente la méthode WFE. Les stratégies impliquées dans le calcul des

courbes de dispersion et des formes d'ondes sont présentées. De plus, les réponses forcées en fréquence et en domaine temporel sont décrites. Ensuite, le calcul des vitesses de groupe dans le cadre de la méthode WFE est présenté. Des exemples sont ensuite proposés pour valider l'approche. Les éléments de couplage sont introduits pour décrire les éléments non périodiques entre les guides d'ondes et sont modélisés à l'aide de matrices de diffusion. Cela est fait en combinant la réduction de Craig-Bampton (CB) basée sur EF et les approches WFE. Enfin, un exemple de deux guides d'ondes droits connectés via un élément de couplage est montré.

Dans le chapitre 3, une approche numérique basée sur la méthode WFE est proposée pour localiser les défauts dans des guides d'ondes élastiques droits connectés par une jonction élastique courbe. Cette stratégie prend en compte les phénomènes de conversion de mode d'onde et les temps de vol lorsque un paquet d'ondes est transmis à travers la jonction et réfléchi par le défaut. Le temps de vol est calculé en utilisant le formalisme des matrices de diffusion. Des expériences numériques sont menées impliquant des guides d'ondes droits connectés par une jonction coudée et un défaut, où le point de mesure est placé avant la jonction. L'approche est appliquée à des poutres en plane-stress 2D et à des tuyaux 3D, afin de mettre en évidence la précision et la robustesse de l'approche proposée.

Le chapitre 4 présente la modélisation des systèmes élasto-acoustiques impliquant des guides d'ondes droits et des jonctions coudées. Les guides d'ondes droits sont modélisés via la méthode WFE, ce qui permet d'accéder aux courbes de dispersion, aux formes d'ondes et aux vitesses de groupe. Les éléments de couplage élasto-acoustiques sont introduits dans ce cadre. Comme cela implique un grand nombre de degrés de liberté, le calcul de leur matrice de rigidité dynamique condensée est obtenu via une réduction de CB avec une technique d'enrichissement de base. Des expériences numériques sont fournies. Les courbes de dispersion et les vitesses de groupe sont discutées, et une comparaison entre les résultats WFE et EF dans les domaines fréquentiel et temporel est fournie. Enfin, les coefficients de réflexion et de transmission pour les jonctions coudées et les défauts sont comparés à ceux des tuyaux sans fluides internes.

Enfin, dans le chapitre 5, les principaux résultats et contributions de ce travail sont résumés. Les perspectives futures et les travaux ultérieurs sont également discutés.

Chapitre 1: Ondes guidées et contrôle non destructif

Contexte

Le contrôle non destructif (CND) est crucial pour maintenir et surveiller l'intégrité des structures. Cela inclut différentes techniques pour évaluer les systèmes ou composants souhaités, dans le but principal de surveiller sans causer d'altérations ou de dommages. Ces techniques peuvent reposer sur les principes de la propagation du son, des champs électromagnétiques et des radiations nucléaires, par exemple. Elles sont des outils importants pour assurer leur sécurité et fiabilité à long terme en identifiant les risques potentiels sans causer de dommages à la structure. Parmi elles, on trouve le test par ondes guidées [6].

Le test par ondes guidées est couramment utilisé pour les structures longues telles que les pipelines et les voies ferrées. Il repose sur la capacité des ondes guidées à se propager sur de longues distances et peut être utilisé pour surveiller des parties du système qui ne sont normalement pas accessibles à d'autres types de techniques. En général, cela implique la génération d'ondes guidées qui se propagent le long de la structure et des signaux réfléchis (également appelés échos) produits par une source de diffusion et enregistrés à un ou plusieurs points de mesure [5, 7].

Les sources de diffusion d'ondes sont couramment associées à un défaut dans des guides d'ondes homogènes. Cependant, les jonctions coudées et autres éléments de couplage liant deux guides d'ondes peuvent également diffuser des ondes guidées. Le signal réfléchi dépend fortement des interactions des ondes avec eux [8, 9]. Un défi consiste à interpréter les signaux émis par des structures complexes composées d'une jonction et d'un défaut [10, 11]. La modélisation de ces systèmes est nécessaire pour une compréhension plus approfondie des phénomènes de diffusion et de la localisation des défauts.

Ce chapitre introduit le concept d'ondes guidées pour les inspections. L'équation d'onde est présentée pour modéliser les ondes volumiques et guidées. L'exemple des tuyaux est discuté. Les résultats de la littérature sur l'interaction des ondes et des défauts/jonctions sont également discutés. Enfin, quelques méthodes numériques pour simuler la propagation des ondes dans les guides d'ondes sont brièvement présentées.

Conclusions

De nombreux articles ont abordé l'utilisation des ondes guidées pour détecter les défauts dans les guides d'ondes, montrant qu'elles sont pertinentes pour le CND. L'approche implique d'analyser à la fois les signaux sources et réfléchis. Pour les pipelines simples et droits, le processus de localisation d'un défaut est simple et est réalisé en décomposant le signal temporel en termes de modes de propagation. Cependant, un élément de couplage de forme arbitraire (comme une jonction coudée) peut compliquer l'analyse car une conversion de mode se produit pendant la transmission et la réflexion, ce qui entraîne un signal réfléchi potentiellement dégradé difficile à interpréter. Par conséquent, pour améliorer les méthodes existantes, il est essentiel d'étudier numériquement l'interaction entre les ondes guidées et les jonction courbées, c'est-à-dire les ondes transmises et réfléchies. Pour cette tâche, la méthode WFE semble appropriée car elle permet le calcul des modes d'ondes dans un guide d'ondes. De plus, à la connaissance de l'auteur, l'impact des jonction courbées dans les pipelines remplis de fluide n'a pas été exploré en profondeur dans la littérature et mérite une enquête plus approfondie.

Chapitre 2: La méthode Wave Finite Element (WFE)

Contexte

La méthode WFE est une procédure numérique basée sur les conditions périodiques de Floquet-Bloch et la méthode des éléments finis pour décrire la réponse dynamique des structures périodiques, c'est-à-dire des structures composées de la répétition d'une cellule unitaire appelée "sous-structure". La méthode WFE examine la propagation des ondes et la réponse forcée des structures simples et complexes. À l'origine, elle a été développée pour analyser la propagation

des ondes dans des structures périodiques 1D. Ses fondements proviennent des travaux de Orris et Petyt [12, 13], Mead [14–18], entre autres. Plus tard, le formalisme de la méthode WFE a ensuite été amélioré à travers différents travaux [19–24].

L'idée principale de la méthode WFE est de calculer les courbes de dispersion et la réponse forcée pour des systèmes longs en utilisant le modèle EF d'une sous-structure. Par conséquent, cela permet de réduire le temps de calcul. La relation entre le déplacement et la force de deux sous-structures consécutives est établie en utilisant une méthode de matrice de transfert, où la matrice de transfert est désignée par \mathbf{S} . Cela permet le calcul des modes d'ondes de voyage, c'est-à-dire les formes de mode et les nombres d'onde. En conséquence, le déplacement et les forces d'une structure périodique peuvent être développés en termes des modes d'ondes. Les problèmes numériques concernant la méthode ont été abordés de différentes manières dans la littérature. Par exemple, la méthode WFE considère un problème aux valeurs propres associé à la matrice de transfert, qui est sujet à un mauvais conditionnement car il implique des vecteurs propres avec des petites et grandes composantes. Pour surmonter cela, Zhong et Williams [25] ont proposé un schéma alternatif au problème aux valeurs propres basé sur la transformation $\mathbf{S} + \mathbf{S}^{-1}$. De plus, certaines applications nécessitent des modèles EF de grande taille, ce qui conduit à des calculs fastidieux. Dans ces cas, certaines stratégies ont été proposées en utilisant des stratégies de réduction d'ordre modal, des procédures de condensation et la réduction de la base d'ondes propagatives [26–28].

En termes d'application, la méthode a été largement utilisée pour étudier différents types de structures, par exemple, des structures de type poutre [28–30], des plaques [19, 31], des tuyaux avec ou sans fluides [32–34], des matériaux piézoélectriques [35, 36], des structures avec symétrie cyclique [37], des structures rotatives [38, 39], des structures hélicoïdales [40]. Lorsqu'on considère une périodicité 2D, la propagation des ondes a également été explorée via la méthode WFE dans [20, 41, 42]. Bien que la méthode ne soit applicable qu'aux structures périodiques, différentes structures peuvent être assemblées au moyen d'éléments de couplage. Cela permet la description de la propagation des ondes dans des tuyaux ou des structures de

type poutre composées de guides d'ondes droits et de jonction courbés [28, 29, 43].

Le reste du chapitre est organisé comme suit. Dans la section 2.2, la formulation de la méthode WFE est détaillée, montrant comment les modes d'ondes peuvent être calculés à l'aide de la matrice de transfert d'une sous-structure. La section 2.3 se concentre sur le calcul de la réponse forcée. Le calcul de la réponse dans le domaine temporel de la structure périodique via la transformée de Fourier est discuté dans la section 2.4. Dans la section 2.5, le calcul des vitesses de groupe et d'énergie est expliqué. Dans la section 2.6, quelques exemples numériques sont proposés pour illustrer la pertinence de l'approche. L'étude des structures périodiques avec des éléments de couplage est abordée dans la section 2.7.

Conclusions

Dans ce chapitre, la méthode WFE a été introduite. Elle permet l'analyse des courbes de dispersion et des réponses forcées pour les structures périodiques. Deux structures spécifiques ont été discutées, à savoir une poutre de Timoshenko et une poutre à contraintes planes 2D. En ce qui concerne la poutre de Timoshenko, les courbes de dispersion et les fonctions de réponse ont été obtenues et comparées aux solutions analytiques. Le deuxième exemple a fourni une comparaison entre les méthodes EF et WFE. Il a été démontré que la méthode WFE peut être utilisée pour calculer la réponse transitoire des structures périodiques et les vitesses de groupe pour les ondes guidées. De plus, la méthode WFE peut être utilisée pour modéliser des guides d'ondes connectés via des éléments de couplage tels qu'une jonction coudée. La modélisation des éléments de couplage repose sur la modélisation EF et la méthode CB. La méthode WFE permet le calcul des ondes diffusées (transmises et réfléchies) au niveau des éléments de couplage. En ce qui concerne les économies de temps de calcul, la méthode WFE est une alternative efficace à la méthode EF, en particulier lorsqu'il s'agit de structures longues.

Chapitre 3: Localisation de défauts dans un guide d'ondes avec des jonctions coudées

Contexte

Une approche numérique est proposée pour localiser les défauts dans des guides d'ondes élastiques connectés à des jonctions élastiques courbées. Des ensembles 2D impliquant des guides d'ondes droits avec une jonction coudée et un défaut sont spécifiquement traités, où la jonction est placée entre le point de mesure (signaux de sortie) et le défaut. Une telle analyse nécessite d'évaluer les phénomènes de conversion d'ondes et les temps de vol des paquets d'ondes lorsqu'ils sont transmis à travers la jonction et réfléchis par le défaut. Une stratégie WFE originale est proposée où les temps de vol, pour les paquets d'ondes transmises ou réfléchies, sont définis à partir des dérivées de fréquence des arguments des matrices de diffusion de la jonction et du défaut. La procédure de localisation d'un défaut découle des expressions des temps de vol. L'approche proposée permet l'identification des types d'ondes qui sont transmises à travers la jonction et réfléchies par le défaut. Des expériences numériques sont menées, mettant en évidence la pertinence, en termes de précision et de robustesse, de l'approche proposée.

L'idée clé de ce chapitre est que les temps de vol pour les paquets d'ondes voyageant dans un élément de couplage (jonction, défaut), en transmission ou en réflexion, peuvent être déterminés à partir des dérivées de fréquence des arguments de sa matrice de diffusion. Les temps de propagation dans les guides d'ondes découlent de l'analyse des vitesses de groupe. En ce sens, une expression théorique du temps mis par les paquets d'ondes incidents pour se propager et être transmis/réfléchis par une jonction/défaut peut être proposée. La position du défaut peut être déterminée en comparant ces temps de vol théoriques avec les temps de vol expérimentaux (mesures). L'approche proposée fournit également un aperçu physique des types d'ondes qui sont transmises à travers la jonction et réfléchies par le défaut (trajectoires). Les contributions de cette partie peuvent être résumées comme suit :

- Expression des temps de vol pour les paquets d'ondes voyageant dans des éléments de

couplage (jonction, défaut) à partir des dérivées de fréquence des arguments de leurs matrices de diffusion.

- Identification des types d'ondes qui sont transmises/réfléchies par une jonction/défaut (trajectoires).
- Fourniture d'une procédure pour localiser un défaut pour différentes trajectoires possibles.

Le reste du chapitre est organisé comme suit. Dans la section 3.2, le modèle EF d'un ensemble de guide d'ondes, comprenant un défaut et une jonction coudée, est présenté. Les problèmes associés à la localisation des défauts sont discutés. Dans la section 3.4, des expressions théoriques des temps de vol en transmission et en réflexion, pour un élément de couplage, sont données. De plus, la procédure pour estimer la position d'un défaut à partir des temps de vol mesurés et théoriques/estimés est détaillée. Dans la section 3.6, des expériences numériques sont menées, portant sur des ensembles de guides d'ondes avec des jonctions courbés de différents angles de courbure et des défauts représentant des trous circulaires de différents rayons.

Conclusions

Ce chapitre propose une approche WFE pour localiser les défauts dans des ensembles de guides d'ondes avec des jonction courbées. Cette stratégie utilise la matrice de diffusion issue de la méthode WFE pour évaluer les paquets d'ondes transmis et réfléchis à travers la jonction, et pour localiser un défaut. Des ensembles en 2D comprenant des guides d'ondes élastiques droits, une jonction élastique coudée et un défaut ont été traités. L'approche proposée fournit des expressions théoriques des temps de vol en transmission ou en réflexion pour les paquets d'ondes se déplaçant dans les éléments de couplage (jonction, défaut). De plus, elle fournit des renseignements sur la nature des ondes qui sont transmises à travers la jonction et réfléchies par le défaut (trajectoires). La position du défaut peut être déterminée en comparant les expressions théoriques des temps de vol avec celles enregistrées dans un ensemble de guides d'ondes. Des expériences numériques sur des poutres en 2D en état plan de contrainte et des tuyaux en 3D ont été réalisées pour démontrer l'exactitude et la robustesse de l'approche proposée pour localiser

un défaut à partir de l'analyse de différents paquets d'ondes réfléchis (plusieurs types d'ondes). L'approche proposée est destinée à être générale et pourrait être utilisée pour localiser des défauts simples ou multiples dans des réseaux de guides d'ondes, y compris plusieurs jonctions coudées.

Chapitre 4: Guides d'ondes élasto-acoustiques

Contexte

Les pipelines remplis de fluide sont utilisés dans diverses industries, notamment le gaz, le pétrole, la distribution d'eau et le génie civil. Par conséquent, l'entretien et la surveillance des pipelines sont cruciaux pour garantir leur intégrité et prévenir les pertes financières. Dans de vastes réseaux de pipelines, le CND à l'aide d'ondes guidées émerge comme une technique utile à cet égard. La compréhension de la propagation des ondes dans les pipelines remplis de fluide est notamment importante lorsque des ondes guidées sont utilisées. En particulier, l'interaction des ondes élasto-acoustiques avec les défauts et les jonctions est importante pour améliorer les techniques de CND.

La localisation des défauts dans les pipelines remplis de fluide a été étudiée de différentes manières. Aristégui et al. [44] ont étudié la propagation des ondes dans les tuyaux avec des fluides internes et externes. Ils ont obtenu un bon accord entre les expériences et les courbes de dispersion calculées par une approche FE. Plus récemment, Vogelaar et Golombok [45] ont étudié expérimentalement la détection de dommages en utilisant le mode de torsion avec différents fluides internes et externes. Ils ont montré que différents fluides internes et externes atténuent le mode de torsion, réduisant ainsi la portée d'inspection de la technique. Cependant, ils ont affirmé que le mode de torsion est adapté à la détection des défauts de tuyauterie. Étant donné que, en général, le mode de torsion fondamental $T(0, 1)$ n'est pas dispersif, il est facile à générer à l'aide de transducteurs, et l'énergie est confinée au tuyau et ne se propage pas. [46–49].

Il est possible de déterminer les courbes de dispersion des ondes propagées dans les tuyaux axisymétriques remplis de fluide, comme discuté par Fuller et Fahy [50] et Sato et Ogiso [51].

Cependant, pour les tuyaux complexes, les solutions analytiques ne sont pas évidentes. Ensuite, les méthodes numériques deviennent un outil essentiel. Néanmoins, pour les structures longues, la méthode des éléments finis devient un défi computationnel numériquement parlant car elle implique de nombreux éléments, ce qui entraîne un grand nombre de degrés de liberté. Pour résoudre ce problème, la méthode WFE est une alternative précieuse.

Mencik et Ichchou [32] ont appliqué la méthode WFE aux tuyaux remplis de fluide pour calculer les courbes de dispersion. Bhuddi et al. [34] ont étudié la propagation des ondes dans des tuyaux axisymétriques remplis de fluide entourés d'un fluide en utilisant la méthode WFE combinée à une couche parfaitement adaptée (PML). Kingan et al. [52] ont analysé la réponse d'un système orthotrope. Manconi et al. [53] ont appliqué la méthode pour analyser des tuyaux précontraints stratifiés remplis de fluide. Maess et al. [54, 55] ont développé une stratégie pour calculer les vitesses d'énergie et de groupe dans le cadre de la méthode WFE. Dans leurs travaux, ils ont analysé des tuyaux droits et ondulés contenant un fluide.

Jusqu'à présent, les études se sont concentrées sur l'analyse de la propagation des ondes dans des systèmes droits, négligeant le phénomène de conversion de mode en présence d'éléments de couplage tels que les jonctions courbées et les défauts. Il est donc important d'incorporer la modélisation de tels éléments de couplage dans la méthode WFE, car cela n'a pas encore été fait dans la littérature du point de vue de la conversion de mode.

Dans le cadre de la méthode WFE, les éléments de couplage sont généralement modélisés via des modèles FE qui peuvent contenir un grand nombre de degrés de liberté puisque des structures remplies de fluide sont considérées. Cela peut entraîner des coûts de calcul élevés, même avec la méthode WFE. Ainsi, une modélisation non réduite de l'élément de couplage peut être considérée comme naïve, et une stratégie de réduction de modèle est nécessaire.

En ce qui concerne la réduction de modèle impliquant des tuyaux remplis de fluide et des modèles FE, Maess et Gaul [56] ont adopté une synthèse de modes de composants en utilisant la méthode CB et un solveur de sous-espace itératif pour générer une approximation du problème

à basse fréquence. Plus tard, Herrmann et al. [57] ont fourni une approche FE pour simuler des pipelines en utilisant la sous-structuration dynamique et une réduction d'interface. Pour cette tâche, ils ont appliqué la méthode CB à des problèmes vibro-acoustiques et ont utilisé une réduction d'interface basée sur des vecteurs de Ritz.

En outre, une réduction basée sur la projection modale peut être envisagée, où les parties acoustique et élastique sont découplées. Cependant, pour assurer la convergence, il est nécessaire de fournir des corrections en utilisant des vecteurs d'enrichissement [58]. Tournour et Atalla [59] ont démontré que la base modale découplée donne une mauvaise convergence car les modes haute fréquence d'un sous-système peuvent être couplés aux modes basse fréquence de l'autre. Pour résoudre ce problème, ils ont proposé des corrections pseudo-statiques dans les deux sous-systèmes. Tran et al. [60] ont utilisé des systèmes découplés enrichis ultérieurement par des termes de correction statique. Cette approche sera utilisée dans ce manuscrit pour modéliser les éléments de couplage dans le cadre de la méthode WFE.

Cette section est organisée comme suit. Dans la section 4.2, la méthode WFE pour les guides d'ondes élasto-acoustiques est présentée. Quelques simulations sont effectuées pour calculer les courbes de dispersion et les vitesses de groupe des modes élasto-acoustiques, et une comparaison entre la réponse de force émise par les méthodes FE et WFE est fournie. Ensuite, dans la section 4.3, une réduction CB pour les éléments de couplage combinée à une technique d'enrichissement est présentée dans le cadre de la méthode WFE. Des résultats numériques sont fournis concernant la réduction CB, les coefficients de transmission et de réflexion. Enfin, une application numérique de l'approche proposée pour localiser un défaut dans des tuyaux remplis de fluide avec une jonction coudée est analysée.

Chapitre 5: Conclusions

Ce chapitre a analysé la propagation des ondes dans des tuyaux remplis de fluide avec des jonctions et des défauts. Les modes de propagation dans les tuyaux ont été obtenus avec succès en utilisant la méthode WFE. Pour le cas des tuyaux droits remplis de fluide, une comparaison

entre les méthodes FE et WFE a été fournie, où une réduction considérable du temps de calcul a été observée. Cela démontre la précision et l'efficacité de la méthode WFE par rapport à la méthode FE classique. De plus, dans le cadre de la méthode WFE, une stratégie de réduction a été proposée pour calculer efficacement les matrices de rigidité dynamique réduits des éléments de couplage. Une jonction courbe reliant deux guides d'ondes a été analysée, et une comparaison entre les résultats WFE et FE dans les domaines temporel et fréquentiel a été fournie. Dans l'ensemble, la stratégie permet une réduction de 65% avec une erreur de 0,5% pour calculer la réponse vibroacoustique.

Enfin, les coefficients de diffusion ont été calculés pour les défauts et les jonctions coudées. Pour les défauts, il n'y avait pas de différence significative entre les cas rempli de fluide et vide. Cependant, des différences dans la transmission et la réflexion produites en raison de la présence de fluide ont été observées pour les jonctions. Le cas d'un défaut après la jonction a été exploré et le concept de temps de vol dans la transmission à travers la jonction s'est avéré précis et pertinent pour estimer la localisation du défaut.

Chapitre 5: Conclusions et perspectives

Dans cette thèse, nous avons étudié certains aspects de la détection et de la localisation de défauts dans des assemblages composés de guides d'ondes droits, de jonctions coudées et de défauts. En particulier, ce travail a fourni des informations sur l'interaction des ondes guidées au niveau des défauts et des jonctions coudées. Ces phénomènes ont été simulés numériquement à l'aide de la méthode WFE.

Dans le chapitre 2, les fondements de la méthode WFE ont été rappelés. La méthode WFE a été utilisée pour modéliser des structures périodiques, c'est-à-dire des structures composées d'un assemblage de sous-structures. Cela a permis le calcul des modes d'ondes et de la réponse forcée dans les domaines temporel et fréquentiel. Dans ce cadre, il est possible de simuler des guides d'ondes liés à des éléments de couplage, tels que des jonctions et des défauts, qui peuvent être modélisés à l'aide de la méthode FE et de la réduction CB. De plus, des expériences

numériques ont été menées pour montrer la robustesse et l'exactitude de la méthode WFE. Des comparaisons entre les solutions WFE et la théorie analytique pour les courbes de dispersion et la réponse forcée dans le domaine fréquentiel ont été fournies ; également, une comparaison entre les solutions WFE et FE pour évaluer les réponses forcées dans les domaines temporel et fréquentiel a été proposée. Enfin, une étude de deux guides d'ondes connectés avec un élément de couplage a été présentée et le concept de matrices de diffusion a été exploré. Le WFE s'est avéré pertinent et efficace pour fournir des solutions précises pour la propagation des ondes dans des guides d'ondes droits avec/sans éléments de couplage.

Dans le cadre du formalisme des matrices de diffusion, une stratégie de localisation d'un défaut dans des structures contenant une jonction coudée a été proposée dans le chapitre 3. Cette stratégie est basée sur le calcul du temps de vol qu'un paquet d'ondes étroit met à être transmis ou réfléchi au niveau d'un élément de couplage. Il a été prouvé que le temps de vol peut être calculé en considérant les dérivées par rapport à la fréquence des arguments des matrices de diffusion de la jonction et du défaut. De plus, un aperçu physique des ondes transmises et réfléchies au niveau d'un élément de couplage a été fourni. Des simulations numériques ont été réalisées pour vérifier l'approche proposée. Tout d'abord, le cas d'une poutre en 2D en contrainte planes a été discuté en considérant des guides d'ondes avec un défaut et des guides d'ondes avec une jonction coudée et un défaut. Il a été démontré que la prise en compte du temps de vol dans la transmission et la réflexion à travers la jonction est pertinente pour localiser le défaut avec précision. En plus de se concentrer sur les jonctions coudées, cette approche vise à être généralisée aux cas d'éléments de couplage complexes.

Enfin, dans le chapitre 4, le cas de structures élasto-acoustiques a été considéré. La méthode WFE utilisait une formulation symétrique du problème élasto-acoustique dans laquelle le vecteur de déplacement est considéré pour la partie élastique et le potentiel de vitesse est considérée pour la partie acoustique. Cela a permis le calcul des modes de propagation des ondes, de leurs courbes de dispersion et de leurs vitesses de groupe. En ce qui concerne les éléments de couplage, une stratégie basée sur la réduction CB avec des bases de vecteurs d'enrichissement a

été proposée. La stratégie de réduction a été testée pour garantir sa validité et sa robustesse. Avec cette stratégie de réduction, la transmission de puissance et la réflexion des ondes pour différents défauts et jonctions ont été analysées. Il a été montré que le mode de torsion constitue une bonne option pour réaliser le CND. En ce qui concerne la détection des défauts, la stratégie de localisation d'un défaut après une jonction a été appliquée, en considérant différents angles de courbure pour la jonction. Il a été montré que le temps de vol est sensible à la présence de fluide. Dans ce cas, il est recommandé de prendre en compte le temps de vol de la jonction élasto-acoustique pour détecter le défaut avec précision.

Perspectives:

Certains sujets pourraient être envisagés pour des perspectives futures et un développement ultérieur :

- Une question importante à résoudre est de savoir si la gravité d'un défaut placé après une jonction peut être estimée. Lorsqu'il n'y a qu'un défaut présent, sa sévérité peut être évaluée. Cependant, les phénomènes de conversion des modes d'onde se produisant dans une jonction peuvent masquer des informations importantes à cet effet, telles que l'amplitude de l'onde réfléchie causée par le défaut;
- Examiner et proposer une stratégie pour localiser un défaut lorsque plusieurs jonctions coudées sont présents dans le système. Cela semble être un défi car plusieurs conversions de mode peuvent se produire, rendant l'interprétation des signaux difficile. À notre connaissance, cela n'a pas été exploré dans la littérature;
- Étudier l'interaction entre les ondes propagatives et les non-linéarités locales dans des structures périodiques infinies. À cet égard, Duhamel et Mencik [61] ont développé une méthode pour les structures périodiques infinies contenant des non-linéarités locales dans le domaine temporel. Cependant, il semble que l'approche proposée n'ait pas été appliquée au CND ;

- Proposer une stratégie pour réduire la base d'enrichissement CB pour un élément de couplage élasto-acoustique en fonction de la sélection des vecteurs gauches $\tilde{\mathcal{U}}^E$ et $\tilde{\mathcal{U}}^A$ lors de la décomposition SVD, voir Sec. 4.3.1 et 4.4.1. Incorporer également la réduction des bases d'onde proposée par Droz et al. [27]. Ces deux stratégies semblent ensemble optimiser les coûts de calcul dans le cadre du WFE ;
- Analyser la propagation des ondes et la détection des défauts dans les tuyaux remplis de fluide, avec un écoulement moyen. Cela semble être significatif car cela est couramment rencontré dans les situations industrielles. Il convient de souligner que, dans le cadre du WFE, la prise en compte de la vitesse de l'écoulement entraîne une matrice \mathbf{S} qui n'est plus symplectique ;
- Étudier l'optimisation topologique des éléments de couplage et/ou des sous-structures pour manipuler la propagation des ondes : bandes d'arrêt, coefficients de diffusion, entre autres propriétés ;

Introduction

Pipelines are essential for transporting production goods in the energy industry, playing a vital role in the global economic system. They connect extraction points, refineries, factories, and residences. According to Wang et al. [1], there were 201.9×10^3 km of pipelines in service by the end of 2020, including those for natural gas, crude oil, and product oil, leading to significant challenges in managing and monitoring them.

Maintaining and monitoring this vast pipeline system involves various techniques and procedures. Kraidi et al. [2] identified several risk factors, such as improper inspection & maintenance and corrosion, that directly impact pipelines. Non-destructive testing (NDT) like X-ray diffraction, magnetic strain, and guided wave techniques are commonly used to mitigate these risks. Specifically, guided wave tests rely on wave propagation in the media, and it is extensively used to detect and monitor cracks and corrosion. Recently, AI algorithms have been introduced to enhance defect detection and manage risks more effectively. [3, 4].

When working with extended pipelines, guided wave testing is the preferred method for defect detection. This approach involves generating guided waves and measuring their reflection to identify defects' presence, type, and location. However, the interpretation of the reflected signal can be drastically modified by curved joints that connect waveguides, due to scattering phenomena. Additionally, these waves' multi-modal and dispersive nature adds complexity to the process. Notwithstanding, the case of a defect after a joint is even more complex and still deserves a better understanding [5].

In this sense, studying wave propagation and its interaction with defects is essential for interpreting collected signals. Thus, developing appropriate numerical tools that accurately describe this phenomenon is vital. Classical methods, such as the Finite Element (FE) method, can result in high computation costs, especially for long structures. To overcome these limitations, wave-based methods have been used, for example, the Wave Finite Element (WFE) and Semi-Analytical Finite Element (SAFE) methods.

This thesis applies the WFE method to model wave propagation and wave scattering in structures composed of waveguides linked by coupling elements. In this framework, curved joints and defects are modeled via FE, allowing the computation of transmission and reflection coefficients. The first part develops a strategy to localize a defect after a joint based on the scattering matrices. In the second part, a reduction model of elasto-acoustic coupling elements in the WFE framework is presented, enabling a time reduction in the computation of scattering matrices.

Organization of the manuscript

Chapter 1 presents concepts involved in the NDT technique for defect localization. A basic introduction to wave propagation in infinite and finite media is shortly presented. Next, the interaction of guided waves with defects/curved joints is briefly described based on the published literature. Those studies highlight the importance of simulations and experiments for improving guided wave techniques.

Chapter 2 presents the WFE method. The strategies involved in the computation of dispersion curves and wave shapes are presented. Also, the forced frequency and time domain responses are described. Next, the computation of group velocities in the WFE framework is presented. Examples are then proposed to validate the approach. Coupling elements are introduced to describe non-periodic elements between waveguides and are modeled using scattering matrices. This is done by combining the FE-based Craig-Bampton (CB) reduction and the WFE approaches. Finally, an example of two straight waveguides connected via a

coupling element is shown.

In Chapter 3, a numerical approach based on the WFE method is proposed to localize defects in straight elastic waveguides connected by a curved elastic joint. This strategy considers the wave mode conversion phenomena and times of flights when a wave packet is transmitted through the joint and reflected by the defect. The time of flight is computed using the scattering matrix formalism. Numerical experiments are carried out involving straight waveguides connected by a curved joint and a defect, where the measurement point is placed before the joint. The approach is applied to 2D plane-stress beams and 3D pipes, which highlights the accuracy and robustness of the proposed approach.

Chapter 4 presents the modeling of elasto-acoustic systems involving straight waveguides and curved joints. Straight waveguides are modeled via the WFE method, which allows access to the dispersion curves, wave shapes, and group velocities. Elasto-acoustic coupling elements are introduced in this framework. As it involves a large number of degrees of freedom, the computation of their condensed dynamic stiffness matrix is obtained via a CB reduction with a basis enrichment technique. Numerical experiments are provided. The dispersion curves and group velocities are discussed, and a comparison between the WFE and the FE results in the frequency and time domains is provided. Finally, reflection and transmission coefficients for curved joints and defects are compared to those of pipes without internal fluids.

Finally, in Chapter 5, the main results and contributions of this work are summarized. Future perspectives and follow-up works are also discussed.

Chapter 1

Guided waves and non-destructive testing

1.1 Overview

Non-destructive testing (NDT) is crucial in maintaining and monitoring the integrity of structures. This includes different techniques to evaluate the desired systems or components, with the primary objective of monitoring without causing any alterations or harm. These techniques can rely on the principles of sound propagation, electromagnetic fields, and nuclear radiation, for example. They are important tools to ensure their long-term safety and reliability by identifying potential risks without causing any damage to the structure. Among them is guided wave testing. [6]

Guided wave testing is commonly used for long structures such as pipelines and railway tracks. It is based on the ability of guided waves to propagate over long distances, and it can be used to monitor parts of the system that are not normally accessible by other types of techniques. In general, this involves the generation of guided waves that propagate along the structure and reflected signals (also known as echoes) produced by a scattering source and recorded at one or

more measuring points [5, 7].

Wave scattering sources are commonly associated with a defect in homogeneous waveguides. However, curved joints and other coupling elements linking two waveguides can also scatter guided waves. The reflected signal strongly depends on the wave's interactions with them [8, 9]. One challenge is interpreting signals issued from complex structures composed of a joint and a defect [10, 11]. Modeling these systems is necessary for a deeper understanding of scattering phenomena and defect localization.

This chapter introduces the concept of guided waves for inspections. The wave equation is presented to model bulk and guided waves. The example of pipes is discussed. Results from the literature about the interaction of waves and defects/joints are also discussed. Finally, some numerical methods are briefly presented to simulate wave propagation in waveguides.

1.2 Wave propagation

Wave propagation in elastic infinite media can be modeled using the classical theory of elasticity for continuum media undergoing small deformations. The Navier governing equations can be used for this task. [62, 63]

Let us consider a linear, isotropic, and infinite solid medium with density ρ . Also, let us denote the Young modulus by E and the Poisson ratio by ν . The displacement $\mathbf{u}(\mathbf{x}, \omega)$ in this solid is modeled through the elastodynamic equation in the frequency domain:

$$-\rho\omega^2\mathbf{u}(\mathbf{x}, \omega) = \frac{E}{(1+\nu)(1-2\nu)}\nabla(\nabla \cdot \mathbf{u}(\mathbf{x}, \omega)) + \frac{E}{2(1+\nu)}\nabla^2\mathbf{u}(\mathbf{x}, \omega), \quad (1.1)$$

where ω represents the angular frequency, which is related to the frequency f by the relation $\omega = 2\pi f$. The above equation is known as the wave equation and can be solved using the Helmholtz decomposition theorem. The displacement $\mathbf{u}(\mathbf{x}, \omega)$ can be expanded in function of a scalar potential ϕ and a vector potential Ψ as follows

$$\mathbf{u}(\mathbf{x}, \omega) = \nabla\phi + \nabla \times \boldsymbol{\Psi}, \quad (1.2)$$

with $\nabla \cdot \boldsymbol{\Psi} = \mathbf{0}$. Inserting Eq. (1.2) into Eq. (1.1) leads to two independent equations for ϕ and $\boldsymbol{\Psi}$

$$-\omega^2\phi = c_{\text{P}}^2\nabla^2\phi \quad \text{and} \quad -\omega^2\boldsymbol{\Psi} = c_{\text{S}}^2\nabla^2\boldsymbol{\Psi}, \quad (1.3)$$

where

$$c_{\text{P}} = \sqrt{\frac{E(1-\nu)}{(1+\nu)(1-2\nu)\rho}} \quad \text{and} \quad c_{\text{S}} = \sqrt{\frac{E}{2\rho(1+\nu)}}. \quad (1.4)$$

In Eq. (1.3), two different propagating waves (also known as bulk waves) can be obtained using the Helmholtz decomposition and are classified as compressional wave (P), which is associated with the scalar potential and shearing wave (S) which is related to the vector potential. Their propagation velocities only depend on the material parameters of the medium and are given by Eq. (1.4). For compressional waves, the material particles move in the same direction of the wave propagation, and for shear waves, the particle moves perpendicularly to the direction of the wave propagation.

The compressional and shearing waves are the only two possible propagating waves in infinite and unbounded medium. They do not interact with each other and are non-dispersive, meaning that their wave velocities do not depend on the frequency. However, different waves, called guided waves, appear in the presence of boundaries in finite or semi-finite media. They are present and used in non-destructive evaluation and are introduced hereafter.

1.3 Guided waves

Here, various aspects of wave propagation are discussed. Concisely, the phase velocity denotes the velocity at which an individual wave (monochromatic) travels, while the group velocity denotes the speed of propagation for a wavepacket; and, essentially, a wavepacket can be understood as the combination of monochromatic waves [62].

Guided waves result from wave interference phenomena induced by the system's boundaries. Plates, beams, and pipes are examples of finite structures in which guided waves can be produced and propagated. Bulk waves have a constant phase velocity and are non-dispersive. Whereas in guided waves, the phase velocity is generally a function of the frequency, and the group velocity is not equal to the phase velocity and is generally dispersive. Moreover, guided waves can travel long distances without experiencing significant energy loss [64].

Guided wave analysis starts by considering Eq. (1.1) with the imposed boundary conditions. The equations are formulated in the frequency domain, resulting in dispersion curves for each wave mode and/or family of modes — i.e., the relation between the wavenumber (β_j) and the frequency. It is important to note that the number of propagating modes is unlimited and increases indefinitely with higher frequencies. Furthermore, the dispersion curves can be used to express the group and energy velocities [62]. The phase velocity (c_{pj}) and the group velocity (c_{gj}) for a mode j can be computed as follows:

$$c_{pj} = \frac{\omega}{\Re\{\beta_j\}} \quad \text{and} \quad c_{gj} = \frac{\partial\omega}{\partial\Re\{\beta_j\}}, \quad (1.5)$$

with $\Re\{\beta_j\}$ represents the real part of β_j . The knowledge of the wavenumber and wave modes as a function of frequency is primordial in wave propagation analysis.

The dispersion relations can be obtained analytically for simple structures like pipes. For more complex structures, numerical methods are required, such as the SAFE method [65–67], the WFE method [14, 21, 68], and the SE method [69]. The simulation of guided waves in the

time domain is usually done via the FE method [70, 71].

For example, the dispersion curves for pipes are well-known and can be found analytically, see [72, 73]. The solution is based on Eq. (1.1) using cylindrical coordinates and free-surface conditions. As a result, different wave modes can be found and categorized. It is customary to classify them into three distinct families: flexural modes $F(\mathbf{m}, \mathbf{n})$, longitudinal modes $L(0, \mathbf{n})$, and torsional modes $T(0, \mathbf{n})$. Here, the variable \mathbf{m} denotes the circumferential order of a mode, while \mathbf{n} represents the group order. For axisymmetric modes, the circumferential order $m = 0$ [6, 74, 75].

In Fig. 1.1, the group velocities of various modes are plotted against frequency for a steel pipe with an internal radius of 50 mm and a wall thickness of 2.5 mm. The longitudinal modes are shown in red, the torsional modes in green, and the flexural modes in blue, pink, and orange. The torsional mode $T(0, 1)$ is non-dispersive and axisymmetric. The $L(0, \mathbf{n})$ mode is generally dispersive, axisymmetric, and experiences low attenuation. Also, the $L(0, 2)$ mode becomes non-dispersive at high frequencies. $F(\mathbf{m}, \mathbf{n})$ modes are non-axisymmetric, dispersive, and present cut-off frequencies, i.e., where modes become propagating. At high frequencies, the group velocity of $F(\mathbf{m}, 1)$ converges to the group velocity of $L(0, 1)$, $F(\mathbf{m}, 2)$ towards $T(0, 1)$, and $F(\mathbf{m}, 3)$ towards $L(0, 2)$. The phase velocity for the torsional mode $T(0, 1)$ is expressed as:

$$c_{T(0,1)} = \sqrt{\frac{E}{2(1+\nu)} \cdot \frac{1}{\rho}}. \quad (1.6)$$

Some observations about the mode $T(0, 1)$ can be made: it is a non-dispersive mode; its phase and group speed are equal; its propagation speed is the same as that found for the shearing wave speed in Eq. (1.4).

It is known that the internal radius and the wall thickness mainly determine the dispersion curves for pipes. The inner radius plays a significant role in the dispersion curves of flexural modes, and the thickness wall in the longitudinal modes [76]. In terms of mode generation, axisymmetric modes can be purely excited using a uniform excitation over the circumference of the pipe using a ring of transducers. The flexural modes can be generated using excitations

that are normal to the pipe surface [6].

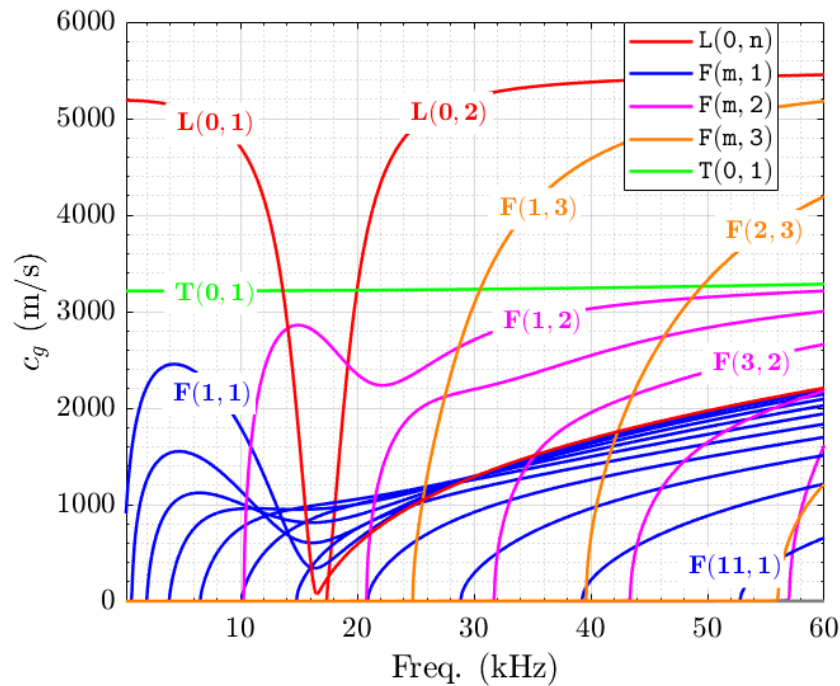


Figure 1.1: Group velocity as the function of frequency for a steel pipe with an internal radius of 50 mm and wall thickness of 2.5 mm. Longitudinal modes are plotted in red, the torsional mode in green, and the flexural modes in blue, pink, and orange.

Fig. 1.2 shows the shapes of some wave modes around 40 kHz, where the colors and modes correspond to Fig. 1.1. The longitudinal modes, $L(0,1)$ and $L(0,2)$, can be seen in Figs. 1.2(a) and (b), respectively. The torsional mode, $T(0,1)$ in Fig. 1.2(c). Finally, the flexural modes, $F(1,1)$, $F(1,2)$, and $F(1,3)$, are shown in Figs. 1.2(a), (b), and (c), respectively.

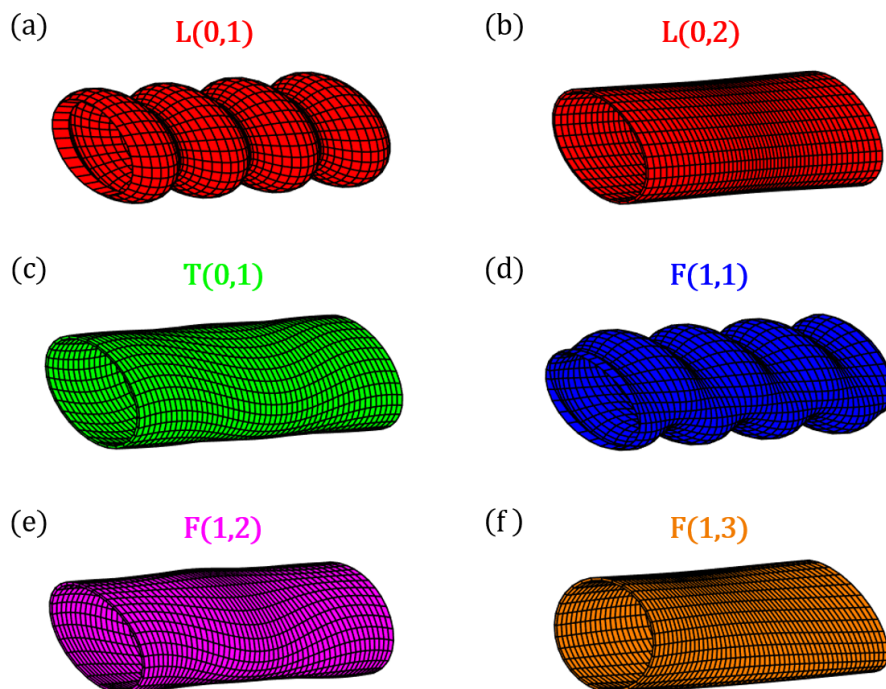


Figure 1.2: Wave modes for a steel pipe with an internal radius of 50 mm and wall thickness of 2.5 mm at 40 kHz: (a) $L(0, 1)$, (b) $L(0, 2)$, (c) $T(0, 1)$, (d) $F(1, 1)$, (e) $F(1, 2)$, and (f) $F(1, 3)$. Colors are in accordance with Fig. 1.1.

1.4 Non-destructive testing using guided waves

Regarding wave propagation, two different techniques can be highlighted [6]: ultrasonic testing and guided wave testing, see Fig. 1.3. During ultrasonic testing, as seen in Fig. 1.3(a), a transducer covers a specific volume along the structure. Then, to examine the whole structure, the transducer is supposed to move along it. This method has a strong penetrating capacity and may be used to determine the thickness of the studied section as well as the size and form of defects. However, it suffers from drawbacks, such as the need for surface preparation, the complexity of the signal for non-homogeneous structures, and the fact that it only covers a

small area. [9]

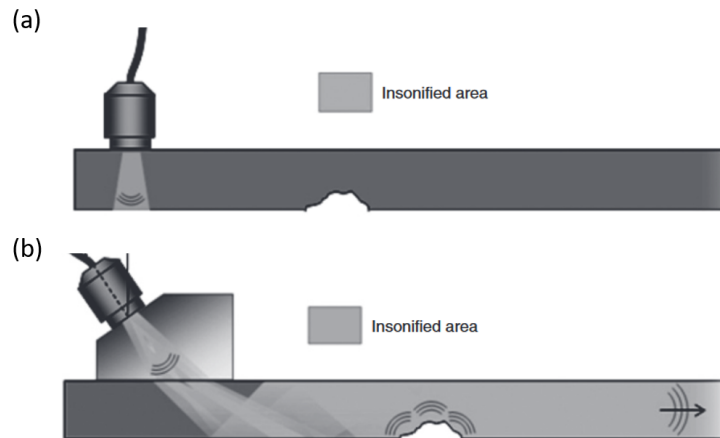


Figure 1.3: Comparison between (a) ultrasonic and (b) guided wave inspections. Adapted from [6].

The guided wave technique involves the generation of a guided wave, which is then converted into reflected and/or transmitted signals measured at one or more points along the structure. It is of interest in situations where access to the interior of a long structure is limited. By analyzing the characteristics of the guided wave and the collected data, technicians can determine the presence, location, and extent of damages or deteriorations within the structure, enabling them to take proactive measures to prevent them and ensure the ongoing safety and reliability of the system.

As seen in Fig. 1.3(b), this technique may cover the whole thickness for long-range inspections and it is widely used for lengthy pipelines and railway rails and can cover the thickness for long-range inspections. Besides its ability to detect internal and external defects, the interpretation of data is complex in the presence of multiple defects and curved joints, for example.

Fig. 1.4 illustrates a real-world engineering application of guided waves in NDT. In Fig. 1.4(a)¹, an example of a pipeline where the accelerators and sensors are placed on the structure is shown. Figs. 1.4(b)¹ and (c)², show trained technicians performing NDT on pipelines.

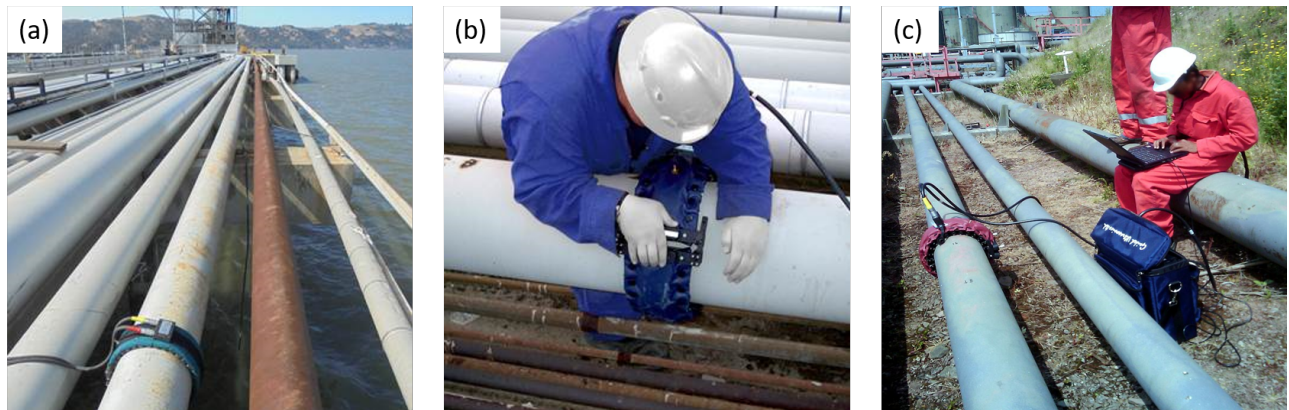


Figure 1.4: Examples of real engineering application of guided waves in NDT : (a) example of a pipeline and the accelerators and detector, (b) and (c) technicians performing the NDT in pipelines.

To optimize signal collection, it is necessary to design the accelerators and sensors specifically for each situation. Figs. 1.5(a), (b), and (c) show three different systems developed by "Guided Ultrasonic Ltd" ³ used in the inspection of large-diameter pipes, sub-sea pipes, and rail inspections, respectively.

¹Available on <https://www.mistrasgroup.com/how-we-help/field-inspections/advanced-ndt/automated-ultrasonic-testing/guided-wave-testing/> Accessed 18 April 2023

²Available on : https://en.wikipedia.org/wiki/Guided_wave_testing Accessed 18 April 2023

³Available on <https://www.guided-ultrasonics.com/> Accessed 20 April 2023



Figure 1.5: Examples of commercial detectors/sources by “*Guided Ultrasonics Ltd.*” used for: (a) inspection of large diameter pipe, (b) subsea inspections, and (c) rail inspections

Signal processing plays a crucial role in identifying propagating modes and the time they take to travel a certain distance. Different signal processing techniques, such as Fourier transforms, wavelet transforms, and digital filtering, are used to post-treat wave signals and identify the different wave modes. It provides information about the structure properties and types of defects. Signal processing is also used to distinguish the noise from the actual signal, which is essential for accurately detecting defects. Overall, signal processing is critical in the NDT process. [77–79]

1.5 Interaction of waves with defects and curved joints

The inspection and monitoring of structures using guided waves was developed around 1970. Since then, the method has been studied and applied to detect defects and mode conversion issued from different defects and curved joints when certain modes are used. [63, 80–83]

In [84, 85], it is shown that a thickness variation of the waveguide directly impacts wave conversion in transmission and reflection. It was observed that when the thickness varies symmetrically, there is mode conversion within the same wave family of modes. On the other hand, non-symmetric thickness variations result in the conversion of waves belonging to different families. Additionally, several recent studies involving NDT in plates corroborate those

results [86–88].

In terms of defect detection, Lowe et al. [89] found that mode conversion from waves of type $L(0, 2)$ to $F(1, 3)$ can be used to identify axisymmetric and non-axisymmetric defects. Bai et al. [90] and Cawley et al. [91] found that the variation of the reflection coefficients of a circumferential crack is dependent on the axial extension of the defect for the modes $L(0, 2)$ and $F(1, 3)$. Also, Demma et al. [92] conducted a numerical and experimental study on the interaction between defects and the torsional mode $T(0, 1)$ from 10 kHz up to 300 kHz. They demonstrated that axisymmetric defects interact with axisymmetric modes. However, non-axisymmetric defects, such as cracks, lead to mode conversion from mode $T(0, 1)$ to mode $F(1, 3)$ at low frequencies and from $T(0, 1)$ to $F(1, 2)$ at high frequencies. Liu et al. [93], experimentally observed mode conversion from $T(0, 1)$ to $F(n, m)$ when two different defects are present (longitudinal and circumferential). Ratassepp et al. [94] showed that the magnitude of the reflection coefficients for the mode $T(0, 1)$ increases with the crack length. Additionally, more recent studies have confirmed and extended the understanding of the interaction of guided waves and defects [95–98].

As mentioned before, the presence of a curved joint yields mode conversion, meaning that an incident wave may change from one type to another as it passes through or is reflected by the joint. For example, a longitudinal wave may be converted into a torsional wave or vice versa. The wave propagation through a curved joint is influenced by different parameters, such as the radius of the joint, its length, and the central frequency of the incoming wave [7]. Demma et al. [99] investigated the transmission and reflection of mode $L(0, 2)$ through a 90-degree curved joint for various radii. They reported that larger curved joint radii, compared to the diameter of the pipe, lead to high transmission rates of the incoming waves. Conversely, mode conversion to other modes is observed for small curved joint radii. Finally, intermediate curved joint radii values produce a time delay in the measured signal. Verma et al. [100] conducted a study on the impact of curved joints on wave propagation using the FE method and experimental techniques. They investigated the transmission and reflection of mode $L(0, 2)$ using different curved joint

angles and radii and demonstrated that the time of flight through it should be considered. They found that the bend can result in a maximum energy loss of 20% during transmission.

Other works have studied the influence of curved joints to localize defects. In [101], the importance of the time of flight is highlighted to localize a defect in a curved joint. Qi et al. [102] used the fundamental torsional mode to analyze the transmission and reflection coefficients in the presence of a damaged 90-degree elbow. Sanderson et al. [103] showed that defect localization can be prone to inaccurate results due to distortion issues for the receiving signals due to curved joints. In [104], the torsional mode is used to localize the circumferential defect beyond an elbow. In addition, the effect of two curved joints on the defect localization was explored in [105] when different joint configurations are present.

Regarding fluid-filled pipes, the wave propagation phenomena and the localization of a defect were analyzed in different works. Duan numerically analyzed the wave propagation in the time and frequency domains using a perfectly matched layer (PML) [106]. Using the SAFE method combined with a PML, Duan and Kirby [107] simulated the wave propagation in buried and immersed multilayered pipes. Aristégui et al. [44] conducted experiments to compute dispersion curves for pipes immersed in water. They also compared the results with the theoretical prediction. In terms of defect detection, Gallezot et al. combined the PML and the SAFE methods to study the scattering of waves by defects in pipes immersed in infinite medium [108]. Vogelaar and Golombok [45] experimentally studied the damage deflection using the torsional mode in fluid-filled pipes with different inner and outer fluids. They showed that identical inner and outer fluids produce an attenuation of 0.1 dB/m, and this value is doubled when inner and outer fluids are different. However, they stated that the torsional mode remains suitable for detecting pipe defects. Different studies regarding buried/immersed pipes have also been published, analyzing the dispersion curves of pipes and wave propagation in different media. In general, the fundamental torsional mode $T(0, 1)$ is preferred in NDT applications since it is not dispersive, it is easy to generate using transducers, and the energy is confined in the pipe [46–49].

1.6 Numerical methods

When working with guided wave techniques, it is crucial to understand the principles of wave propagation. This involves calculating and examining wave modes and their dispersion curves. In this sense, numerical simulations have helped the understanding of wave propagation modes. [109]

Various methods have been employed to calculate dispersion curves for different waveguide configurations. Among them, we can emphasize the analytical solutions, the FE, the SAFE, and the WFE methods. Concerning analytical approaches, the focus is to solve the partial differential equation related to wave propagation and the imposed boundary conditions to compute the desired variables. The analytical approach is highly accurate but cannot be applied to assess wave propagation in structures with complex geometries. [63, 66, 110]

The FE method is a better solution compared to the analytical approach when dealing with complex geometries. It is well-established, tested, and applied to wave propagation phenomena. It has also been used to simulate waveguide scattering problems in time-domain. However, spatial and time discretization should be wisely chosen to model ultrasonic-guided waves and may lead to huge computation efforts. One way to reduce the computation costs is to use reduced models. Besides that, the FE method also allows the treatment of multiphysics and non-linear problems. [111]

Alternatives to the FE method are the wave-based methods, like the SAFE and the WFE methods, where wave functions approximate the desired mechanical variables [112]. The SAFE and WFE methods are briefly explained hereafter using a simple example.

1.6.1 SAFE method

Let us consider an infinite and homogeneous straight waveguide of thickness h and an FE discretization along its thickness, as shown in Fig. 1.6(a).

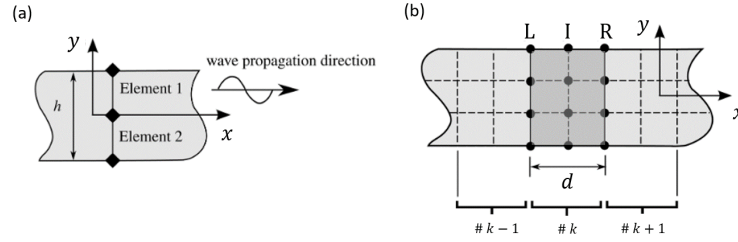


Figure 1.6: (a) Waveguide model for SAFE method (b) Waveguide model for WFE method, where the periodic length of a unit cell is denoted by d . Figure adapted from Ref. [113].

The SAFE method is used to model the wave propagation in the perpendicular direction of the cross-section, i.e., the x -direction. Also, the displacement field is assumed to be space harmonic in the wave propagation direction:

$$\mathbf{u}(x, y, t) = \begin{bmatrix} u_x(y) \\ u_y(y) \end{bmatrix} e^{-\mathbf{i}(\beta x - \omega t)}, \quad (1.7)$$

where t represent the time, and $\mathbf{i} = \sqrt{-1}$. Then, considering Eqs. (1.1) and (1.7), and approximating the displacement for each element $\mathbf{u}^{(e)}$ by means of shape functions $\mathbf{P}(y)$ as $\mathbf{u}^e = \mathbf{P}(y)\mathbf{q}^e$, it is possible to obtain an eigenvalue problem [113]:

$$\left[\beta^2 \mathbf{K}_1 + \beta \mathbf{K}_2 + \mathbf{K}_1 - \omega^2 \mathbf{M} \right] \mathbf{q} = 0, \quad (1.8)$$

where \mathbf{q} is the global nodal displacement vector; $\mathbf{K}_{1,2,3}$ and \mathbf{M} are stiffness and mass matrices (for details about these matrices, see [114]). The solution of the eigenvalue problem in Eq. (1.8) leads to the dispersion relations of the wave modes — i.e., the variation of β as a function of ω . This leads to both complex and real wavenumbers.

This method can compute the dispersion curves/wave modes for various cases such as rails [115], plates [66], and pipes [116, 117]. It is generally used for wave propagation in one direction in systems where the cross-section remains constant. For example, the SAFE method

can be applied to helicoidal structures. In this case, a curvilinear coordinate system must be considered to describe the wave propagation in a certain direction. [108, 118]

1.6.2 WFE method

Unlike the SAFE method, the WFE method is based on the periodicity of the waveguide, where one unit cell is considered. Following the previous example, a unit cell (also called substructure) of length d can be decomposed into left, internal, and right degrees-of-freedom (DoFs), denoted by \mathbf{L} , \mathbf{I} , \mathbf{R} , respectively, see Fig. 1.6(b). The dynamical equation of this unit cell is then given by:

$$\mathbf{D}\mathbf{q} = \mathbf{F}, \quad (1.9)$$

where \mathbf{q} and \mathbf{F} are the vectors of nodal displacement and nodal forces related to the DoFs of the unit cell. Also, $\mathbf{D} = -\omega^2\mathbf{M} + i\omega\mathbf{C} + \mathbf{K}$ is the dynamic stiffness matrix with \mathbf{M} , \mathbf{C} , \mathbf{K} the mass, damping, and stiffness matrices, respectively. These matrices are obtained via FE algorithms. Using the action-reaction rule and the displacement continuity at the shared interface (k) between two consecutive cells $\#k$ and $\#k - 1$, the following relation can be established:

$$\begin{bmatrix} \mathbf{q}_{\mathbf{R}}^{(k+1)} \\ \mathbf{F}_{\mathbf{R}}^{(k+1)} \end{bmatrix} = \begin{bmatrix} \mathbf{q}_{\mathbf{L}}^{(k+1)} \\ -\mathbf{F}_{\mathbf{L}}^{(k+1)} \end{bmatrix} = \mathbf{S} \begin{bmatrix} \mathbf{q}_{\mathbf{L}}^{(k)} \\ -\mathbf{F}_{\mathbf{L}}^{(k)} \end{bmatrix}, \quad (1.10)$$

where \mathbf{S} is so-called transfer matrix. The eigenvalues of \mathbf{S} are related to the wavenumber such as $\mu_j = e^{-i\beta_j d}$, where j is a mode, and the eigenvectors are related to the wavemodes. In this way, the relation between the frequency and the wavenumber can be found. This method will be further explored in Chapter 2.

Originally developed for straight waveguides, the SAFE and WFE methods were formulated to calculate wave numbers and wave shapes. Nevertheless, these techniques can be combined with the FE method to characterize wave interactions and account for arbitrarily shaped coupling elements, like defects or curved joints. For instance, it can be used to determine

the transmission and reflection coefficients of waves through these coupling elements.

Regarding computational efficiency, wave-based methods represent a good alternative to the FE method for the following reasons:

1. Dispersion curves and wavemodes can be easily computed;
2. Scattering coefficients, involving the conversion of modes in the presence of perturbed waveguide sections, can be found;
3. Small computational time is required, especially for long waveguides.

Compared to the SAFE method, the WFE approach can deal with complex cells and not only straight unit cells. However, it should be noted that the WFE method might become cumbersome when handling a large number of DoFs within the unit cell.

1.7 Conclusions

Numerous articles have addressed the use of guided waves to detect defects in waveguides, showing that they are relevant for the NDT. The approach involves analyzing both the source and reflected signals. For simple and straight pipelines, the process to localize a defect is straightforward and it is achieved by decomposing the time signal in terms of propagating modes. However, an arbitrary-shaped coupling element (such as a curved joint) can complicate the analysis as mode conversion occurs during transmission and reflection, leading to a potentially degraded reflected signal that is challenging to interpret. Therefore, to improve existing methods, it is essential to numerically investigate the interaction between guided waves and curved joints, i.e., transmitted and reflected waves. For this task, the WFE method seems to be appropriate since it allows the computation of wave modes in a waveguide. Moreover, to the author's knowledge, the impact of curved joints in fluid-filled pipelines has not been thoroughly explored in the literature and deserves further investigation.

Chapter 2

The Wave Finite Element (WFE) method

2.1 Overview

The WFE method is a numerical procedure based on Floquet-Bloch periodic conditions and the FE method to describe the dynamic response of periodic structures, i.e., structures made up of the repetition of a unit cell called “substructure”. The WFE method investigates wave propagation and forced response of simple and complex structures. Originally, it was developed to analyze wave propagation in 1D periodic structures. Its foundations originate from the works of Orris and Petyt [12, 13], Mead [14–18], among others. Later, the formalism of the WFE method has been enhanced through different works [19–24].

The main idea of the WFE method is to compute the dispersion curves and forced response for long systems using the FE model of a substructure. As a consequence, it allows the reduction of the computational time. The relation between the displacement and force of two consecutive substructures is established using a transfer matrix method, where the transfer matrix is denoted by \mathbf{S} . It allows the computation of the traveling wave modes, i.e., mode

shapes and wavenumbers. As a consequence, the displacement and forces of a periodic structure can be expanded in terms of the wave modes. The numerical issues concerning the method have been addressed in various ways in the literature. For example, the WFE method considers an associated eigenproblem related to the transfer matrix, which is prone to ill-conditioning since it involves eigenvectors with small and large components. To overcome this, Zhong and Williams [25] proposed an alternative scheme to the eigenproblem based on $\mathbf{S} + \mathbf{S}^{-1}$ transformation. Also, some applications require large-size FE models, leading to cumbersome computations. In these cases, some strategies have been proposed using modal order reduction strategies, condensation procedures, and reduction of propagating wave basis [26–28].

In terms of application, the method has been broadly used to study various types of structures, for example, beam-like structures [28–30], plates [19, 31], pipes with and without fluids [32–34], piezoelectric materials [35, 36], structures with cyclic symmetry [37], rotating structures [38, 39], helicoidal structures [40]. When considering 2D periodicity, wave propagation was also explored via the WFE method in [20, 41, 42]. Although the method is only applicable to periodic structures, different structures can be assembled by means of coupling elements. This enables the description of wave propagation in pipes or beam-like structures composed of straight waveguides and curved joints [28, 29, 43].

The rest of the chapter is organized as follows. In Sec. 2.2, the formulation of the WFE method is detailed, showing how the wave modes can be computed using the transfer matrix of a substructure. Sec. 2.3 focuses on the forced response computation. The computation of the time domain response of periodic structure via Fourier transform is discussed in Sec. 2.4. In Sec. 2.5, the group and energy velocities computation is explained. In Sec. 2.6, some numerical examples are proposed to illustrate the relevance of the approach. The study of periodic structures with coupling elements is addressed in Sec. 2.7.

2.2 Wave mode computation

Let us consider a linear periodic elastic structure composed of N identical substructures of length d along a certain direction, as shown in Fig. 2.1(a). The left and right boundaries are supposed to share the same FE meshes and number of DoFs, as in Fig. 2.1(b). In the WFE framework, only one substructure is considered.

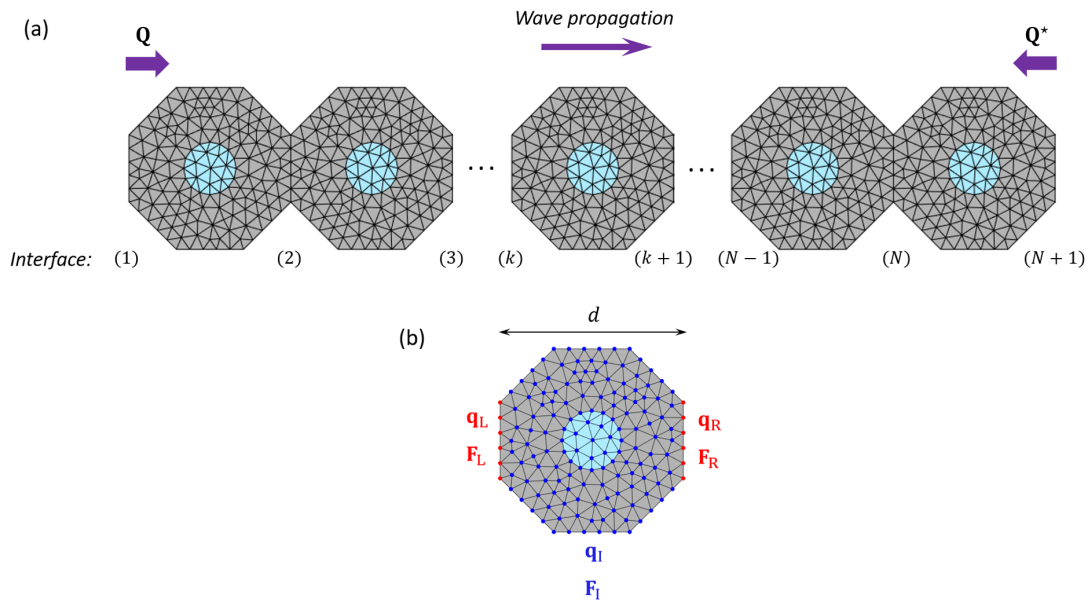


Figure 2.1: (a) Schematic of linear periodic elastic structure (periodic mesh); (b) Substructure mesh.

The DoFs of a substructure can be decomposed into left, right, and internal, denoted by L, R, and I, respectively. The left and right sides contain the same number n of DoFs. The stiffness, mass, and damping matrices of the substructure can be obtained using any commercial FE or Matlab codes and are denoted by \mathbf{K} , \mathbf{M} , and \mathbf{C} , respectively. In the frequency domain, the dynamical equilibrium equation of the substructure can be written as (see Sec. 1.6.2):

$$\mathbf{D}\mathbf{q} = \mathbf{F}, \quad (2.1)$$

where \mathbf{q} and \mathbf{F} are the displacement and force vectors, and \mathbf{D} is the dynamical stiffness matrix (DSM), which is given by:

$$\mathbf{D} = -\omega^2\mathbf{M} + i\omega\mathbf{C} + \mathbf{K}. \quad (2.2)$$

The DoFs can be reorganized in terms of left and right boundary and internal DoFs as follows:

$$\begin{bmatrix} \mathbf{D}_{LL} & \mathbf{D}_{LI} & \mathbf{D}_{LR} \\ \mathbf{D}_{IL} & \mathbf{D}_{II} & \mathbf{D}_{IR} \\ \mathbf{D}_{RL} & \mathbf{D}_{RI} & \mathbf{D}_{RR} \end{bmatrix} \begin{bmatrix} \mathbf{q}_L \\ \mathbf{q}_I \\ \mathbf{q}_R \end{bmatrix} = \begin{bmatrix} \mathbf{F}_L \\ \mathbf{F}_I \\ \mathbf{F}_R \end{bmatrix}. \quad (2.3)$$

The classical WFE method assumes that no external loads are applied to the interior DoFs ($\mathbf{F}_I = 0$), i.e., they are only applied to the left and right boundaries. Then, the following condensed equilibrium equation can be expressed as:

$$\begin{bmatrix} \mathbf{D}_{LL}^* & \mathbf{D}_{LR}^* \\ \mathbf{D}_{RL}^* & \mathbf{D}_{RR}^* \end{bmatrix} \begin{bmatrix} \mathbf{q}_L \\ \mathbf{q}_R \end{bmatrix} = \begin{bmatrix} \mathbf{F}_L \\ \mathbf{F}_R \end{bmatrix} \implies \mathbf{D}^* \mathbf{q}_B = \mathbf{F}_B, \quad (2.4)$$

where $\mathbf{D}^* = \mathbf{D}_{BB} - \mathbf{D}_{BI}\mathbf{D}_{II}^{-1}\mathbf{D}_{IB}$, with B the set of DoFs on the left (L) and right (R). Also, \mathbf{q}_L and \mathbf{q}_R (resp. \mathbf{F}_L and \mathbf{F}_R) are the displacement (resp. force) vectors of size $n \times 1$. The matrices \mathbf{D}_{LL}^* , \mathbf{D}_{LR}^* , \mathbf{D}_{RL}^* , and \mathbf{D}_{RR}^* are square matrices of size $n \times n$, with $\mathbf{D}_{LL}^* = (\mathbf{D}_{LL}^*)^T$, $\mathbf{D}_{RR}^* = (\mathbf{D}_{RR}^*)^T$, and $\mathbf{D}_{LR}^* = (\mathbf{D}_{RL}^*)^T$.

Let us consider two consecutive substructures $\#k-1$ and $\#k$, see Fig. 2.2. The following equilibrium conditions should be satisfied at the interface (k):

$$\mathbf{q}_L^{(k)} - \mathbf{q}_R^{(k)} = 0 \quad \text{and} \quad \mathbf{F}_L^{(k)} + \mathbf{F}_R^{(k)} = 0. \quad (2.5)$$

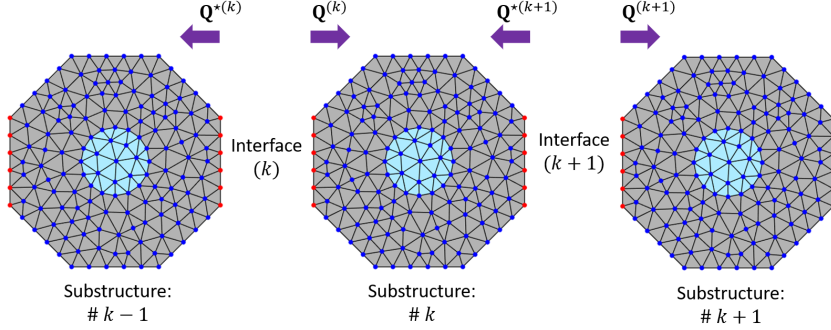


Figure 2.2: Schematics of substructures.

When Eqs. (2.4) and (2.5) are considered, it is possible to express the displacement and force of the right and the left boundaries of the substructure $\#k$ [119]. So, the transfer matrix equation is given by:

$$\mathbf{u}_R^{(k+1)} = \mathbf{S}\mathbf{u}_R^{(k)} \quad \text{or} \quad \mathbf{u}_L^{(k+1)} = \mathbf{S}\mathbf{u}_L^{(k)}, \quad (2.6)$$

where $\mathbf{u}_R^{(k)}$ and $\mathbf{u}_L^{(k)}$ are $2n \times 1$ vectors comprising displacement and forces on the boundaries left and right of the substructure $\#k$ (see Fig. 2.2), and are expressed by:

$$\mathbf{u}_R^{(k)} = \begin{bmatrix} \mathbf{q}_R^{(k)} \\ \mathbf{F}_R^{(k)} \end{bmatrix} \quad \text{and} \quad \mathbf{u}_L^{(k)} = \begin{bmatrix} \mathbf{q}_L^{(k)} \\ -\mathbf{F}_L^{(k)} \end{bmatrix}. \quad (2.7)$$

In Eq. (2.6), \mathbf{S} is the transfer matrix (size $2n \times 2n$) and it is expressed as [21]:

$$\mathbf{S} = \begin{bmatrix} -\mathbf{D}_{LR}^{*-1}\mathbf{D}_{LL}^* & -\mathbf{D}_{LR}^{*-1} \\ \mathbf{D}_{RL}^* - \mathbf{D}_{RR}^*\mathbf{D}_{LR}^{*-1}\mathbf{D}_{LL}^* & -\mathbf{D}_{RR}^*\mathbf{D}_{LR}^{*-1} \end{bmatrix}. \quad (2.8)$$

It is well known that \mathbf{S} is symplectic [19, 21], i.e.,

$$\mathbf{S}^T \mathbf{J} \mathbf{S} = \mathbf{J} \quad \text{where} \quad \mathbf{J} = \begin{bmatrix} \mathbf{0} & \mathbf{I} \\ -\mathbf{I} & \mathbf{0} \end{bmatrix}. \quad (2.9)$$

and that its eigensolutions represent waves. The related eigenvalue problem to be solved can be written as:

$$\mathbf{S}\phi_j = \mu_j\phi_j \quad \text{with} \quad \phi_j = \begin{bmatrix} \phi_{\mathbf{q}j}^T & \phi_{\mathbf{F}j}^T \end{bmatrix}^T, \quad (2.10)$$

with ϕ_j being the right eigenvectors of \mathbf{S} , and μ_j the corresponding eigenvalues. The eigenvectors represent the wave shapes and can be divided into two contributions $\phi_j = [\phi_{\mathbf{q}j}^T \ \phi_{\mathbf{F}j}^T]^T$, where $\phi_{\mathbf{q}j}$ and $\phi_{\mathbf{F}j}$ are vectors of displacement and force components, respectively. The symplectic property of \mathbf{S} provides paired eigenvalues $(\mu_j, \mu_j^* = 1/\mu_j)$, with $|\mu_j| < 1$, and their related eigenvectors ϕ_j and ϕ_j^* . Finally, the eigensolutions can be categorized into a set of n right-going waves $\{\mu_j, \phi_j\}_{j=1, \dots, n}$ and n left-going waves $\{\mu_j^*, \phi_j^*\}_{j=1, \dots, n}$. Also, Bloch's theorem states that the eigenvalues μ_j can be expressed as $\mu_j = e^{-i\beta_j d}$, where β_j denotes the wavenumber of a mode j .

The displacement and force vectors at an interface (k) can be expanded in terms of wave modes [23, 28]:

$$\mathbf{u}_L^{(k)} = \Phi \mathbf{Q}^{(k)} + \Phi^* \mathbf{Q}^{*(k)} \quad \text{and} \quad \mathbf{u}_R^{(k)} = \Phi \mathbf{Q}^{(k)} + \Phi^* \mathbf{Q}^{*(k)} \quad (2.11)$$

where

$$\Phi = \begin{bmatrix} \Phi_{\mathbf{q}} \\ \Phi_{\mathbf{F}} \end{bmatrix} \quad \text{and} \quad \Phi^* = \begin{bmatrix} \Phi_{\mathbf{q}}^* \\ \Phi_{\mathbf{F}}^* \end{bmatrix}, \quad (2.12)$$

and $\Phi_{\mathbf{q}}, \Phi_{\mathbf{q}}^*, \Phi_{\mathbf{F}}$ and $\Phi_{\mathbf{F}}^*$ are $n \times n$ full rank matrices defined by $\Phi_{\mathbf{q}} = [\phi_{\mathbf{q}1} \cdots \phi_{\mathbf{q}n}]$, $\Phi_{\mathbf{q}}^* = [\phi_{\mathbf{q}1}^* \cdots \phi_{\mathbf{q}n}^*]$, $\Phi_{\mathbf{F}} = [\phi_{\mathbf{F}1} \cdots \phi_{\mathbf{F}n}]$ and $\Phi_{\mathbf{F}}^* = [\phi_{\mathbf{F}1}^* \cdots \phi_{\mathbf{F}n}^*]$. Also, $\mathbf{Q}^{(k)}$ and $\mathbf{Q}^{*(k)}$ are wave amplitude vectors, see Fig. 2.2. It can be shown that $\mathbf{Q}^{(k)} = \boldsymbol{\mu}^{k-1} \mathbf{Q}$ and $\mathbf{Q}^{*(k)} = \boldsymbol{\mu}^{N+1-k} \mathbf{Q}^*$ where $\mathbf{Q} = \mathbf{Q}^{(1)}$ and $\mathbf{Q}^* = \mathbf{Q}^{*(N+1)}$ represent wave amplitude vectors at the left and right ends of the structure(respectively), see Fig. 2.1; with $\boldsymbol{\mu} = \text{diag}\{\mu_j\}_{j=1}^n$ being a diagonal matrix composed of eigenvalues μ_j for the right-going waves.

The wave amplitudes can be obtained by considering boundary conditions, which is

addressed in Sec. 2.3. The WFE method may lead to high computational costs when dealing with substructures with a huge number of DoFs. This becomes particularly evident during the condensation of the internal DoFs, where the inversion of the matrix \mathbf{D}_{II} is required. The construction of the symplectic transfer matrix \mathbf{S} also involves the inversion of \mathbf{D}_{LR} , which can also yield numerical errors. The direct computation of the eigenproblem in Eq. (2.10) is prone to numerical errors, since the matrix of eigenvectors contains small and large components from the displacement and force parts. To avoid it, the WFE eigenproblem can be computed using different strategies described hereafter. [25, 120]

2.2.1 (N,L) transformation

As indicated by Zhong and Williams [25], the direct computation of the eigenproblem described by Eq. (2.10) is prone to numerical errors, since it involves eigenvectors with small and large components. To solve it, they have proposed an equivalent approach. The idea is to decompose the matrix \mathbf{S} into two distinct matrices \mathbf{L} and \mathbf{N} , where $\mathbf{S} = \mathbf{NL}^{-1}$, and then proceed with an intermediary step to solve the original eigenproblem. Indeed, it can be proven that:

$$\mathbf{N}\mathbf{w}_j = \mu_j\mathbf{L}\mathbf{w}_j, \quad (2.13)$$

where

$$\mathbf{N} = \begin{bmatrix} \mathbf{I} & \mathbf{0} \\ -\mathbf{D}_{\text{LL}}^* & -\mathbf{D}_{\text{LR}}^* \end{bmatrix}, \quad \mathbf{L} = \begin{bmatrix} \mathbf{0} & \mathbf{I} \\ \mathbf{D}_{\text{RL}}^* & \mathbf{D}_{\text{RR}}^* \end{bmatrix} \quad \text{and} \quad \mathbf{w}_j = \begin{bmatrix} \phi_{\mathbf{q}j} \\ \mu_j\phi_{\mathbf{q}j} \end{bmatrix}. \quad (2.14)$$

The waveshapes are derived from $\phi_j = \mathbf{L}\mathbf{w}_j$, which represents the right-going wave modes. This problem is well-conditioned as the eigenvector \mathbf{w}_j only consists of displacement components. However, due to numerical dispersion in computing the wave modes, the eigenvalues for the right-going wave modes μ_j^* and the left-going wave modes μ_j may not strictly follow the relation $\mu_j^* = 1/\mu_j$. This can result in an ill-conditioned matrix system when computing the forced response of the system. As described by Mencik [22], to overcome this issue, one strategy is

to consider symmetric substructures with respect to their mid-plane. In doing so, a relation between the left- and right-going modes can be proposed by employing a symmetry matrix transformation:

$$\phi_{\mathbf{q}j}^* = \mathcal{R}\phi_{\mathbf{q}j} \quad \text{and} \quad \phi_{\mathbf{F}j}^* = -\mathcal{R}\phi_{\mathbf{F}j}, \quad (2.15)$$

where \mathcal{R} is the symmetry matrix transformation, that represents a diagonal matrix with ± 1 as components, such that $\mathcal{R}^2 = \mathbf{I}_n$.

As discussed by Fan et al. [35, 36], the eigenproblem in Eq. (2.13) can still be prone to numerical issues. It happens because significant differences in magnitude occur between matrices \mathbf{D}_{LR}^* and \mathbf{I} , leading to large conditioning numbers. To solve this issue, they have introduced the parameter $\sigma = \|\mathbf{D}_{\text{RR}}^*\|_2/n^2$. Then, a final approach using the modified matrices \mathbf{L}_m and \mathbf{N}_m can be written as:

$$\mathbf{N}_m(\mathbf{w}_m)_j = \mu_j \mathbf{L}_m(\mathbf{w}_m)_j, \quad (2.16)$$

where

$$\mathbf{N}_m = \begin{bmatrix} \sigma \mathbf{I} & \mathbf{0} \\ -\mathbf{D}_{\text{LL}}^* & -\mathbf{D}_{\text{LR}}^* \end{bmatrix}, \quad \mathbf{L}_m = \begin{bmatrix} \mathbf{0} & \sigma \mathbf{I} \\ \mathbf{D}_{\text{RL}}^* & \mathbf{D}_{\text{RR}}^* \end{bmatrix} \quad \text{and} \quad (\mathbf{w}_m)_j = \begin{bmatrix} \sigma \phi_{\mathbf{q}j} \\ \mu_j \phi_{\mathbf{q}j} \end{bmatrix}. \quad (2.17)$$

The computation of the waveshapes can be easily achieved with this approach, and the wavenumbers are the same as those computed with the eigenproblem described in Eq. (2.13).

2.2.2 $(\mathbf{S} + \mathbf{S}^{-1})$ transformation

For non-symmetric substructures, the eigenvalues of \mathbf{S} may not follow strictly the relation $\mu_j^* = 1/\mu_j$, and the symmetry matrix transformation (\mathcal{R}) cannot be applied to ensure the symplectic nature of the wave modes. An alternative procedure has been proposed to solve this issue. It consists in using the $(\mathbf{S} + \mathbf{S}^{-1})$ transformation that leads to the following eigenproblem:

$$\left((\mathbf{N}'\mathbf{J}\mathbf{L}'^T + \mathbf{L}'\mathbf{J}\mathbf{N}'^T) - \lambda_j\mathbf{L}'\mathbf{J}\mathbf{L}'^T \right) \mathbf{z}_j = \mathbf{0}, \quad (2.18)$$

for the eigenvalues $\lambda_j = \mu_j + 1/\mu_j$ and the eigenvectors \mathbf{z}_j [25, 119]. Here, we define:

$$\mathbf{N}' = \begin{bmatrix} \mathbf{D}_{\text{RL}}^* & \mathbf{0} \\ -(\mathbf{D}_{\text{LL}}^* + \mathbf{D}_{\text{RR}}^*) & -\mathbf{I} \end{bmatrix} \quad \text{and} \quad \mathbf{L}' = \begin{bmatrix} \mathbf{0} & \mathbf{I} \\ \mathbf{D}_{\text{LR}}^* & \mathbf{0} \end{bmatrix}. \quad (2.19)$$

Thus,

$$\mathbf{N}'\mathbf{J}\mathbf{L}'^T + \mathbf{L}'\mathbf{J}\mathbf{N}'^T = \begin{bmatrix} (\mathbf{D}_{\text{RL}}^* - \mathbf{D}_{\text{LR}}^*) & (\mathbf{D}_{\text{LL}}^* + \mathbf{D}_{\text{RR}}^*) \\ -(\mathbf{D}_{\text{LL}}^* + \mathbf{D}_{\text{RR}}^*) & (\mathbf{D}_{\text{RL}}^* - \mathbf{D}_{\text{LR}}^*) \end{bmatrix}, \quad (2.20)$$

and

$$\mathbf{L}'\mathbf{J}\mathbf{L}'^T = \mathbf{N}'\mathbf{J}\mathbf{N}'^T = \begin{bmatrix} \mathbf{0} & -\mathbf{D}_{\text{RL}}^* \\ \mathbf{D}_{\text{LR}}^* & \mathbf{0} \end{bmatrix}. \quad (2.21)$$

The eigenvalues related to the wave mode μ_j can be found analytically by solving the quadratic equation $\mu_j^2 - \lambda_j\mu_j + 1 = 0$, whose solutions are:

$$\mu_j = \frac{1}{2} \left(\lambda_j \pm \sqrt{\lambda_j^2 - 1} \right). \quad (2.22)$$

The eigenvectors of \mathbf{S} follow as:

$$\phi_j = \begin{bmatrix} \mathbf{I} & \mathbf{0} \\ \mathbf{D}_{\text{RR}}^* & \mathbf{I} \end{bmatrix} \mathbf{w}'_j \quad \text{with} \quad \mathbf{w}'_j = \mathbf{J}(\mathbf{L}'^T - \mu_j^* \mathbf{N}'^T) \mathbf{z}_j \quad (2.23)$$

and

$$\phi_j^* = \begin{bmatrix} \mathbf{I} & \mathbf{0} \\ \mathbf{D}_{\text{RR}}^* & \mathbf{I} \end{bmatrix} \mathbf{w}_j^*, \quad \text{with} \quad \mathbf{w}_j^* = \mathbf{J}(\mathbf{L}'^T - \mu_j \mathbf{N}'^T) \mathbf{z}_j. \quad (2.24)$$

With this approach, the wave modes $\{\mu_j, \phi_j\}_{j=1, \dots, n}$ and $\{\mu_j^*, \phi_j^*\}_{j=1, \dots, n}$ can be accurately computed.

2.2.3 Tracking criteria

For certain applications, it is interesting to track a given wave mode along a frequency band. To track a wave mode between two consecutive discrete frequencies a modal assurance criterion (MAC) can be adopted [121, 122]. The objective of this criterion is to provide a means to measure the level of correlation between two different modes.

The main goal is to identify a certain mode ϕ_s at two consecutive frequencies ω and $\omega + \Delta\omega$, where $\Delta\omega$ is sufficiently small to capture slight shape variations that may happen between these frequencies. Two criteria have been adopted for this purpose: the Euclidean and the symplectic criteria. Let us consider two wave modes ϕ_r , and ϕ_s , the Euclidean criterion gives:

$$\frac{|\phi_r^H(\omega)\phi_r(\omega + \Delta\omega)|}{\|\phi_r(\omega)\|\|\phi_r(\omega + \Delta\omega)\|} = \max_s \left\{ \frac{|\phi_r^H(\omega)\phi_s(\omega + \Delta\omega)|}{\|\phi_r(\omega)\|\|\phi_s(\omega + \Delta\omega)\|} \right\}, \quad (2.25)$$

and the symplectic criterion, where the orthogonality relation of modes is given by $\phi_r^{*T}\mathbf{J}\phi_s = 0$, for $\mu_s \neq 1/\mu_r$ (as discussed by Zhong and Williams [25]). This results in:

$$\left| \frac{\phi_r^{*T}(\omega)\mathbf{J}\phi_r(\omega + \Delta\omega)}{\|\phi_r^*(\omega)\|\|\phi_r(\omega + \Delta\omega)\|} \right| = \max_s \left\{ \left| \frac{\phi_r^{*T}(\omega)\mathbf{J}\phi_s(\omega + \Delta\omega)}{\|\phi_r^*(\omega)\|\|\phi_s(\omega + \Delta\omega)\|} \right| \right\}. \quad (2.26)$$

The above criteria mean that the maximum correlation between modes at each frequency happens when $s = r$. The Euclidean norm does not employ mode orthogonality [119]. However, the criterion remains useful for interpreting solutions and dispersion curves.

2.3 Forced response

The WFE method allows the computation of the forced response of periodic structures. Considering a finite periodic structure composed of N substructures. As a result of Eq. (2.11), the displacement and forces vectors at an interface (k) can be written as follows:

$$\mathbf{q}_L^{(k)} = \mathbf{q}_R^{(k)} = \Phi_q \mu^{k-1} \mathbf{Q} + \Phi_q^* \mu^{N+1-k} \mathbf{Q}^* \quad k = 1, \dots, N+1, \quad (2.27)$$

and

$$-\mathbf{F}_L^{(k)} = \mathbf{F}_R^{(k)} = \Phi_F \mu^{k-1} \mathbf{Q} + \Phi_F^* \mu^{N+1-k} \mathbf{Q}^* \quad k = 1, \dots, N+1. \quad (2.28)$$

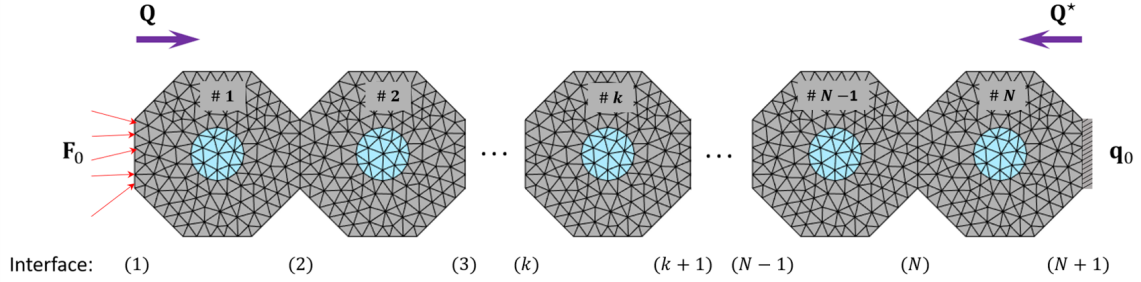


Figure 2.3: Schematics of the wave amplitudes along a periodic structure. As an example of boundary conditions, a force vector is applied at the left end and a displacement vector at the right end.

The amplitude vectors \mathbf{Q} and \mathbf{Q}^* are determined from the boundary conditions. As a simple example, let us consider a force vector \mathbf{F}_0 on the left side and a displacement vector on the right \mathbf{q}_0 side of the structure as in Fig.(2.3). It is possible to express the boundary conditions in terms of wave modes as follows:

$$\begin{cases} -\mathbf{F}_0 = \Phi_F \mathbf{Q} + \Phi_F^* \mu^N \mathbf{Q}^* \\ \mathbf{q}_0 = \Phi_q \mu^N \mathbf{Q} + \Phi_q^* \mathbf{Q}^* \end{cases} \quad (2.29)$$

The above equation is then organized in a linear system to find the wave amplitude vectors \mathbf{Q} and \mathbf{Q}^* :

$$\begin{bmatrix} \Phi_F & \Phi_F^* \mu^N \\ \Phi_q \mu^N & \Phi_q^* \end{bmatrix} \begin{bmatrix} \mathbf{Q} \\ \mathbf{Q}^* \end{bmatrix} = \begin{bmatrix} -\mathbf{F}_0 \\ \mathbf{q}_0 \end{bmatrix}. \quad (2.30)$$

The solution of the linear system in Eq. (2.30) involves the inversion of a matrix that is partitioned into displacement and force components, which may again lead to ill-conditioning [22].

To overcome this, it is possible to precondition this matrix equation by multiplying the first line by $\Phi_{\mathbf{F}}^{-1}$, and the second line by $\Phi_{\mathbf{q}}^{\star-1}$. The following well-conditioning linear system to be solved is given by [23]:

$$\begin{bmatrix} \mathbf{I} & \Phi_{\mathbf{F}}^{-1}\Phi_{\mathbf{F}}^{\star}\mu^N \\ \Phi_{\mathbf{q}}^{\star-1}\Phi_{\mathbf{q}}\mu^N & \mathbf{I} \end{bmatrix} \begin{bmatrix} \mathbf{Q} \\ \mathbf{Q}^{\star} \end{bmatrix} = \begin{bmatrix} -\Phi_{\mathbf{F}}^{-1}\mathbf{F}_0 \\ \Phi_{\mathbf{q}}^{\star-1}\mathbf{q}_0 \end{bmatrix}, \quad (2.31)$$

Solving Eq (2.31) yields \mathbf{Q} and \mathbf{Q}^{\star} ; then, the displacements/forces along the structure can be retrieved via Eqs. (2.27) and (2.28). It should be pointed out that the procedure can be applied to different boundary conditions, for example, using surface impedances [23].

2.4 Time response

Originally, the WFE method analyses guided waves in structures in the frequency domain, and then the structure behavior at different frequencies. To describe the behavior of the structure in the time domain, it is necessary to convert the harmonic responses into the time domain. This can be done via the Inverse Discrete Fourier Transform (IDFT).

In the case of discrete frequencies, the conversion from the frequency domain to the time domain is achieved via IDFT using the scheme proposed by Marzani [117]. The computation of the time response depends on the applied force and the time range. The following procedure can be considered:

1. The sampling frequency f_s is chosen according to the Nyquist–Shannon sampling theorem;
2. The time span is built as $t = [0, dt, 2dt, \dots, T - dt]$, with $dt = 1/f_s$. Here, T is chosen to capture the slowest propagating wave. In this sense, the time span is composed of $N = T \times f_s$ points;
3. The force is expressed in the time domain $F(t)$, and its spectrum $F(\omega)$ is obtained via DFT using the `fft` function provided by MATLAB;

4. The frequency span is then built as $f = [0, f_c, 2f_c, \dots, f_s]$, with $f_c = f_s/(N - 1)$.
5. The frequency response is obtained using the WFE method for the first N_F values, where:

$$N_F = \begin{cases} (N + 2)/2 & \text{if } N \text{ is even} \\ (N + 1)/2 & \text{if } N \text{ is odd} \end{cases}$$

6. The displacement is stored for the analyzed frequencies. The complex conjugate of each c -th element of stored displacement is filed in a $N - c + 2$ vector, where:

$$c = \begin{cases} (2, 3, \dots, NF - 2, NF - 1) & \text{if } N \text{ is even} \\ (2, 3, \dots, NF - 1, NF) & \text{if } N \text{ is odd} \end{cases}$$

7. The IDFT is performed, and the time response is found. This can be obtained using MATLAB's `ifft` function.

This method provides the displacement at the monitored point as a function of time. This will be extensively used to compute the traveling wave packets along different structures, for example, to simulate the reflected signal at the sensor point issued from a defect or a joint. The propagation of the wave packets along the structure depends on the group velocity and the nature of the mode. This can be addressed in two different ways in the WFE framework as explained hereafter.

2.5 Group velocity

For NDT applications, it is important to determine the velocity at which a wavepacket travels along the structure. It is used to determine the time of flight for reflected/transmitted wavepackets issued from a defect and/or a curved joint. The velocity at which a wavepacket propagates is known as the group velocity and can be found with the WFE method.

The computation of the group velocity can be achieved in different ways, i.e., by considering (i) the dispersion curves or (ii) an energy balance. In the first approach, the group velocity c_{gj} for a given wave j is obtained as [62]:

$$c_{gj} = \frac{\partial \omega}{\partial \Re\{\beta_j\}}, \quad (2.32)$$

where β_j is the related wave number. The first method is purely determined by the derivative of the frequency in function of the real part of the wavenumber. So, the group velocity can be found if the dispersion curve is known.

The second approach involves computing the energy velocity of each mode. When dealing with low-damped structures, the energy and group velocities are equal. Given this condition, the group and energy velocities for a certain mode j are given by [123, 124]:

$$c_{gj} \approx c_j^e = \frac{P_j}{T_j + U_j}, \quad (2.33)$$

where P_j is the energy flow, T_j is the averaged kinetic energy, and U_j is the averaged potential energy contribution of the j -th mode through the cross-section. In terms of displacement and forces, they can be computed as [68]:

$$P_j(\omega) = \frac{i\omega}{4} \begin{bmatrix} \mathbf{q}_{Lj}^{(k)} \\ -\mathbf{F}_{Lj}^{(k)} \end{bmatrix}^H \mathbf{J} \begin{bmatrix} \mathbf{q}_{Lj}^{(k)} \\ -\mathbf{F}_{Lj}^{(k)} \end{bmatrix}, \quad (2.34)$$

$$T_j(\omega) = \frac{\omega^2}{4d} \begin{bmatrix} \mathbf{q}_{Lj}^{(k)} \\ \mathbf{q}_{Lj}^{(k+1)} \end{bmatrix}^H \mathbf{M}_{BB} \begin{bmatrix} \mathbf{q}_{Lj}^{(k)} \\ \mathbf{q}_{Lj}^{(k+1)} \end{bmatrix}, \quad (2.35)$$

and

$$U_j(\omega) = \frac{1}{4d} \begin{bmatrix} \mathbf{q}_{Lj}^{(k)} \\ \mathbf{q}_{Lj}^{(k+1)} \end{bmatrix}^H \mathbf{K}_{BB} \begin{bmatrix} \mathbf{q}_{Lj}^{(k)} \\ \mathbf{q}_{Lj}^{(k+1)} \end{bmatrix}, \quad (2.36)$$

where \mathbf{K}_{BB} , and \mathbf{M}_{BB} are the stiffness and mass matrices associated with the boundary DoFs. Here, the contribution of each wave mode j for the displacement and force at an interface (k)

are computed as:

$$\mathbf{q}_{Lj}^{(k)} = \phi_{qj} \mu_j^{k-1} Q_j + \phi_{qj}^* \mu_j^{N+1-k} Q_j^* \quad \text{and} \quad -\mathbf{F}_{Lj}^{(k)} = \phi_{Fj} \mu_j^{k-1} Q_j + \phi_{Fj}^* \mu_j^{N+1-k} Q_j^*. \quad (2.37)$$

It is worth mentioning that the second approach only works when no internal DoFs are present in the substructure. [68]

2.6 Numerical results and discussion

Two different structures are analyzed, i.e., a Timoshenko's beam and the 2D plane-stress beam. In the first case, the analytical solution of the dynamical equation is available. Then, a comparison with the WFE method for dispersion curves and forced response is done. In the second case, the comparison is made between the FE and WFE methods in the frequency and time domains.

2.6.1 Timoshenko beam

The Timoshenko model for beams is well established and an analytical solution can be found for dispersion curves and forced response [125]. To compare the WFE approach with the analytical solution, a FE discretization is considered to obtain the mass and stiffness matrices of the beam structure. Friedman and Kosmatka [126] developed a two-node Timoshenko FE beam using a cubic shape function for the transverse displacement and a quadratic shape function for the rotation. This formulation leads to a closed form for the elementary stiffness \mathbf{K}_e and mass \mathbf{M}_e matrices for a substructure of length d :

$$\mathbf{K}_e = \frac{EI}{(1 + \gamma)d^3} \begin{bmatrix} 12 & 6L & -12 & 6d \\ & (4 + \gamma)d^2 & -6d & (2 - \gamma)d^2 \\ & & 12 & -6d \\ \text{symm.} & & & (4 + \gamma)d^2 \end{bmatrix} \quad (2.38)$$

and

$$\mathbf{M}_e = \mathbf{M}_{e1} + \mathbf{M}_{e2} \quad (2.39)$$

where each one is given by:

$$\mathbf{M}_{e1} = \frac{\rho S d}{210(1 + \gamma)^2} \begin{bmatrix} m_1 & m_2 & m_3 & m_4 \\ & m_5 & -m_4 & m_6 \\ & & m_1 & -m_2 \\ \text{symm.} & & & m_5 \end{bmatrix} \quad (2.40)$$

and

$$\mathbf{M}_{e2} = \frac{\rho I}{30(1 + \gamma)^2 d} \begin{bmatrix} 36 & m_7 & -36 & m_7 \\ & m_8 & -m_7 & m_9 \\ & & 36 & -m_7 \\ \text{symm.} & & & m_8 \end{bmatrix} \quad (2.41)$$

where

$$\begin{aligned} m_1 &= (70\gamma^2 + 147\gamma + 78), & m_2 &= 0.25d(35\gamma^2 + 77\gamma + 44), \\ m_3 &= (35\gamma^2 + 63\gamma + 27), & m_4 &= -0.25d(35\gamma^2 + 63\gamma + 26), \\ m_5 &= 0.25d^2(7\gamma^2 + 14\gamma + 8), & m_6 &= -0.25d^2(7\gamma^2 + 14\gamma + 6), \\ m_7 &= -d(15\gamma - 3), & m_8 &= d^2(10\gamma^2 + 5\gamma + 4), \\ m_9 &= d^2(5\gamma^2 - 5\gamma - 1), & \gamma &= (12EI)/(kGSd^2). \end{aligned}$$

Fig. 2.4(a) shows the FE mesh for the Timoshenko beam where the following physical and geometrical parameters are used: Young's modulus $E = 210$ GPa, density $\rho = 7800$ kg/m³, Poisson's ratio $\nu = 0.3$. The damping is supposed to be mass proportional, i.e., $\mathbf{C} = \eta\mathbf{M}$, with $\eta = 0.01$ s⁻¹. Here, $I = (1/12)10^{-8}$ m⁴ and $S = 10^{-6}$ m² are the second moment of area and the cross-section area, respectively. The shear correction factor is $k = 0.89$, and the beam length is $L = 0.10$ m. Within the WFE framework, a substructure without internal DoFs and

length $d = 1 \times 10^{-4}$ m with matrices \mathbf{M}_e and \mathbf{K}_e is considered (see Fig. 2.4(b)). A shear force $F_s = 1$ N is applied at $x = 0$, and the beam is clamped at $x = L$. The response obtained via the WFE method is assessed from 0 Hz to 100 kHz, and compared with the theoretical solutions concerning the dispersion curves and the frequency responses.

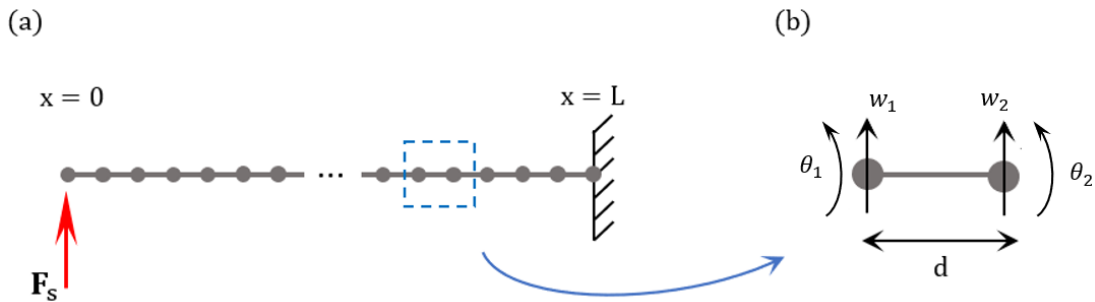


Figure 2.4: (a) FE mesh for the Timoshenko beam. A force is applied at $x = 0$, and the system is clamped at $x = L$. (b) Mesh of a substructure of length d , with displacement w and rotation θ DoFs.

The dispersion curves are presented in Fig. 2.5(a), where the continuous lines represent the WFE solutions and the dashed lines show the theoretical results [125]. The red line represents the flexural mode, while the purple line represents the shearing mode. The cut-off frequency occurs at 16.5kHz, where the mode becomes purely propagating. Fig. 2.5(b) compares the group velocities computed using the WFE method and the theoretical approach across the frequency range.

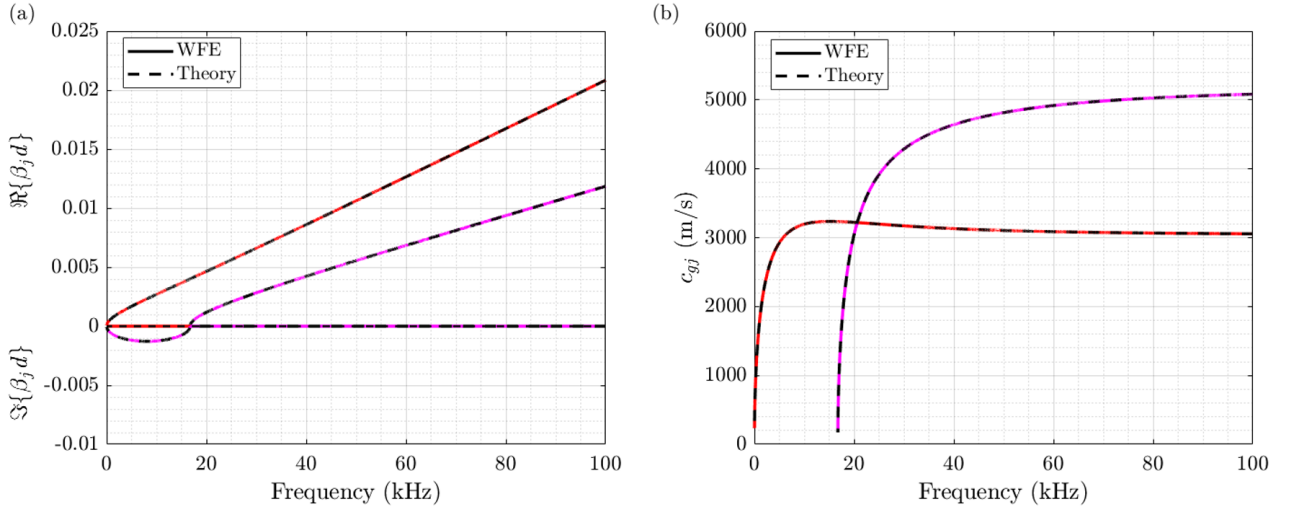


Figure 2.5: Comparison of the (a) dispersion curves and (b) group velocity curves as a function of frequency between the theoretical approach and the WFE method for the Timoshenko beam.

The WFE method and the theoretical approach are used to compute the transverse displacement at $x = 0$, as illustrated in Fig. 2.6(a). Fig. 2.6(b) depicts the relative error between the two approaches. The relative error at the observation point is expressed in percentage and computed by summing the differences between the reference and the WFE solution for each frequency and after summing over sub-frequency bands as follows:

$$\text{Rel. Error (\%)} = 100 \times \frac{\sum_{\text{Sub-frequency band}} \|\mathbf{q}_{\text{Ref.}} - \mathbf{q}_{\text{WFE}}\|}{\sum_{\text{Sub-frequency band}} \|\mathbf{q}_{\text{Ref.}}\|}, \quad (2.42)$$

where \mathbf{q} refers to the measured displacement, and the subscripts **Ref.** and **WFE** denote the reference and WFE results.

The relative error is less than 1% for the whole analyzed frequency band. Moreover, one can observe an increase in the error values around the resonance peaks. It is due to a slight shift generated by the WFE method around the resonance peaks. Also, the relative error increases with the frequency – i.e., low frequencies have lower errors when compared to higher frequencies. Overall, both methods yield similar results, indicating that the WFE approach is consistent

with the theoretical one.

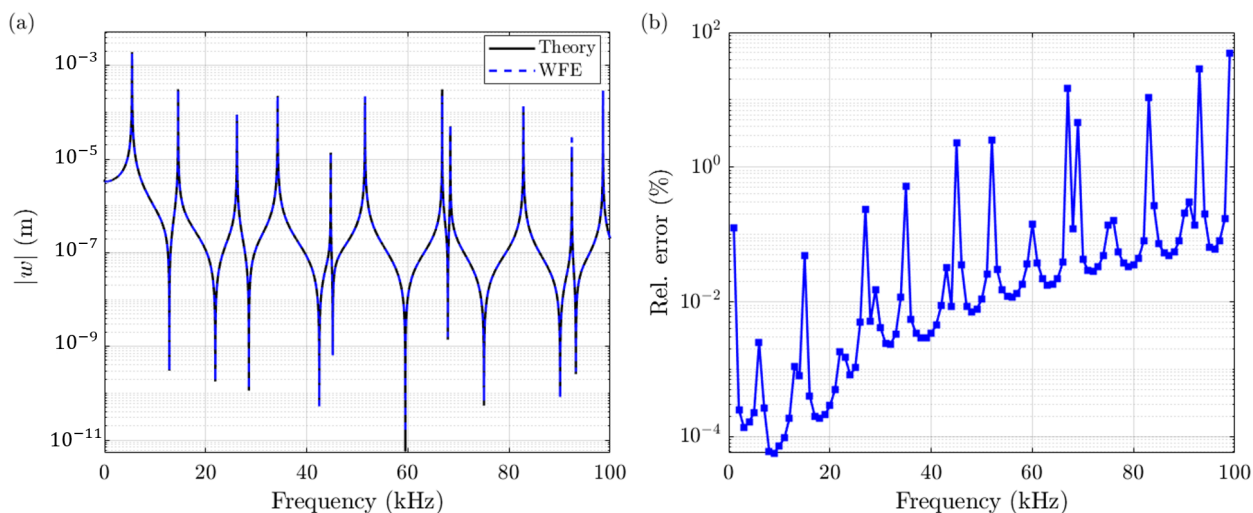


Figure 2.6: (a) Comparison between the magnitude of the vertical displacement obtained using the theoretical and WFE method for the Timoshenko beam. (b) Relative error between the approaches, see Eq. (2.42).

2.6.2 2D plane-stress beam

The WFE method is applied to a 2D structure, and results are compared to the FE method. Let us consider a straight, uniform, linear beam of length $L = 2$ m, as in Fig. (2.7). The system is modeled as a 2D structure under plane stress conditions (in-plane motion). A force $\mathbf{F}_{0x} = 1$ kN is applied to one node on the left boundary, and the right boundary is clamped (i.e. $\mathbf{q}_0 = \mathbf{0}$). The related material properties are: Young's modulus $E = 210$ GPa, density $\rho = 7800$ kg/m³, Poisson's ratio $\nu = 0.3$. Also, a Rayleigh damping model is considered — i.e., $\mathbf{C} = a\mathbf{M} + b\mathbf{K}$, with coefficients $a = 10^{-3}$ s⁻¹ and $b = 10^{-8}$ s. The geometric parameters of the substructure are: thickness $e = 1$ mm, length $d = 2.5$ mm, and height $h = 0.1$ m. In this case, the FE mesh of the substructure is built from 1×40 four-node plane stress rectangular elements with two DoFs per node. In this way, the substructure does not contain internal DoFs. Consequently, the condensation procedure involved in Eq. (2.4) is not required.

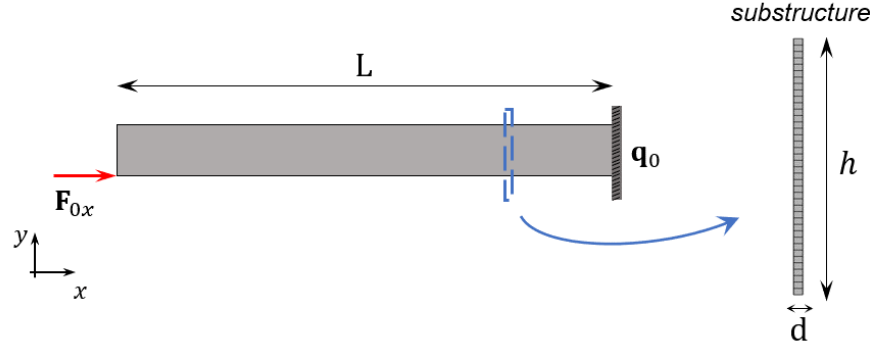


Figure 2.7: Schematics of a 2D plane-stress beam and the FE mesh of the substructure. The beam is subject to a force on the left side and a clamped boundary condition on the right side.

Following the WFE procedure, the dispersion curves can be plotted, i.e., wavenumbers β_j over a frequency band $[0, 60]$ kHz. This can be done by solving the eigenproblem using the methods (\mathbf{N}, \mathbf{L}) method or $(\mathbf{S} + \mathbf{S}^{-1})$ transformation, see Sec. 2.2.1 and Sec. 2.2.2. Here, $n = 82$ DoFs along the height on the left/right boundaries are used. This means computing $n = 82$ right/left-going waves. Fig. 2.8(a) shows the dispersion curves for a few right-going waves associated with "low-order" modes. The real (propagating) and imaginary (evanescent) parts of the wavenumber are plotted in continuous and dashed lines, respectively. Classical waves can be observed, i.e., flexural (red), longitudinal (yellow), and shearing (light green) modes; higher-order modes are also plotted in other colors. As expected, the flexural and longitudinal modes do not contain evanescent parts, i.e., only propagating ones. Moreover, the shearing mode behavior can be also predicted, where a cut-off frequency is observed around 15 kHz. For high-order modes, the behavior of the dispersion curve is complex, with multiple cut-off frequencies. Those high-order modes contribute to the dynamic response of the waveguide at high frequencies since they become propagating.

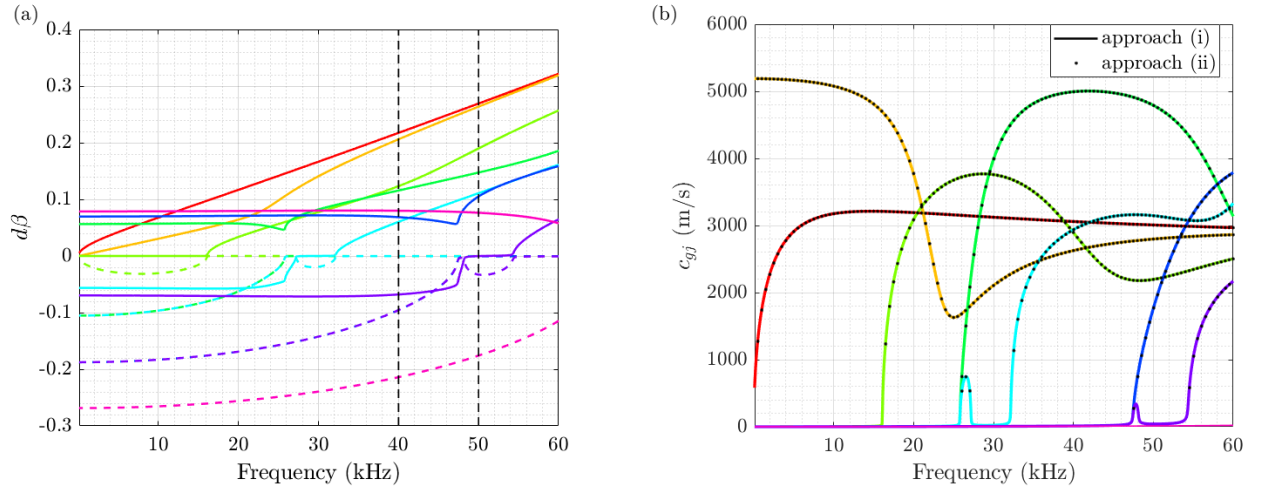


Figure 2.8: (a) Dispersion curves (real part and imaginary parts of the wavenumbers β_j are plotted in continuous and dashed lines, respectively) and (b) group velocities, (i) using Eq. (2.33) and (ii) using Eq. (2.32), for the flexural (red), longitudinal (yellow), shearing (light green), and higher-order (green, pink and purple, respectively) modes.

The group velocities can be computed in two ways: (i) using Eq. (2.33) and (ii) using Eq. (2.32). The results are shown in Fig. 2.8(b). One can see that both approaches produce the same results. This is due to low damping. However, as explained by Langley [123], for the general case of a damped system, this equality can no longer hold. Hence, the energy propagates with a velocity that is not the group velocity.

Figs. 2.9(a) and (b) show four different wave shapes (ϕ_{qj}) at 40 kHz and at 50 kHz, respectively. The colors of the plotted wave shapes correspond to those highlighted as in Fig. 2.8; the non-deformed substructure is plotted in black lines. It is worth mentioning that the shape of each mode can vary along the frequency, illustrating the difficulty of tracking a specific mode over frequencies when a frequency step is not chosen carefully.

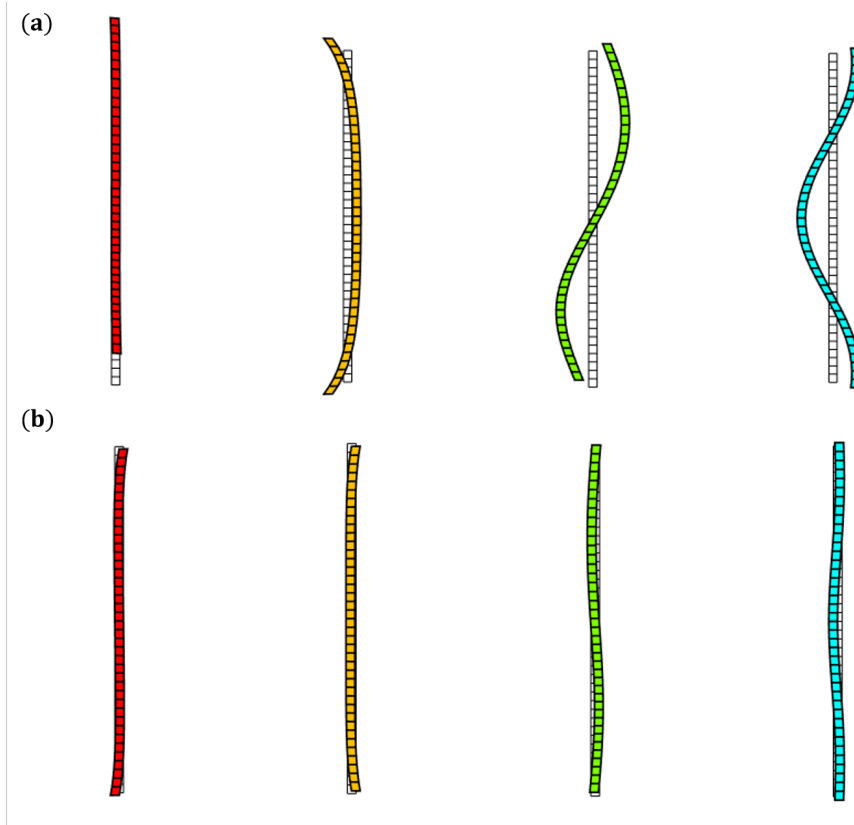


Figure 2.9: Spatial representation of different wave mode shapes for the 2D beam at (a) 40 kHz and (b) 50 kHz for flexural (red), longitudinal (yellow), shearing (green), and a high-order (blue) modes.

The frequency response of the 2D plane stress beam is shown in Fig. 2.10(a), where the displacement q_x is taken at the excitation point. The FE solution is also computed as a reference for comparison purposes. The relative errors between the two solutions are displayed in Fig. 2.10(b), which shows good accuracy, with a relative error below 10^{-4} %. In terms of computational time, the FE solution takes around 94 s, while the WFE solution only takes 17 s for the wave mode computation and the forced response. This represents a time reduction of 82%. This interesting property of the WFE method has been extensively reported in the literature in various systems other than beam-like structures, see for example [23, 27, 28]. The

computational time difference is more evident for long structures such as pipes and thin-walled structures. This is explained by the fact that the FE method operates with large matrices, while the WFE method only uses the FE model of a substructure.

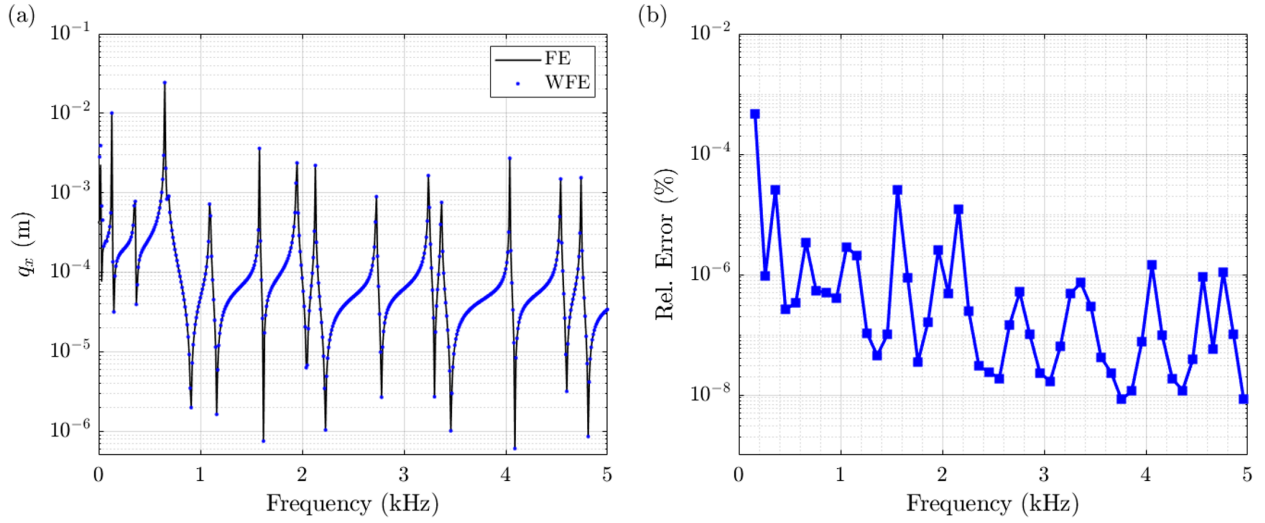


Figure 2.10: (a) Comparison between the magnitude of the vertical displacement obtained with the FE and WFE methods for the 2D plane stress beam. (b) Relative error between the approaches computed by means of Eq. (2.42).

For the validation of the proposed approach in the time domain, a time-dependent force $F(t)$ is applied. This force represents a Gaussian pulse centered at 25 kHz as shown in Fig. 2.11(a), whose frequency spectrum is shown in Fig. 2.11(b). The frequency response is measured at the point where the force is applied, as seen in Fig. 2.7. As discussed in Sec. 2.4, it is possible to obtain the displacement in function of time using the DFT. This means (i) choosing the sampling frequency and building the time span; (ii) computing the DFT of the force $F(t)$ to obtain $F(\omega)$; (iii) computing the forced frequency response at one or more points; and (iv) performing the IDFT.

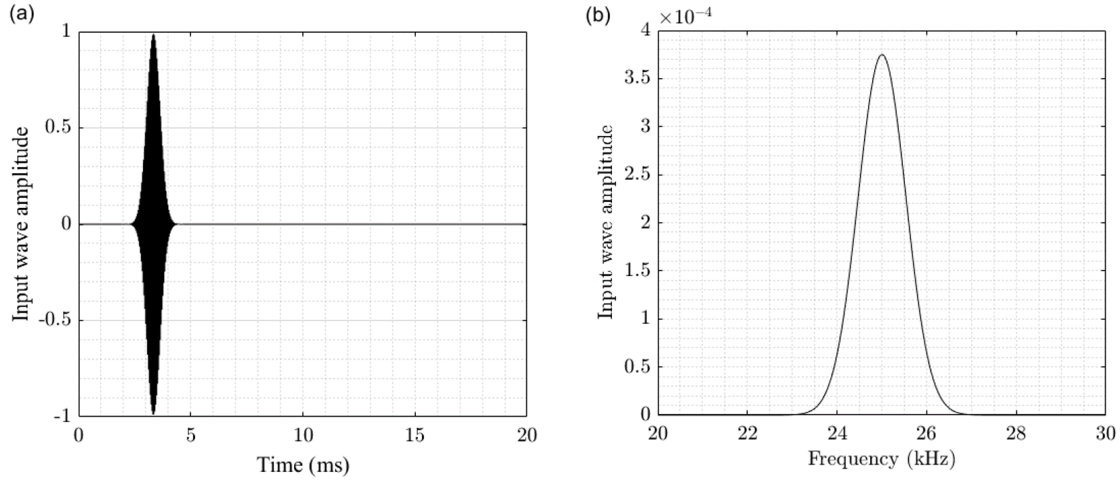


Figure 2.11: (a) Pulse excitation in the time domain and (b) absolute value of the Fourier transform.

The numerical simulation uses a sampling frequency $f_s = 800$ kHz and $T = 25$ ms, which is sufficient to respect the Nyquist–Shannon sampling requirement. This leads to a time step of $dt = 1.25 \mu\text{s}$. Comparison with a FE time-domain simulation is proposed, in which the Newmark method with parameters $\beta = 0.25$ and $\gamma = 0.5$ is used [111]. It appears that the FE solution converges when the time step is $\Delta t = 0.1 \mu\text{s}$. A priori, there is no reason to expect the same time step when using the Newmark method and the Fourier transformation, since different approaches are used. The comparison between these methods is displayed in Figs. 2.12(a) and (b), where the normalized longitudinal and transversal displacements (denoted by q_x and q_y , respectively) at the excitation point is shown.

Again, the small time step required for the convergence of the solution in the time domain and the number of degrees of freedom involved (around 65600 DoFs in this case) make the FE method slower than the WFE method combined with the Fourier transform to obtain the same time response. The FE method takes 57.12 minutes and the WFE method takes 9.56 minutes. This represents a reduction of 83.2 % for the computational time. So, the WFE approach seems appropriate in terms of time saving and accuracy to compute the time response in long

waveguides.

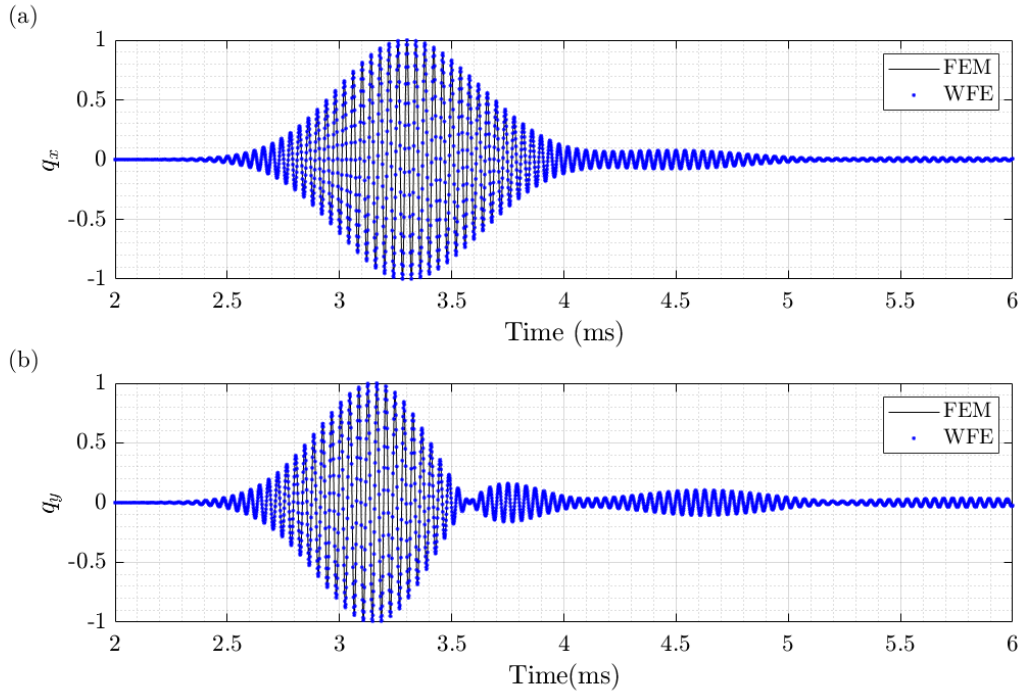


Figure 2.12: Comparison between FE and WFE solutions for measured displacements as a function of time for a 2D plane stress beam when a Gaussian pulse centered at 25 kHz is applied: (a) longitudinal displacement (q_x) and (b) vertical displacement (q_y) at the excitation point.

2.7 Coupling elements

The WFE method aims to describe the wave propagation in 1D periodic structures. In this framework, two different structures/waveguides can be coupled by means of coupling elements. This can be achieved by combining the WFE method for modeling the waveguides and the FE approach for the coupling element. For instance, Fig. 2.13 shows two waveguides connected by a coupling element (in this case, a curved joint).

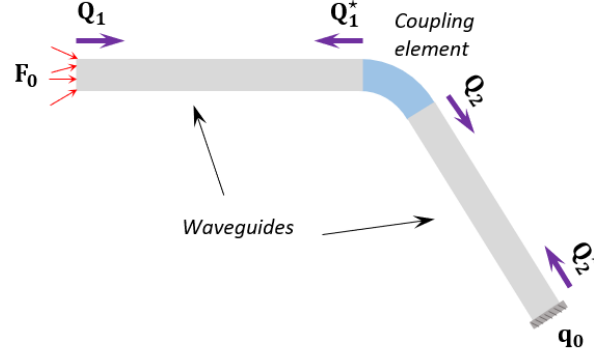


Figure 2.13: Schematic of two waveguides 1 and 2 connected by a coupling element. Waveguide 1 is subjected to a force at the left boundary, and waveguide 2 is clamped at the right boundary. Here, $(\mathbf{Q}_1, \mathbf{Q}_1^*)$ and $(\mathbf{Q}_2, \mathbf{Q}_2^*)$ denote wave amplitude vectors for waveguides 1 and 2, respectively.

Within the WFE framework, the modeling of the structure is achieved by considering wave base modes for waveguides 1 and 2, and coupling conditions. The coupling elements are not necessarily periodic structures and can represent curved joints or defects. The procedure is based on the computation of the so-called scattering matrices for describing transmitted and reflected waves.

2.7.1 Scattering matrix

For the sake of simplicity, let us consider two waveguides 1 and 2 with the same cross-section and material properties. Waveguides 1 and 2 are composed of N_1 and N_2 substructures, respectively. The dynamic equilibrium equation of the coupling element expressed at the interfaces with waveguides 1 and 2, denoted by Γ_1 and Γ_2 , is given by:

$$\mathbf{D}^{c*} \begin{bmatrix} \mathbf{q}_{\Gamma_1} \\ \mathbf{q}_{\Gamma_2} \end{bmatrix} = \begin{bmatrix} \mathbf{F}_{\Gamma_1} \\ \mathbf{F}_{\Gamma_2} \end{bmatrix}, \quad (2.43)$$

where \mathbf{D}^{c*} is the condensed DSM of the coupling element, and \mathbf{q}_{Γ_1} and \mathbf{q}_{Γ_2} (resp. \mathbf{F}_{Γ_1} and \mathbf{F}_{Γ_2})

are the displacement (resp. force) vectors on Γ_1 and Γ_2 . These vectors can be accessed via wave expansions (see Eqs. (2.27 and (2.28)), i.e.:

$$\mathbf{q}_{\Gamma_1} = \mathcal{L}_1 \left(\Phi_q \mu^{N_1} \mathbf{Q}_1 + \Phi_q^* \mathbf{Q}_1^* \right) \quad \text{and} \quad \mathbf{F}_{\Gamma_1} = \mathcal{L}_1 \left(\Phi_F \mu^{N_1} \mathbf{Q}_1 + \Phi_F^* \mathbf{Q}_1^* \right), \quad (2.44)$$

and

$$\mathbf{q}_{\Gamma_2} = \mathcal{L}_2 \left(\Phi_q \mathbf{Q}_2 + \Phi_q^* \mu^{N_2} \mathbf{Q}_2^* \right) \quad \text{and} \quad \mathbf{F}_{\Gamma_2} = -\mathcal{L}_2 \left(\Phi_q \mathbf{Q}_2 + \Phi_q^* \mu^{N_2} \mathbf{Q}_2^* \right), \quad (2.45)$$

where \mathbf{Q}_1 and \mathbf{Q}_1^* are wave amplitude vectors for waveguide 1, and \mathbf{Q}_2 and \mathbf{Q}_2^* are wave amplitude vectors for waveguide 2, as shown in Fig. 2.13. \mathcal{L}_1 and \mathcal{L}_2 are direction cosine matrices introduced to project waveguide's local coordinate systems 1 and 2 onto a global one. Inserting Eqs (2.44) and (2.45) into Eq. (2.43) leads to:

$$\begin{aligned} \mathbf{D}^{c*} \begin{bmatrix} \mathcal{L}_1 \Phi_q & \mathbf{0} \\ \mathbf{0} & -\mathcal{L}_2 \Phi_q^* \end{bmatrix} \begin{bmatrix} \mu^{N_1} \mathbf{Q}_1 \\ \mu^{N_2} \mathbf{Q}_2^* \end{bmatrix} + \mathbf{D}^{c*} \begin{bmatrix} \mathcal{L}_1 \Phi_q^* & \mathbf{0} \\ \mathbf{0} & \mathcal{L}_2 \Phi_q \end{bmatrix} \begin{bmatrix} \mathbf{Q}_1^* \\ \mathbf{Q}_2 \end{bmatrix} = \\ - \begin{bmatrix} \mathcal{L}_1 \Phi_F & \mathbf{0} \\ \mathbf{0} & -\mathcal{L}_2 \Phi_F^* \end{bmatrix} \begin{bmatrix} \mu^{N_1} \mathbf{Q}_1 \\ \mu^{N_2} \mathbf{Q}_2^* \end{bmatrix} - \begin{bmatrix} \mathcal{L}_1 \Phi_F & \mathbf{0} \\ \mathbf{0} & -\mathcal{L}_2 \Phi_F^* \end{bmatrix} \begin{bmatrix} \mathbf{Q}_1^* \\ \mathbf{Q}_2 \end{bmatrix}. \end{aligned} \quad (2.46)$$

This yields:

$$\begin{aligned} \left(\mathbf{D}^{c*} \begin{bmatrix} \mathcal{L}_1 \Phi_q^* & \mathbf{0} \\ \mathbf{0} & \mathcal{L}_2 \Phi_q \end{bmatrix} + \begin{bmatrix} \mathcal{L}_1 \Phi_F^* & \mathbf{0} \\ \mathbf{0} & -\mathcal{L}_2 \Phi_F \end{bmatrix} \right) \begin{bmatrix} \mathbf{Q}_1^* \\ \mathbf{Q}_2 \end{bmatrix} = \\ - \left(\mathbf{D}^{c*} \begin{bmatrix} \mathcal{L}_1 \Phi_q & \mathbf{0} \\ \mathbf{0} & \mathcal{L}_2 \Phi_q^* \end{bmatrix} + \begin{bmatrix} \mathcal{L}_1 \Phi_F & \mathbf{0} \\ \mathbf{0} & -\mathcal{L}_2 \Phi_F^* \end{bmatrix} \right) \begin{bmatrix} \mu^{N_1} \mathbf{Q}_1 \\ \mu^{N_2} \mathbf{Q}_2^* \end{bmatrix}. \end{aligned} \quad (2.47)$$

In Eq. (2.47), the relation between incoming wave amplitude vectors $\left[(\boldsymbol{\mu}^{N_1} \mathbf{Q}_1)^T \quad (\boldsymbol{\mu}^{N_2} \mathbf{Q}_2^*)^T \right]^T$ and outgoing wave amplitude vectors $\left[\mathbf{Q}_1^{*T} \quad \mathbf{Q}_2^T \right]^T$ at the coupling element is given by [127]:

$$\begin{bmatrix} \mathbf{Q}_1^* \\ \mathbf{Q}_2 \end{bmatrix} = \mathbb{C} \begin{bmatrix} \boldsymbol{\mu}^{N_1} \mathbf{Q}_1 \\ \boldsymbol{\mu}^{N_2} \mathbf{Q}_2^* \end{bmatrix} = \begin{bmatrix} \mathbb{C}_{11} & \mathbb{C}_{12} \\ \mathbb{C}_{21} & \mathbb{C}_{22} \end{bmatrix} \begin{bmatrix} \boldsymbol{\mu}^{N_1} \mathbf{Q}_1 \\ \boldsymbol{\mu}^{N_2} \mathbf{Q}_2^* \end{bmatrix}, \quad (2.48)$$

where

$$\begin{aligned} \mathbb{C} = & - \left(\mathbf{D}^{\text{c}*} \begin{bmatrix} \mathcal{L}_1 \boldsymbol{\Phi}_q^* & \mathbf{0} \\ \mathbf{0} & \mathcal{L}_2 \boldsymbol{\Phi}_q \end{bmatrix} + \begin{bmatrix} \mathcal{L}_1 \boldsymbol{\Phi}_F^* & \mathbf{0} \\ \mathbf{0} & -\mathcal{L}_2 \boldsymbol{\Phi}_F \end{bmatrix} \right)^{-1} \\ & \times \left(\mathbf{D}^{\text{c}*} \begin{bmatrix} \mathcal{L}_1 \boldsymbol{\Phi}_q & \mathbf{0} \\ \mathbf{0} & \mathcal{L}_2 \boldsymbol{\Phi}_q^* \end{bmatrix} + \begin{bmatrix} \mathcal{L}_1 \boldsymbol{\Phi}_F & \mathbf{0} \\ \mathbf{0} & -\mathcal{L}_2 \boldsymbol{\Phi}_F^* \end{bmatrix} \right). \end{aligned} \quad (2.49)$$

In Eqs. (2.49) and (2.48), \mathbb{C} is the so-called scattering matrix. Its components represent wave transmission and reflection coefficients between the two waveguides. The wave amplitudes \mathbf{Q}_1^* and \mathbf{Q}_2 represent the reflected waves at the interface of the coupling element; $\boldsymbol{\mu}^{N_1} \mathbf{Q}_1$ and $\boldsymbol{\mu}^{N_2} \mathbf{Q}_2^*$ are the wave amplitudes of the incident waves at the interface of the coupling element. The scattering matrix only depends on the properties of the coupling elements and the wave modes of the waveguides, see Eq. (2.48). The determination of the wave amplitudes depends on the boundary conditions at the other waveguide end.

The computation of the condensed DSM of the coupling element $\mathbf{D}^{\text{c}*}$ involves the condensation of the internal DoFs, with the calculation of $(\mathbf{D}_{\text{II}}^{\text{c}})^{-1}$ at each discrete frequencies, see Eq. (2.4). Depending on the number of internal DoFs, the computation of the condensed DSM can introduce numerical error and can be computationally cumbersome [28, 128]. This numerical step can be sped up using the Craig-Bampton (CB) reduction method, which involves considering static modes and a reduced number of fixed-interface modes of the coupling element [129]. The method to compute the condensed DSM is described hereafter.

2.7.2 CB method

Consider the FE model of a coupling element as shown in Fig. 2.14. Here, the FE mesh of the left and right boundaries of the coupling element are supposed to be compatible with the FE meshes of the connected waveguides. The dynamic equilibrium equation of the coupling element is written as:

$$\left(-\omega^2 \begin{bmatrix} \mathbf{M}_{II}^c & \mathbf{M}_{IB}^c \\ \mathbf{M}_{BI}^c & \mathbf{M}_{BB}^c \end{bmatrix} + i\omega \begin{bmatrix} \mathbf{C}_{II}^c & \mathbf{C}_{IB}^c \\ \mathbf{C}_{BI}^c & \mathbf{C}_{BB}^c \end{bmatrix} + \begin{bmatrix} \mathbf{K}_{II}^c & \mathbf{K}_{IB}^c \\ \mathbf{K}_{BI}^c & \mathbf{K}_{BB}^c \end{bmatrix} \right) \begin{bmatrix} \mathbf{q}_I^c \\ \mathbf{q}_B^c \end{bmatrix} = \begin{bmatrix} \mathbf{F}_I^c \\ \mathbf{F}_B^c \end{bmatrix} \quad (2.50)$$

where \mathbf{F}^c and \mathbf{q}^c denote force and displacement vectors; \mathbf{M}^c , \mathbf{C}^c , and \mathbf{K}^c denote the mass, damping, and stiffness matrices, respectively. The damping matrix \mathbf{C}^c is supposed to be proportional to the mass and stiffness matrices (Rayleigh type): $\mathbf{C}^c = a\mathbf{M}^c + b\mathbf{K}^c$, with a and b real positive constants. In the same way as in Eq. (2.3), the DoFs can be grouped into internal (I) and boundary (B), with (B) the set of DoFs on the left (L) and right (R) boundaries. Also, let us denote as n_B and n_I the numbers of boundary and internal DoFs, respectively.

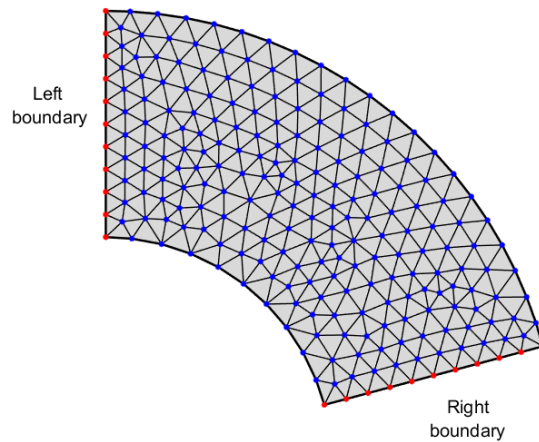


Figure 2.14: FE mesh of 2D coupling element. The left and right boundary nodes are highlighted in red, while interior nodes are highlighted in blue.

Within the framework of the CB method [28, 129], the displacement vector \mathbf{q}_I^c is approximated as follows:

$$\mathbf{q}_I^c \approx \tilde{\mathbf{q}}_I^c = \mathbf{X}_{st} \mathbf{q}_B^c + \tilde{\mathbf{X}}_{e1} \tilde{\boldsymbol{\alpha}} \quad (2.51)$$

where $\tilde{\boldsymbol{\alpha}}$ denotes a vector of generalized coordinates, and \mathbf{X}_{st} represents the matrix of static modes of size $n_I \times n_B$, and it is defined as:

$$\mathbf{X}_{st} = -(\mathbf{K}_{II}^c)^{-1} \mathbf{K}_{IB}^c, \quad (2.52)$$

In Eq. (2.51), $\tilde{\mathbf{X}}_{e1}$ denotes the matrix of fixed-interface modes defined as $\tilde{\mathbf{X}}_{e1} = [(\mathbf{x}_{e1})_1 \cdots (\mathbf{x}_{e1})_{m_I}]$, where $(\mathbf{x}_{e1})_j$ are the eigenvectors obtained from the following eigenproblem:

$$\mathbf{K}_{II}^c (\mathbf{x}_{e1})_j = \omega_j^2 \mathbf{M}_{II}^c (\mathbf{x}_{e1})_j, \quad (2.53)$$

where ω_j is the eigenfrequency associated to a fixed-interface mode $(\mathbf{x}_{e1})_j$. The modes are supposed to be normalized with respect to the mass matrix, i.e., $(\mathbf{x}_{e1})_k^T \mathbf{M}_{II}^c (\mathbf{x}_{e1})_l = \delta_{kl}$, with δ_{kl} the Kronecker delta. The reduction is based on the choice of the number of fixed interface modes whose eigenfrequencies are below a certain threshold. The number of retained modes is denoted by m_I , with $m_I < n_I$. From a computational point of view, m_I can be determined through a convergence analysis of the WFE solution over the frequency band of interest. Then, Eq. (2.55) can be written as:

$$\begin{bmatrix} \mathbf{q}_I^c \\ \mathbf{q}_B^c \end{bmatrix} \approx \begin{bmatrix} \tilde{\mathbf{q}}_I^c \\ \mathbf{q}_B^c \end{bmatrix} = \begin{bmatrix} \tilde{\mathbf{X}}_{e1} & \mathbf{X}_{st} \\ \mathbf{0} & \mathbf{I} \end{bmatrix} \begin{bmatrix} \tilde{\boldsymbol{\alpha}} \\ \mathbf{q}_B^c \end{bmatrix} = \mathbf{T}_{CB} \begin{bmatrix} \tilde{\boldsymbol{\alpha}} \\ \mathbf{q}_B^c \end{bmatrix}. \quad (2.54)$$

where \mathbf{T}_{CB} is the CB transformation matrix. Eq. (2.54) together with Eq. (2.50) lead to the reduced DSM of the coupling element:

$$\tilde{\mathbf{D}}^c = \mathbf{T}_{\text{CB}}^T \mathbf{D}^c \mathbf{T}_{\text{CB}} = \begin{bmatrix} \tilde{\mathbf{D}}_{\text{e1-e1}}^c & \tilde{\mathbf{D}}_{\text{e1-st}}^c \\ (\tilde{\mathbf{D}}_{\text{e1-st}}^c)^T & \mathbf{D}_{\text{st-st}}^c \end{bmatrix}, \quad (2.55)$$

where

$$\tilde{\mathbf{D}}_{\text{e1-e1}}^c = \tilde{\mathbf{X}}_{\text{e1}}^T \mathbf{D}_{\text{II}}^c \tilde{\mathbf{X}}_{\text{e1}} \quad (2.56)$$

$$\tilde{\mathbf{D}}_{\text{e1-st}}^c = \tilde{\mathbf{X}}_{\text{e1}}^T \mathbf{D}_{\text{II}}^c \tilde{\mathbf{X}}_{\text{st}} + \tilde{\mathbf{X}}_{\text{e1}}^T \mathbf{D}_{\text{IB}}^c \quad (2.57)$$

$$\mathbf{D}_{\text{st-st}}^c = \tilde{\mathbf{X}}_{\text{st}}^T \mathbf{D}_{\text{II}}^c \tilde{\mathbf{X}}_{\text{st}} + \tilde{\mathbf{X}}_{\text{e1}}^T \mathbf{D}_{\text{IB}}^c + \mathbf{D}_{\text{IB}}^c \tilde{\mathbf{X}}_{\text{st}}^T + \mathbf{D}_{\text{BB}}^c \quad (2.58)$$

Finally, the condensed DSM of the coupling element is:

$$\mathbf{D}^{c*} \approx \tilde{\mathbf{D}}^{c*} = \tilde{\mathbf{D}}_{\text{st-st}}^c - \tilde{\mathbf{D}}_{\text{st-e1}}^c \left(\tilde{\mathbf{D}}_{\text{e1-e1}}^c \right)^{-1} \tilde{\mathbf{D}}_{\text{e1-st}}^c. \quad (2.59)$$

The computation of $\left(\tilde{\mathbf{D}}_{\text{e1-e1}}^c \right)^{-1}$ is less cumbersome due to its reduced size and because it is diagonal. This can be proven using Eqs. (2.50), (2.53), and (2.56):

$$\begin{aligned} (\mathbf{X}_{\text{e1}})_k^T \mathbf{D}_{\text{II}}^c (\mathbf{X}_{\text{e1}})_j &= (\mathbf{X}_{\text{e1}})_k^T \left[(-\omega^2 + \mathbf{i}a\omega) \mathbf{M}_{\text{II}}^c + (1 + \mathbf{i}b\omega) \mathbf{K}_{\text{II}}^c \right] \tilde{\mathbf{X}}_{\text{e1}} \\ &= (-\omega^2 + \mathbf{i}a\omega) (\mathbf{X}_{\text{e1}})_k^T \mathbf{M}_{\text{II}}^c (\mathbf{X}_{\text{e1}})_j + (1 + \mathbf{i}b\omega) (\mathbf{X}_{\text{e1}})_k^T \mathbf{K}_{\text{II}}^c (\mathbf{X}_{\text{e1}})_j \\ &= \delta_{kj} \left[(-\omega^2 + \mathbf{i}a\omega) + \omega_j^2 (1 + \mathbf{i}b\omega) \right]. \end{aligned} \quad (2.60)$$

This proof only holds when the damping is proportional to the mass and stiffness. For a general damping model, it is not possible to ensure that $\tilde{\mathbf{D}}_{\text{e1-e1}}^c$ remains diagonal.

2.7.3 Forced response

The determination of the wave amplitude vectors depends on the system's boundary conditions. For example, let us consider two straight waveguides connected by a coupling

element, see Fig. 2.13. Apart from coupling conditions, the boundary conditions of the assembly are written as:

$$\mathbf{F}_0 = -\mathcal{L}_1 \left(\Phi_{\mathbf{F}} \mathbf{Q}_1 + \Phi_{\mathbf{F}} \boldsymbol{\mu}^{N_1} \mathbf{Q}_1^* \right) \quad (2.61)$$

$$\mathbf{q}_0 = \mathcal{L}_2 \left(\Phi_{\mathbf{q}} \boldsymbol{\mu}^{N_2} \mathbf{Q}_2 + \Phi_{\mathbf{q}}^* \mathbf{Q}_2^* \right). \quad (2.62)$$

Also, coupling conditions between the two waveguides are formulated by Eq. (2.48). Then, the following matrix system of size $4n \times 4n$ is found [29]:

$$\begin{bmatrix} \mathbf{I} & \mathbb{C}_{\mathbf{F}} \boldsymbol{\mu}^{N_1} & \mathbf{0} & \mathbf{0} \\ -\mathbb{C}_{11} \boldsymbol{\mu}^{N_1} & \mathbf{I} & \mathbf{0} & -\mathbb{C}_{12} \boldsymbol{\mu}^{N_2} \\ -\mathbb{C}_{21} \boldsymbol{\mu}^{N_1} & \mathbf{0} & \mathbf{I} & -\mathbb{C}_{22} \boldsymbol{\mu}^{N_2} \\ \mathbf{0} & \mathbf{0} & \mathbb{C}_{\mathbf{q}} \boldsymbol{\mu}^{N_2} & \mathbf{I} \end{bmatrix} \begin{bmatrix} \mathbf{Q}_1 \\ \mathbf{Q}_1^* \\ \mathbf{Q}_2 \\ \mathbf{Q}_2^* \end{bmatrix} = \begin{bmatrix} -(\Phi_{\mathbf{F}})^{-1} \mathbf{F}_0 \\ \mathbf{0} \\ \mathbf{0} \\ (\Phi_{\mathbf{q}}^*)^{-1} \mathbf{q}_0 \end{bmatrix}, \quad (2.63)$$

where $\mathbb{C}_{\mathbf{F}} = (\Phi_{\mathbf{F}})^{-1} (\Phi_{\mathbf{F}}^*)$ and $\mathbb{C}_{\mathbf{q}} = (\Phi_{\mathbf{q}}^*)^{-1} (\Phi_{\mathbf{q}})$. Eq. (2.63) has to be solved for several discrete frequencies since the wave shapes and wavenumbers are frequency-dependent. The computation of the wave amplitude vectors allows the description of the forces and displacements along the structure, see Eqs. (2.27) and (2.28).

2.7.4 Numerical example

A simple system involving two waveguides and a coupling element, as shown in Fig. 2.15, is analyzed over the frequency band $[0, 50]$ kHz. The waveguides are modeled in the same way, see Sec. 2.6.2. The coupling element represents a square of size $d_c \times h = 0.1 \text{ m} \times 0.1 \text{ m}$ with a hole of size $R_h = 0.02 \text{ m}$. The related mesh is obtained via DistMesh [130] where 3202 three-node plane stress triangular elements are considered, and 41 nodes are used on the left and right boundaries. Waveguide 1 has a length $l_1 = 0.5 \text{ m}$, and it is excited at its first node

by a vector force \mathbf{F}_0 . The displacement is assessed at the same point. Also, waveguide 2 has a length $l_2 = 0.5$ m, and its right side is clamped.

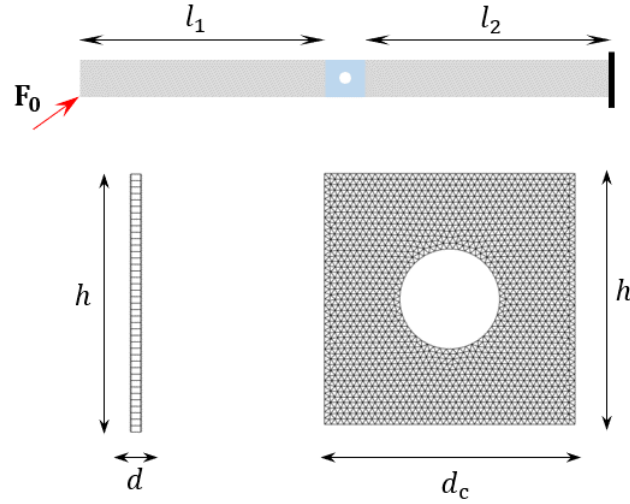


Figure 2.15: Schematics of two waveguides coupled by a coupling element representing a square with a hole. The system is subjected to a vector force at the left boundary and it is clamped on the right boundary.

The WFE model of this system can be performed in the frequency domain as follows:

- (i) Computing wave modes $\{\mu_j, \phi_j\}_{j=1, \dots, n}$ and $\{\mu_j^*, \phi_j^*\}_{j=1, \dots, n}$ using the (\mathbf{N}, \mathbf{L}) or $(\mathbf{S} + \mathbf{S}^{-1})$ methods, see Secs. 2.2.1 and 2.2.2;
- (ii) Computing the scattering matrix of the coupling elements \mathbb{C} , see Sec. 2.7.1;
- (iii) Solving a linear matrix equation to obtain the wave amplitude vectors, see Sec. 2.7.3;
- (iv) Assessing the displacements and forces via wave expansion, see Eqs. (2.27) and (2.28).

To express the scattering matrix, the condensation of the DSM of the coupling element is applied. For this purpose, the CB method with different numbers of fixed-interface modes is used. Results for the WFE and FE methods are shown in Fig. 2.16. The FE method is used as a reference.

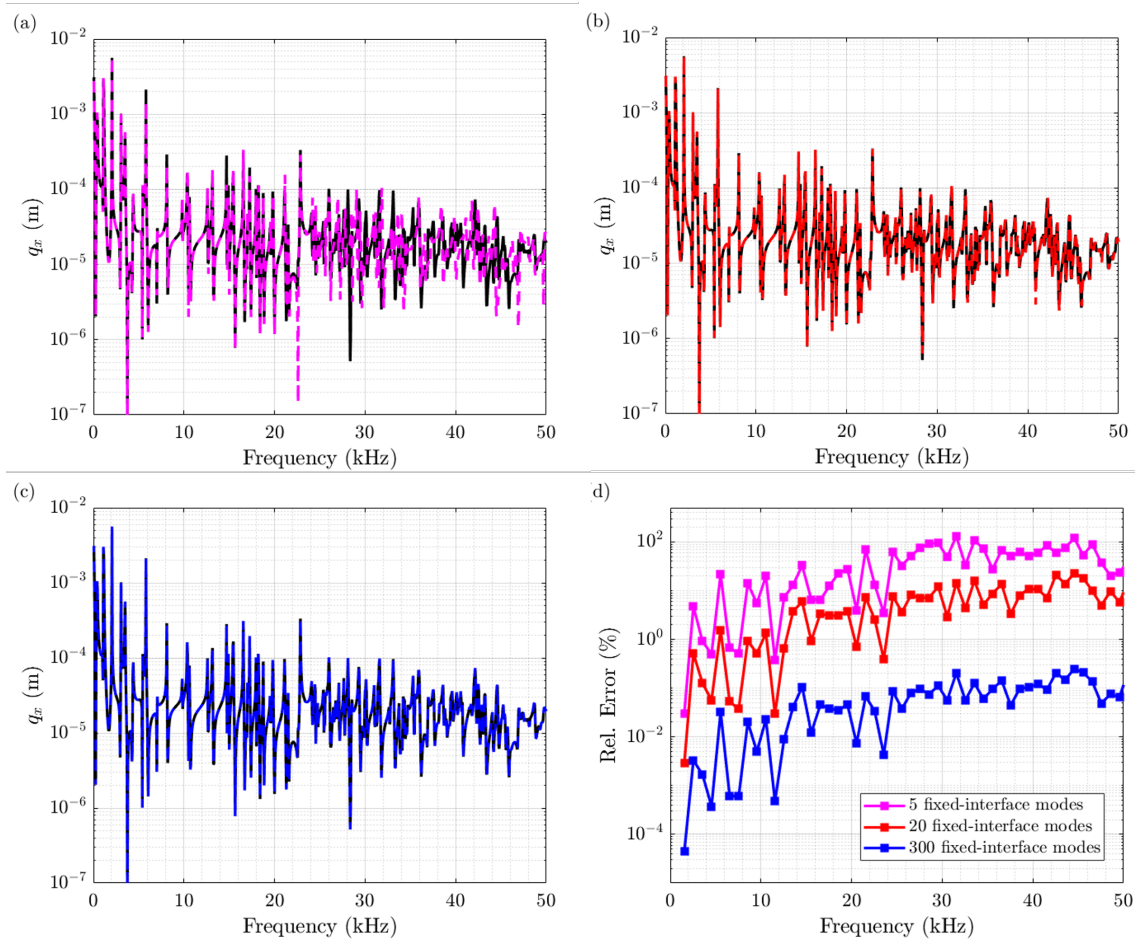


Figure 2.16: Measured displacement obtained with the FE (black curve), and WFE (colored curves) methods when (a) 5, (b) 20, and (c) 300 fixed-interface modes are retained in the Craig-Bampton reduction; (d) shows the relative error between the FE and WFE results for each case.

Three different cases are analyzed with 5, 20, and 300 fixed interface modes in the CB reduction. For each case, the maximum eigenfrequency of the retained fixed-interface modes and the computational time are displayed in Table 2.1. It is possible to see that the computational time related to the WFE method with the CB reduction for the coupling element does not change considerably for the three cases. However, it appears to be significantly small compared to the FE simulation. When 300 retained modes are considered, the errors made to compute the response are below 1% over the frequency range; see Fig. 2.16(d). In Table 2.1, it is shown that half of the computational time is spent to calculate Eqs. (2.59), (2.63), and (2.49). The study of the relative error when a certain number of fixed-interface modes is retained is well reported in the literature, for instance [28]. Although not done here, reducing the wave basis is an interesting topic since the size of the linear system and the scattering matrix problem can be drastically reduced.

Table 2.1: Elapsed times for FE method and WFE method + CB reduction. The number of retained fixed-interface modes analyzed is 5, 20, and 300. For comparison purposes, the time associated with the computation of the wave modes $\{\mu_j, \phi_j\}_{j=1,\dots,n}$ and $\{\mu_j^*, \phi_j^*\}_{j=1,\dots,n}$ is also shown. f_{max} is the maximum frequency of the frequency band.

Method	Number of fixed-interface modes retained	Maximum eigenfrequency (kHz)	Time (s)
FE	—	—	226.7
WFE + CB	5	28.6 ($0.57f_{max}$)	29.9
WFE + CB	20	70.7 ($1.41f_{max}$)	31.3
WFE + CB	300	302.7 ($6.05f_{max}$)	32.5
Computation of $\{\mu_j, \phi_j\}_{j=1,\dots,n}$ and $\{\mu_j^*, \phi_j^*\}_{j=1,\dots,n}$			15.9

The scattering matrices can be accessed via the WFE method, i.e., the transmission and reflections coefficients between waveguides. Fig. 2.17 shows the absolute value of some

components of the scattering matrix of the coupling element. The transmission coefficients of waveguide 1 to waveguide 2 are plotted in dashed lines, while the reflected coefficients from waveguide 1 to itself are plotted in continuous lines (color convention is similar to Fig. 2.8). For example, Fig. 2.17(a) shows the reflection and transmission coefficient for the flexural wave. Fig. 2.17(b-d) show the absolute values of the reflection and transmission coefficients for the longitudinal, shearing, and high order mode (H.O.).

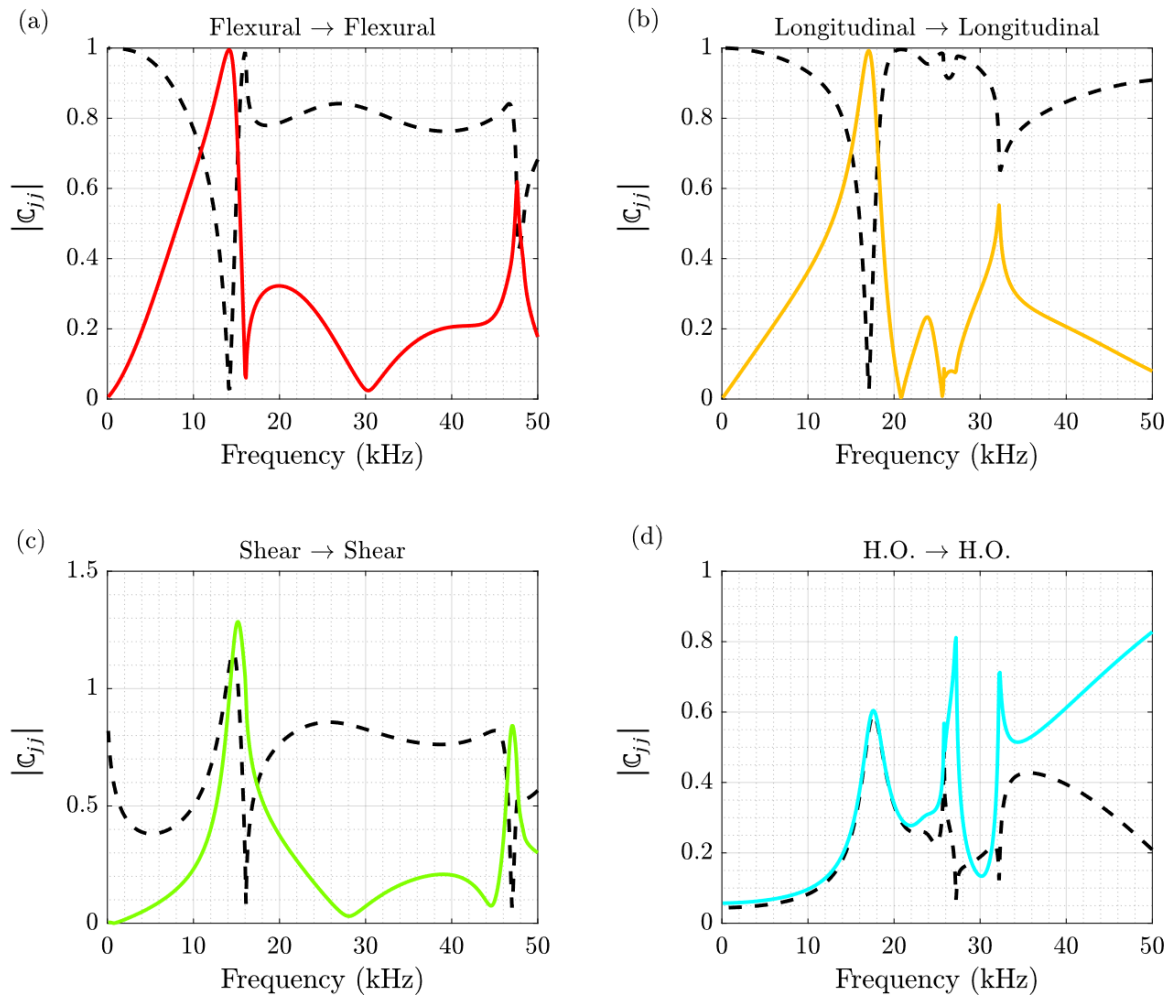


Figure 2.17: Absolute value of the transmission coefficients (dashed line) from waveguide 1 to waveguide 2, and reflection coefficients (continuous line) from waveguide 1 to itself.

In Fig. 2.17, peaks can be observed along the frequency; some are related to cut-off frequencies of some modes, and others are associated with resonances of the coupling element. Scattering phenomena are complex and depend on the energy exchange between modes and on how guided waves interact with the coupling element. It should be pointed out that the values of the reflection and transmission coefficients could exceed one. It happens because the computation of the scattering matrix is based on the wave shapes and wave amplitudes, and then the scattering matrix depends on the normalization of the wave modes [127].

2.8 Conclusions

In this chapter, the WFE method was introduced. It enables the analysis of the dispersion curves and forced responses for periodic structures. Two specific structures were discussed, i.e., a Timoshenko's beam and a 2D plane-stress beam. Considering Timoshenko's beam, the dispersion curves and the response functions were obtained and compared with analytical solutions. The second example provided a comparison between the FE and the WFE methods. It was demonstrated that the WFE method can be employed for computing the transient response of periodic structures and the group velocities for guided waves. Also, the WFE method can be used to model waveguides connected via coupling elements like a curved joint. The modeling of coupling elements relies on FE modeling and the CB method. The WFE method enables the computation of scattered waves (transmitted and reflected) at coupling elements. Regarding computational time savings, the WFE method is an efficient alternative to the FE method, especially when long structures are dealt with.

Chapter 3

Defect localization in waveguide assemblies with curved joints

This chapter is an extraction of the papers: [\[30, 131\]](#).

3.1 Overview

A numerical approach is proposed to localize defects in elastic waveguides connected to curved elastic joints. 2D assemblies involving straight waveguides with a curved joint and a defect are specifically dealt with, where the joint is placed between the measurement point (output signals) and the defect. Such an analysis requires assessing wave conversion phenomena and times of flight for wave packets when they are transmitted through the joint and reflected by the defect. An original WFE strategy is proposed where the times of flight, for transmitted or reflected wave packets, are defined from the frequency derivatives of the arguments of the scattering matrices of the joint and the defect. The procedure to localize a defect follows from

the expressions of the times of flight. The proposed approach enables the identification of the types of waves that are transmitted through the joint and reflected by the defect. Numerical experiments are carried out which highlight the relevance, in terms of accuracy and robustness, of the proposed approach.

The key idea behind the present chapter is that the times of flight for wave packets traveling in a coupling element (joint, defect), in transmission or reflection, can be determined from the frequency derivatives of the arguments of its scattering matrix. The propagation times in waveguides follow from the analysis of the group velocities. In this sense, a theoretical expression of the time that incident wave packets takes to propagate and be transmitted/reflected by a joint/defect can be proposed. The position of the defect can be determined by comparing these theoretical times of flight with the experimental ones (measurements). The proposed approach also provides a physical insight into the types of waves that are transmitted through the joint and reflected by the defect (pathways). The contributions of this part can be summed up as follows:

- Expressing the times of flight for wave packets traveling in coupling elements (joint, defect) from the frequency derivatives of the arguments of their scattering matrices.
- Identifying the types of waves that are transmitted/reflected by a joint/defect (pathways).
- Providing a procedure to localize a defect for different possible pathways.

The rest of the chapter is organized as follows. In Sec. 3.2, the FE model of a waveguide assembly, including a defect and a curved joint, is presented. The related issues about defect localization are discussed. In Sec. 3.4, theoretical expressions of the times of flight in transmission and reflection, for a coupling element, are given. Also, the procedure for estimating the position of a defect from measured and theoretical/estimated times of flight is detailed. In Sec. 3.6, numerical experiments are carried out, which concern waveguide assemblies with curved joints of different angles of curvature, and defects representing circular holes of different radii.

3.2 Problem description

The problem addressed here concerns the dynamic analysis of straight elastic waveguides connected via curved elastic joints and containing defects. A waveguide assembly involving three waveguides, a curved joint, and a defect is shown in Fig. 3.1. For simplicity and without loss of generality, the assumption is made that the waveguides have similar cross-sections and material properties. Those waveguides are usually modeled with periodic FE meshes, i.e., FE meshes that are built from assembling identical substructures (similar between the waveguides) along some straight directions. On the other hand, the curved joint and the defect can be modeled using arbitrary FE meshes where the term “defect” is understood as a part of a waveguide – namely, a coupling element – with a defect.

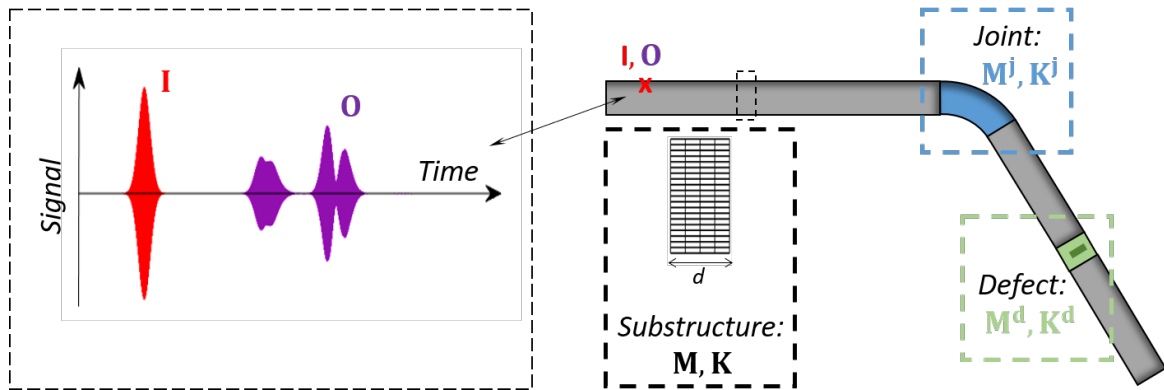


Figure 3.1: Schematic of a waveguide assembly with a curved joint and a defect. Input (I) and output (O) signals are recorded as functions of time (the red cross represents the measurement point).

The propagation of waves in periodic waveguides – i.e., structures described with periodic FE meshes – is well mastered nowadays. The question arises as to how to localize a defect in such waveguide assemblies considering one input wave packet transmitted through a joint and reflected by a defect, which gives rise to several output wave packets (several types of waves) measured at several times. Typical wave packets, for different types of waves, are shown in

Fig. 3.1. Here, considering a curved elastic joint makes the present topic much more complicated compared to the usual pulse-echo procedure for straight waveguides with one defect. The underlying issue concerns the description of the wave conversion phenomena inside the joint and the lack of procedure to quantify the time a certain wave packet takes to get transmitted through it. This makes the defect localization hard to figure out. [99]

Prior to any wave propagation analysis (next section) and defect localization procedure, the FE modeling of the waveguide substructures, the joint, and the defect are detailed. First, let us denote by \mathbf{M} , \mathbf{C} and \mathbf{K} the mass, damping, and stiffness matrices (respectively) of a substructure expressed in its local reference frame and which are assumed to be symmetric. The FE mesh of a substructure is shown in Fig. 3.1. In the frequency domain, the dynamic equilibrium equation of this substructure is expressed by:

$$\mathbf{D}\mathbf{q} = \mathbf{F}, \quad (3.1)$$

where \mathbf{q} and \mathbf{F} are the vectors of nodal displacements and nodal forces of the substructure, respectively, and \mathbf{D} is the related dynamic stiffness matrix (DSM), similar for all the substructures, expressed by:

$$\mathbf{D} = -\omega^2\mathbf{M} + i\omega\mathbf{C} + \mathbf{K}, \quad (3.2)$$

where ω is the angular frequency, and i is the imaginary unit. Considering Rayleigh damping, the matrix \mathbf{C} can be expressed as:

$$\mathbf{C} = a\mathbf{M} + b\mathbf{K}, \quad (3.3)$$

where a and b are two real positive constants. Also, let us denote by \mathbf{D}^* the condensed DSM of the substructure, i.e., the DSM condensed on the interface degrees of freedom (DoFs) with the other substructures:

$$\mathbf{D}^* = \mathbf{D}_{\text{BB}} - \mathbf{D}_{\text{BI}} (\mathbf{D}_{\text{II}})^{-1} \mathbf{D}_{\text{IB}}, \quad (3.4)$$

where subscripts B and I refer to the boundary/interface DoFs and the internal DoFs – i.e., those which do not belong to the interfaces with the other substructures –, respectively.

As for the curved joint and the defect, the dynamic equilibrium equations are written as:

$$\mathbf{D}^{\mathbf{d}}\mathbf{q}^{\mathbf{d}} = \mathbf{F}^{\mathbf{d}} \quad , \quad \mathbf{D}^{\mathbf{j}}\mathbf{q}^{\mathbf{j}} = \mathbf{F}^{\mathbf{j}}, \quad (3.5)$$

where superscripts \mathbf{d} and \mathbf{j} denote the defect and the joint, respectively. Here, the DSMs of the defect and the joint are given by:

$$\mathbf{D}^{\mathbf{d}} = -\omega^2\mathbf{M}^{\mathbf{d}} + i\omega\mathbf{C}^{\mathbf{d}} + \mathbf{K}^{\mathbf{d}} \quad , \quad \mathbf{D}^{\mathbf{j}} = -\omega^2\mathbf{M}^{\mathbf{j}} + i\omega\mathbf{C}^{\mathbf{j}} + \mathbf{K}^{\mathbf{j}}. \quad (3.6)$$

The related condensed DSMs – namely $\mathbf{D}^{\mathbf{d}*}$ and $\mathbf{D}^{\mathbf{j}*}$ – can be expressed in the same way as Eq. (3.4). It is worth emphasizing that the computation of these condensed DSMs, including that of the substructures, is not computationally prohibitive and can be easily achieved via CB method, see Sec. 2.7.2.

3.3 Scattering matrices for coupling elements

A waveguide assembly involving three waveguides 1, 2 and 3 (N_1 , N_2 and N_3 substructures), a curved joint and a defect, is shown in Fig. 3.2. Within the WFE framework, scattering matrices of the joint and the defect — namely, $\mathbb{C}^{\mathbf{j}}$ and $\mathbb{C}^{\mathbf{d}}$ — are expressed by [21, 128]:

$$\begin{aligned} \mathbb{C}^{\mathbf{j}} = & - \left(\mathbf{D}^{\mathbf{j}*} \begin{bmatrix} \mathcal{L}_1\Phi_{\mathbf{q}}^* & \mathbf{0} \\ \mathbf{0} & \mathcal{L}_2\Phi_{\mathbf{q}} \end{bmatrix} + \begin{bmatrix} \mathcal{L}_1\Phi_{\mathbf{F}}^* & \mathbf{0} \\ \mathbf{0} & -\mathcal{L}_2\Phi_{\mathbf{F}} \end{bmatrix} \right)^{-1} \\ & \times \left(\mathbf{D}^{\mathbf{j}*} \begin{bmatrix} \mathcal{L}_1\Phi_{\mathbf{q}} & \mathbf{0} \\ \mathbf{0} & \mathcal{L}_2\Phi_{\mathbf{q}}^* \end{bmatrix} + \begin{bmatrix} \mathcal{L}_1\Phi_{\mathbf{F}} & \mathbf{0} \\ \mathbf{0} & -\mathcal{L}_2\Phi_{\mathbf{F}}^* \end{bmatrix} \right). \end{aligned} \quad (3.7)$$

and

$$\begin{aligned} \mathbb{C}^{\mathbf{d}} = & - \left(\mathbf{D}^{\mathbf{d}*} \begin{bmatrix} \mathcal{L}_2\Phi_{\mathbf{q}}^* & \mathbf{0} \\ \mathbf{0} & \mathcal{L}_3\Phi_{\mathbf{q}} \end{bmatrix} + \begin{bmatrix} \mathcal{L}_2\Phi_{\mathbf{F}}^* & \mathbf{0} \\ \mathbf{0} & -\mathcal{L}_3\Phi_{\mathbf{F}} \end{bmatrix} \right)^{-1} \\ & \times \left(\mathbf{D}^{\mathbf{d}*} \begin{bmatrix} \mathcal{L}_2\Phi_{\mathbf{q}} & \mathbf{0} \\ \mathbf{0} & \mathcal{L}_3\Phi_{\mathbf{q}}^* \end{bmatrix} + \begin{bmatrix} \mathcal{L}_2\Phi_{\mathbf{F}} & \mathbf{0} \\ \mathbf{0} & -\mathcal{L}_3\Phi_{\mathbf{F}}^* \end{bmatrix} \right). \end{aligned} \quad (3.8)$$

where \mathcal{L}_1 , \mathcal{L}_2 and \mathcal{L}_3 are direction cosine matrices which are introduced here to project the local coordinate systems of waveguides 1, 2 and 3 onto a global one, see in Sec. 2.7.

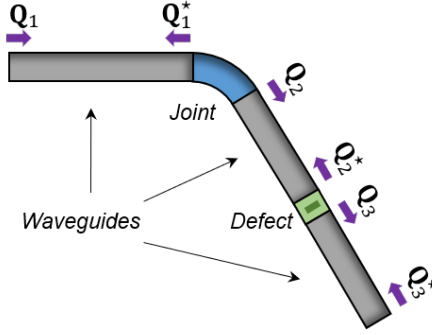


Figure 3.2: Schematic of a waveguide assembly with three waveguides 1, 2 and 3, a curved joint and a defect. $(\mathbf{Q}_1, \mathbf{Q}_1^*)$, $(\mathbf{Q}_2, \mathbf{Q}_2^*)$ and $(\mathbf{Q}_3, \mathbf{Q}_3^*)$ are wave amplitude vectors.

By considering the scattering matrices, the wave amplitude vectors for the outgoing and incoming/incident waves at the boundaries of the joint/defect can be related as follows:

$$\begin{bmatrix} \mathbf{Q}_1^* \\ \mathbf{Q}_2 \end{bmatrix} = \mathbb{C}^j \begin{bmatrix} \boldsymbol{\mu}^{N_1} \mathbf{Q}_1 \\ \boldsymbol{\mu}^{N_2} \mathbf{Q}_2^* \end{bmatrix} = \begin{bmatrix} \mathbb{C}_{11}^j & \mathbb{C}_{12}^j \\ \mathbb{C}_{21}^j & \mathbb{C}_{22}^j \end{bmatrix} \begin{bmatrix} \boldsymbol{\mu}^{N_1} \mathbf{Q}_1 \\ \boldsymbol{\mu}^{N_2} \mathbf{Q}_2^* \end{bmatrix} \quad (3.9)$$

and

$$\begin{bmatrix} \mathbf{Q}_2^* \\ \mathbf{Q}_3 \end{bmatrix} = \mathbb{C}^d \begin{bmatrix} \boldsymbol{\mu}^{N_2} \mathbf{Q}_2 \\ \boldsymbol{\mu}^{N_3} \mathbf{Q}_3^* \end{bmatrix} = \begin{bmatrix} \mathbb{C}_{22}^d & \mathbb{C}_{23}^d \\ \mathbb{C}_{32}^d & \mathbb{C}_{33}^d \end{bmatrix} \begin{bmatrix} \boldsymbol{\mu}^{N_2} \mathbf{Q}_2 \\ \boldsymbol{\mu}^{N_3} \mathbf{Q}_3^* \end{bmatrix}, \quad (3.10)$$

where \mathbf{Q}_1^* and \mathbf{Q}_2 (resp. \mathbf{Q}_2^* and \mathbf{Q}_3) are the wave amplitude vectors for the outgoing waves at the boundaries of the joint (resp. defect), see Fig. 3.2; also, $\boldsymbol{\mu}^{N_1} \mathbf{Q}_1$ and $\boldsymbol{\mu}^{N_2} \mathbf{Q}_2^*$ (resp. $\boldsymbol{\mu}^{N_2} \mathbf{Q}_2$ and $\boldsymbol{\mu}^{N_3} \mathbf{Q}_3^*$) are the wave amplitude vectors for the incoming waves at the same boundaries.

3.4 Times of flight

3.4.1 Group velocities in waveguides

As discussed in Sec. 2.5 and recalled here, the group velocities for waves traveling along a certain waveguide can be calculated in two different ways, i.e., by considering (i) the dispersion curves (frequency variations of wave numbers) or (ii) the transmission matrix of a substructure. Concerning the first approach (i), the group velocity c_{gj} for a given wave j is obtained as [62]:

$$c_{gj} = \frac{\partial \omega}{\partial \Re\{\beta_j\}}, \quad (3.11)$$

where β_j is the related wave number, computed by means of the WFE method. The procedure then involves computing a numerical derivative (Eq. (3.11)), which implies considering a small frequency step. On the other hand, the second way (ii) involves considering the scattering matrix \mathbb{C}^s of a substructure. The scattering matrix \mathbb{C}^s follows from the strategy explained in Sec. 3.3. By considering the conventions defined earlier, one has:

$$\begin{bmatrix} \boldsymbol{\mu}^{N+1-k} \mathbf{Q}^* \\ \boldsymbol{\mu}^k \mathbf{Q} \end{bmatrix} = \mathbb{C}^s \begin{bmatrix} \boldsymbol{\mu}^{k-1} \mathbf{Q} \\ \boldsymbol{\mu}^{N-k} \mathbf{Q}^* \end{bmatrix} = \begin{bmatrix} \mathbf{0} & \boldsymbol{\mu} \\ \boldsymbol{\mu} & \mathbf{0} \end{bmatrix} \begin{bmatrix} \boldsymbol{\mu}^{k-1} \mathbf{Q} \\ \boldsymbol{\mu}^{N-k} \mathbf{Q}^* \end{bmatrix}. \quad (3.12)$$

In this case, since the waveguide is purely periodic with identical substructures, the scattering matrix \mathbb{C}^s only contains transmission coefficients which are stored in the off-diagonal block terms $\boldsymbol{\mu}$ (diagonal matrix of wave parameters $\mu_j = e^{-i\beta_j d}$). By computing the arguments of the diagonal components of the transmission matrix $\boldsymbol{\mu}$, this yields:

$$\arg(\mu_j) = \arg(e^{-i\beta_j d}) = -\Re\{\beta_j\}d. \quad (3.13)$$

As a result, the group velocities can be alternatively defined as:

$$c_{gj} = -d \frac{\partial \omega}{\partial \arg(\mu_j)}. \quad (3.14)$$

The present strategy can be extended to the analysis of a waveguide with N' substructures, of length $l = N'd$. In this case, the group velocities would be given by:

$$c_{gj} = -l \frac{\partial \omega}{\partial \arg(T_{jj})}. \quad (3.15)$$

where $T_{jj} = \mu_j^{N'}$ are the transmission coefficients.

3.4.2 Times of flight in transmission

From Eq. (3.15), the time of flight τ_{jj} taken by a wave j to get across a straight coupling element of length l made up of N' substructures, connecting two waveguides 1 and 2, can be defined as follows:

$$\tau_{jj} = \frac{l}{c_{gj}} = -\frac{\partial \arg(T_{jj})}{\partial \omega}. \quad (3.16)$$

In this case, the coupling element and the waveguides are supposed to share the same characteristics – i.e., the same substructures – which means that the coupling element does not give rise to wave reflection and wave conversion. Following the same idea, the time of flight that would spend a given wave j to get across a coupling element of arbitrary shape – which could be a curved joint or a defect – from waveguide 1 to waveguide 2 may be assessed in a general way as follows:

$$\tau_{ij}^{1-2} = -\frac{\partial \arg(\mathbb{C}_{21ij})}{\partial \omega}, \quad (3.17)$$

where \mathbb{C}_{21} is the transmission matrix between waveguides 1 and 2, while subscripts i and j are used to describe the general case of a coupling element which gives rise to wave conversion

between waveguide 1 and waveguide 2, i.e., the time taken by a given wave j to be converted into a wave i . It should be remarked that a coupling element of arbitrary shape (e.g., a curved joint) has no associated length, and in this case, the notion of group velocity is somewhat dubious. Thus, the notion of time of flight proposed here appears to be more appropriate.

3.4.3 Times of flight in reflection

The proposed approach also intends to assess the time of flight taken by a wave j to be reflected by a coupling element. Again, note that a coupling element is likely to induce wave conversion, e.g., a given wave j in waveguide 1 is supposed to give one or several reflected waves i ($i = j$ or $i \neq j$) in the same waveguide. In this sense, different wave pathways can be distinguished (i.e., $j \leftarrow j$ or $i \leftarrow j$). In this case, the time of flight (reflection in waveguide 1) may be defined as:

$$\tau_{ij}^{1-1} = -\frac{\partial \arg(\mathbb{C}_{11ij})}{\partial \omega}, \quad (3.18)$$

where \mathbb{C}_{11ij} is the reflection matrix for the waves in waveguide 1.

Remark 1. From the practical point of view, Eq. (3.18) requires the wave shape vectors ϕ_j and ϕ_j^* to be post-processed. Indeed, even though these vectors are normalized properly [23], their orientation in the complex plane is not defined a priori. Indeed, the multiplication of any of these vectors by any complex number of unit modulus would yield a “valid” vector, but of a different orientation. In other words, for a given frequency, the orientations of ϕ_j and ϕ_j^* in the complex plane can be different and arbitrary. Also, the relative orientation between ϕ_j and ϕ_j^* is likely to change as the frequency does. Considering the transmission and reflection coefficients, this means that their arguments are not necessarily defined in the same way at each frequency. This issue can be solved by fixing the orientation of the wave shape vectors between two consecutive frequencies f and $f + \Delta f$, which can be done by setting the argument of $(\phi_j)_f^H (\phi_j)_{f+\Delta f}$ to zero (H being the conjugate transpose). Also, by imposing

symmetry conditions between the right-going and left-going wave shape vectors ϕ_j and ϕ_j^* [23], their relative orientations can be set to zero too.

Remark 2. In some cases, the times of flight in reflection or transmission (Eqs (3.18)-(3.17)) between two waves j and i can be difficult to comprehend physically, considering irregular behavior of the functions $\mathbb{C}_{11ij}(\omega)$ and $\mathbb{C}_{12ij}(\omega)$ around some frequency ω . This might happen at local resonances of the coupling element [127]. In this case, it is advised to analyze other types of waves, i.e., those with components \mathbb{C}_{11ij} and \mathbb{C}_{12ij} which are less impacted by the local resonances of the coupling element (see Sec. 3.6.1.2).

3.4.4 Discussion

In the present work, it is proposed to assess the times of flight for waves transmitted through, or reflected by, a coupling element – that could be of arbitrary nature (e.g., joint, defect) – from the frequency derivatives of the arguments of its scattering matrix, see Eqs. (3.17) and (3.18). The procedure can be generalized to any wave packet having a narrow envelope $\hat{E}(\omega - \omega_0)$ centered around some angular frequency ω_0 . A proof of this statement is given hereafter.

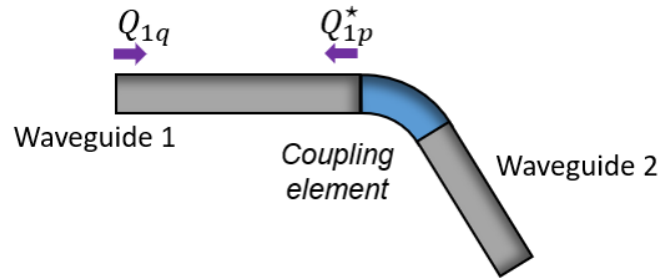


Figure 3.3: Schematic of two waveguides 1 and 2 connected with an arbitrary coupling element (curved joint or defect). Q_{1q} and Q_{1p}^* are wave amplitudes for two waves q and p in waveguide 1.

Let us consider two waveguides 1 and 2 which are connected with a coupling element as

shown in Fig. 3.3. Without loss of generality, let us assume that the scattering matrix of this coupling element is null except for one component (p, q) that could be a reflection coefficient (wave q to wave p in waveguide 1), i.e.,

$$\mathbb{C} = \begin{bmatrix} \mathbb{C}_{11} & \mathbb{C}_{21} \\ \mathbb{C}_{12} & \mathbb{C}_{22} \end{bmatrix}, \quad (3.19)$$

where $\mathbb{C}_{21} = \mathbf{0}$, $\mathbb{C}_{12} = \mathbf{0}$, $\mathbb{C}_{22} = \mathbf{0}$, and:

$$\mathbb{C}_{11ij} = \begin{cases} 0 & \text{for } (i, j) \neq (p, q), \\ c(\omega) e^{i\theta(\omega)} & \text{for } (i, j) = (p, q). \end{cases} \quad (3.20)$$

Here, the amplitude $c(\omega)$ and phase $\theta(\omega)$ of the non-zero reflection coefficient \mathbb{C}_{11pq} depend on the frequency. Then, let us consider in the frequency domain a traveling wave packet q of narrow envelope $\hat{E}(\omega - \omega_0)$ that could represent a Gaussian, and whose inverse Fourier transform is denoted by $E(t)$. The related displacement vector in waveguide 1, at the interface with the coupling element, may be approximated as:

$$\mathbf{q}(\omega) \approx \phi_{qq}(\omega_0) \underline{Q}_{1q}(\omega), \quad (3.21)$$

where $\underline{Q}_{1q} = \mu^{N_1} Q_{1q}$ is the amplitude of the incident wave q at the interface between waveguide 1 and the coupling element:

$$\underline{Q}_{1q}(\omega) = \hat{E}(\omega - \omega_0). \quad (3.22)$$

Then, the amplitude of the reflected wave packet in the waveguide 1 is given by:

$$Q_{1p}^*(\omega) = \hat{E}(\omega - \omega_0) c(\omega) e^{i\theta(\omega)}. \quad (3.23)$$

Let us linearize $\theta(\omega)$ around ω_0 , i.e.:

$$\theta(\omega) \approx \theta(\omega_0) + (\omega - \omega_0) \left. \frac{\partial \theta(\omega)}{\partial \omega} \right|_{\omega_0}. \quad (3.24)$$

Introducing Eq.(3.24) into Eq.(3.23) leads to:

$$Q_{1p}^*(\omega) = \hat{E}(\omega - \omega_0)c(\omega_0)e^{i[\theta(\omega_0) - \omega_0 \frac{\partial \theta(\omega)}{\partial \omega}|_{\omega_0}]} e^{i\omega \frac{\partial \theta(\omega)}{\partial \omega}|_{\omega_0}}, \quad (3.25)$$

where assumption is made that $c(\omega) \approx c(\omega_0)$. Finally, considering the inverse Fourier transform of the reflected wave packet, this yields $\phi_{qp}^*(\omega_0)\mathcal{F}^{-1}[Q_{1p}^*(\omega)]$ where:

$$\mathcal{F}^{-1}[Q_{1p}^*(\omega)] = E \left(t + \frac{\partial \theta(\omega)}{\partial \omega} \Big|_{\omega_0} \right) c(\omega_0) e^{i[\theta(\omega_0) - \omega_0 \frac{\partial \theta(\omega)}{\partial \omega}|_{\omega_0}]}. \quad (3.26)$$

Eq. (3.26) shows that the reflected wave packet occurs in waveguide 1 with a delay of $-\partial \theta(\omega)/\partial \omega|_{\omega_0}$ (time of flight), as expected. The procedure for determining the times of flight in transmission can be proven in a similar way.

3.5 Defect localization

The localization of a defect in a waveguide assembly can be achieved as follows. Let us consider the following test cases (see Fig. 3.4), i.e., (a) two waveguides with a defect, and (b) three waveguides with a curved joint and a defect. In both cases, the assumption is made that the scattering matrices of the defect and the joint are known.

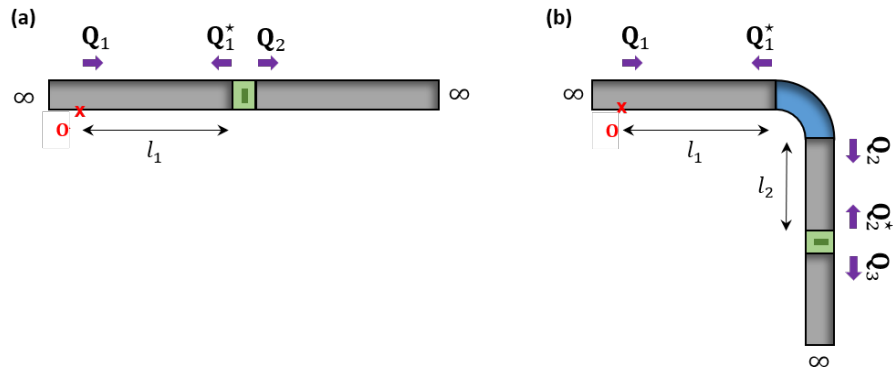


Figure 3.4: Waveguide assemblies: (a) two waveguides with a defect; (b) three waveguides with a curved joint and a defect. The red cross highlights the measurement point.

In case (a), a traveling wave packet j is generated in waveguide 1 and sent towards the defect. Then, a reflected wave packet i is measured in waveguide 1. The distance between the measurement point and the defect is l_1 , see Fig. 3.4(a). Let us denote by c_{gj} and c_{gi} the group velocities of the wave packets j and i , respectively. Then, the delay between the excitation time (wave packet j) and the measurement time (wave packet i) is given by:

$$\tau_{ij} = \frac{l_1}{c_{gj}} + \tau_{ij}^{\text{d}} + \frac{l_1}{c_{gi}}, \quad (3.27)$$

where τ_{ij}^{d} is the time of flight in reflection for the defect, see Eq. (3.18). From the knowledge of τ_{ij} , the localization of the defect can therefore be estimated as:

$$l_1 = (\tau_{ij} - \tau_{ij}^{\text{d}}) \left(\frac{1}{c_{gj}} + \frac{1}{c_{gi}} \right)^{-1}. \quad (3.28)$$

In case (b), a traveling wave packet l is generated in waveguide 1, transmitted through the joint in waveguide 2 (wave packet k), reflected by the defect in waveguide 2 (wave packet j), and transmitted through the joint in waveguide 1 back to the measurement point (wave packet i). In this case, the delay between the excitation time (wave packet l) and the measurement time (wave packet i) is given by:

$$\tau_{ijkl} = \frac{l_1}{c_{gl}} + \tau_{kl}^{\text{j}} + \frac{l_2}{c_{gk}} + \tau_{jk}^{\text{d}} + \frac{l_2}{c_{gj}} + \tau_{ij}^{\text{j}} + \frac{l_1}{c_{gi}}, \quad (3.29)$$

where τ_{kl}^{j} and τ_{ij}^{j} are the times of flight in transmission taken by wave packets l and j (respectively) to get across the joint, see Eq. (3.17). Also, τ_{jk}^{d} is the time of flight in reflection for the defect, see Eq. (3.18). In this case, the sought position is l_2 which is the distance between the joint and the defect, see Figs. 3.4(b). From Eq. (3.29), this distance can be estimated as follows:

$$l_2 = \left(\tau_{ijkl} - \frac{l_1}{c_{gl}} - \tau_{kl}^{\text{j}} - \tau_{jk}^{\text{d}} - \tau_{ij}^{\text{j}} - \frac{l_1}{c_{gi}} \right) \left(\frac{1}{c_{gk}} + \frac{1}{c_{gj}} \right)^{-1}. \quad (3.30)$$

Here, the challenge is to identify reflected and transmitted wavepackets correctly (wave packets j , k , i) to be able to compute l_2 (the localization of the defect) using the scattering matrix of the joint. The procedure is detailed as follows:

1. A Gaussian wavepacket is sent, and the reflected signal is recorded for a certain type of waves;
2. An analysis of the scattering matrix of the curved joint is done at the central frequency of the Gaussian wavepacket;
3. The waves associated with higher transmission coefficients of the scattering matrix of the joint are considered in the analysis;
4. The times of flight in reflection and transmission for the joint are calculated by Eqs. (3.17) and (3.18);
5. Values of l_2 are found by Eq. (3.30), and different pathways give indications of the defect localization.

3.6 Numerical results

3.6.1 2D plane-stress beam

Numerical experiments are carried out considering waveguide assemblies as shown in Fig. 3.4, where the influence of a curved joint on the localization of a defect is analyzed. 2D thin structures (thickness $e = 0.001$ m) undergoing in-plane motion are considered. The FE meshes of a waveguide substructure, the defect, and the joint are shown in Fig. 3.5. The related material properties are: Young's modulus $E = 210$ GPa, density $\rho = 7800$ kg/m³, Poisson's ratio $\nu = 0.3$ and damping coefficients $a = 10^{-3}$ s⁻¹ and $b = 10^{-8}$ s ($\mathbf{C} = a\mathbf{M} + b\mathbf{K}$). Also, the geometrical properties are: dimensions of the substructures (waveguides) $d \times h = 0.0025$ m \times 0.1 m, height of the joint $h = 0.1$ m and internal radius of the joint $R_{int} = 0.1$ m. Here, a defect representing a square coupling element of size $d^d \times h = 0.1$ m \times 0.1 m, including a hole of size $R_h = 0.02$ m is considered.

In the present case, all the waveguides are supposed to share the same material properties,

height, and thickness, and are modeled using identical substructures. The FE mesh of a substructure is built from 1×40 four-node plane stress rectangular elements with two DoFs per node, as shown in Fig. 3.5. As such, the substructures used to model the waveguides do not contain internal DoFs. The joint is meshed using 40×40 (circumferential and radial directions) four-node plane stress elements. These FE meshes and related FE models can be generated straightforwardly in MATLAB. Also, the FE mesh of the defect (square with hole) can be generated in MATLAB, e.g., via the mesh generator DistMesh [130] where 3202 three-node plane stress triangular elements are considered, including 40 elements on each boundary (see Fig. 3.5). The scattering matrices of the defect and the joint involve computing their condensed DSMs, as explained in Sec. 2.7.2. The CB method is used to speed up this numerical task. This requires computing the static modes of each component (defect, joint) and a reduced number of fixed interface modes, say 400 fixed interface modes for both the defect and the joint, which is supposed to be high enough to accurately represent their dynamical behavior within the frequency band analyzed.

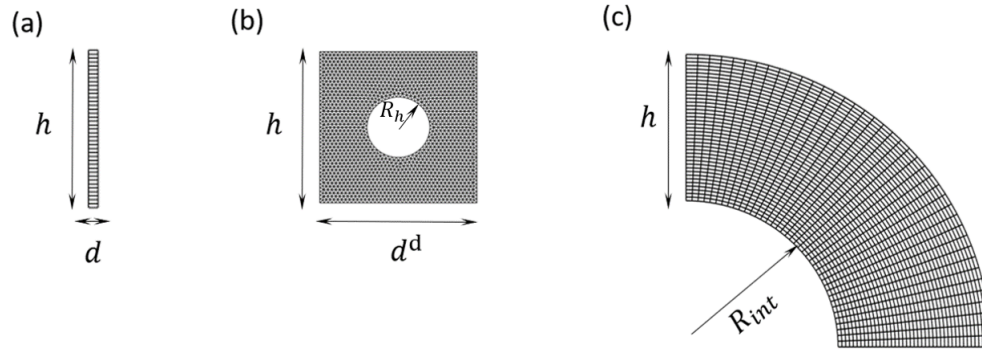


Figure 3.5: FE meshes of (a) a waveguide substructure, (b) the defect, and (c) the curved joint.

Following the WFE method (see Chapter 2), the dispersion curves for the waves traveling in the waveguides can be computed, e.g., over a frequency band of $[0, 40]$ kHz as shown in Fig. 3.6(a). This involves assessing the wave numbers β_j from the eigenvalues μ_j of the transfer matrix \mathbf{S} of a substructure (see Sec. 2.2.2), and plotting the variations of the wave numbers

against frequency. In the present case, each substructure is modeled by means of 40 elements along their height, which means $n = 82$ DoFs on the left/right boundary and, therefore, $n = 82$ right/left-going waves. Here, only a few wave numbers are displayed, i.e., those associated with some “low-order” right-going waves. In particular, the wave numbers for the flexural (blue), longitudinal (red), and shearing (orange) waves, and for three higher-order waves (green, pink, and purple) are displayed. Also, the group velocities for these waves can be computed by means of Eq. (3.14) and displayed as shown in Fig. 3.6(b). At low frequency – i.e., up to 15 kHz –, the wave behavior of the waveguides is quite classical and may be described in terms of the classical flexural (propagating and evanescent) and longitudinal waves. Results show that, at higher frequencies, other types of waves propagate (shearing, high-order) and contribute to the dynamic response of the waveguides. At this stage, the dynamics of the waveguides start being characterized by complex behavior like wave conversion at coupling conditions (defect, joint).

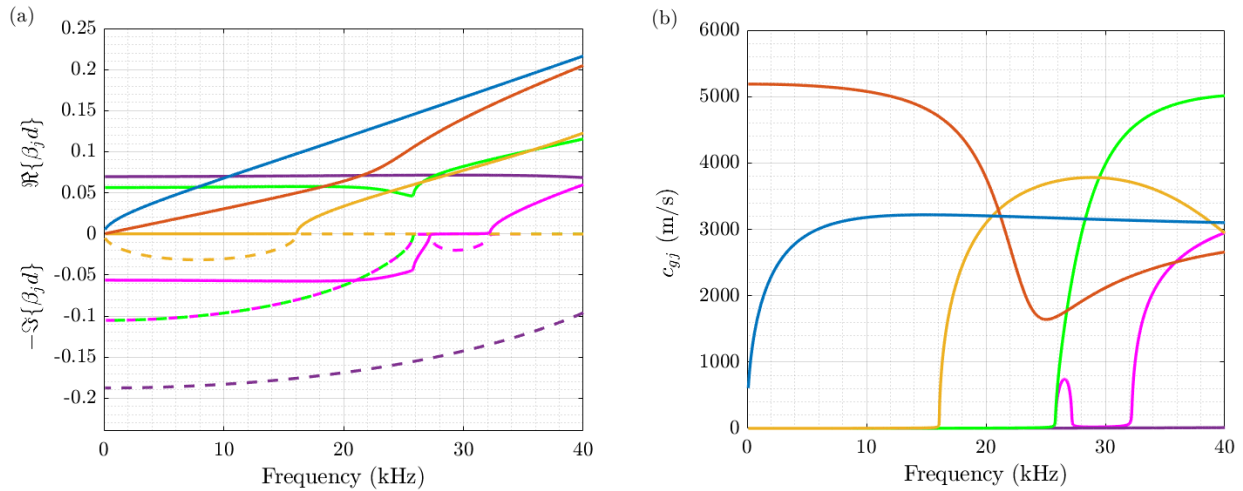


Figure 3.6: (a) Dispersion curves (real part and imaginary parts of the wave numbers β_j are plotted in continuous and dashed lines, respectively) and (b) group velocities for the flexural (blue), longitudinal (red), shearing (orange), and higher-order (green, pink and purple waves).

The next subsections address the time response of the waveguide assemblies and the localization of the defect. The kinds of systems analyzed are shown in Fig. 3.4 and involve

waveguide assemblies with two or three waveguides. Waveguide 1 is excited at some position, and the reflected time signals issued from the defect/joint are recorded at a measurement point representing some node along waveguide 1 at a distance l_1 from the defect or the joint. Here, the first and last waveguides are supposed to be semi-infinite, which means a one-way wave propagation (i.e., before the excitation point in waveguide 1 and after the defect in waveguide 2 or 3).

The WFE modeling of the waveguide assemblies can be easily performed in the frequency domain. This means: (i) computing waves in waveguides (wave parameters, wave shape vectors), see Chap. 2; (ii) computing the scattering matrices of the defect and the joint, see Sec. 3.3; (iii) solving a wave-based matrix equation to determine the wave amplitude vectors and the displacement vectors (see [23] for details). Infinite boundary conditions can be easily taken into account by setting the wave amplitudes for the waves scattered at infinity to zero. Here, the relevant lengths are: $l_1 = 10$ m which represents the distance between the measurement point and the defect (Fig. 3.4(a)) or between the measurement point and the joint (Fig. 3.4(b)), and $l_2 = 5$ m which represents the distance between the joint and the defect (Fig. 3.4(b)).

The input time signal considered in the next subsections is supposed to represent a given wave packet (flexural, or shearing waves) described by a Gaussian pulse centered at 25 kHz as shown in Fig 2.11. The related Fourier transform can be obtained via the `fft` function of MATLAB and the procedure described in [117] and Sec. 2.4. The frequency problem is then solved with the WFE method by considering an input right-going flexural (or shearing) wave packet in waveguide 1, and assessing the measured displacement which results from the multiple scattered waves issued from the defect and the joint. The time response can finally be rebuilt from the inverse Fourier transform (`ifft` function of MATLAB) of the frequency response.

3.6.1.1 Defect localization in a waveguide assembly without joint

Consider the assembly displayed in Fig. 3.4(a), which concerns two aligned waveguides (same properties) with a defect. The distance between the measurement point and the defect

is $l_1 = 10$ m. The motivation behind the present subsection is to obtain an estimate of this distance (which in practice is unknown) from the analysis of the times of flight proposed in Sec. 3.4. Then, an input flexural wave packet (central frequency of 25 kHz) is sent and recorded at the measurement point as shown in Fig. 3.7(a). The measured signals represent the longitudinal displacement at some node located at $l_1 = 10$ m in waveguide 1. The reflected time signal is shown in Fig. 3.7(b) and can be decomposed into flexural, longitudinal, and shearing wave packets (see Figs. 3.7(c-e)). It should be pointed out that the amplitude of the reflected longitudinal wave packet appears to be small compared to the other ones, which means a small conversion effect with flexural waves. From the experimental point of view, the identification of these different reflected wave packets might be done using sensors at several points along the height of waveguide 1, at the abscissa of the measurement point. The measured time of flight, between the input incident wave packet and each reflected one, can be defined as the time delay between the tips of the wave packets as shown in Fig. 3.7 (see red crosses).

On the other hand, the estimated/theoretical time of flight τ_{ij} for each reflected wave packet (flexural, longitudinal, and shearing) is expressed by Eq. (3.27). Here, the group velocities are determined from Fig. 3.6(b) at 25kHz (see also Eq. (3.14)). In Fig. 3.8, the estimated times of flight for the reflected wave packets shown in Fig. 3.7 are plotted as functions of frequency (see continuous curves). These curves show non-smooth behavior – i.e., with localized sudden variations (peaks) after 15 kHz – which reveal mode conversion phenomena between waves (see comments about Fig. 3.6). Also, the measured/experimental times of flight issued from Fig. 3.7 are highlighted by yellow spots in Fig. 3.7, as well as the central frequency of the wave packets (25 kHz, white dashed line). For each type of wave, results show that the estimated time of flight perfectly matches the measured one, as expected, see Figs. 3.8(b-d).

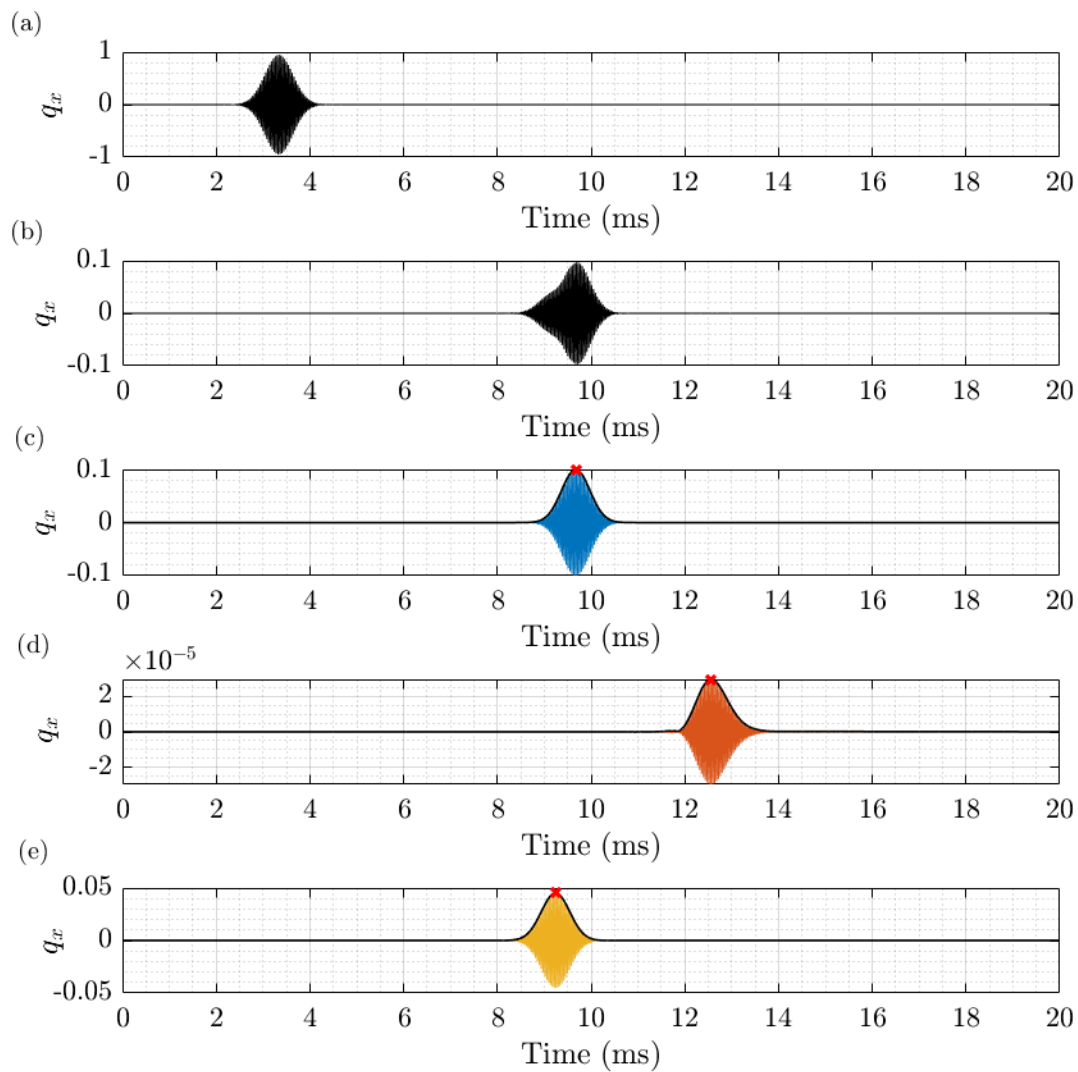


Figure 3.7: Time signals at measurement point for a waveguide assembly without joint: (a) input signal (flexural waves), (b) total reflected signal, (c) reflected flexural wave packet, (d) reflected longitudinal wave packet and (e) reflected shearing wave packet. Red crosses highlight tips (highest magnitudes) of reflected wave packets.

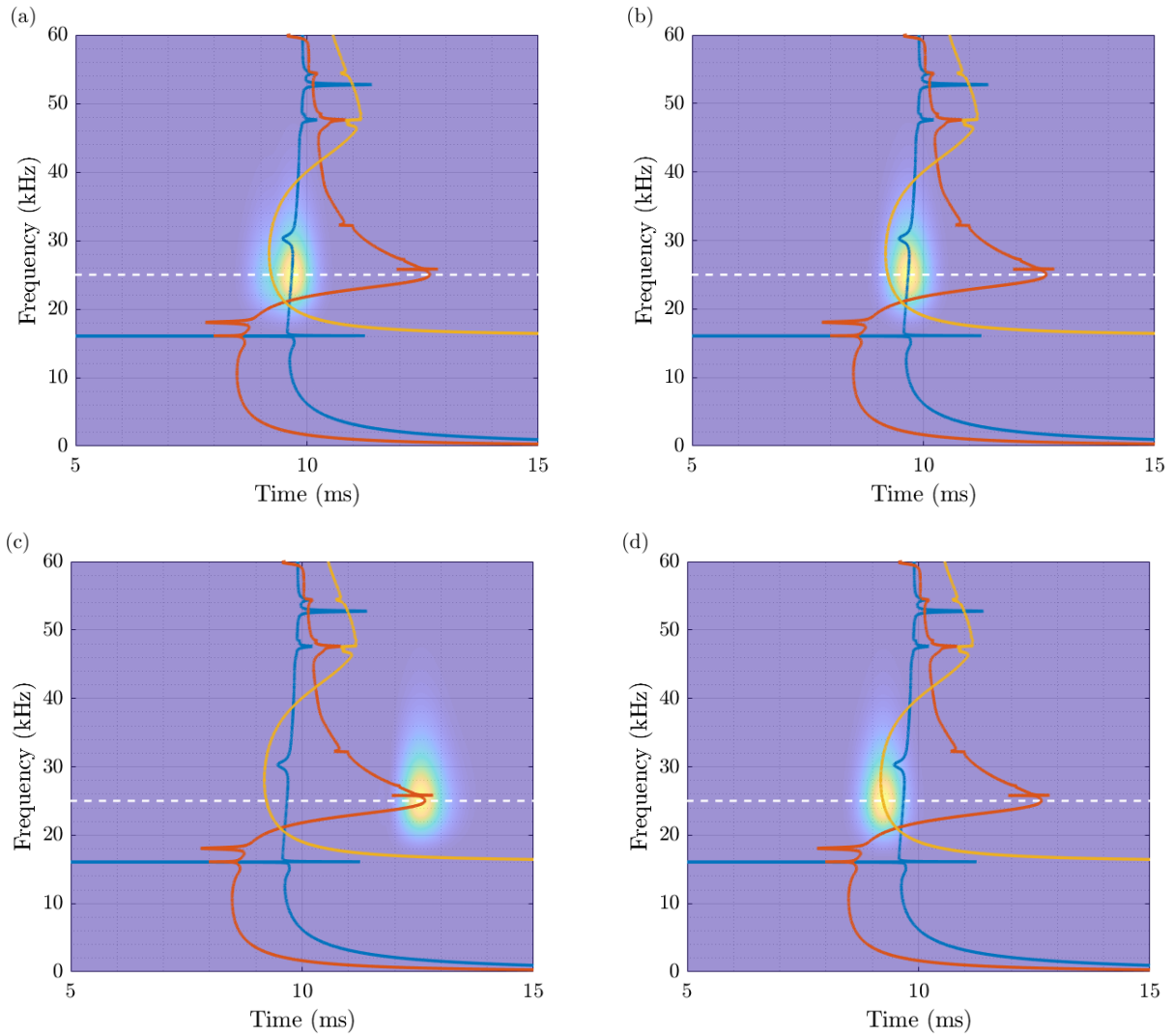


Figure 3.8: Frequency-time map of the reflected signals for a waveguide assembly without joint. Measured times of flight are highlighted by yellow spots. Estimated times of flight represent the crossing points between the curves and the white dashed line: (a) total signal, (b) flexural wave packet (blue), (c) longitudinal wave packet (red) and (d) shearing wave packet (orange).

Note that the curves in Fig. 3.8 can be drawn provided the position of the defect l_1 is known a priori. To address this issue, a fitting procedure can be considered, e.g., by adjusting the length l_1 in order to make these curves coincide with the yellow spots. In this sense, a

raw estimate of the location of the defect can be made, and the types of waves arising from the defect can be identified. Another possibility is to plot the times of flight τ_{ij} as functions of the length l_1 , for different types of reflected waves, and to seek the common value l_1 where the curves $\tau_{ij}(l_1)$ meet the measured value of the times of flight, see Sec. 3.6.1.2. In fact, this can be seen as a linear regression problem, and in the case of a single defect, it can be solved easily. However, in the case of a joint between the observation point and the defect, the linear regression is not straightforward, since the transmitted waves through the joint is unknown a priori.

Tab. 3.1 reports the estimated defect positions obtained from Eq. (3.28) by considering the measured times of flight τ_{ij} (Fig. 3.7) for different reflected wave packets (flexural, longitudinal, shearing). For each wave packet, the estimated value accurately predicts the localization of the defect (i.e., $l_1 = 10$ m) with a relative error smaller than 1%. This also highlights the robustness of the proposed approach, in the sense that the results appear to be roughly similar regardless of the type of wave packet analyzed.

Table 3.1: Estimated position of the defect obtained from Eq. (3.28) and relative error (reference is $l_1 = 10$ m).

	ij	τ_{ij} (ms)	c_{gj} (m/s)	c_{gi} (m/s)	l_1 (m)	Relative error (%)
(1)	flexural \leftarrow flexural	9.67	3178	3178	10.06	0.6
(2)	longitudinal \leftarrow flexural	12.53	3178	1644	9.96	0.4
(3)	shearing \leftarrow flexural	9.24	3178	3688	10.09	0.9

Following Eq. (3.28), it is possible to plot the times of flight τ_{ij} as a function of l_1 for different pathways, as shown in Fig. 3.9. Here, the horizontal black lines represent the measured times of flight, and the oblique lines in blue, red, and orange colors represent τ_{ij} for the pathways associated with the wave packets shown in Fig. (3.7). These oblique lines intersect the horizontal lines around $l_1 = 10$ m. It is a way to illustrate the relevance of the proposed approach.

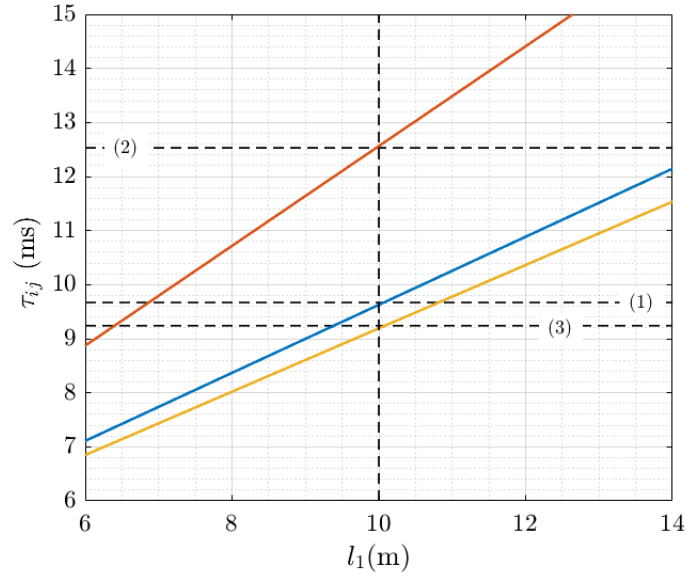


Figure 3.9: Times of flight τ_{ij} as functions of l_1 , for different pathways (blue, red and orange curves are pathways associated with the wave packets shown in Fig. 3.7); measured times of flight are highlighted by horizontal dashed lines.

Aside from defect localization, a sensitivity analysis of the measured time response to the geometrical properties of the defect can be conducted. This could help the selection of the best input signals to detect certain types of defects. For instance, the variation of the output signal amplitude to the input flexural pulse's central frequency and the radius of the hole R_h (defect) radius can be analyzed as shown in Fig. 3.10. Fig. 3.10(a) concerns the amplitude of the reflected flexural wave packet, which shows a monotonic increase with respect to R_h before 15 kHz, and an oscillating behavior at higher frequencies. Fig. 3.10(b) concerns the amplitude of the reflected shearing wave packet, which also shows an oscillating behavior after 15 kHz, i.e., after the cut-off frequency of the shearing wave (below, the magnitude of the reflected signal is null). Given their small amplitudes, reflected signals for longitudinal waves are not investigated here. Those results make it feasible to identify the radius of the defect (R_h) for some known excitation frequency and output signal amplitude or to identify the types of waves that are

mostly sensitive to detect a hole with a given radius R_h .

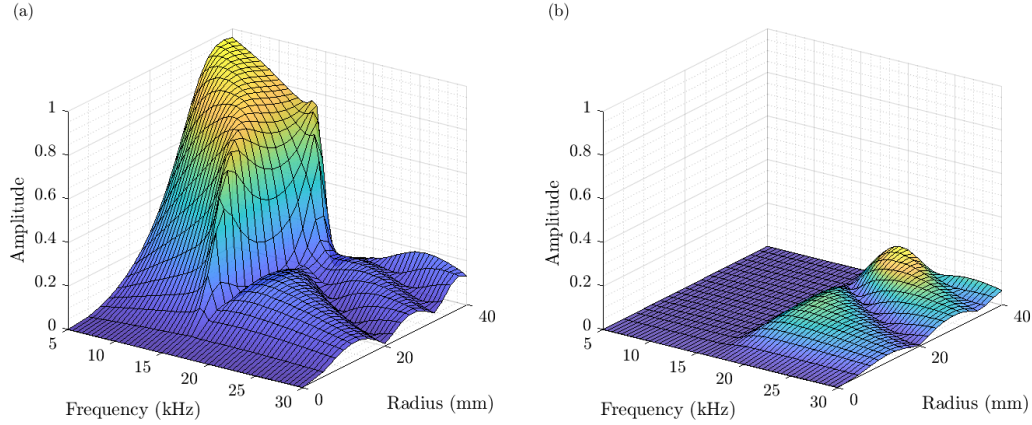


Figure 3.10: Amplitudes of the (a) reflected flexural wave packet and (b) reflected shearing wave packet as functions of the central frequency (input flexural pulse) and the radius of the hole R_h (defect).

3.6.1.2 Defect localization in a waveguide assembly with a joint

Consider now a waveguide assembly with a defect and a curved joint, as shown in Fig. 3.4(b). In this case, the sought defect position is $l_2 = 5$ m, which represents the distance between the joint and the defect. Here, any input wave packet will likely give rise to many transmitted/reflected wave packets of different natures due to wave conversion phenomena inside the joint and the defect. Following the WFE method, the input (flexural wave packet) and output time signals can be assessed as shown in Fig. 3.11. The total reflected signal is shown in Fig. 3.11(b) as well as the contributions issued from the flexural, longitudinal and shearing waves, see Figs. 3.11(c-e). It can be observed that, for a given type of wave, several reflected wave packets occur which result from wave conversion phenomena (transmission and reflection at coupling elements), as mentioned earlier. Hence, it is expected that a curved joint can strongly affect the detection and localization of a defect because of the occurrence of many reflected and transmitted signals which can be difficult to comprehend.

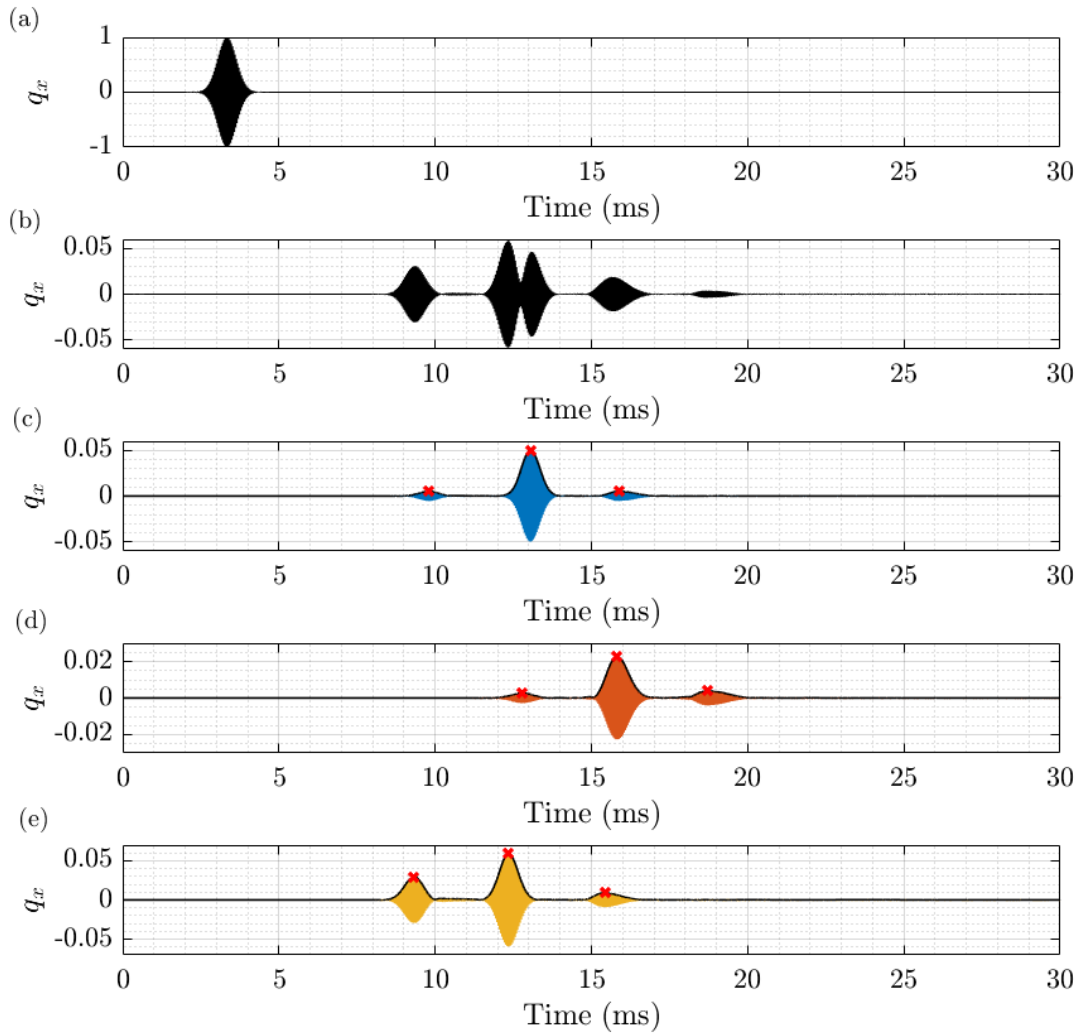


Figure 3.11: Time signals at measurement point for a waveguide assembly with a joint: (a) input signal (flexural waves), (b) total reflected signal, (c) reflected flexural wave packet, (d) reflected longitudinal wave packet and (e) reflected shearing wave packet. Red crosses highlight tips (highest magnitudes) of reflected wave packets.

A closer look at Fig. 3.11 reveals, for each type of wave, three reflected wave packets. The first/fastest one represents the reflected waves issued from the joint; the second packet – which is of main interest here and of highest magnitude – represents the reflected waves from the defect (i.e., transmitted through the joint towards the measurement point); the third packet represents the reflected waves from the defect that result from extra reflections with the joint. In this case, the time of flight (for each packet) can be defined as the time delay between the tip of the input pulse and the tip of the second reflected signal (see red crosses in Fig. 3.11).

Again, the estimated/theoretical times of flight τ_{ijkl} can be assessed, see Eq. (3.29). The related frequency-time maps are shown in Fig. 3.12. There are, in theory, many waves of different natures propagating in each waveguide (due to conversion phenomena), but only a few of them truly happen physically. The analysis of the frequency-time maps in Fig. 3.12 can help identify these “wave pathways” by comparing, for each possible pathway, the theoretical time of flight τ_{ijkl} with the measured one. For instance, in Fig. 3.12, three continuous curves are drawn which appear to be good candidates to accurately estimate the measured times of flight, and which are associated with the following wave pathways: $(i \leftarrow j \leftarrow k \leftarrow l) = (\mathbf{f} \leftarrow \mathbf{f} \leftarrow \mathbf{f} \leftarrow \mathbf{f})$, $(\mathbf{l} \leftarrow \mathbf{f} \leftarrow \mathbf{f} \leftarrow \mathbf{f})$ and $(\mathbf{s} \leftarrow \mathbf{s} \leftarrow \mathbf{s} \leftarrow \mathbf{f})$ (\mathbf{f} : flexural, \mathbf{l} : longitudinal, \mathbf{s} : shearing). In other words, while providing accurate results, the proposed approach is also able to provide physical insight into the pathways taken by a certain wave packet in different parts of a waveguide assembly. This appears to be the main contribution of the present work. In Figs. 3.12(b-d), the measured time of flight represents the second yellow spot, i.e., the one with the highest magnitude. Other yellow spots highlight first-wave reflection from the joint and extra wave reflection from the defect. The related times of flight can be predicted using the same procedure as before, as shown in Fig. 3.12. In this case, the predicted times of flight represent the crossing points between the colored dashed lines and the white dashed line in Fig. 3.12(b-d). Again, the proposed approach correctly agrees with the measurements, i.e., the crossing points between these colored and white dashed lines match the first and third yellow spots.

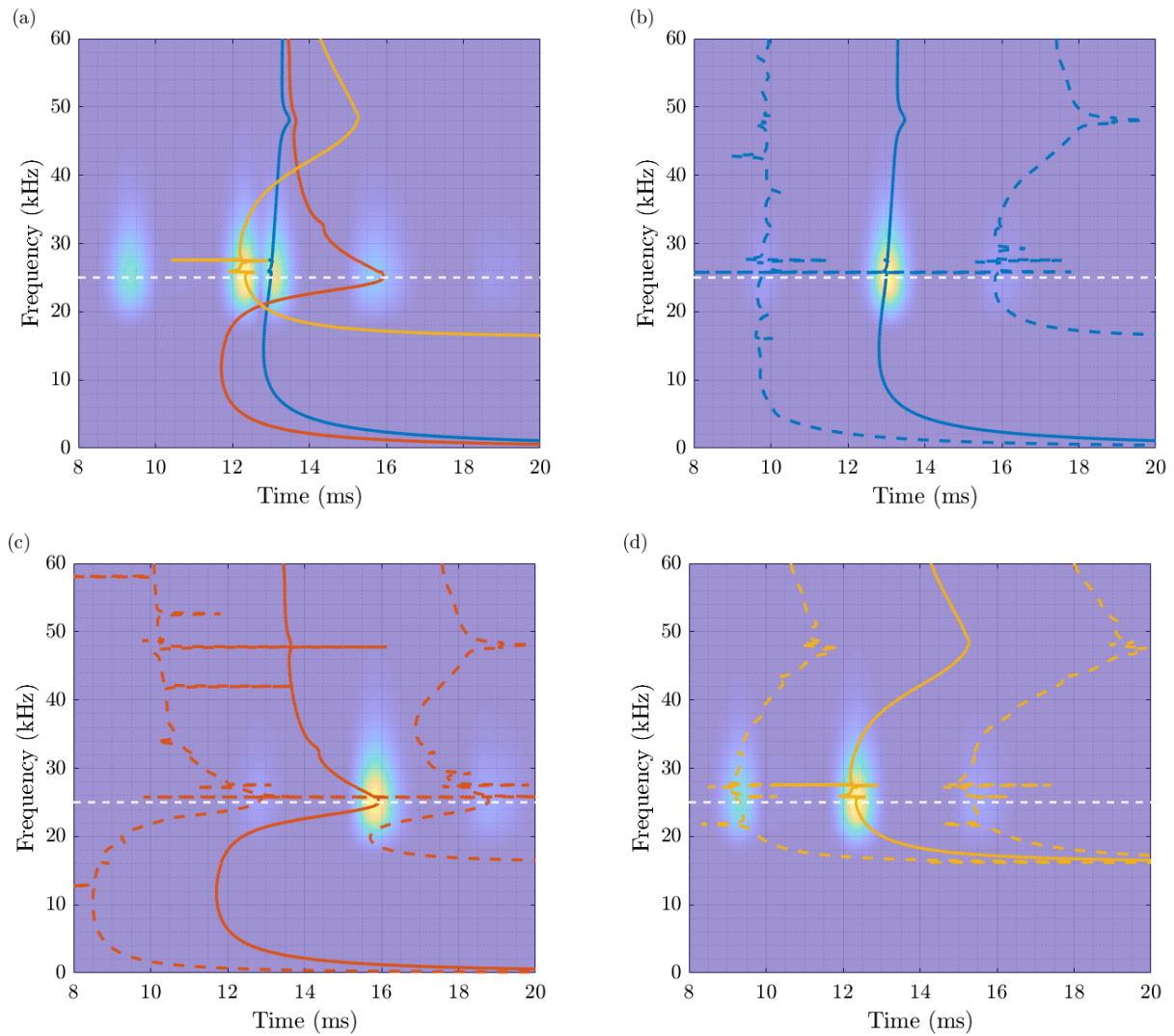


Figure 3.12: Frequency-time map of the reflected signal for a waveguide assembly with a joint. Measured times of flight are highlighted by yellow spots. Estimated times of flight represent the crossing points between the continuous curves and the white dashed line: (a) total signal, (b) flexural wave packet (blue), (c) longitudinal wave packet (red) and (d) shearing wave packet (orange). The first reflections from the joint and extra reflections from the defect are represented by dashed lines.

The following strategy can be considered to obtain a raw estimate of the position of the defect l_2 in Eq. (3.29). This consists in plotting the times of flight τ_{ijkl} , for different pathways, as functions of l_2 via Eq. (3.29) and seeking those pathways that give the same result l_2 as shown in Fig. 3.13. Here, the horizontal black dashed lines represent the measured times of flight; also, the oblique lines in blue, red and orange colors represent $\tau_{ijkl}(l_2)$ for the pathways associated with the wave packets shown in Fig. 3.11, and intersect the horizontal lines at about the same abscissa $l_2 = 5$ m. Other pathways (gray oblique lines) lead to wrong estimates of l_2 , meaning that they do not occur physically.

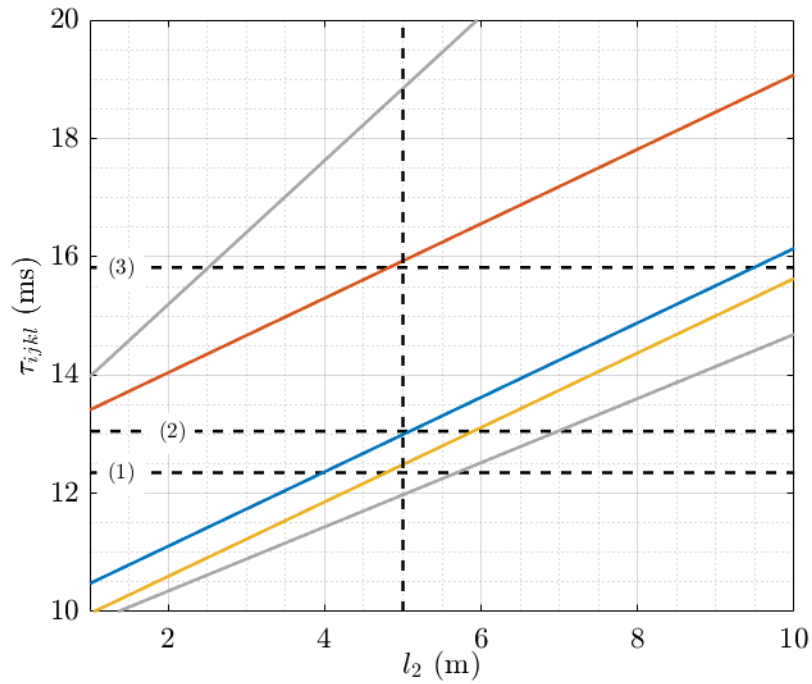


Figure 3.13: Times of flight τ_{ijkl} as functions of l_2 , for different pathways (blue, red and orange curves are pathways associated to the wave packets shown in Fig. 3.11); measured times of flight are highlighted by horizontal dashed lines.

An accurate estimate of the position of the defect (length $l_2 = 5$ m) follows from Eq. (3.30). The idea is to show that this position can be determined regardless of the pathways taken by the waves in the assembly. The estimated positions of the defect issued from the analysis of three different pathways are reported in Tab. 3.2. Also, to highlight the robustness of the numerical strategy, three additional pathways are analyzed which concern results for an input shearing (instead of flexural) wave packet. As expected, for each case, the position of the defect l_2 can be accurately predicted with a relative error smaller than 3%. To better investigate the influence of the times of flight in transmission τ_{kl}^j and τ_{ij}^j through the joint upon the localization of the defect, and therefore the relevance of the proposed approach based on Eq. (3.17), results issued from Eq. (3.30) without considering the time of flight in transmission through the joint (τ_{kl}^j and τ_{ij}^j) are also reported (length l_2^*). In that case, the estimated positions appear to be less accurate (relative error about 9%).

To further highlight the robustness of the proposed approach, the predicted positions of the defect issued from analyzing extra reflected wave packets from the defect (third output signals, instead of the second ones) are determined, see Tab. 3.3. Again, the position of the defect l_2 can be accurately predicted (relative error less than 2%), regardless of the wave pathway which is analyzed.

Table 3.2: Estimated position of the defect obtained from Eq. (3.30) and relative error (reference is $l_2 = 5$ m).

	$ijkl$	τ_{ijkl} (ms)	l_2^* (m)	l_2 (m)	Relative error (%)
(1)	s ← s ← s ← f	12.35	5.40	5.05	1.0
(2)	f ← f ← f ← f	13.05	5.43	5.10	2.0
(3)	1 ← f ← f ← f	15.82	5.20	4.85	3.0

Table 3.3: Estimated position of the defect issued from analyzing extra reflected wave packets, and relative error (reference is $l_2 = 5$ m).

$ijklmn$	τ_{ijklmn} (ms)	l_2^* (m)	l_2 (m)	Relative error (%)
f ← f ← s ← s ← f ← f	15.89	5.35	5.06	1.2
l ← f ← f ← f ← f ← f	18.72	5.25	4.97	0.6
s ← s ← f ← s ← s ← s	15.43	5.32	5.06	1.2

Let us remark that, in Fig. 3.12, some estimated times of flight τ_{ijkl} may be difficult to comprehend for some particular frequencies. This particularly concerns the sharp peaks of the continuous curves which can overlap the white dashed lines at these frequencies, e.g., at 27.3 kHz for the orange curve. As explained in Sec. 3.4 (see Remark 2), this behavior results from the resonant behavior of the coupling elements (joint, defect) which affects the assessment of the times of flight. As a second issue, times of flight for waves close to their cut-off frequencies are difficult to quantify due to the singular behavior of the group velocities at these frequencies. Input wave packets at these frequencies are likely to lead to complex reflected time signals which are difficult to analyze as shown in Fig. 3.14 at 16.1 kHz (black) at the cut-off frequency of the shearing wave, and 27.3 kHz (blue) at an internal resonance of the joint. At these frequencies, the measured signals are widely spread in time, which as such make these excitation frequencies not suitable to localize the defect. It should be emphasized that this issue is not linked to numerical modeling, but results from physical phenomena. It is therefore advised to consider different values of excitation frequencies. Again, the proposed wave-based approach could be advantageously considered to quickly select these excitation frequencies in a pre-processing step.

In Fig. 3.15, the sensitivity of the amplitudes of the flexural, longitudinal and shearing reflected signals to angles of curvature of the joint varying from 30° to 90° , and excitation frequencies varying from 20 kHz to 25 kHz, is analyzed. Results show that, for a given angle, the amplitudes of the reflected signals can be optimized by properly selecting the excitation

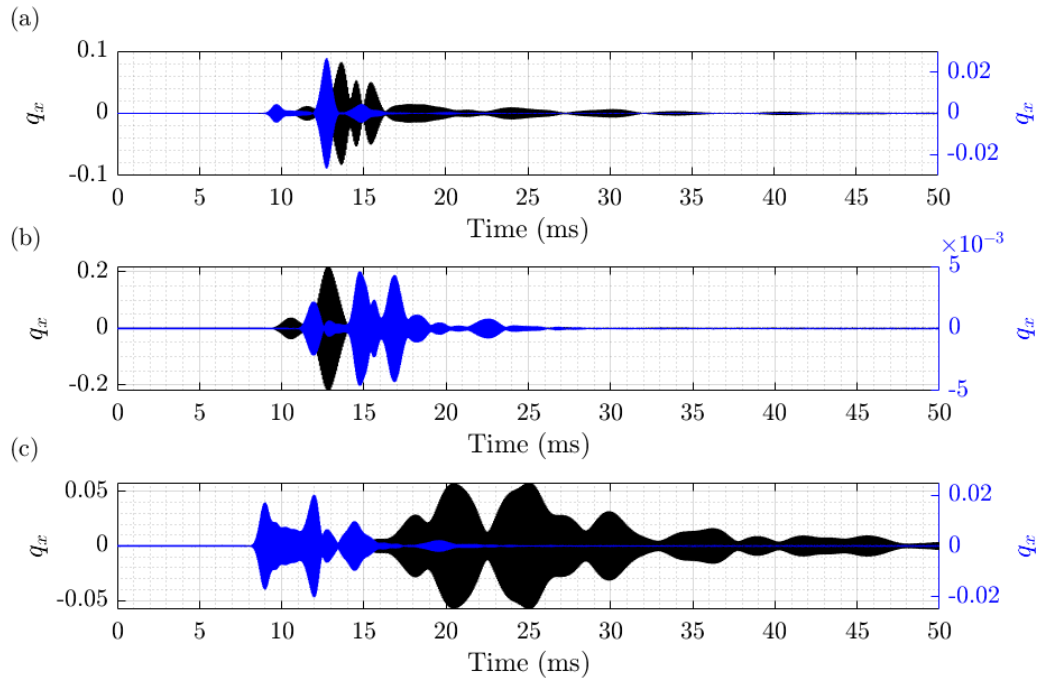


Figure 3.14: Measured time signals for an input flexural wave packet at 16.1 kHz (black) and 27.3 kHz (blue): (a) reflected flexural wave packet, (b) reflected longitudinal wave packet and (c) reflected shearing wave packet.

frequency. In fact, the variations of the wave amplitudes against frequency, for a given angle, are not necessarily monotonic (as it would be the case for the extreme case 90°) as they can be more complex. Here, the WFE method appears to be an interesting numerical tool to carry out such an optimization analysis (see for instance [29]).

A validation of the WFE approach for detecting and localizing a defect in a waveguide assembly with joint (see Fig. 3.4(b)) is finally proposed through comparisons with the FE method, i.e., via time simulations issued from a full FE model of the system. In this case, infinite conditions before waveguide 1 and after waveguide 3 are described by considering two extra 25 m-long waveguides which are supposed to be long enough to prevent wave reflections at ends within the time band analyzed. This, as such, yields a FE model of large size. Within

the FE framework, an input force vector $\mathbf{F}(t) = \Re\{\phi_{F_j}(\omega)\} \times f(t)(1 + \delta(t))$ representing an input flexural wave packet j at 25 kHz is considered at the abscissa of the measurement point. Here, ϕ_{F_j} represents the force component for the flexural wave shape vector (size $n \times 1$), $f(t)$ is a Gaussian and $\delta(t)$ is a uniform random variable defined on $[-1, 1] \times 10^{-3}$ to simulate noise, and therefore, to add uncertainties in the excitation signal.

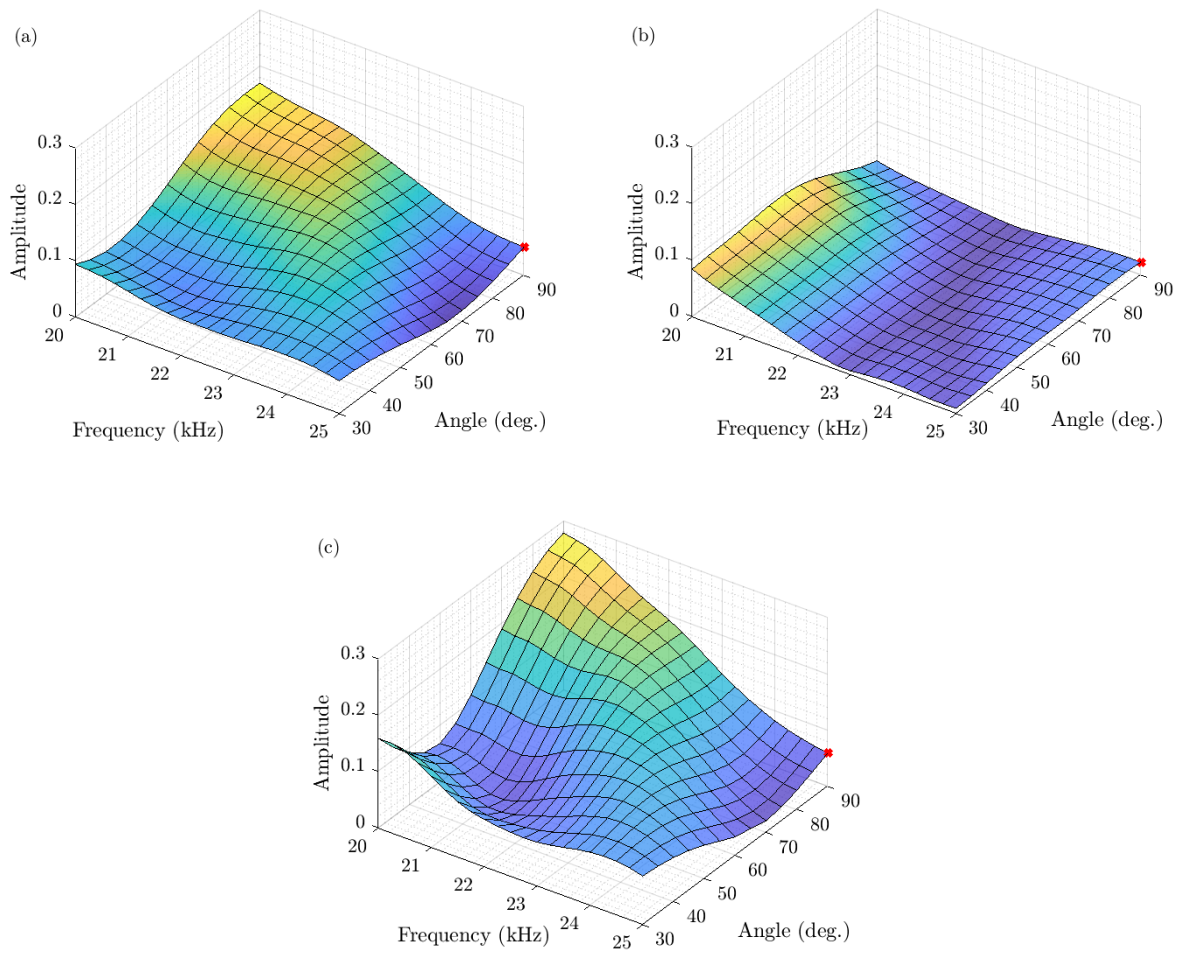


Figure 3.15: Amplitudes of the (a) reflected flexural wave packet, (b) reflected longitudinal wave packet and (c) reflected shearing wave packet as functions of the central frequency (input flexural pulse) and the angle of curvature of the joint. Red cross highlights values initially considered to obtain Fig. 3.11

Regarding the full FE model, the time response is computed with the Newmark method with a time step of $\Delta t = 5 \times 10^{-7}$ s. The normalized input wave packet is shown in Fig. 3.16(a) in the same way as Fig. 2.11(a). Reflected time signals are shown in Fig. 3.16(a) which concern (i) waves reflected by the joint and (ii) waves reflected by the defect and transmitted through the joint back to the measurement point. These reflected signals are highlighted in dark color in Figs. 3.16(b) and 3.16(c). For comparison purposes, the WFE results about the previously identified reflected signals are also shown; see Fig. 3.11. Regarding Figs. 3.16(b) and 3.16(c), it appears that the reflected signals issued from FE simulations can be roughly retrieved from superposing the flexural and shearing wave packets issued from the WFE method. In other words, the reflected time signals issued from the WFE method match the FE solution. Small differences between the two signals appear, since in the WFE signal the contribution of the flexural and shearing modes are plotted separately. Also, the other modes are not considered and the superposition of signals (from different modes) at the observing point is ignored. The tips of the reflected pulses (highest magnitudes), for the flexural and shearing wave packets, can be clearly identified via the FE response and correspond to those obtained with the WFE method. This highlights the accuracy of the proposed approach for computing the time responses of waveguide assemblies and, therefore, predicting the reflected wave signals from the defect and the related times of flight. This also highlights the robustness of the approach, i.e., it is able to describe systems subject to small uncertainties (excitation conditions in the present case). It should be emphasized, again, that the advantages of the WFE method over the FE method are: (i) the computation of the dynamic response of waveguide assemblies using wave-based matrix equations of small size; (ii) a straightforward identification of the waves which are reflected by the defect and transmitted through the joint.

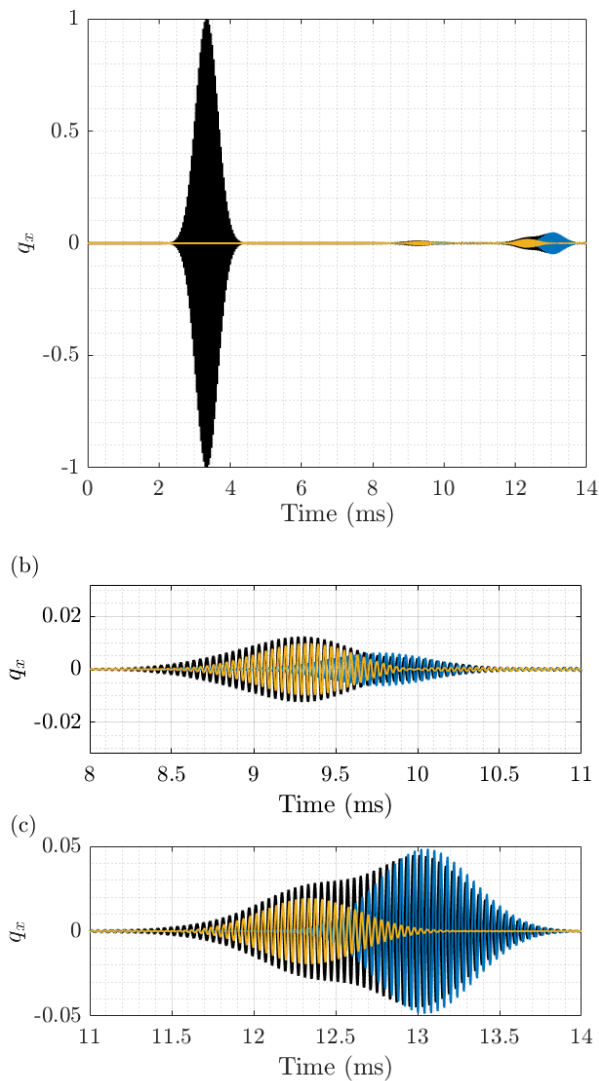


Figure 3.16: Incident and reflected time signals for a waveguide assembly with a joint (total signal (a), reflected signals from the joint (b) and reflected signals from the defect (c)): (black) FE solution; (blue) WFE solution for the reflected flexural wave packet; (yellow) WFE solution for the reflected shearing wave packet.

3.6.2 Pipeline with an elastic foundation

The analysis of long pipelines using wave propagation methods is of great interest due to the characteristics of the waves encountered. The occurrence of multiple defects and curved joints in networks of pipes can be challenging during an inspection. These coupling elements generate to mode conversion during transmission and reflection, resulting in complex measured signals, thus hindering the effectiveness of the inspection. Consequently, understanding and studying wave mode conversions caused by these coupling elements become crucial to proceed with the inspection process.

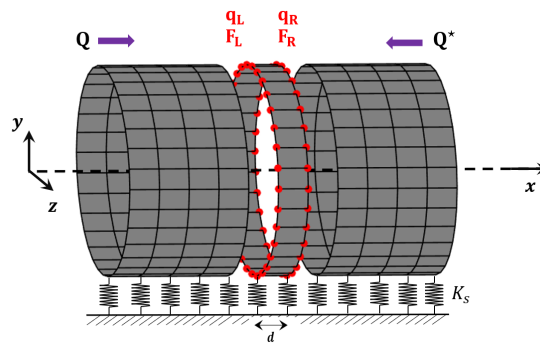


Figure 3.17: Schematic of a pipe described from identical substructures on an elastic foundation (periodic mesh).

To localize a defect, a time response analysis based on the study of the times of flight, for reflected or transmitted wave packets, can be used [132]. For straight pipes, assessing the times of flight follows directly from the analysis of the group velocities. However, as reported earlier, assessing the group velocities for waves transmitted or reflected through arbitrary coupling elements, like defects or curved joints, is more dubious, see Sec. 3.4.

Let us consider a pipeline lying on an elastic foundation, as shown in Fig. 3.17. The pipe substructure is modeled using "S4R" 4-node rectangular elements (ABAQUS) with 6 DoFs per node. Each element represents a quadrilateral finite-membrane-strain element with reduced integration to avoid shear and membrane locking. The pipe substructure is meshed with 32

elements around the circumference and 1 element along its length. Finally, the elastic foundation is modeled via periodic supports of stiffness $K_s = 10^8 \text{N}$ (vertical direction) at the bottom nodes of the structure.

The dispersion curves of the traveling waves in the pipes can be obtained with the WFE method (see Sec. 2) as shown in Fig. 3.18. Here, those associated with “low-order” right-going waves are displayed over the frequency band $[0, 50]$ kHz. Fig. 3.18(a) shows the real and imaginary parts of $\beta_j d$ (β_j and d being the wavenumbers and the substructure length, respectively), and Fig. 3.18(b) shows the related group velocities. The dispersion curves issued from the WFE method appear fairly different from those in pipes, see Fig. 1.1. This is explained by the fact that an elastic foundation is added. Note that the double roots related to the flexural modes, as observed by Wang et al. [133], are no longer present due to a spring foundation. Indeed, the pipe symmetry is broken, and an orientation is established. Here, the fundamental torsional wave mode $T(0, 1)$, which is non-dispersive, is highlighted together with low-order dispersive non-axisymmetric flexural wave modes $F(1, 2)$, $F(1, 3)$ and $F(2, 2)$, and low-order longitudinal wave modes (see blue, yellow and purple curves). As explained earlier, wave mode conversion among these waves is supposed to occur inside the coupling elements (transmission, reflection).

Remark 3. The problem of double-roots modes observed in axisymmetric structures was noticed by Zhong and Williams [25]. However the authors only treated the case of single-root modes (observed in beams and plates structures) in the WFE framework. It is worth mentioning that the computation of dispersion curves and forced responses can be obtained normally for both cases. More recently, Wang et al. [133] adapted the WFE method to deal with double-root problems. However, for axisymmetric structures, the computation of the reflection and transmission coefficients for axisymmetric structures via scattering matrices, as described in Sec. 2.7, is yet not well defined and remains a problem of interest.

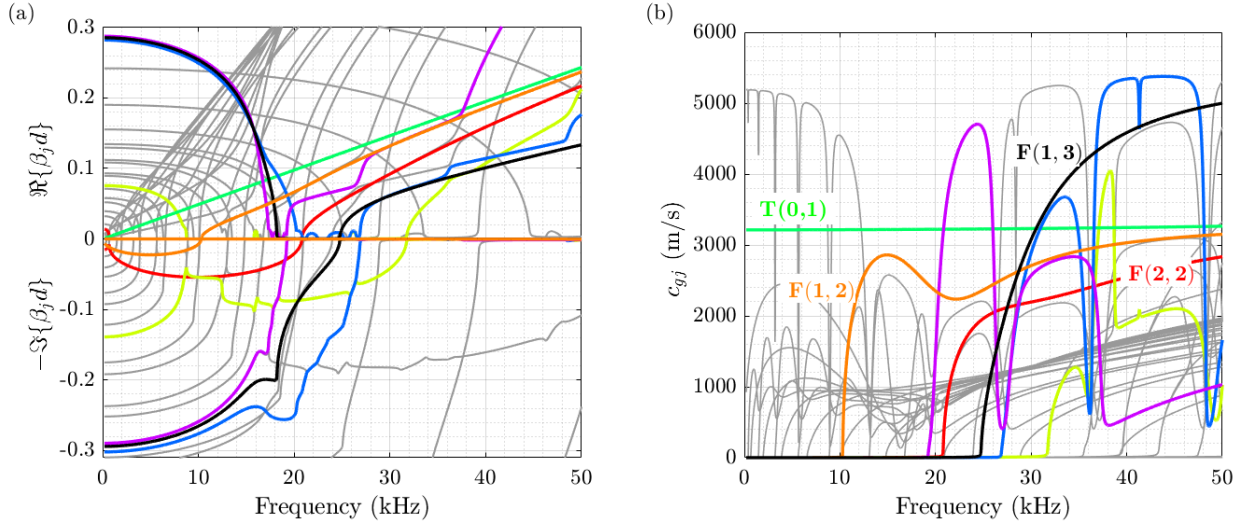


Figure 3.18: (a) Real and imaginary parts of $\beta_j d$ and (b) group velocities c_{gj} : (green line) torsional mode T(0, 1), (orange line) flexural mode F(1, 2); (black line) flexural mode F(1, 3); (red line) flexural mode F(2, 2); (blue, yellow and purple lines) longitudinal modes.

Let us consider a pipeline composed of waveguides of length $l_1 = 10$ m and $l_2 = 10$ m connected by a curved joint of curvature angle 90° , see Fig. 3.19(a). The joint, the defect, and the pipes share the following material properties: Young's modulus $E = 210$ GPa, density $\rho = 7800$ kg/m³, Poisson's ratio $\nu = 0.3$, and a Rayleigh damping model is considered — i.e., $\mathbf{C} = a\mathbf{M} + b\mathbf{K}$, with coefficients $a = 10^{-3}$ s⁻¹ and $b = 10^{-8}$ s. The source and observation points are the same and located at $l_1 = 10$ m in waveguide 1 away from the joint. Also, the waveguides before the source point and after the defect are supposed to be semi-infinite.

The joint and the defect are discretized using four-node rectangular elements with 6 DoFs per node. The schematics and FE mesh of the joint are shown in Fig. 3.19(b). It uses 32 elements around the circumference and 40 elements around the curvature. The length of the coupling element representing a defect is $d_a = 7.5$ mm, and it contains a crack of length $l_a = 2.5$ mm, see Fig. 3.19(c). The circumferential extent of the defect is $\theta_a = 22.5^\circ$. Here, the radius of curvature of the joint is $R^j = 0.1$ m.

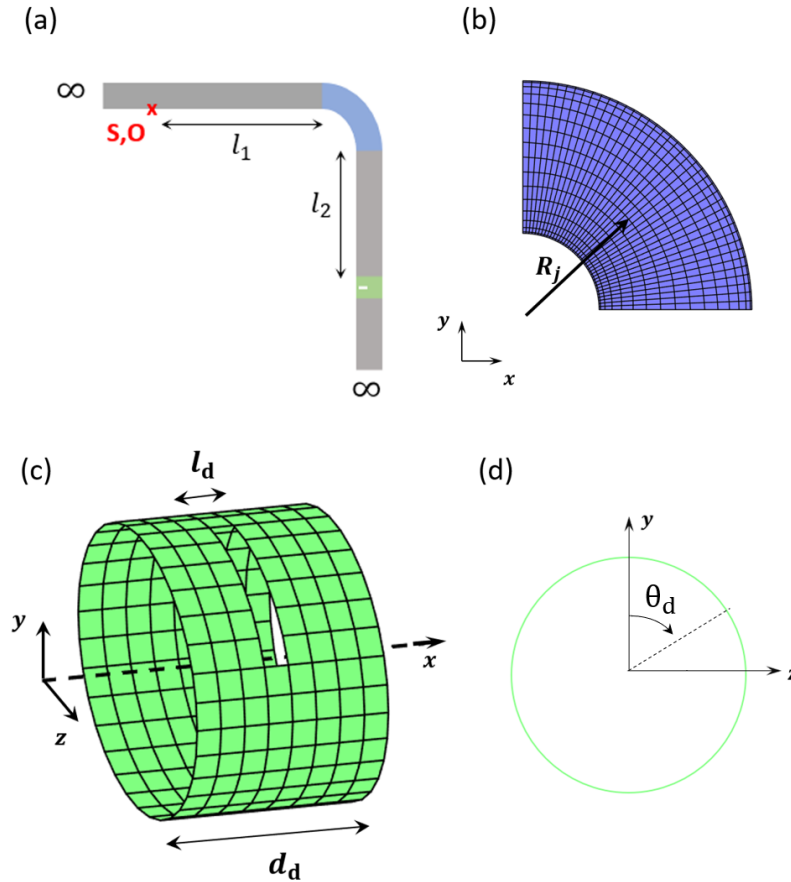


Figure 3.19: (a) Schematic of a pipe described from identical substructures on an elastic foundation; mesh for (b) joint and (c) coupling element with a defect; (d) representation of the angular extent of the defect θ_d .

The time response of the pipe assembly is investigated, with an input excitation/measurement point in pipe 1; see Fig. 2.17. The distance between the joint and the defect is $l_2 = 10$ m, representing the length of pipe 2. An input Gaussian pulse centered at 30 kHz representing a right-going wave packet “T(0, 1)” is considered as shown in Fig. 3.20. The problem is solved in the frequency domain with the WFE method, and the time response is obtained via an inverse Fourier transform of the frequency response, see Sec. 2 for the methodology.

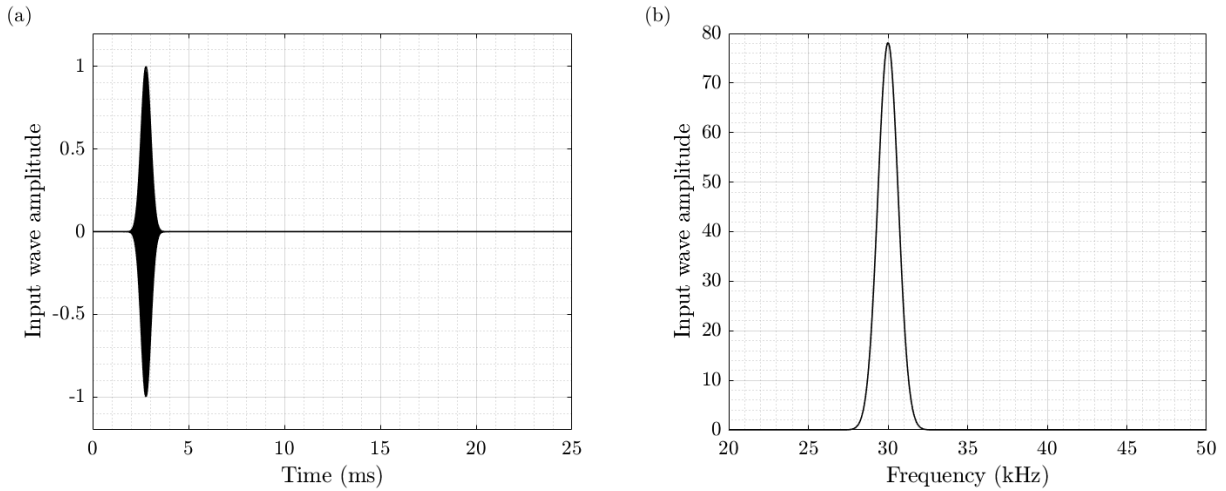


Figure 3.20: (a) Pulse excitation in the time domain and (b) absolute value of the related Fourier transform.

Fig. 3.21 shows the normalized circumferential displacement at the measurement point as a function of time, specifically showing the contribution of the "T(0, 1)" mode in terms of displacement. The incident and reflected wave packets are of "T(0, 1)" type. The contribution of the wave packet of type "T(0, 1)" can be extracted by decomposing the signal into different contributions and selecting the desired wave type, as described in [99, 134]. Here, five wave packets of T(0, 1)-type are observed. These result from reflection at the joint (wave packet (1)) and reflection at the defect via transmission through the joint (wave packets (2), (3), (4) and (5)). As reported earlier, wave packets (2)-(5) are associated with different pathways and wave conversions inside the joint and the defect. This illustrates the difficulty of localizing a defect after a joint, i.e., given the occurrence of different wave pathways for a given input/output wave type. It should be recalled that these pathways, for an input wave packet, are to be understood as the different possible wave packets that are transmitted through the joint in pipe 2, reflected via the defect in the same pipe, and transmitted via the joint back to the measurement point.

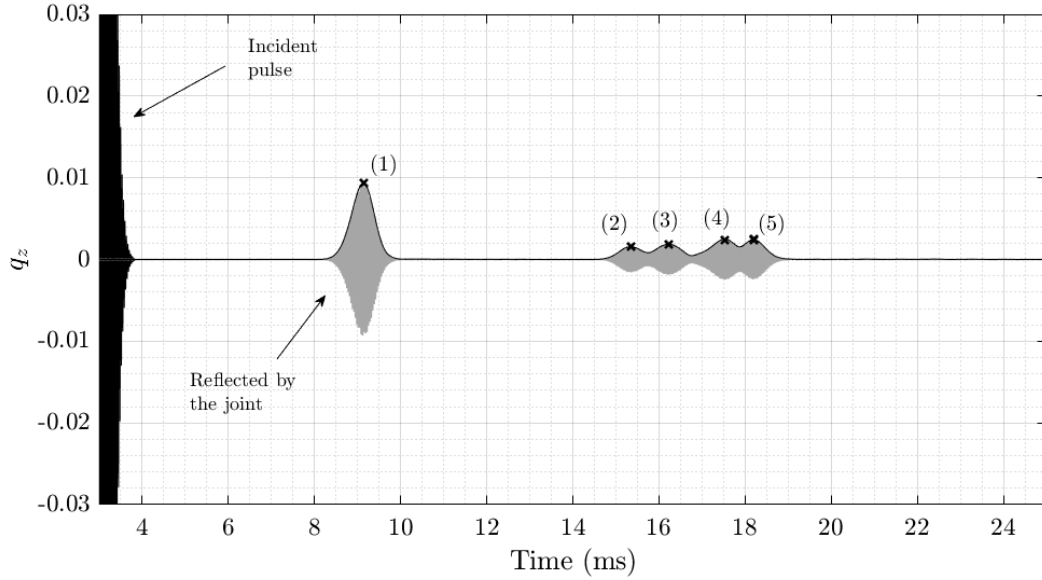


Figure 3.21: Reflected wave packets $T(0, 1)$ at the measurement point: (1) wave packet reflected by the joint; (2)-(5) wavepackets issued from the defect. Dark crosses highlight the tips of the wave packets.

Following the procedure described in Sec. 3.5, an analysis of the components of the scattering matrices of the joint and the defect can help identify these different pathways. For instance, the transmission coefficients for the incident wave $T(0, 1)$ through the joint are shown in Fig. 3.22(a). Here, the waves transmitted in pipe 2 — i.e., those with the highest transmission coefficient at 30 kHz — are highlighted by colored curves. For instance, the red curve represents the transmission coefficient from wave $T(0, 1)$ to wave $F(2, 2)$, and the green curve represents the transmission coefficient from wave $T(0, 1)$ to wave $T(0, 1)$. Also, several possible pathways can be postulated by analyzing the reflection coefficients at the defect. Some of these are physical, others are not.

The localization of the defect $l_2 = 10$ m depends on the strategy to determine the wave pathways. The idea is that for a certain measured time of flight τ_{ijkl} , different choices for pathways can give the same estimate of l_2 . Fig. 3.22(b) shows the variation of τ_{ijkl} against

the length l_2 for different pathways, see Eq. (3.30). Also, the measured times of flight, for the reflected wave packets, are shown via horizontal dashed lines in Fig. 3.22(b). It can be seen that the intersection of oblique and horizontal lines at $l_2 = 10$ m can be obtained for three pathways, indicated with black circles. Other pathways may give wrong results — i.e., the purple curve in Fig. 3.22(b) — which means that they do not physically happen.

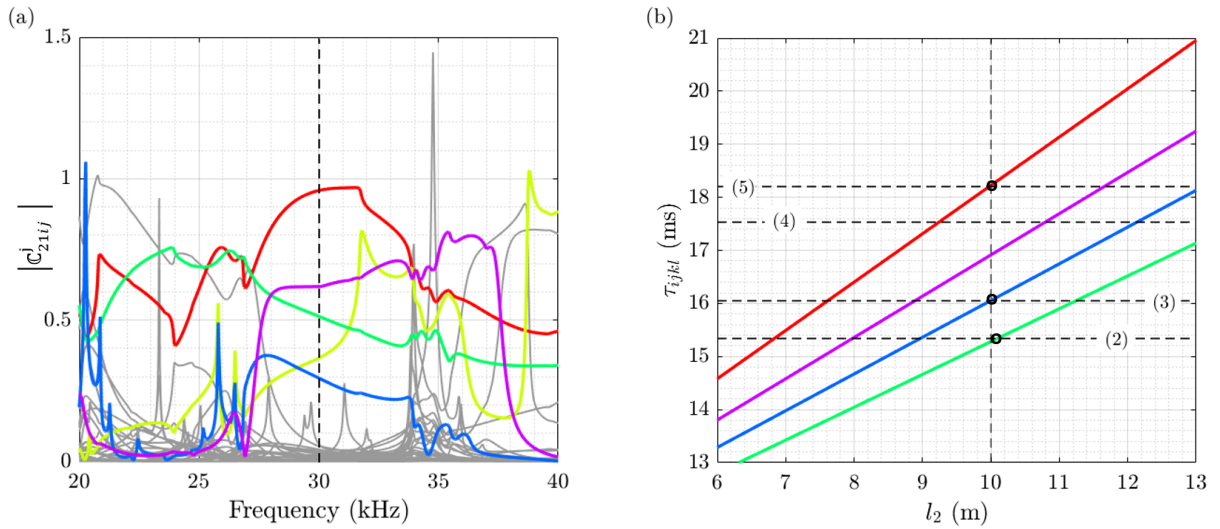


Figure 3.22: (a) Transmission coefficients for the incident wave $T(0, 1)$ through the joint; highest coefficients at 30 kHz are highlighted by colored curves. (b) Times of flight τ_{ijkl} as functions of the length l_2 , for different pathways; measured times of flight are plotted using horizontal dashed lines.

Accurate estimates of the position of the defect l_2 can be obtained from Eq. (3.30), i.e., from the measured times of flight τ_{ijkl} and several identified pathways (2), (3) and (5). Results are shown in Tab. 3.1, where “H.O.” means high-order wave modes. In this case, the position of the defect can be identified with an error smaller than 1%.

Table 3.4: Estimated position of the defect from Eq. (3.30), and relative error (reference is $l_2 = 10$ m).

	$ijkl$	τ_{ijkl} (ms)	l_2 (m)	Relative error (%)
(2)	T(0, 1) ← T(0, 1) ← T(0, 1) ← T(0, 1)	15.34	10.09	0.9
(3)	T(0, 1) ← H.O. ← H.O. ← T(0, 1)	16.05	9.99	0.1
(5)	T(0, 1) ← F(2, 2) ← F(2, 2) ← T(0, 1)	18.20	10.08	0.8

To further investigate the relevance of the proposed approach, a frequency-time map of the measured reflected signals can be considered as shown in Fig. 3.23. Here, the yellow spots highlight the measured reflected signals. The black curves represent the theoretical times of flight for different pathways (2), (3), and (5), see Eq. (3.29). Otherwise, in Fig. 3.23, the white horizontal curve at 30 kHz represents the excitation frequency. This procedure allows a verification of the pathways identified via Fig. 3.22(b). For these pathways indeed, one can check that the intersection points between the black curves and the white ones match with the center of the yellow spots, i.e., with the tips of the reflected signals shown in Fig. 3.21.

Fig. 3.23 provides additional information about the reflected times of flight. For instance, the black curves contain sharp horizontal peaks at some particular frequencies. This phenomenon can strongly affect the detection of reflected wave packets — e.g., the one corresponding to certain pathways — which is explained by the difficulty of determining the crossing points between these curves and the white one positioned at these frequencies. Such behavior occurs at the resonance frequencies of the coupling elements (joint, defect) or at the cut-off frequencies of the waves where the group velocities exhibit a singular behavior. Input wave packets at these frequencies are likely to induce reflected signals that are spread in time, making these excitation frequencies not suitable to localize the defect, as illustrated in Fig. 3.14. It must be emphasized that this problem is not related to numerical modeling, but is due to physical phenomena, as explained in Sec. 3.6.1.2. Therefore, it is recommended to consider different

excitation frequencies. The proposed WFE approach can be advantageously used to quickly select these excitation frequencies in the pre-processing step.

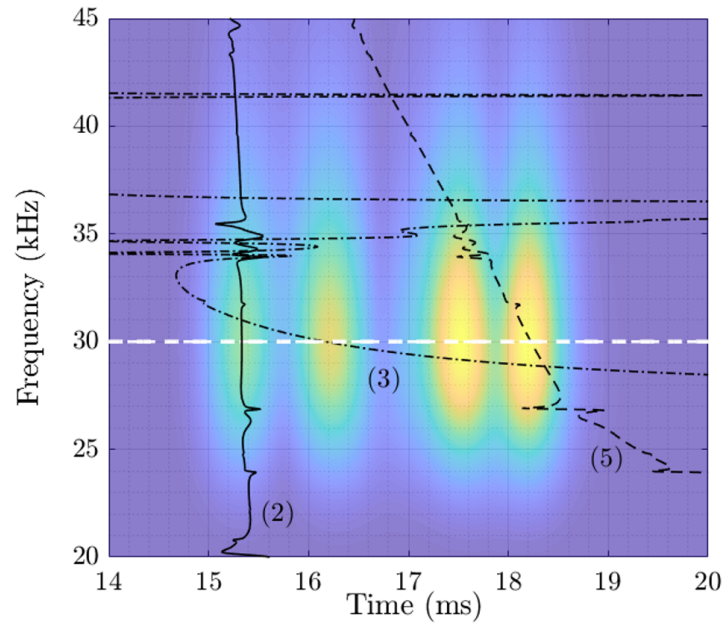


Figure 3.23: Frequency-time map of the reflected waves issued from the defect. Measured times of flight are highlighted by yellow spots. Estimated times of flight represent the crossing points between the black curves and the white dashed line.

3.7 Conclusions

This chapter proposed a WFE approach to localize defects in waveguide assemblies with curved joints. This strategy uses the scattering matrix issued from the WFE method to assess transmitted and reflected wavepackets through the joint, and to localize a defect. 2D assemblies involving straight elastic waveguides, a curved elastic joint and a defect have been dealt with. The proposed approach provides theoretical expressions of the times of flight in transmission or reflection for wave packets traveling in coupling elements (joint, defect). Also, it provides physical insights into the nature of the waves which are transmitted through the

joint and reflected by the defect (pathways). The position of the defect can be determined by comparing the theoretical expressions of the times of flight with those recorded in a waveguide assembly. Numerical experiments for 2D plane-stress beams and 3D pipes have been carried out to demonstrate the accuracy and robustness of the proposed approach to localize a defect from the analysis of different reflected wave packets (several types of waves). The proposed approach is intended to be general and could be used to localize single or multiple defects in networks of waveguides, including several curved joints.

Chapter 4

Elasto-acoustic waveguides

4.1 Overview

Fluid-filled pipes find application across various industries, including gas, oil, water distribution, and civil engineering. Consequently, upkeep and monitoring of pipelines are crucial to safeguard their integrity and prevent financial losses. In extensive pipeline networks, NDT using guided waves emerges as a useful technique for it. The understanding of wave propagation in fluid-filled pipes is primarily important when guided waves are used. Especially the interaction of elasto-acoustic waves with defects and joints is important to improve NDT techniques.

The localization of defects for fluid-filled pipes was studied in different ways. Aristégui et al. [44] investigated the wave propagation in pipes with internal and external fluids. They obtained a good agreement between experiments and dispersion curves calculated by a FE approach. More recently, Vogelaar and Golombok [45] experimentally investigated damage detection using the torsional mode with different internal and external fluids. They showed that different inner and outer fluids attenuate the torsional mode, hence reducing the inspection range of the technique. However, they stated that the torsional mode is suitable for detecting pipe defects. Since, in general, the fundamental torsional mode $T(0, 1)$ is not dispersive, it is easy to

generate using transducers, and the energy is confined to the pipe and does not radiate. [46–49].

It is possible to determine the dispersion curves of propagating waves in fluid-filled axisymmetric pipes, as discussed by Fuller and Fahy [50] and Sato and Ogiso [51]. However, for complex pipes, analytical solutions are not straightforward. Then, numerical methods become an essential tool. Nevertheless, for long structures, the FE method becomes computationally challenging since it involves many elements, resulting in a large number of DoFs. To tackle this problem, the WFE method is a valuable alternative.

Mencik and Ichchou [32] applied the WFE method to fluid-filled pipes to compute dispersion curves. Bhuddi et al. [34] studied the wave propagation in axisymmetric fluid-filled pipes surrounded by a fluid using the WFE method combined with a perfectly matched layer (PML). Kingan et al. [52] analyzed the response of an orthotropic system. Manconi et al. [53] applied the method to analyze laminated pre-stressed fluid-filled pipes. Maess et al. [54, 55] developed a strategy to compute the energy and group velocities in the WFE framework. In their works, they analyzed straight and corrugated pipes containing a fluid.

So far, the studies focused on analyzing wave propagation in straight systems overlooking the phenomenon of mode conversion in the presence of coupling elements like curved joints and defects. Thus, it is important to incorporate the modeling of such coupling elements within the WFE method, since it has not been done yet in the literature from the point of view of mode conversion.

Within the WFE method, coupling elements are usually modeled via FE models that can contain a large number of DoFs since fluid-filled structures are considered. This can lead to high computational costs, even with the WFE method. Thus, an unreduced modeling of the coupling element can be considered naive, and a reduced modeling strategy is necessary.

In terms of model reduction involving fluid-filled pipes and FE models, Maess and Gaul [56] adopted a component mode synthesis using the CB method and an iterative subspace solver to generate an approximation to the low-frequency problem. Later, Herrmann et al. [57]

provided an FE approach to simulate pipelines using dynamic substructuring and interface reduction. For this task, they applied the CB method to vibroacoustic problems and used an interface reduction based on Ritz vectors.

Also, a reduction based on modal projection can be considered where the acoustic and elastic parts are decoupled. However, to ensure convergence, it is necessary to provide corrections using enrichment vectors [58]. Tournour and Atalla [59] demonstrated that the decoupled modal basis results in poor convergence since high-frequency modes of one subsystem can be coupled to low-frequency modes of the other. To solve this issue, they proposed pseudo-static corrections in both subsystems. Tran et al. [60] used decoupled systems that are later enriched by static correction terms. This approach will be used in this manuscript to model coupling elements in the WFE framework.

This section is organized as follows. In Sec. 4.2, the WFE method for elasto-acoustic waveguides is presented. Some simulations are carried out to compute the dispersion curves and the group velocities of the elasto-acoustic modes, and a comparison between the force response issued from the FE and WFE methods is provided. Next, in Sec. 4.3, a CB reduction for coupling elements combined with an enrichment technique is presented in the WFE framework. Numerical results are provided regarding the CB reduction, transmission and reflection coefficients. Finally, a numerical application of the proposed approach to localize a defect in fluid-filled pipes with a curved joint is analyzed.

4.2 WFE modeling

Fluid-filled pipes are examples of periodic systems that can be seen as an assembly of elasto-acoustic substructures. In this sense, the WFE method can be applied to investigate wave propagation along these systems. In this framework, a substructure is modeled via FE, see Fig. 4.1. Here, the left and right boundaries of the substructure are meshed in the same way. Let us denote by n^E and n^A the number of DoFs for the elastic and acoustic parts on the left or

right boundaries and by n_{Γ}^E and n_{Γ}^A the related numbers of internal DoFs.

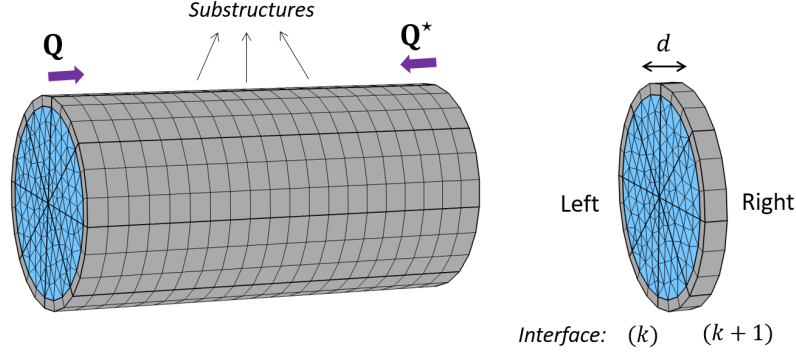


Figure 4.1: FE mesh of an elasto-acoustic waveguide and FE mesh of a substructure of length d . The elastic part is plotted in gray, and the acoustic part is plotted in blue.

The FE model of the elasto-acoustic substructure can be formulated using the following system of equations involving displacement vector \mathbf{U} and pressure vector \mathbf{p} [135]:

$$\underbrace{\left(-\omega^2 \begin{bmatrix} \mathbf{M}^E & \mathbf{0} \\ \rho^A \mathbf{G}^T & \mathbf{M}^A \end{bmatrix} + i\omega \begin{bmatrix} \mathbf{C}^E & \mathbf{0} \\ \mathbf{0} & \mathbf{C}^A \end{bmatrix} + \begin{bmatrix} \mathbf{K}^E & -\mathbf{G} \\ \mathbf{0} & \mathbf{K}^A \end{bmatrix} \right)}_{\mathbf{D}} \begin{bmatrix} \mathbf{U} \\ \mathbf{p} \end{bmatrix} = \begin{bmatrix} \mathbf{F}^E \\ \mathbf{F}^A \end{bmatrix}, \quad (4.1)$$

where ρ^A is the density of the acoustic part, and \mathbf{D} denotes the DSM of the substructure. Here, \mathbf{F}^E and \mathbf{F}^A are the elastic and acoustic force vectors with size $(2n^E + n_{\Gamma}^E)$ and $(2n^A + n_{\Gamma}^A)$, respectively. Also, the elastic displacement vector \mathbf{U} and the pressure vector \mathbf{p} are of size $(2n^E + n_{\Gamma}^E)$ and $(2n^A + n_{\Gamma}^A)$, respectively. In Eq. (4.1), \mathbf{M}^E , \mathbf{C}^E and \mathbf{K}^E are $(2n^E + n_{\Gamma}^E) \times (2n^E + n_{\Gamma}^E)$ mass, damping and stiffness matrices for the elastic part, and \mathbf{M}^A , \mathbf{C}^A and \mathbf{K}^A are $(2n^A + n_{\Gamma}^A) \times (2n^A + n_{\Gamma}^A)$ mass, damping and stiffness matrices for the acoustic part. Also, \mathbf{G} represents the elasto-acoustic coupling matrix of size $(2n^E + n_{\Gamma}^E) \times (2n^A + n_{\Gamma}^A)$. Eq. (4.1) is known as the (\mathbf{U}, \mathbf{p}) -formulation for elastic-acoustic problems.

Note that the (\mathbf{U}, \mathbf{p}) -formulation is not well suited for the WFE framework. This is explained by the fact that the DSM is not symmetric, consequently, the corresponding transfer matrix \mathbf{S} of the substructure is not symplectic. To solve this issue, the $(\mathbf{U}, \mathbf{\Psi})$ symmetric formulation can be proposed, where $\mathbf{\Psi}$ is the vector of velocity potential [32]:

$$\mathbf{\Psi} = -\frac{\mathbf{P}}{i\omega\rho_A}, \quad (4.2)$$

Then, inserting Eq. (4.2) into Eq. (4.1) leads to:

$$\mathbb{D} \begin{bmatrix} \mathbf{U} \\ \mathbf{\Psi} \end{bmatrix} = \begin{bmatrix} \mathbf{F}^E \\ \mathbf{F}^A/(i\omega) \end{bmatrix}, \quad (4.3)$$

where \mathbb{D} is the symmetric DSM of size $(2n + n_I)$, with $n = n^E + n^A$ and $n = n_I^E + n_I^A$, expressed as:

$$\mathbb{D} = -\omega^2\mathbb{M} + i\omega\mathbb{G} + \mathbb{K}, \quad (4.4)$$

where

$$\mathbb{M} = \begin{bmatrix} \mathbf{M}^E & \mathbf{0} \\ \mathbf{0} & -\rho_A\mathbf{M}^A \end{bmatrix}, \quad \mathbb{K} = \begin{bmatrix} \mathbf{K}^E & \mathbf{0} \\ \mathbf{0} & -\rho_A\mathbf{K}^A \end{bmatrix} \quad \text{and} \quad \mathbb{G} = \begin{bmatrix} \mathbf{C}^E & \rho_A\mathbf{G} \\ \rho_A\mathbf{G}^T & -\rho_A\mathbf{C}^A \end{bmatrix}. \quad (4.5)$$

Following the WFE procedure, Eq. (4.4) can be reorganized with respect to boundary and internal DoFs. The consideration of $\mathbf{F}_I = \mathbf{0}$, leads to the following equation for the substructure:

$$\begin{bmatrix} \mathbb{D}_{BB} & \mathbb{D}_{BI} \\ \mathbb{D}_{IB} & \mathbb{D}_{II} \end{bmatrix} \begin{bmatrix} \mathbf{q}_B \\ \mathbf{q}_I \end{bmatrix} = \begin{bmatrix} \mathbf{F}_B \\ \mathbf{0} \end{bmatrix}, \quad (4.6)$$

where

$$\mathbf{q}_B = \begin{bmatrix} \mathbf{U}_B \\ \mathbf{\Psi}_B \end{bmatrix}, \quad \mathbf{q}_I = \begin{bmatrix} \mathbf{U}_I \\ \mathbf{\Psi}_I \end{bmatrix} \quad \text{and} \quad \mathbf{F}_B = \begin{bmatrix} \mathbf{F}_B^E \\ \mathbf{F}_B^A/(i\omega) \end{bmatrix}. \quad (4.7)$$

Here, subscript B denotes the boundary DoFs encompassing the left (L) and right (R) boundaries of the substructure. Then Eq. (4.6) leads to:

$$\begin{bmatrix} \mathbb{D}_{LL}^* & \mathbb{D}_{LR}^* \\ \mathbb{D}_{RL}^* & \mathbb{D}_{RR}^* \end{bmatrix} \begin{bmatrix} \mathbf{q}_L \\ \mathbf{q}_R \end{bmatrix} = \begin{bmatrix} \mathbf{F}_L \\ \mathbf{F}_R \end{bmatrix}, \quad (4.8)$$

where the condensed DSM of the substructure is given by $\mathbb{D}^* = \mathbb{D}_{BB} - \mathbb{D}_{BI}\mathbb{D}_{II}^{-1}\mathbb{D}_{IB}$; \mathbf{q}_L and \mathbf{q}_R (resp. \mathbf{F}_L and \mathbf{F}_R) are displacement (resp. force) vectors of size $n \times 1$. Also, \mathbb{D}_{LL}^* , \mathbb{D}_{LR}^* , \mathbb{D}_{RL}^* and \mathbb{D}_{RR}^* are square $n \times n$ matrices such that $\mathbb{D}_{LL}^* = (\mathbb{D}_{LL}^*)^T$, $\mathbb{D}_{LR}^* = (\mathbb{D}_{RL}^*)^T$ and $\mathbb{D}_{RR}^* = (\mathbb{D}_{RR}^*)^T$. Considering Eq. (4.8), the following transfer relation between the displacement, pressure and force vectors, at the right and left boundaries, can be written as:

$$\begin{bmatrix} \mathbf{q}_R \\ \mathbf{F}_R \end{bmatrix} = \mathbf{S} \begin{bmatrix} \mathbf{q}_L \\ -\mathbf{F}_L \end{bmatrix}, \quad (4.9)$$

where \mathbf{S} is the transfer matrix of the substructure (size $2n \times 2n$), given by [21]:

$$\mathbf{S} = \begin{bmatrix} -\mathbb{D}_{LR}^{*-1}\mathbb{D}_{LL}^* & -\mathbb{D}_{LR}^{*-1} \\ \mathbb{D}_{RL}^* - \mathbb{D}_{RR}^*\mathbb{D}_{LR}^{*-1}\mathbb{D}_{LL}^* & -\mathbb{D}_{RR}^*\mathbb{D}_{LR}^{*-1} \end{bmatrix}. \quad (4.10)$$

Following Bloch's theorem, the eigensolutions of \mathbf{S} refer to the wave properties of a waveguide made up of these substructures. The eigenvalues of \mathbf{S} , denoted by μ_j , refer to the wave parameters with the property that $\mu_j = e^{-i\beta_j d}$ (β_j being the wave numbers) for a given wave j . Also, the eigenvectors of \mathbf{S} , denoted by ϕ_j , represent the wave shape vectors, as discussed in Chap. 2. For fluid-filled pipes, ϕ_j includes displacement and velocity potential parts, i.e.,

$$\phi_j = [(\phi_{qj}^E)^T (\phi_{qj}^A)^T (\phi_{Fj}^E)^T (\phi_{Fj}^A)^T]^T. \quad (4.11)$$

Each wave shape ϕ_j represents a $2n \times 1$ vector, given in Eq (4.11), which includes elastic and acoustic parts: $\phi_{\mathbf{q}j}^E$ is the displacement vector of size $(n^E \times 1)$, $\phi_{\mathbf{q}j}^A$ is the velocity potential vector of size $(n^A \times 1)$, $\phi_{\mathbf{F}j}^E$ is the elastic force vector of size $(n^E \times 1)$, and $\phi_{\mathbf{F}j}^A$ is the acoustic force vector of size $(n^A \times 1)$. The related eigenproblem can be computed with the (\mathbf{N}, \mathbf{L}) or $(\mathbf{S} + \mathbf{S}^{-1})$ methods, see Secs. 2.2.1 and 2.2.2.

4.2.1 Forced response

The forced response of the elasto-acoustic system can also be predicted with the WFE method. As developed in Sec. 2.3, the vectors \mathbf{q} and \mathbf{F} at an interface (k) can be decomposed in terms of waves:

$$\mathbf{q}_L^{(k)} = \mathbf{q}_R^{(k)} = \Phi_{\mathbf{q}} \mu^{k-1} \mathbf{Q} + \Phi_{\mathbf{q}}^* \mu^{N+1-k} \mathbf{Q}^* \quad k = 1, \dots, N+1, \quad (4.12)$$

$$-\mathbf{F}_L^{(k)} = \mathbf{F}_R^{(k)} = \Phi_{\mathbf{F}} \mu^{k-1} \mathbf{Q} + \Phi_{\mathbf{F}}^* \mu^{N+1-k} \mathbf{Q}^* \quad k = 1, \dots, N+1. \quad (4.13)$$

In Eq. (4.12), \mathbf{Q} and \mathbf{Q}^* are wave amplitude vectors, see Fig. 4.1. Here, $\Phi_{\mathbf{q}} = [(\Phi_{\mathbf{q}}^E)^T \ (\Phi_{\mathbf{q}}^A)^T]^T$, $\Phi_{\mathbf{F}} = [(\Phi_{\mathbf{F}}^E)^T \ (\Phi_{\mathbf{F}}^A)^T]^T$, $\Phi_{\mathbf{q}}^* = [(\Phi_{\mathbf{q}}^{*E})^T \ (\Phi_{\mathbf{q}}^{*A})^T]^T$, and $\Phi_{\mathbf{F}}^* = [(\Phi_{\mathbf{F}}^{*E})^T \ (\Phi_{\mathbf{F}}^{*A})^T]^T$. The determination of the wave amplitudes is found by considering the boundary conditions of the system.

Assume, for instance, that the elastic part is subject to a force at its left boundary and clamped at its right boundary; and that the acoustic part is subject to rigid wall condition, at the left and right boundaries. In this case, the boundary conditions lead to:

$$-\mathbf{F}_0^E = \Phi_{\mathbf{F}}^E \mathbf{Q} + \Phi_{\mathbf{F}}^{*E} \mu^N \mathbf{Q}^* \quad \text{and} \quad \mathbf{0} = \Phi_{\mathbf{q}}^E \mu^N \mathbf{Q} + \Phi_{\mathbf{q}}^{*E} \mathbf{Q}^*, \quad (4.14)$$

$$\mathbf{0} = \Phi_{\mathbf{F}}^A \mathbf{Q} + \Phi_{\mathbf{F}}^{*A} \mu^N \mathbf{Q}^* \quad \text{and} \quad \mathbf{0} = \Phi_{\mathbf{F}}^A \mu^N \mathbf{Q} + \Phi_{\mathbf{F}}^{*A} \mathbf{Q}^*, \quad (4.15)$$

where $\Phi_{\mathbf{q}}^E = [\phi_{\mathbf{q}1}^E \dots \phi_{\mathbf{q}n}^E]$, $\Phi_{\mathbf{q}}^{*E} = [\phi_{\mathbf{q}1}^{*E} \dots \phi_{\mathbf{q}n}^{*E}]$, $\Phi_{\mathbf{F}}^{E,A} = [\phi_{\mathbf{F}1}^{E,A} \dots \phi_{\mathbf{F}n}^{E,A}]$ and $\Phi_{\mathbf{F}}^{*E,A} = [\phi_{\mathbf{F}1}^{*E,A} \dots \phi_{\mathbf{F}n}^{*E,A}]$;

also, $\boldsymbol{\mu} = \text{diag}\{\mu_j\}_{j=1}^n$ is the diagonal matrix of eigenvalues μ_j for the right-going waves. In order to find the wave amplitude vectors \mathbf{Q} and \mathbf{Q}^* . Eqs. (4.14) and (4.15) can be reorganized as [34]:

$$\underbrace{\begin{bmatrix} \Phi_F^E \\ \Phi_F^A \end{bmatrix}}_{\mathbf{A}_1} \mathbf{Q} + \underbrace{\begin{bmatrix} \Phi_F^{*E} \\ \Phi_F^{*A} \end{bmatrix}}_{\mathbf{A}_1^*} \boldsymbol{\mu}^N \mathbf{Q}^* = \begin{bmatrix} -\mathbf{F}_0^E \\ \mathbf{0} \end{bmatrix} \quad (4.16)$$

and

$$\underbrace{\begin{bmatrix} \Phi_q^E \\ \Phi_F^A \end{bmatrix}}_{\mathbf{A}_2} \boldsymbol{\mu}^N \mathbf{Q} + \underbrace{\begin{bmatrix} \Phi_q^{*E} \\ \Phi_F^{*A} \end{bmatrix}}_{\mathbf{A}_2^*} \mathbf{Q}^* = \begin{bmatrix} \mathbf{0} \\ \mathbf{0} \end{bmatrix}. \quad (4.17)$$

Eqs. (4.16) and (4.17) lead to the following matrix system:

$$\begin{bmatrix} \mathbf{A}_1 & \mathbf{A}_1^* \boldsymbol{\mu}^N \\ \mathbf{A}_2 \boldsymbol{\mu}^N & \mathbf{A}_2^* \end{bmatrix} \begin{bmatrix} \mathbf{Q} \\ \mathbf{Q}^* \end{bmatrix} = \begin{bmatrix} -\mathbf{F}_0^E \\ \mathbf{0} \end{bmatrix}. \quad (4.18)$$

The matrix in Eq. (4.18) may be ill-conditioned, see Sec. 2.3. This issue is solved using a pre-conditioner, i.e., by multiplying the matrix equation by $\text{blkdiag}(\mathbf{A}_1^{-1}, \mathbf{A}_2^{*-1})$. This yields:

$$\begin{bmatrix} \mathbf{I} & (\mathbf{A}_1)^{-1} \mathbf{A}_1^* \boldsymbol{\mu}^N \\ (\mathbf{A}_2^*)^{-1} \mathbf{A}_2 \boldsymbol{\mu}^N & \mathbf{I} \end{bmatrix} \begin{bmatrix} \mathbf{Q} \\ \mathbf{Q}^* \end{bmatrix} = \begin{bmatrix} -(\mathbf{A}_1)^{-1} \mathbf{F}_0^E \\ \mathbf{0} \end{bmatrix}. \quad (4.19)$$

Solving the Eq. (4.18) yields the wave amplitude vectors \mathbf{Q} and \mathbf{Q}^* . Finally, the displacement/pressure can be retrieved from Eqs. (4.12) and (4.13) (see Chap. 2 for further details).

4.2.2 Group velocity

In fluid-filled pipes, the computation of the group velocities can be achieved via Eq. (2.32) when the dispersion curves are known, see Sec. 2.5. In the present framework, the approach based on the energy should be modified in order to take into account both elastic and acoustic parts. By adapting Eqs. (2.34), (2.35) and (2.36), the group velocity for a certain mode j can be expressed as [54]:

$$c_{gj} = \frac{P_j}{T_j + U_j} = \frac{P_j^E + P_j^A}{T_j^E + U_j^E + T_j^A + U_j^A}, \quad (4.20)$$

where P_j is the energy flow of the j -th mode through the cross-section, with P_j^E and P_j^A the elastic and acoustic energy flow contributions; also, T_j is the kinetic energy, and U_j is the potential energy. In Eq. (4.20), the energy flow, the kinetic and potential energies are decomposed into elastic and acoustic contributions, which are calculated as follows [55]:

$$P_j^E = \frac{-i\omega}{4} \begin{bmatrix} \mathbf{U}_{Lj}^{(k)} \\ -\mathbf{F}_{Lj}^{E(k)} \end{bmatrix}^H \mathbf{J} \begin{bmatrix} \mathbf{U}_{Lj}^{(k)} \\ -\mathbf{F}_{Lj}^{E(k)} \end{bmatrix} \quad \text{and} \quad P_j^A = \frac{-i}{4\omega\rho_A} \begin{bmatrix} \mathbf{p}_{Lj}^{(k)} \\ -\mathbf{F}_L^A(k) \end{bmatrix}^H \mathbf{J} \begin{bmatrix} \mathbf{p}_{Lj}^{(k)} \\ -\mathbf{F}_L^A(k) \end{bmatrix}, \quad (4.21)$$

$$T_j^E = \frac{\omega^2}{4d} \begin{bmatrix} \mathbf{U}_{Lj}^{(k)} \\ \mathbf{U}_{Lj}^{(k+1)} \end{bmatrix}^H \mathbf{M}_{BB}^E \begin{bmatrix} \mathbf{U}_{Lj}^{(k)} \\ \mathbf{U}_{Lj}^{(k+1)} \end{bmatrix} \quad \text{and} \quad T_j^A = \frac{1}{4d\rho_A\omega^2} \begin{bmatrix} \mathbf{p}_{Lj}^{(k)} \\ \mathbf{p}_{Lj}^{(k+1)} \end{bmatrix}^H \mathbf{K}_{BB}^A \begin{bmatrix} \mathbf{p}_{Lj}^{(k)} \\ \mathbf{p}_{Lj}^{(k+1)} \end{bmatrix}, \quad (4.22)$$

and

$$U_j^E = \frac{1}{4d} \begin{bmatrix} \mathbf{U}_{Lj}^{(k)} \\ \mathbf{U}_{Lj}^{(k+1)} \end{bmatrix}^H \mathbf{K}_{BB}^E \begin{bmatrix} \mathbf{U}_{Lj}^{(k)} \\ \mathbf{U}_{Lj}^{(k+1)} \end{bmatrix} \quad \text{and} \quad U_j^A = \frac{1}{4d\rho_A} \begin{bmatrix} \mathbf{p}_L \\ \mathbf{p}_{Lj}^{(k+1)} \end{bmatrix}^H \mathbf{M}_{BB}^A \begin{bmatrix} \mathbf{p}_L \\ \mathbf{p}_{Lj}^{(k+1)} \end{bmatrix}. \quad (4.23)$$

In Eqs. (4.21), (4.22), and (4.23), the displacement, pressure, and forces are computed considering the contribution of each mode j . The approach using Eq. (2.32) involving the

numerical derivative of the frequency with respect to the wavenumber can lead to numerical errors around the cut-off frequencies. This is explained because the curve is not differentiable at these points. Instead, the approach based on energy can be used without substantial errors.

4.2.3 Numerical results

The dispersion curves and the vibroacoustic response for an 0.5 m long fluid-filled pipe are computed. The elastic part has a density of $\rho_E = 7800 \text{ kg/m}^3$, a Young's modulus of $E = 210 \text{ GPa}$, and a Poisson's ratio of $\nu = 0.3$. The acoustic part has a density of $\rho_A = 1000 \text{ kg/m}^3$ and a speed of sound of 1500 m/s. In terms of geometry, the pipe has a thickness of 0.005 m and an external radius of 0.05 m. The considered substructure has a length of $d = 0.002 \text{ m}$. So, the whole waveguide contains $N = 250$ identical substructures. The damping is modeled using the Rayleigh damping model for acoustic and elastic parts: $\mathbf{C}^E = 10^{-3}\mathbf{M}^E + 10^{-8}\mathbf{M}^E$, and $\mathbf{C}^A = 10^{-3}\mathbf{M}^A + 10^{-8}\mathbf{M}^A$.

The substructure is discretized as follows: the elastic part is meshed with linear hexahedral elements with eight nodes and three DoFs per node (representing displacements in the x, y, z -directions), and the acoustic part is meshed with linear prismatic elements with six nodes and one DoFs per node (representing the pressure). Each substructure is discretized by means of $n = 271$ DoFs on each right/left boundary and no internal DoFs. Also, the elastic and acoustic parts account for $n^E = 144$ DoFs and $n^A = 127$ DoFs, respectively.

Following the WFE method, the wave modes of the elasto-acoustic modes are obtained using the $\mathbf{S} + \mathbf{S}^{-1}$ strategy (as in Sec. 2.2.2). The number of left/right-going waves is $n = 271$, representing elasto-acoustic modes. Fig. 4.2(a) shows the dispersion curves for some modes over $[100 - 40 \times 10^3] \text{ Hz}$ — i.e., the frequency evolution of the real and imaginary part of $\beta_j d$. Fig. 4.2(b) shows the group velocities for these modes.

Moreover, in Fig. 4.2, some modes of each family are highlighted and labeled as follows: $\text{FS}(\mathbf{n}, \mathbf{m})$ in green, $\text{SF}(\mathbf{n}, \mathbf{m})$ in pink, red, and orange, and $\text{T}(0, \mathbf{m})$ in blue, where \mathbf{n} and \mathbf{m} stand

for the circumferential mode order and the sequence of modes in the circumferential family, respectively (as similarly discussed for empty pipes in Sec 1.3). Those labels were introduced by Duan and Kirby [107] to consider the energy transfer between the elastic and the acoustic parts as a function of frequency.

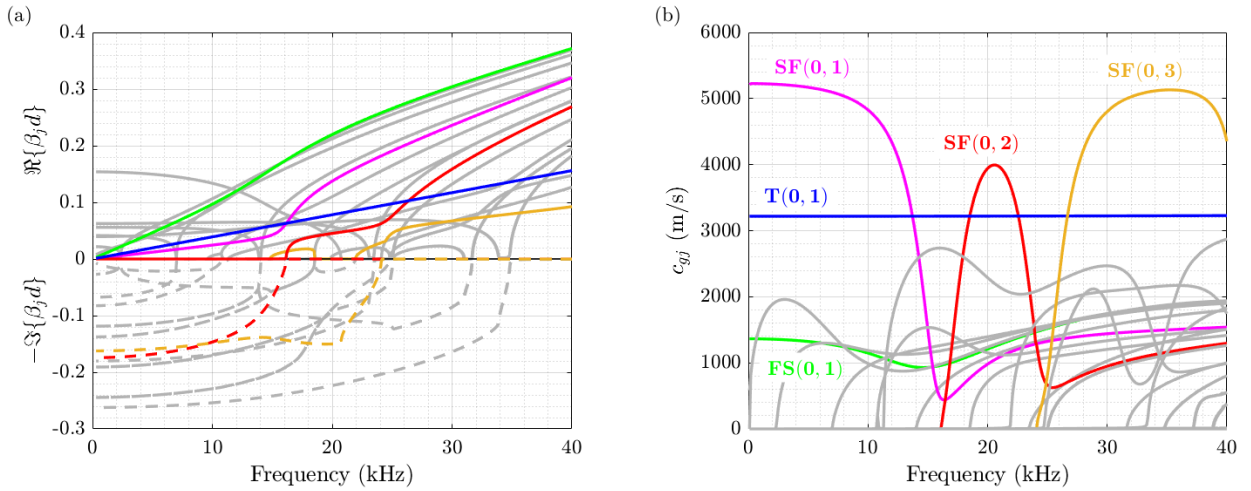


Figure 4.2: (a) Dispersion curves (real and imaginary parts of $\beta_j d$ are plotted in continuous and dashed lines, respectively) and (b) group velocities for modes: T(0, 1) (in blue), SF(0, 1) (in magenta), SF(0, 2) (in red), SF(0, 3) (in orange), and FS(0, 1) (in green). Other modes are plotted in gray lines.

Figs. 4.3(a) and (b) show power ratios for elastic and acoustic parts for some modes as a function of the frequency: in the family mode FS(n, m), the energy is confined in the acoustic part at low frequencies, and at high frequencies, energy is transferred from the acoustic part to the elastic part. Concerning the family mode SF(n, m), the energy is confined in the elastic part at low frequencies, and at high frequencies, energy is transferred from the elastic to the acoustic part. Finally, the torsional family mode T(0, m) remains similar to those encountered in empty pipes. In this case, the energy remains confined in the elastic part for the whole frequency range since no coupling between elastic and acoustic parts is observed.

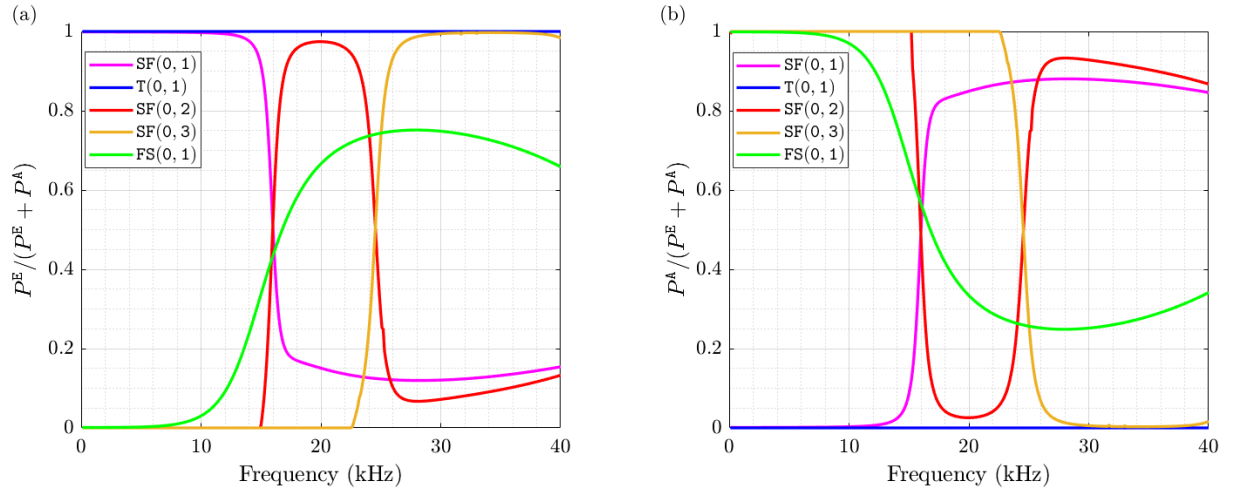


Figure 4.3: Ratios (a) $P^E / (P^E + P^A)$ and (b) $P^A / (P^E + P^A)$ for the modes: T(0, 1) in blue, SF(0, 1) in magenta, SF(0, 2) in red, SF(0, 3) in orange, and FS(0, 1) in green.

Fig. 4.4 shows some wave shapes obtained via WFE method at 20 kHz, i.e., the modes (a) T(0, 1), (b) SF(0, 1), (c) and (d) flexurals. The pressure, as well as the displacements, are normalized with respect to their maximum. The z -displacement in (direction of propagation) is plotted in grayscale, and the x, y -displacements are plotted using red arrows. For the mode T(0, 1), it is possible to observe that the pressure is null, and that the displacements are tangent to the propagation direction of the wave throughout the circumference of the pipe. For the mode SF(0, 1), symmetrical and radial fluid compression by the elastic part is observed. Finally, the flexural modes can be associated with the classical flexural modes in empty pipes and are double-root modes, i.e., two modes with the same dispersion curves are found, but their orientations in the space differ. In Figs. 4.4(c) and (d), one side of the pipe is compressed, and the opposite side is expanded. Those dispersion curves and wave mode shapes highlight the system complexity compared to previous examples for elastic structures without fluids (Timoshenko beam, 2D-stress beam, and pipe). Here, the coupling between the fluid and the elastic parts plays an important role and the exchange of energy from one part to another can vary along the frequency.

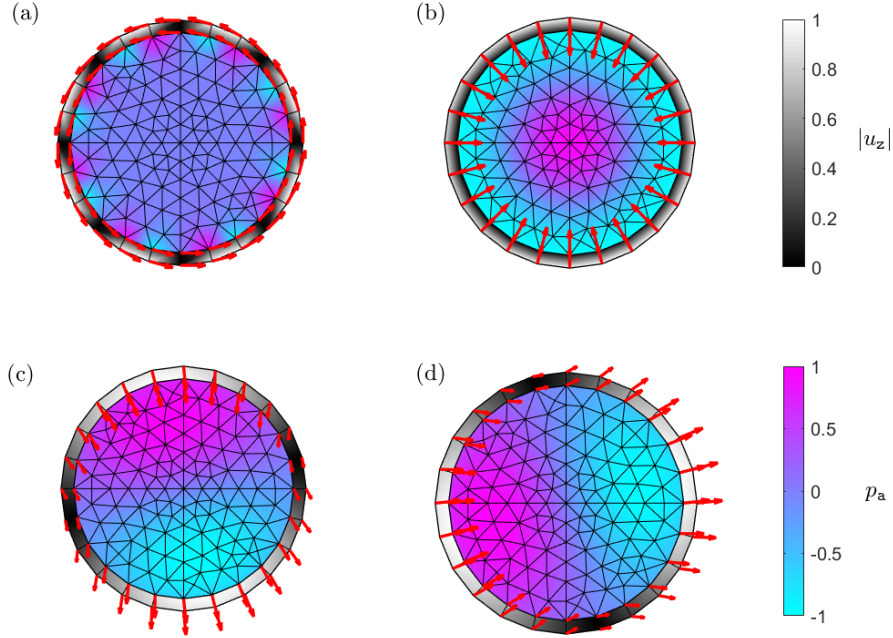


Figure 4.4: Wave shapes at 20 kHz for modes: (a) $T(0, 1)$, (b) $SF(0, 1)$, (c) and (d) flexural. The pressure is plotted using colored scale, the in-plane displacement (x and y directions) is plotted using red arrows, and the out-plane displacement (z-direction) is plotted in grayscale.

For validation proposes, a numerical comparison between the elastic displacement $|U_z|$ at one point obtained with FE and WFE methods is shown in Fig. 4.5(a). Here, a force $F_{0z} = 1$ kN is applied at eight points equally spaced around the circumference of the pipe. The forced response is obtained via Eq. (4.19) from 100 to 10kHz with a frequency step of 25Hz. The error between the FE and WFE approaches is computed using Eq. (2.42) using sub-frequency bands of 200 Hz. The error along the frequency band is shown in Fig. 4.5(b): it remains smaller than 0.1% except around the first anti-resonance peak (around 4 kHz), where it reaches approximately 0.3%.

Fig. 4.6(a) shows the acoustic pressure $20 \log(|p|/p_{\text{ref}})$ with $p_{\text{ref}} = 10^{-6}$ Pa at the center of the pipe along the frequency band obtained with the FE and WFE methods. Fig. 4.6(b)

shows the relative error between the two approaches. Overall, the error remains inferior to 0.1%, except around 0.8 kHz where it reaches an error of 1.4%.

Tab. 4.1 shows the elapsed times spent to simulate the vibro-acoustic response of the fluid filled pipe with the FE and WFE methods. The FE simulation accounts for 68021 DoFs in total (including pressure and displacements). Regarding the elapsed times, it takes 2469 s to compute the frequency response using the FE method and 269 s with the WFE method. In the WFE method, 249 s are used to compute the wave basis, and 20 s to compute Eq. (4.18). There is a reduction of approximately 89 % in terms of computational time when using the WFE method. For the FE and WFE methods, the mesh and matrix assembly processes are not taken into account.

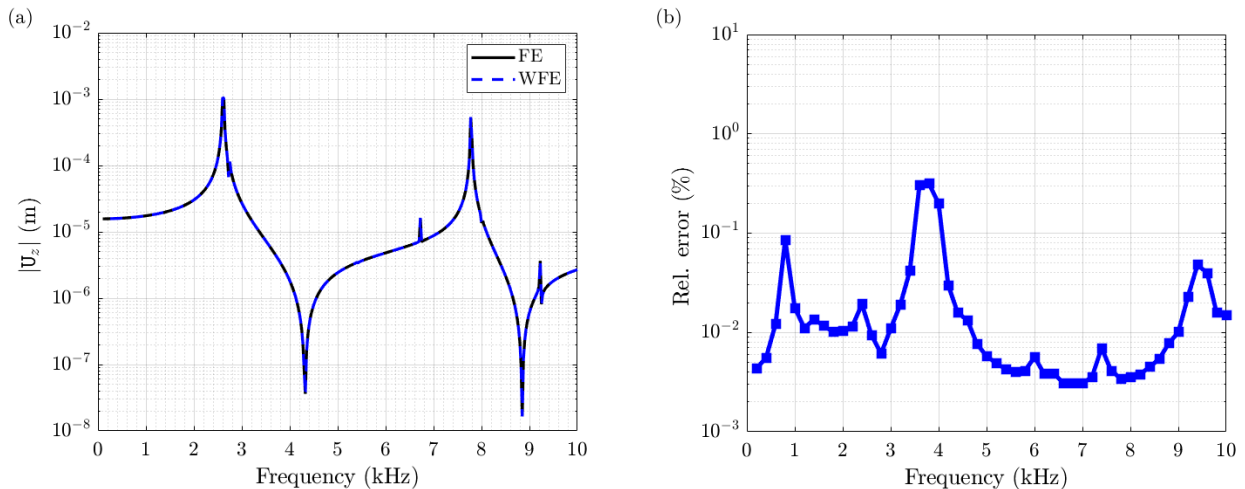


Figure 4.5: (a) Comparison between the displacement obtained via FE method, in black continuous line, and WFE method, in blue dot lines, for the fluid-filled pipe case. (b) Relative error between the two solutions.

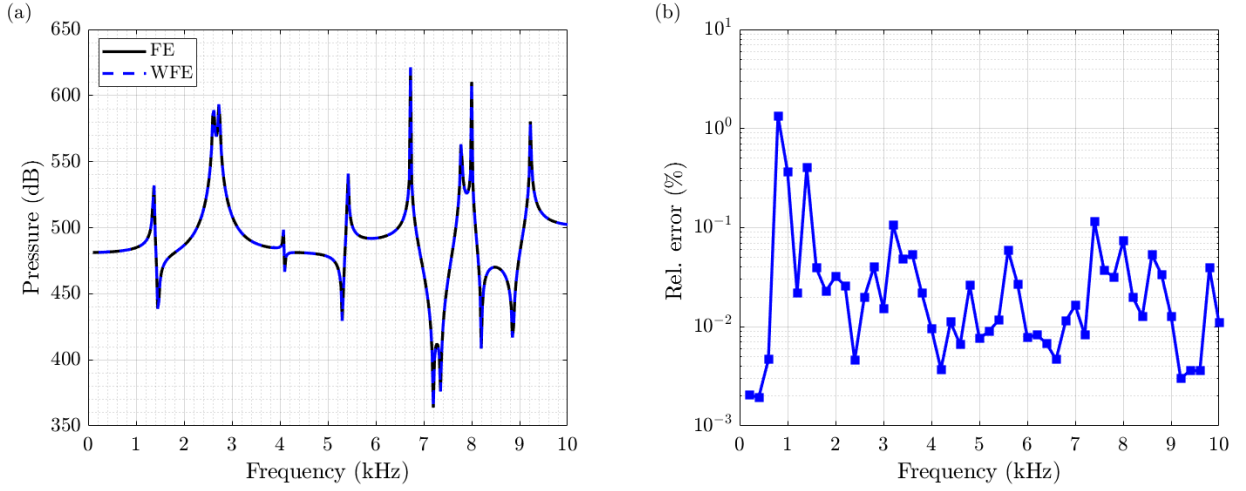


Figure 4.6: (a) Comparison between the acoustic pressure obtained via FE method, in black continuous line, and WFE method, in blue dot lines, for the fluid-filled pipe case. (b) Relative error between the two solutions.

Table 4.1: Elapsed times for FE and WFE methods for a straight fluid-filled pipe.

Method		Time (s)	
FE		2469.5	
WFE	Computation of $\{\mu_j, \phi_j\}_{j=1,\dots,n}$ and $\{\mu_j^*, \phi_j^*\}_{j=1,\dots,n}$	268.5	288.6
	Computation of Eq. (4.18)	19.9	

4.3 Elasto-acoustic coupling element

Within the WFE framework, a scattering matrix can be used to assess transmission and reflection coefficients of waves at coupling elements in fluid-filled pipes (joints and/or defects). Let us consider a coupling element connecting two waveguides, as shown in Fig. 4.7. The FE mesh of the substructure of the waveguide and the FE mesh of the joint can be easily generated using FE software or Matlab.

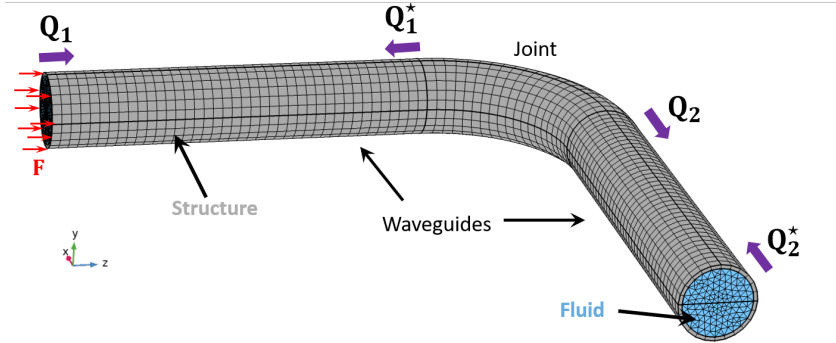


Figure 4.7: Two fluid-filled pipes connected by a curved joint.

In this case, the DSM of the coupling element, denoted by \mathbb{D}^c , is written as:

$$\mathbb{D}^c = -\omega^2 \mathbb{M}^c + i\omega \mathbb{G}^c + \mathbb{K}^c, \quad (4.24)$$

where $\mathbb{M}^c, \mathbb{G}^c, \mathbb{K}^c$ are the mass, coupling, and stiffness matrices issued from the $(\mathbf{U}, \mathbf{\Psi})$ -formulation, see Eq. (4.4). In the WFE formalism, the scattering matrix can be obtained in the same way as in Sec. 2.7.1. The strategy is briefly recalled here. Let us consider a system composed of two waveguides with N_1 and N_2 substructures connected to an arbitrary joint, as shown in Fig. 4.7. The scattering matrix for the joint is given by:

$$\begin{aligned} \mathbb{C}^c = & - \left(\mathbb{D}^{c*} \begin{bmatrix} \mathcal{L}_1 \Phi_q^* & \mathbf{0} \\ \mathbf{0} & \mathcal{L}_2 \Phi_q \end{bmatrix} + \begin{bmatrix} \mathcal{L}_1 \Phi_F^* & \mathbf{0} \\ \mathbf{0} & -\mathcal{L}_2 \Phi_F \end{bmatrix} \right)^{-1} \\ & \times \left(\mathbb{D}^{c*} \begin{bmatrix} \mathcal{L}_1 \Phi_q & \mathbf{0} \\ \mathbf{0} & \mathcal{L}_2 \Phi_q^* \end{bmatrix} + \begin{bmatrix} \mathcal{L}_1 \Phi_F & \mathbf{0} \\ \mathbf{0} & -\mathcal{L}_2 \Phi_F^* \end{bmatrix} \right). \end{aligned} \quad (4.25)$$

In this way, the wave amplitude vectors for the incoming and outgoing waves at the boundaries of the joint can be related as follows:

$$\begin{bmatrix} \mathbf{Q}_1^* \\ \mathbf{Q}_2 \end{bmatrix} = \mathbb{C}^c \begin{bmatrix} \boldsymbol{\mu}^{N_1} \mathbf{Q}_1 \\ \boldsymbol{\mu}^{N_2} \mathbf{Q}_2^* \end{bmatrix} = \begin{bmatrix} \mathbb{C}_{11}^c & \mathbb{C}_{12}^c \\ \mathbb{C}_{21}^c & \mathbb{C}_{22}^c \end{bmatrix} \begin{bmatrix} \boldsymbol{\mu}^{N_1} \mathbf{Q}_1 \\ \boldsymbol{\mu}^{N_2} \mathbf{Q}_2^* \end{bmatrix}, \quad (4.26)$$

where \mathbf{Q}_1^* and \mathbf{Q}_2 are the wave amplitude vectors for the outgoing waves at the boundaries of the joint; also, $\boldsymbol{\mu}^{N_1} \mathbf{Q}_1$ and $\boldsymbol{\mu}^{N_2} \mathbf{Q}_2^*$ are the wave amplitude vectors for the incoming waves at the same boundaries.

Using Eq. (4.26), it is possible to investigate the vibroacoustic response of the system following the same procedure as described in Sec. 2.7.3 with the desired boundary conditions. However, the scattering matrix involves the condensed DSM of the coupling element, which means calculating $(\mathbb{D}_{\text{II}}^c)^{-1}$, where I stands for the internal DoFs of the joint. In the present case, the coupling element usually involves many internal DoFs including pressure and displacement components, which can strongly affect the computation of the condensed DSM. To solve this issue, a reduction method can be applied to diminish the computational costs. The CB reduction, as discussed in Sec. 2.7.2, can be adapted with basis enrichment to account for the fluid-structure interaction.

4.3.1 CB reduction

Let us consider the acoustic and the elastic parts of the coupling element. The elastic displacement and the velocity potential vectors are denoted by \mathbf{U}^c and $\boldsymbol{\Psi}^c$, respectively. Let us denote the number of the elastic and acoustic boundary DoFs by n_B^E and n_B^A , and the number of internal DoFs for the elastic and acoustic parts by n_I^E and n_I^A , respectively. Using the CB method, the internal DoFs for the elastic part \mathbf{U}_I^c and the potential velocity $\boldsymbol{\Psi}_I^c$ can be expressed in terms of static modes and fixed-interface modes:

$$\mathbf{U}_I^c \approx \tilde{\mathbf{U}}_I^c = \mathbf{X}_{\text{st}}^E \mathbf{U}_B^c + \tilde{\mathbf{X}}_{\text{el}}^E \tilde{\boldsymbol{\alpha}}_E \quad \text{and} \quad \boldsymbol{\Psi}_I^c \approx \tilde{\boldsymbol{\Psi}}_I^c = \mathbf{X}_{\text{st}}^A \boldsymbol{\Psi}_B^c + \tilde{\mathbf{X}}_{\text{el}}^A \tilde{\boldsymbol{\alpha}}_A, \quad (4.27)$$

where $\tilde{\boldsymbol{\alpha}}_E$ and $\tilde{\boldsymbol{\alpha}}_A$ are vectors of generalized coordinates for the elastic and acoustic parts. Here, \mathbf{X}_{st}^E is the matrix of static modes of the elastic part of size $(n_I^E \times n_B^E)$ given by:

$$\mathbf{X}_{\text{st}}^E = - \left[(\mathbf{K}_{\text{II}}^E)^c \right]^{-1} (\mathbf{K}_{\text{IB}}^E)^c, \quad (4.28)$$

also, \mathbf{X}_{st}^A is the matrix of static modes of the acoustic part of size $(n_I^A \times n_B^A)$:

$$\mathbf{X}_{\text{st}}^A = - \left[(\mathbf{K}_{\text{II}}^A)^c \right]^{-1} (\mathbf{K}_{\text{IB}}^A)^c. \quad (4.29)$$

Here, the matrices of fixed-interface modes for the elastic and acoustic parts are denoted by $\tilde{\mathbf{X}}_{\text{e1}}^E = [(\mathbf{X}_{\text{e1}}^E)_1 \cdots (\mathbf{X}_{\text{e1}}^E)_{m_I}]$ and $\tilde{\mathbf{X}}_{\text{e1}}^A = [(\mathbf{X}_{\text{e1}}^A)_1 \cdots (\mathbf{X}_{\text{e1}}^A)_{m_I}]$, where $(\mathbf{X}_{\text{e1}}^E)_j$ and $(\mathbf{X}_{\text{e1}}^A)_j$ are the eigenvectors related to the following eigenproblems:

$$(\mathbf{K}_{\text{II}}^E)^c (\mathbf{X}_{\text{e1}}^E)_j = (\omega_E)_j^2 (\mathbf{M}_{\text{II}}^E)^c (\mathbf{X}_{\text{e1}}^E)_j \quad \text{and} \quad (\mathbf{K}_{\text{II}}^A)^c (\mathbf{X}_{\text{e1}}^A)_j = (\omega_A)_j^2 (\mathbf{M}_{\text{II}}^A)^c (\mathbf{X}_{\text{e1}}^A)_j, \quad (4.30)$$

where $(\omega_{E,A})_j$ are the eigenfrequencies for the mode $(\mathbf{X}_{\text{e1}}^{E,A})_j$. Note that $(\omega_E)_j$ and $(\omega_A)_j$ can be different. The reduction is based on the number of retained fixed-interface modes related to Eqs. (4.30) — i.e., the retained fixed-interface modes are those whose eigenfrequencies are below a certain threshold. The number of retained modes are different for the fluid and the acoustic parts and are denoted by m_I^E and m_I^A , respectively, with $m_I^E \ll n_I^E$ and $m_I^A \ll n_I^A$. Then, Eqs. (4.27) can be written as:

$$\begin{bmatrix} \mathbf{U}_I^c \\ \mathbf{U}_B^c \\ \Psi_I^c \\ \Psi_B^c \end{bmatrix} \approx \begin{bmatrix} \tilde{\mathbf{U}}_I^c \\ \mathbf{U}_B^c \\ \tilde{\Psi}_I^c \\ \Psi_B^c \end{bmatrix} = \underbrace{\begin{bmatrix} \mathbf{T}_{\text{CB}}^E & \mathbf{0} \\ \mathbf{0} & \mathbf{T}_{\text{CB}}^A \end{bmatrix}}_{\mathbf{T}_{\text{CB}}} \begin{bmatrix} \tilde{\boldsymbol{\alpha}}_E \\ \mathbf{U}_B^c \\ \tilde{\boldsymbol{\alpha}}_A \\ \Psi_B^c \end{bmatrix}, \quad (4.31)$$

where $\mathbf{T}_{\text{CB}}^{\text{E}}$ and $\mathbf{T}_{\text{CB}}^{\text{A}}$ are the CB transformation matrices of sizes $(n_{\text{I}}^{\text{E}} + n_{\text{B}}^{\text{E}}) \times (m_{\text{I}}^{\text{E}} + n_{\text{B}}^{\text{E}})$ and $(n_{\text{I}}^{\text{A}} + n_{\text{B}}^{\text{A}}) \times (m_{\text{I}}^{\text{A}} + n_{\text{B}}^{\text{A}})$, respectively, given by:

$$\mathbf{T}_{\text{CB}}^{\text{E}} = \begin{bmatrix} \tilde{\mathbf{X}}_{\text{el}}^{\text{E}} & \mathbf{X}_{\text{st}}^{\text{E}} \\ \mathbf{0} & \mathbf{I} \end{bmatrix} \quad \text{and} \quad \mathbf{T}_{\text{CB}}^{\text{A}} = \begin{bmatrix} \tilde{\mathbf{X}}_{\text{el}}^{\text{A}} & \mathbf{X}_{\text{st}}^{\text{A}} \\ \mathbf{0} & \mathbf{I} \end{bmatrix}. \quad (4.32)$$

Eqs. (4.24) and (4.31), lead to the reduced DSM of the coupling element $\tilde{\mathbb{D}}^{\text{c}}$:

$$\tilde{\mathbb{D}}^{\text{c}} \approx \mathbf{T}_{\text{CB}}^{\text{T}} \mathbb{D}^{\text{c}} \mathbf{T}_{\text{CB}} = \begin{bmatrix} \tilde{\mathbb{D}}_{\text{el-el}}^{\text{c}} & \tilde{\mathbb{D}}_{\text{el-st}}^{\text{c}} \\ \left(\tilde{\mathbb{D}}_{\text{el-st}}^{\text{c}}\right)^{\text{T}} & \mathbb{D}_{\text{st-st}}^{\text{c}} \end{bmatrix}. \quad (4.33)$$

The condensed DSM of the coupling element $\mathbb{D}^{\text{c}\star}$ is a square matrix of size $(m_{\text{I}}^{\text{E}} + m_{\text{I}}^{\text{A}} + 2n)$ expressed as:

$$\mathbb{D}^{\text{c}\star} \approx \tilde{\mathbb{D}}_{\text{st-st}}^{\text{c}} - \tilde{\mathbb{D}}_{\text{st-el}}^{\text{c}} \left(\tilde{\mathbb{D}}_{\text{el-el}}^{\text{c}}\right)^{-1} \tilde{\mathbb{D}}_{\text{el-st}}^{\text{c}}. \quad (4.34)$$

In this case, Eq. (4.34) can be computed as explained in Sec. 2.7.2. The issue with this approach is that it does not consider the coupling between the acoustic and the elastic parts, since the fixed interface and static modes are calculated separately — i.e., the action of the acoustic part on the elastic part and vice versa is not taken into account. To solve this issue, the CB basis can be enriched to include coupling terms.

Static response vectors can be used to enrich the CB basis [60], the idea is to use a reduced number of fixed-interface modes together with static correction terms to account for the coupling between the elastic and acoustic parts. The quasi-static contribution of the acoustic part over the elastic and vice-versa can be found by neglecting the inertia terms in Eq. (4.5):

$$\begin{cases} \mathbf{U}_{\text{I}} &= -i\omega\rho_{\text{A}}(\mathbf{K}_{\text{II}}^{\text{E}})^{-1} \mathbf{G}_{\text{II}} \boldsymbol{\Psi}_{\text{I}} \\ \boldsymbol{\Psi}_{\text{I}} &= i\omega(\mathbf{K}_{\text{II}}^{\text{A}})^{-1} \mathbf{G}_{\text{II}}^{\text{T}} \mathbf{U}_{\text{I}} \end{cases} \quad (4.35)$$

In Eq. (4.35), the correction due to the approximation of the internal DoFs using a reduced set of fixed-interface modes is written as:

$$\begin{cases} \mathbf{U}_I \approx -i\omega\rho_A (\mathbf{K}_{II}^E)^{-1} \mathbf{G}_{II} \tilde{\mathbf{X}}_{e1}^A \tilde{\boldsymbol{\alpha}}_A \\ \boldsymbol{\Psi}_I \approx i\omega (\mathbf{K}_{II}^A)^{-1} \mathbf{G}_{II}^T \tilde{\mathbf{X}}_{e1}^E \tilde{\boldsymbol{\alpha}}_E \end{cases} \quad (4.36)$$

In this case, the vectors \mathbf{U}_I and $\boldsymbol{\Psi}_I$ are spanned by the column spaces of $(\mathbf{K}_{II}^E)^{-1} \mathbf{G}_{II} \tilde{\mathbf{X}}_{e1}^A$ and $(\mathbf{K}_{II}^A)^{-1} \mathbf{G}_{II}^T \tilde{\mathbf{X}}_{e1}^E$. Then the following matrices of Ritz vectors can be used to enrich the CB bases:

$$\begin{cases} \Delta \mathbf{T}_{\text{cor}}^E = (\mathbf{K}_{II}^E)^{-1} \mathbf{G}_{II} \tilde{\mathbf{X}}_{e1}^A \\ \Delta \mathbf{T}_{\text{cor}}^A = (\mathbf{K}_{II}^A)^{-1} \mathbf{G}_{II}^T \tilde{\mathbf{X}}_{e1}^E \end{cases} \quad (4.37)$$

From the numerical point of view, these vectors need to go through an orthogonalization process to regularize the reduced bases. It can be achieved using the singular value decomposition (SVD):

$$\Delta \mathbf{T}_{\text{cor}}^E = \mathcal{U}^E \boldsymbol{\Sigma}^E (\mathcal{V}^E)^T \quad \text{and} \quad \Delta \mathbf{T}_{\text{cor}}^A = \mathcal{U}^A \boldsymbol{\Sigma}^A (\mathcal{V}^A)^T, \quad (4.38)$$

where $\boldsymbol{\Sigma}^E$ (resp. $\boldsymbol{\Sigma}^A$) is the matrix of singular values of $\Delta \mathbf{T}_{\text{cor}}^E$ (resp. $\Delta \mathbf{T}_{\text{cor}}^A$). Also, \mathcal{U}^E (resp. \mathcal{U}^A) and \mathcal{V}^E (resp. \mathcal{V}^A) are respectively the matrices of left and right vectors of $\Delta \mathbf{T}_{\text{cor}}^E$ (resp. $\Delta \mathbf{T}_{\text{cor}}^A$).

The idea is to select a reduced set of left singular vectors to be later used in the projection matrices. Indeed, let us denote by \tilde{m}_E and \tilde{m}_A the numbers of the retained left vectors of \mathcal{U}^E and \mathcal{U}^A associated with the highest singular values. The matrices of enrichment vectors are written as: $\tilde{\mathcal{U}}^E = [(\mathcal{U}^E)_1 \cdots (\mathcal{U}^E)_{\tilde{m}_E}]$ and $\tilde{\mathcal{U}}^A = [(\mathcal{U}^A)_1 \cdots (\mathcal{U}^A)_{\tilde{m}_A}]$. Then, Eq. (4.31) leads to:

$$\mathbf{U}_I^c \approx \tilde{\mathbf{U}}_I^c = \tilde{\mathbf{X}}_{\text{el}}^E \tilde{\boldsymbol{\alpha}}_E + \tilde{\mathcal{U}}^E \tilde{\boldsymbol{\beta}}_E + \mathbf{X}_{\text{st}}^E \mathbf{U}_B^c \quad (4.39)$$

$$\boldsymbol{\Psi}_I^c \approx \tilde{\boldsymbol{\Psi}}_I^c = \tilde{\mathbf{X}}_{\text{el}}^A \tilde{\boldsymbol{\alpha}}_A + \tilde{\mathcal{U}}^A \tilde{\boldsymbol{\beta}}_A + \mathbf{X}_{\text{st}}^A \boldsymbol{\Psi}_B^c \quad (4.40)$$

where $\tilde{\boldsymbol{\alpha}}_{E,A}$ and $\tilde{\boldsymbol{\beta}}_{E,A}$ are vectors of generalized coordinates related to the elastic and acoustic parts. The new projection matrix $\boldsymbol{\Gamma}_{\text{CB}}$ updated from Eq. (4.32) becomes:

$$\begin{bmatrix} \mathbf{U}_I^c \\ \mathbf{U}_B^c \\ \boldsymbol{\Psi}_I^c \\ \boldsymbol{\Psi}_B^c \end{bmatrix} \approx \begin{bmatrix} \tilde{\mathbf{U}}_I^c \\ \mathbf{U}_B^c \\ \tilde{\boldsymbol{\Psi}}_I^c \\ \boldsymbol{\Psi}_B^c \end{bmatrix} = \underbrace{\begin{bmatrix} \boldsymbol{\Gamma}_{\text{CB}}^E & \mathbf{0} \\ \mathbf{0} & \boldsymbol{\Gamma}_{\text{CB}}^A \end{bmatrix}}_{\boldsymbol{\Gamma}_{\text{CB}}} \begin{bmatrix} \tilde{\boldsymbol{\alpha}}_E \\ \tilde{\boldsymbol{\beta}}_E \\ \mathbf{U}_B^c \\ \tilde{\boldsymbol{\alpha}}_A \\ \tilde{\boldsymbol{\beta}}_A \\ \boldsymbol{\Psi}_B^c \end{bmatrix}, \quad (4.41)$$

with $\boldsymbol{\Gamma}_{\text{CB}}$ the updated transformation matrix, $\boldsymbol{\Gamma}_{\text{CB}}^E$ and $\boldsymbol{\Gamma}_{\text{CB}}^A$ the new projection matrices for the elastic and acoustic parts, given by:

$$\boldsymbol{\Gamma}_{\text{CB}}^E = \begin{bmatrix} \tilde{\mathbf{X}}_{\text{el}}^E & \tilde{\mathcal{U}}^E & \mathbf{X}_{\text{st}}^E \\ \mathbf{0} & \mathbf{0} & \mathbf{I} \end{bmatrix} \quad \text{and} \quad \boldsymbol{\Gamma}_{\text{CB}}^A = \begin{bmatrix} \tilde{\mathbf{X}}_{\text{el}}^A & \tilde{\mathcal{U}}^A & \mathbf{X}_{\text{st}}^A \\ \mathbf{0} & \mathbf{0} & \mathbf{I} \end{bmatrix}. \quad (4.42)$$

Here, $\boldsymbol{\Gamma}_{\text{CB}}^E$ has a size of $(n_I^E + n_B^E) \times (m_I^E + \tilde{m}_E + 2n_B^E)$ and $\boldsymbol{\Gamma}_{\text{CB}}^A$ has a size of $(n_I^A + n_B^A) \times (m_I^A + \tilde{m}_A + 2n_B^A)$. This strategy aims to minimize the computational costs in scenarios where a coupling element (defect and/or joint) has a significant number of internal DoFs. The reduced DSM of the coupling element is found as:

$$\tilde{\mathbb{D}}^c \approx \boldsymbol{\Gamma}_{\text{CB}}^T \mathbb{D}^c \boldsymbol{\Gamma}_{\text{CB}} = \begin{bmatrix} \tilde{\mathbb{D}}_{\text{el-el}}^c & \tilde{\mathbb{D}}_{\text{el-st}}^c \\ (\tilde{\mathbb{D}}_{\text{el-st}}^c)^T & \mathbb{D}_{\text{st-st}}^c \end{bmatrix}. \quad (4.43)$$

In this case, the condensed DSM of the coupling element \mathbb{D}^{c^*} is a square matrix of size $(m_I^E + \tilde{m}_E + m_I^A + \tilde{m}_A + 2n_B)$. The CB reduction approach in Eq. (4.31), in which transformation

matrices are separately constructed for the elastic and acoustic parts, is inadequate to guarantee accuracy. Consequently, enhancing the approach by enriching the CB basis with static correction vectors is recommended. This process enables fast convergence with a small number of fixed interface modes. It is due to the small computation costs of condensing the reduced DSM $\tilde{\mathbb{D}}^c$, as opposed to condensing \mathbb{D}^c . The proposed strategy can be summarized as follows:

1. Obtain the DSM of the coupling element \mathbb{D}^c in the global coordinate system;
2. Compute the static modes for the elastic and acoustic parts \mathbf{X}_{st}^E and \mathbf{X}_{st}^A , as in Eqs. (4.28) and (4.29);
3. Compute the fixed-interface modes for the elastic and acoustic parts $\tilde{\mathbf{X}}_{\text{el}}^{E,A}$, as in Eq. (4.30), and select those whose eigenfrequencies are below a certain value;
4. Compute enrichment vectors $\Delta \mathbf{T}_{\text{cor}}^E$ and $\Delta \mathbf{T}_{\text{cor}}^A$ using Eq. (4.37), and then perform an SVD procedure to build orthogonal enrichment vectors $\tilde{\mathbf{U}}^E$ and $\tilde{\mathbf{U}}^A$;
5. Build the projection matrix $\mathbf{\Gamma}_{\text{CB}}$ and compute $\tilde{\mathbb{D}}^c = \mathbf{\Gamma}_{\text{CB}}^T \mathbb{D}^c \mathbf{\Gamma}_{\text{CB}}$;

4.3.2 Power scattering coefficients

Using the reduction strategy related to the coupling element, it is possible to calculate transmission and reflection coefficients quickly and accurately. One way to analyze the reflection and transmission of waves at a coupling element is of computing the scattering matrix as in Eq. (4.25). This can be done quickly using the proposed reduction for the coupling element. It is also possible to compute scattering coefficients considering energy flows at the coupling element. For this task, let us consider two waveguides with a coupling element (joint or defect), as shown in Fig. 4.7. In this sense, the power reflection coefficient R_{pr} when an incident mode p is converted in a certain reflected mode r is computed as follows [124, 127]:

$$R_{pr} = \frac{(P_r)_{\text{ref}}}{(P_p)_{\text{inc}}} = \frac{(P_r^E + P_r^A)_{\text{ref}}}{(P_p^E + P_p^A)_{\text{inc}}}, \quad (4.44)$$

where P^E and P^A are computed via Eq. (4.21) for incident and reflected waves. Similarly, the power transmission coefficient when an incident mode p , from waveguide 1, is converted into a transmitted mode t in waveguide 2 is given by:

$$T_{pt} = \frac{(P_t)_{\text{trans}}}{(P_p)_{\text{inc}}} = \frac{(P_t^E + P_t^A)_{\text{trans}}}{(P_p^E + P_p^A)_{\text{inc}}}. \quad (4.45)$$

It is worth mentioning that the power transmission and reflection coefficients can vary with the frequency since the wave shapes are frequency-dependent. Also, this approach does not depend on how the vectors of wave shapes are normalized.

4.4 Numerical results

4.4.1 Reduced modeling of the coupling element

An example of two waveguides of length $l_1 = l_2 = 0.5$ m connected with a curved joint is investigated. The waveguides have the same characteristics as in Sec. 4.2.3. Both waveguides contain $N = 250$ identical substructures. The joint has a radius of $R_j = 0.2$ m, an angle of $\pi/2$, and shares the same internal and external diameters as the waveguides, see Fig. 4.7.

Fig. 4.8 shows a comparison between the forced response issued from the WFE and the FE methods along the frequency. Here, the comparison is provided from $f_{\min} = 100$ Hz to $f_{\max} = 10$ kHz with a frequency step of 25 Hz. In Fig. 4.8(a), the WFE solution is obtained without reducing the \mathbb{D}_j^* and it is plotted in blue dashed lines. While Fig. 4.8(b) shows the result using the reduction strategy to compute $\tilde{\mathbb{D}}_j^*$ for the joint proposed in Sec. 4.3.1.

In terms of CB reduction, $m_E = 250$ and $m_A = 200$ fixed-interface modes are retained for the elastic and acoustic parts, respectively. The highest eigenfrequency associated with the fixed-interface modes for the elastic and acoustic parts are $f_{\max}^E = 43.2$ kHz and $f_{\max}^A = 57.8$ kHz, respectively. In this case, $f_{\max}^E > 4f_{\max}$ and $f_{\max}^A > 5f_{\max}$ which are sufficient to capture an

accurate response. Also, the number of enrichment vectors are $\tilde{m}_E = 150$ and $\tilde{m}_A = 200$. Fig. 4.9 shows the error between the FE and WFE (with and without reduction) solutions computed by means of Eq. (2.42) in steps of 200 Hz. The maximum error bounds 0.25% when no reduction is used and 1 % using the proposed reduction.

Tab. 4.2 shows the computational times related to: FE method, WFE method without reduction, and WFE method with reduction. The FE model has 141191 DoFs in total, encompassing pressure and displacements DoFs. The related computational time is 8.711×10^3 s (approx. 2h and 25 min). The WFE solution without reduction requires 6.904×10^3 s (approx. 1h and 55 min), in which 95 % of the time is employed to the computation of \mathbb{D}_j^* . This represents a reduction of 20.75 % compared to the FE solution. With the reduction, this yields in 68.95 % of time saving compared to the FE model. In this case, the computation of $\tilde{\mathbb{D}}_j^*$ represents approximately 84 % of the total elapsed time.

Fig. 4.10 shows a good agreement of the time response between FE and WFE methods calculated from 0 ms to 20 ms. The force is a Gaussian pulse centered at 5 kHz. Also, the reduction strategy to compute $\tilde{\mathbb{D}}_j^*$ with $m_s = 250$, $m_a = 200$, $\tilde{m}_s = 150$ and $\tilde{m}_a = 200$ is employed. The FE result is found using the Newmark method using average constant acceleration ($\beta = 0.25$ and $\gamma = 0.5$), and with time step of $\Delta t = 1 \mu\text{s}$. Meanwhile, the WFE result is found via FFT with a sampling frequency of $f_s = 400$ kHz and $T = 300$ ms (see Sec. 2.4), sufficient to respect the Nyquist–Shannon sampling theorem. Also, the considered FFT parameters lead to a time step of $dt = 2.5 \mu\text{s}$. Again, there is no reason to use the same time step for both methods since different approaches are employed (see Sec. 2.4).

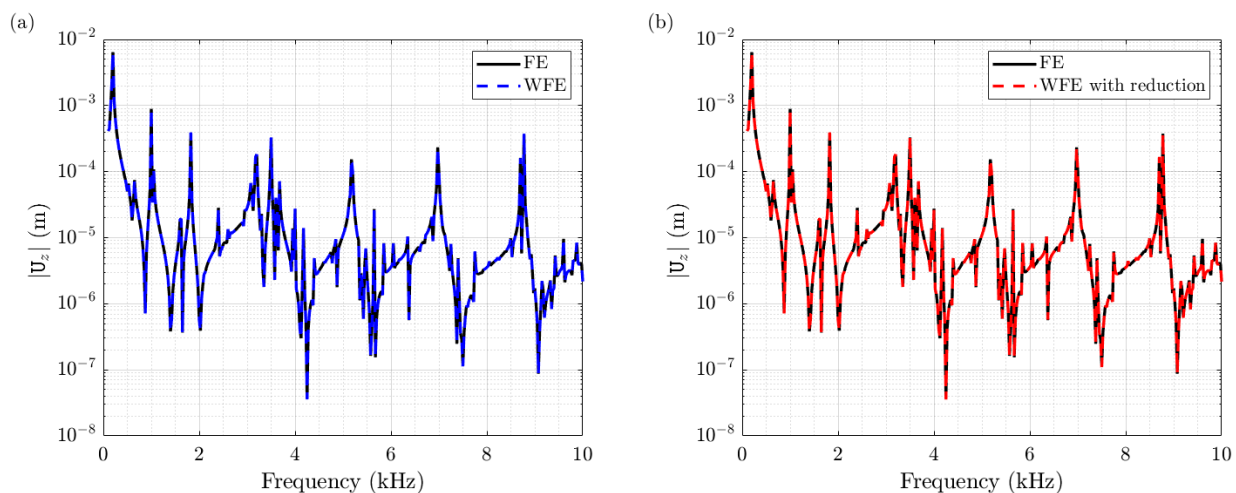


Figure 4.8: Comparison between the displacement obtained using the FE method (black continuous line), and the WFE method for fluid-filled networks: (a) without reduction and (b) with reduction for the joint.

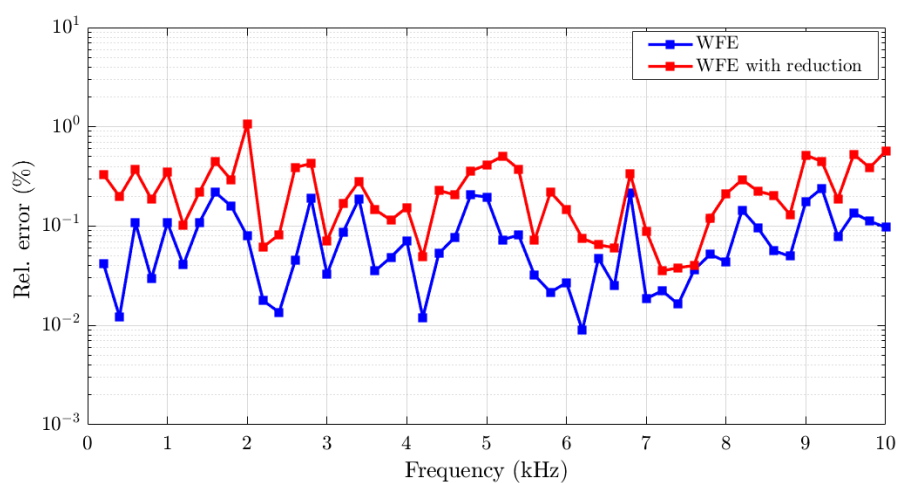


Figure 4.9: Relative error between the FE method and the WFE method for fluid-filled pipes networks: without reduction (blue) and with reduction (red).

Table 4.2: Elapsed times to compute the solutions using the FE method, the full WFE, and the WFE method with CB reduction for the joint.

Method		Time (s)		Reduction (%)
FE		8.711×10^3		—
WFE	\mathbb{D}_j^*	6.55×10^3	6.904×10^3	20.75
	Computation of $\{\mu_j, \phi_j\}_{j=1, \dots, n}$ and $\{\mu_j^*, \phi_j^*\}_{j=1, \dots, n}$	265.10		
WFE + reduction	$\tilde{\mathbb{D}}_j^*$	2.27×10^3	2.704×10^3	68.95
	Computation of $\{\mu_j, \phi_j\}_{j=1, \dots, n}$ and $\{\mu_j^*, \phi_j^*\}_{j=1, \dots, n}$	265.10		

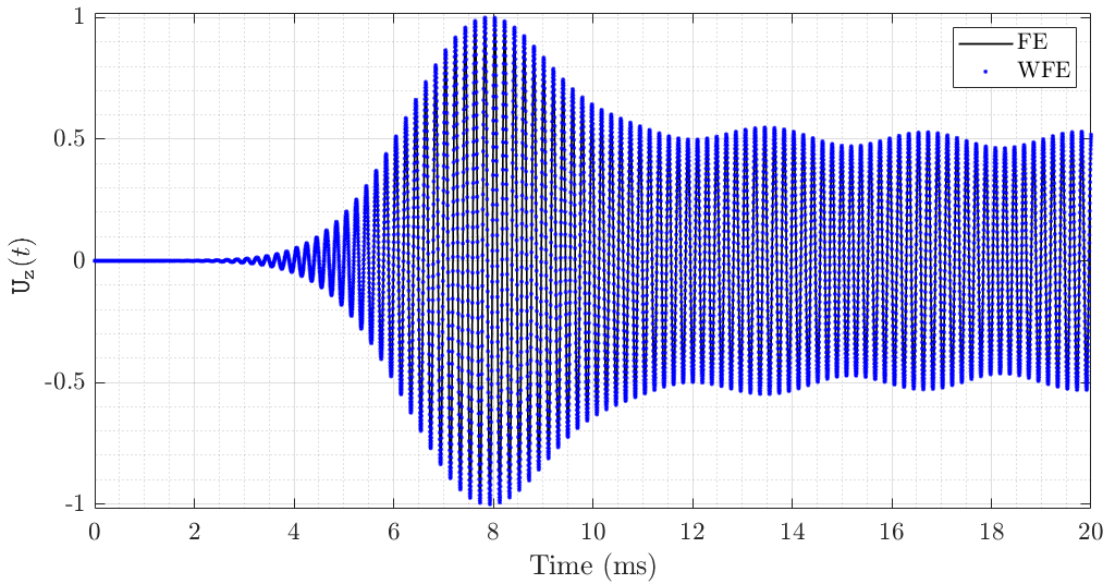


Figure 4.10: FE and WFE time response (displacement) for fluid-filled networks connected with a joint when a force given by a Gaussian pulse centered at 5 kHz is applied.

4.4.2 Influence of the size of the enrichment basis

It is possible to analyze the influence of the numbers of enrichment vectors in $\tilde{\mathcal{U}}^E$ and $\tilde{\mathcal{U}}^A$ used when the number of fixed-interface modes for the elastic part is $m_E = 250$ and acoustic part is $m_A = 200$. Fig. 4.11 depicts the error as a function of the frequency for different values of \tilde{m}_E and \tilde{m}_A . It is possible to observe that different combinations of these values can lead to the same errors, see for example, the cases $(\tilde{m}_E, \tilde{m}_A) = (150, 150)$ and $(200, 150)$. In these cases, the maximum error is around 6.67 %. The number of enrichment vectors of $\tilde{\mathcal{U}}^A$ plays a more important role, given that increasing the number of enrichment vectors \tilde{m}_E does not change the error drastically. Tab. 4.3 summarizes the total elapsed times and the maximum error related to different choices of \tilde{m}_E and \tilde{m}_A . Overall, the reduction in computational time is around 65% for all cases.

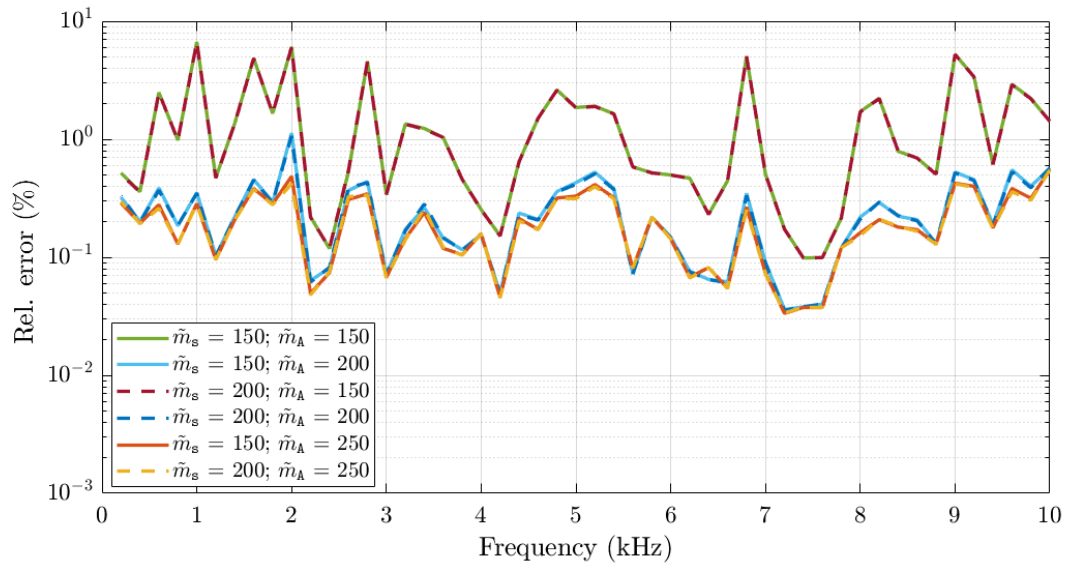


Figure 4.11: Relative error between the FE method and the WFE method with CB reduction for the joint when considering different \tilde{m}_E of \tilde{m}_A .

Table 4.3: Total elapsed time for different values of \tilde{m}_E and \tilde{m}_A . The reduction of the computational time and the maximum error compared to the FE method are also displayed. The errors as a function of the frequency can be seen in Fig. 4.11.

\tilde{m}_E	\tilde{m}_A	Total elapsed time (s)	Reduction (%)	max. error (%)
150	150	2.470×10^3	71.65	6.67
150	200	2.704×10^3	68.96	1.13
200	150	2.631×10^3	69.80	6.67
200	200	2.858×10^3	67.19	1.07
150	250	3.049×10^3	65.00	0.49
200	250	3.193×10^3	63.35	0.42

4.4.3 Defect localization

To compare the influence of the fluid on the scattering coefficients, some numerical examples are carried out considering empty and fluid-filled pipes.

The joint is modeled using the same physical parameters as the elastic and acoustic parts of the waveguides, see Sec. 4.4.1. It has a radius of $R_j = 0.2$ m, an angle of $\theta_j = 90^\circ$, and it shares the same internal and external diameters as the waveguides, see Fig. 4.12(b). The FE mesh of the joint and waveguides employs linear hexahedral elements with eight nodes and three degrees of freedom (DoFs) per node (representing displacements in the x, y, z -directions) for the elastic part, and linear prism elements with six nodes and one DOF per node (representing pressure) for the acoustic part.

An axisymmetric defect is introduced in waveguide 2 as shown in Fig. 4.12(a). It is modeled as a local decrease in the Young modulus $E_d = (1 - \gamma)E$, where E is the Young modulus of the waveguide. Here, $\gamma = 0.7$ resulting $E_d = 63$ GPa. The coupling element representing a defect does not contain internal DoFs and has a length of 0.002 m.

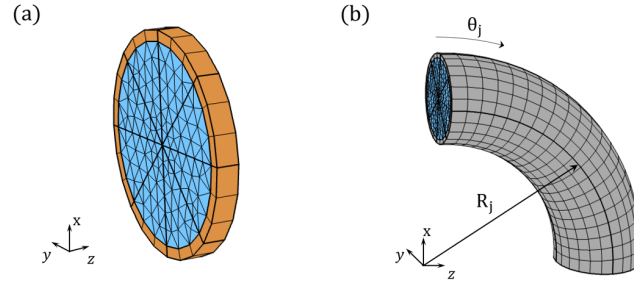


Figure 4.12: Schematics of the coupling elements: (a) defect and (b) joint.

Let us consider the case of two waveguides connected by a defect. Fig. 4.13(a) shows the transmission and reflection coefficients at the defect for an incident $T(0, 1)$ mode. It is possible to observe large transmission and small reflection coefficients. The reflection (resp. transmission) coefficient slightly increases (resp. decreases) along the frequency. The same behavior is observed for an incident $SF(0, 1)$ mode to itself, as seen in Fig. 4.13(b). For the case $SF(0, 1) \rightarrow SF(0, 1)$, a peak in the transmission coefficient is observed around 15 kHz. This peak is related to the energy transferring to another mode. In both cases, a reflected signal can still be observed in the time domain, as shown later in this manuscript.

Consider now two waveguides connected by a curved joint as shown in Fig. 4.13(b). Fig. 4.14 shows the (a) transmission and (b) reflection for empty (in black line) and fluid-filled pipes (in blue line). In Fig. 4.14(a), it is interesting to note a large discrepancy between the two systems. For the fluid-filled pipes, a maximum transmission is reached around 10 kHz and no transmission is observed around 14 kHz. In this frequency range, the transmission coefficient of the torsional mode for empty pipes varies between 0.4 and 0.6. In Fig. 4.14(b), reflected peaks occur around 4 kHz in both cases. After this peak, the reflection coefficients tend to 0. In this case, both systems exhibit similar behavior.

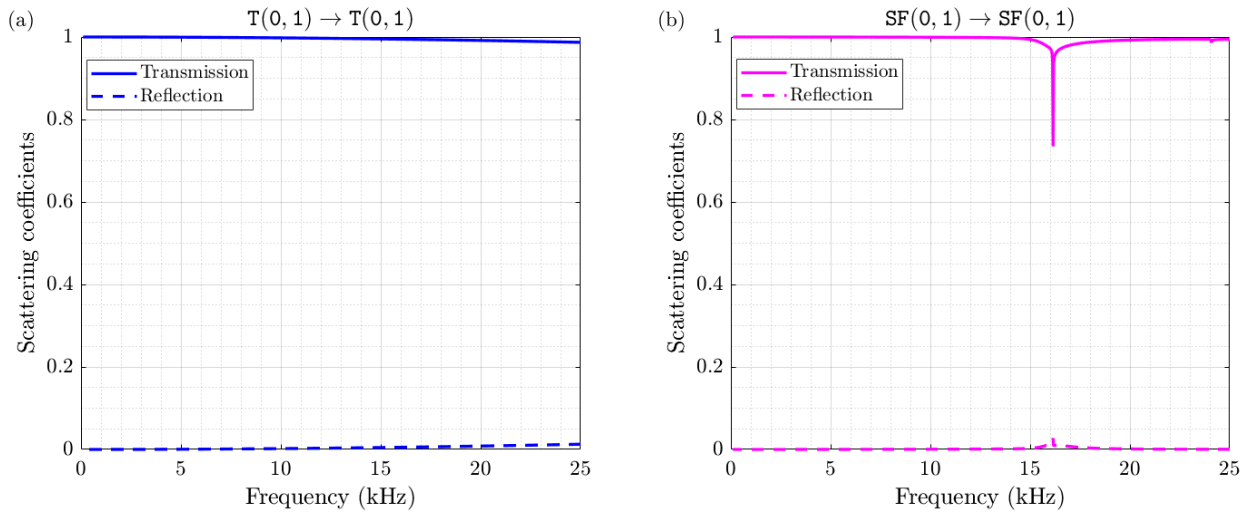


Figure 4.13: Power scattering coefficients for the defect: (a) $T(0, 1) \rightarrow T(0, 1)$ and (b) $SF(0, 1) \rightarrow SF(0, 1)$. Transmission and reflection coefficients are plotted in continuous and dashed lines, respectively.

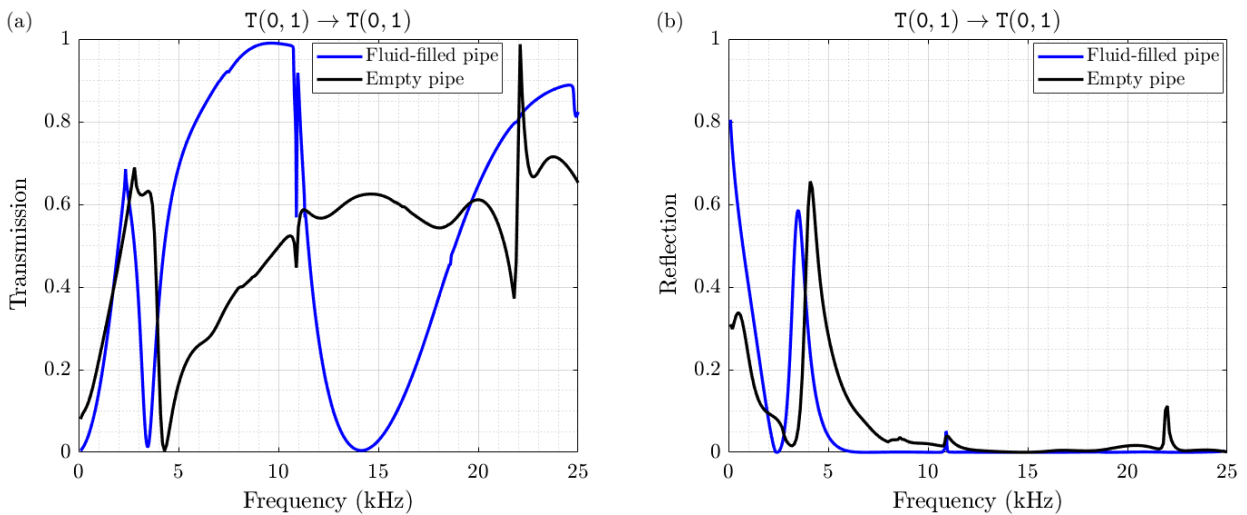


Figure 4.14: Power scattering coefficients for the joint: (a) transmission and (b) reflection $T(0, 1) \rightarrow T(0, 1)$. Fluid-filled pipe in blue lines, and empty pipe in black lines.

Fig. 4.14 shows the power (a) transmission and (b) reflection coefficients for the incident mode $T(0, 1)$. High energy transfer between the mode $T(0, 1)$ and a flexural mode is observed from 10 kHz to 20 kHz. Also, there is no significant energy transfer from the incident mode into the modes $FS(0, 1)$, $SF(0, 1)$ and $SF(0, 2)$. In terms of reflection, no significant energy transfer is observed.

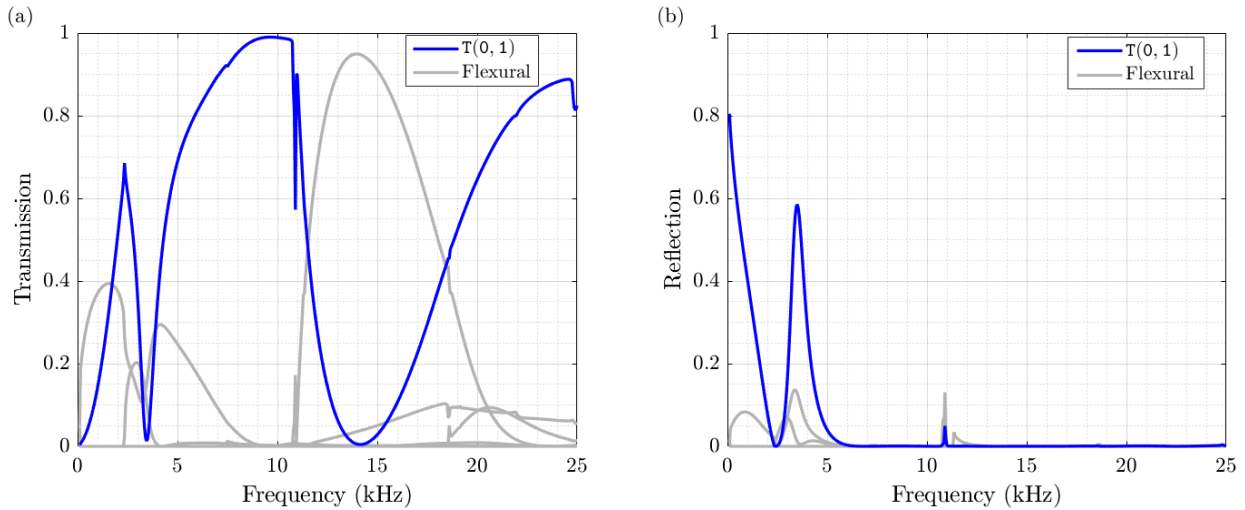


Figure 4.15: Power coefficients for the joint: (a) transmission and (b) reflection from $T(0, 1)$ to flexural modes (in gray) and to $T(0, 1)$ (in blue) for fluid-filled pipes.

Fig. 4.16 shows the (a) transmission and (b) reflection power coefficients for the incident mode $SF(0, 1)$. Mode conversion in transmission is observed from the incident mode to $SF(0, 1)$, $FS(0, 1)$ and flexural modes, showed in gray continuous lines. High transmission from the incident mode to itself is observed from 5 kHz to 10 kHz. A power reflection coefficient for $SF(0, 1)$ to $SF(0, 1)$ is seen at low frequencies but decreases to 0 at 10 kHz. Also, low reflection coefficients are found at high frequencies for the analyzed modes.

Finally, the influence of the radius of the joint is analyzed. Figs. 4.17(a) and (b) depict the transmission and reflection coefficients for different joints with radius $R_j = 0.2$ m, 0.4 m, 0.5 m, and 0.6 m in the case of fluid-filled pipes. It is possible to see that large radii provide

high transmission coefficients for the $T(0, 1)$ mode through the joint between 3 kHz and 13 kHz. However, the minimum of the transmission coefficient still occurs around 14 kHz. The energy is mainly transmitted to a flexural mode in this range. In terms of reflection coefficients, peaks are observed below 5 kHz. The larger the radius, the greater the $T(0, 1)$ mode transmission. This trend is also observed for empty pipes.

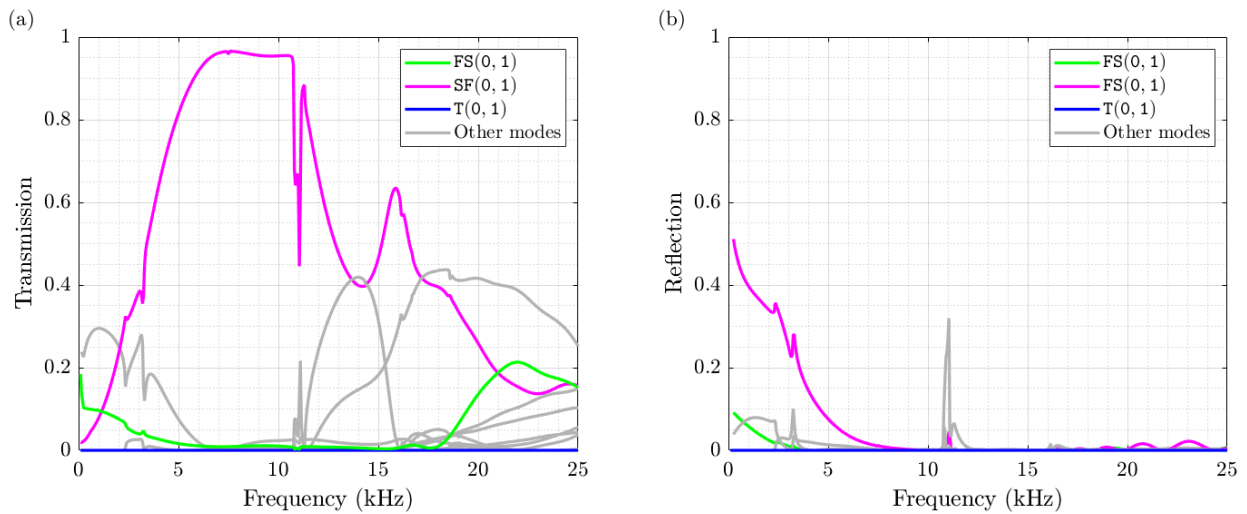


Figure 4.16: Power coefficients for the joint: (a) transmission and (b) reflection from $SF(0, 1)$ to other modes.

In general, it appears that the $T(0, 1)$ mode seems suitable for identifying defects in the elastic part. This is because the energy associated with this mode remains confined within the elastic part over the entire frequency band. Concerning the mode $SF(0, 1)$, its energy remains confined to the elastic part up to approximately 15 kHz and, after, the energy is mostly confined in the acoustic part (see Fig. 4.3). This indicates that the mode $SF(0, 1)$ is unsuitable for defect detection at high frequencies, as defects in the elastic part of the waveguide have minimal impact on reflection/transmission coefficients for this mode.

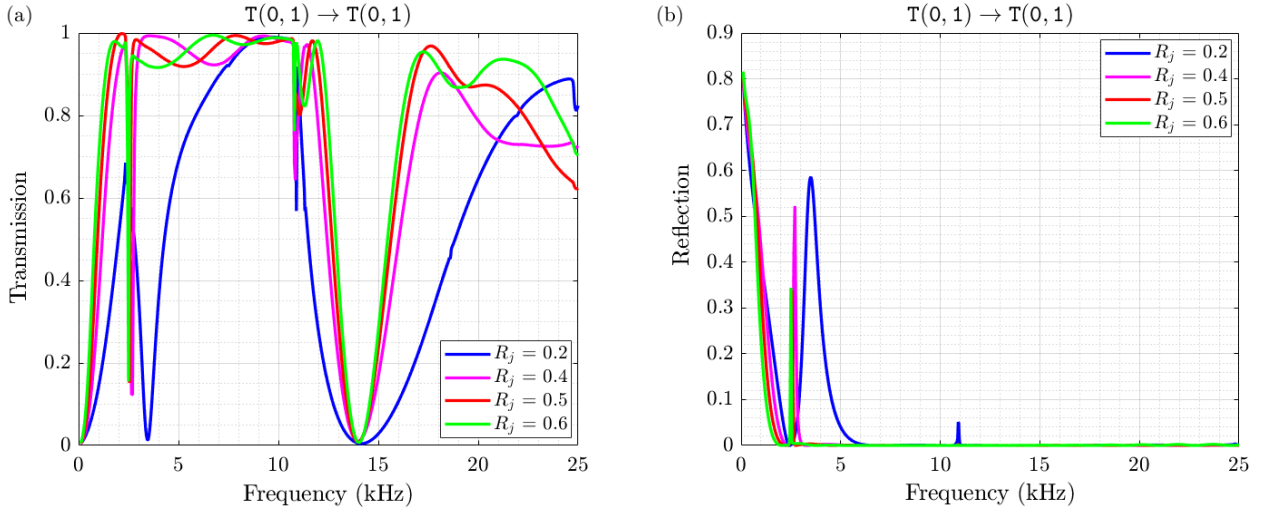


Figure 4.17: Power coefficients using different radii for the joint: (a) transmission and (b) reflection from $T(0,1)$ to itself.

To be able to localize a defect, it is necessary to compute the time of flight in transmission through the joint. Here, the time of flight that a mode $T(0,1)$ takes to be transmitted and reflected through a joint can be computed via Eqs. (3.17) and (3.18). Fig. 4.18(a) and (b) show the time of flight in transmission τ_{jj}^{1-2} and reflection τ_{jj}^{1-1} through a curved joint of radius $R_j = 0.2$ m and angle of curvature $\theta_j = 90^\circ$. Here, the times of flight related to the empty and fluid-filled pipes are plotted in black and blue lines, respectively.

Different sharp peaks can be observed in Fig 4.18. Those peaks are related to cut-off frequencies for certain propagating modes or to internal resonances of the joint, as already discussed in Sec. 3.6.1.2. Aside from those sharp peaks, it is possible to observe that the mode $T(0,1)$ can be transmitted and reflected at different frequencies compared to empty pipes. Also, the times of flight related to this mode in transmission and reflection are not constant along the frequency.

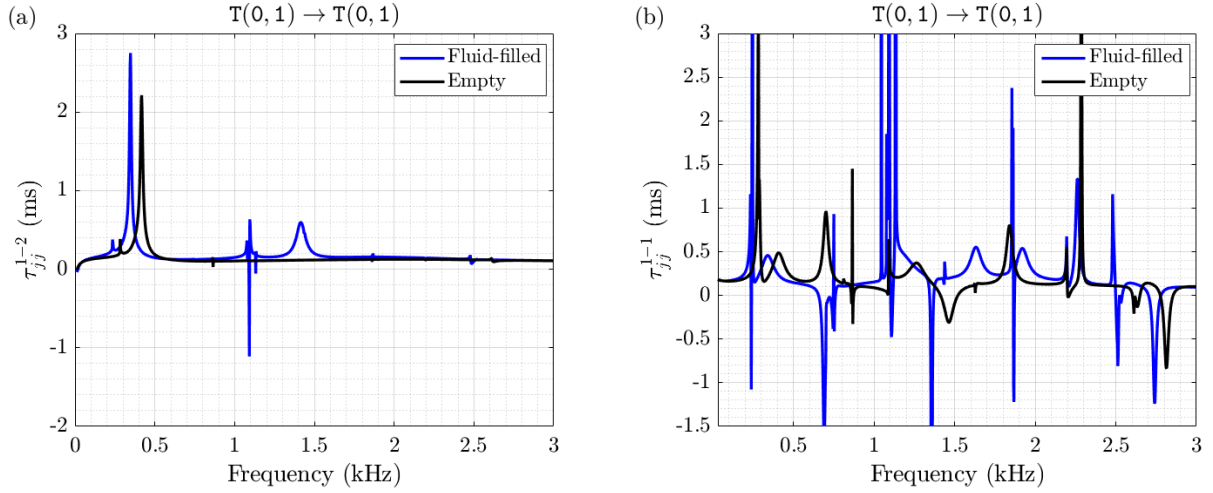


Figure 4.18: Time of flight in: (a) transmission and (b) reflection for the joint considering the mode $T(0,1)$. Results for fluid-filled and empty pipes are plotted in blue and black lines, respectively.

The localization of a defect in fluid-filled pipelines is now studied. Consider the pipe assembly with a curved joint and a defect, as shown in Fig. 3.4(b) — i.e. three waveguides with a curved joint and a defect. Here, the defect is supposed to be axisymmetric; also, the joint has a radius $R_j = 0.2$ m and angle of curvature of $\theta_j = 90^\circ$. The scattering matrix is computed with the WFE method.

The distance between the measurement point and the joint is $l_1 = 10$ m, and the sought position of the defect is $l_2 = 10$ m, which represents the distance between the joint and the defect. Fig. 4.19 depicts the normalized circumferential displacement at the measurement point as a function of time, specifically showing the contribution of $T(0,1)$ in terms of displacement of the elastic. Both incident and reflected wave packets are of $T(0,1)$ type. This can be achieved by decomposing the signal into different contributions and selecting the desired wave type, as described in [134]. In Fig. 4.19, the wavepacket (1) corresponds to the input signal, the wavepacket (2) is related to the joint reflection, and the wavepacket (3) is related to the defect reflection. In this case, the mode $T(0,1)$ undergoes low reflection at the joint and it is almost

totally transmitted through it without undergoing different mode conversions.

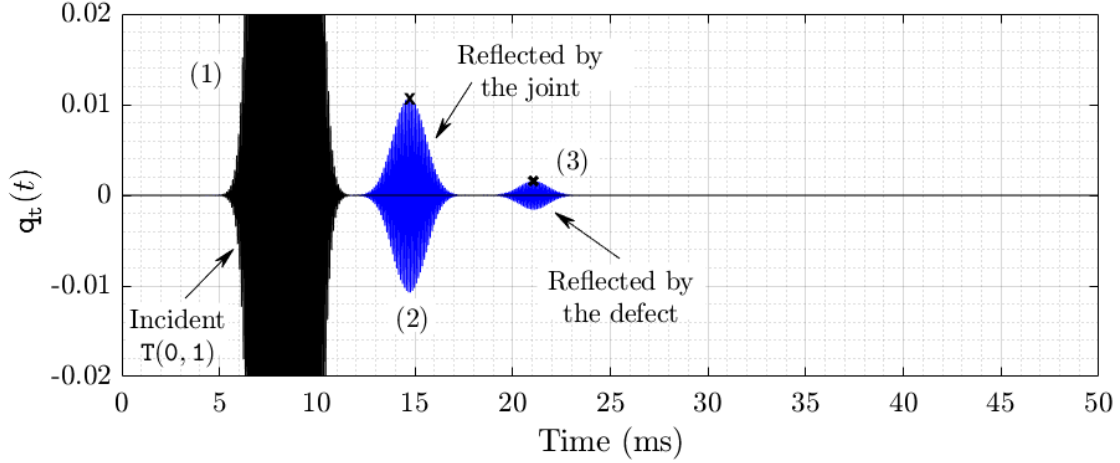


Figure 4.19: Tangential displacement at the measurement point: (1) input wavepacket; (2) reflected wavepacket at the joint, and (3) reflected wavepacket issued from the defect. The dark cross highlights the tip of the wave packets. The incident pulse is a Gaussian "T(0, 1)" at 10 kHz.

The distance of l_2 can be found via Eq. (3.30). For this task, let us consider the measured time τ_{ijkl} and the time-of-flight in transmission τ_{jj}^{1-2} as plotted in Fig. 4.18(a). Here the considered pathway is $(i \leftarrow j \leftarrow k \leftarrow l) = (T(0, 1) \leftarrow T(0, 1) \leftarrow T(0, 1) \leftarrow T(0, 1))$. To highlight the importance of the approach, three different cases are provided as shown in Tab. 4.4.

Table 4.4: Estimated position of the defect from Eq. (3.30), and relative error (reference is $l_2 = 10$ m).

Case	τ_{ijkl} (ms)	l_2 (m)	Relative error (%)
Disregarding τ_{jj}^{1-2}	21.08	10.49	4.9
Considering τ_{jj}^{1-2} for the empty joint	21.08	10.15	1.5
Considering τ_{jj}^{1-2} for the elasto-acoustic joint	21.08	10.01	0.1

In this case, the position of the defect l_2 can be accurately predicted with a relative error

smaller than 0.1 % when considering the presence of the fluid. By disregarding the time of flight in transmission through the joint, this yields a relative error of 4.9 %. Finally, different values of τ_{jj}^{1-2} for empty and fluid-filled pipes lead to different values of l_2 . It is important to note that the proposed approach is supposed to be applied to an arbitrarily shaped coupling element in which the concept of group velocity is not defined.

To analyze the impact of joint curvature on defect detection, three additional cases are examined: $\theta_a = 30^\circ$, 45° , and 60° . The computation of the time of flight and l_2 from the procedure proposed earlier. The results for these cases are organized in Table 4.5. Notably, accurate defect localization is achieved by considering the time of flight in transmission through the joint. The results show that l_2 can be determined with an error below 0.3% when incorporating the time of flight in transmission for elasto-acoustic joints. Conversely, neglecting the time of flight in transmission results in an error of approximately 5%, while considering the time of flight for empty pipes yields an error of 1.6%. These results highlight the importance of time of flight increases with joint length. Indeed, the wavepackets require a longer time to be transmitted through the long joints.

Table 4.5: Estimated position of the defect from Eq. (3.30), and relative error (reference is $l_2 = 10$ m).

θ_d	Case	τ_{ijkl} (ms)	l_2 (m)	Relative error (%)
30°	Disregarding τ_{jj}^{1-2}	20.88	10.17	1.7
	Considering τ_{jj}^{1-2} for the empty joint		9.98	0.2
	Considering τ_{jj}^{1-2} for the elasto-acoustic joint		10.01	0.1
45°	Disregarding τ_{jj}^{1-2}	20.94	10.27	2.7
	Considering τ_{jj}^{1-2} for the empty joint		10.12	1.2
	Considering τ_{jj}^{1-2} for the elasto-acoustic joint		10.01	0.1
60°	Disregarding τ_{jj}^{1-2}	21.01	10.38	3.8
	Considering τ_{jj}^{1-2} for the empty joint		10.16	1.6
	Considering τ_{jj}^{1-2} for the elasto-acoustic joint		10.03	0.3
90°	Disregarding τ_{jj}^{1-2}	21.08	10.49	4.9
	Considering τ_{jj}^{1-2} for the empty joint		10.15	1.5
	Considering τ_{jj}^{1-2} for the elasto-acoustic joint		10.01	0.1

4.5 Conclusions

This chapter analyzed the wave propagation in fluid-filled pipes with joints and defects. The propagating modes in the pipes were successfully retrieved using the WFE method. For the case of straight fluid-filled pipes, the comparison between the FE and WFE methods was provided, where a considerable reduction of computational time was observed. This demonstrates the accuracy and efficiency of the WFE method compared to the classical FE method. Also, in the WFE framework, a reduction strategy was proposed to compute reduced DSM of coupling elements efficiently. A curved joint linking two waveguides was analyzed, and a comparison between the WFE and the FE results in time and frequency domains was provided. Overall,

the strategy enables a reduction of 65% with an error of 0.5% to compute the vibroacoustic response.

Finally, the scattering coefficients were computed for defects and curved joints. There was no significant difference between the fluid-filled and empty cases for defects. However, differences in transmission and reflection produced due to the presence of the fluid were observed for the joints. The case of a defect after the joint was explored and the concept of time of flight in transmission through the joint was proven accurate and relevant to estimate the defect localization.

Chapter 5

Conclusions and perspectives

In this thesis, we investigated some aspects of defect detection and localization in assemblies composed of straight waveguides, curved joints and defects. Especially, the present work provided insights into the interaction of guided waves at defects and curved joints. These phenomena were numerically simulated using the WFE method.

In Chapter 2, the foundations of the WFE method were recalled. The WFE method was used to model periodic structures, i.e., structures composed of an assembly of substructures. This enabled the computation of the wave modes and forced response in the time and frequency domains. In this framework, it is possible to simulate waveguides linked with coupling elements, such as joints and defects, which can be modeled using the FE method and the CB reduction. Also, numerical experiments were carried out to show the robustness and accuracy of the WFE method. Comparisons between the WFE solutions and the analytical theory for the dispersion curves and forced response in the frequency domain were provided; also, a comparison between the WFE and FE solutions for assessing the forced responses in the frequency and time domains was proposed. Finally, a study of two waveguides connected with a coupling element was presented and the concept of scattering matrices was explored. The WFE was proven relevant and efficient in providing accurate solutions for wave propagation in straight

waveguides with/without coupling elements.

Within the scattering matrix formalism, a strategy to localize a defect in structures containing a curved joint was proposed in Chapter 3. This strategy is based on the computation of the time of flight that a narrow wavepacket takes to be transmitted or reflected at a coupling element. It was proven that the time of flight can be computed by considering the frequency derivatives of the arguments of the scattering matrices of the joint and the defect. Also, a physical insight into the transmitted and reflected waves at a coupling element was provided. Numerical simulations were carried out to verify the proposed approach. First, the case of a 2D plane-stress beam was discussed, considering waveguides with a defect and waveguides with a curved joint and a defect. It was shown that considering the time of flight in transmission and reflection through the joint is relevant to localizing the defect accurately. Besides focusing on curved joints, this approach intends to be generalized to complex coupling elements cases.

Finally, in Chapter 4, the case of elasto-acoustic structures was considered. The WFE method used a symmetrical formulation of the elasto-acoustic problem in which the displacement vector is considered for the elastic part and the potential velocity is considered for the acoustic part. This enabled the computation of wave propagation modes, dispersion curves, and group velocities. A strategy based on the CB reduction with enrichment vector bases was proposed regarding coupling elements. The reduction strategy was tested to ensure its validity and robustness. With this reduction strategy, the power transmission and reflection of waves for different defects and joints were analyzed. It was shown that the torsional mode constitutes a good option to perform NDT. Regarding defect detection, the strategy to localize a defect after a joint was applied, considering different curvature angles for the joint. It was shown that the time of flight is sensitive to the presence of the fluid. In this case, it is recommended to consider the time of flight of the elasto-acoustic joint to detect the defect accurately.

Future work:

Certain topics could be considered for future perspectives and further development:

- An important question to be answered is whether the severity of a defect placed after a joint can be estimated. When only a defect is present, the severity can be assessed. However, wave mode conversion phenomena occurring in a joint can hide important information for this purpose, such as the reflected wave amplitude caused by the defect;
- Investigate and propose a strategy to localize a defect when multiple curved joints are present in the system. It appears to be challenging since multiple mode conversion may occur, making the interpretation of signals difficult. To the author's knowledge, it has not been exploited in the literature;
- Study the interaction between propagating waves and local non-linearities in infinite periodic structures. Regarding this, Duhamel and Mencik [61] developed a method for infinite periodic structures containing local non-linearities in the time domain. However, it appears that the proposed approach was not applied to NDT;
- Propose a strategy to reduce the CB-enrichment basis for an elasto-acoustic coupling element based on the selection of left vectors $\tilde{\mathbf{U}}^E$ and $\tilde{\mathbf{U}}^A$ when considering the SVD decomposition, see Sec. 4.3.1 and 4.4.1. Also, incorporate the reduction of wave bases proposed by Droz et al. [27]. These two strategies together seem to optimize the computational costs in the WFE framework;
- Analysis of wave propagation and defect detection in fluid-filled pipes, with mean flow. It appears to be significant since this is commonly encountered in industry situations. It should be highlighted that, in the WFE framework, the consideration of the flow speed results in a matrix \mathbf{S} that is not symplectic anymore;
- Study topological optimization for coupling elements and/or substructures to manipulate wave propagation: stopbands, scattering coefficients, among other properties;

Bibliography

- [1] G. Wang, Q. Cheng, W. Zhao, Q. Liao, and H. Zhang. Review on the transport capacity management of oil and gas pipeline network: Challenges and opportunities of future pipeline transport. *Energy Strategy Reviews*, 43:100933, 2022.
- [2] L. Kraidi, R. Shah, W. Matipa, and F. Borthwick. Analyzing stakeholders' perceptions of the critical risk factors in oil and gas pipeline projects. *Periodica Polytechnica Architecture*, 50(2):155–162, 2019.
- [3] L. Kraidi, R. Shah, W. Matipa, and F. Borthwick. An investigation of mitigating the safety and security risks allied with oil and gas pipeline projects. *Journal of Pipeline Science and Engineering*, 1(3):349–359, 2021. Publisher: Elsevier.
- [4] Z. Li, Y. Liang, Y. Liang, Q. Liao, B. Wang, L. Huang, J. Zheng, and H. Zhang. Review on intelligent pipeline technologies: A life cycle perspective. *Computers & Chemical Engineering*, 175:108283, 2023.
- [5] A. R. Diogo, B. Moreira, C. A. J. Gouveia, and J. M. R. S. Tavares. A Review of Signal Processing Techniques for Ultrasonic Guided Wave Testing. *Metals*, 12(6):936, June 2022. Number: 6 Publisher: Multidisciplinary Digital Publishing Institute.
- [6] J. L. Rose. *Ultrasonic Guided Waves in Solid Media*. Cambridge University Press, Cambridge, 2014.
- [7] J. L. Rose, L. Zhang, M. J. Avioli Jr., and P. J. Mudge. A Natural Focusing Low Frequency Guided Wave Experiment for the Detection of Defects Beyond Elbows. *Journal of Pressure Vessel Technology*, 127(3):310–316, February 2005.
- [8] S. W. Liu and S. K. Datta. Scattering of Ultrasonic Wave by Cracks in a Plate. *Journal of*

- Applied Mechanics*, 60(2):352–357, 1993.
- [9] S. C. Olisa, M. A. Khan, and A. Starr. Review of Current Guided Wave Ultrasonic Testing (GWUT) Limitations and Future Directions. *Sensors*, 21(3):811, January 2021. Number: 3 Publisher: Multidisciplinary Digital Publishing Institute.
- [10] A.J. Croxford, P.D. Wilcox, B.W. Drinkwater, and G. Konstantinidis. Strategies for guided-wave structural health monitoring. *Proceedings of the Royal Society A: Mathematical, Physical and Engineering Sciences*, 463(2087):2961–2981, November 2007. Publisher: Royal Society.
- [11] A. Ghavamian, F. Mustapha, B. T. H. Tu. Baharudin, and N. Yidris. Detection, Localisation and Assessment of Defects in Pipes Using Guided Wave Techniques: A Review. *Sensors*, 18(12):4470, December 2018. Number: 12 Publisher: Multidisciplinary Digital Publishing Institute.
- [12] R. M. Orris and M. Petyt. A finite element study of harmonic wave propagation in periodic structures. *Journal of Sound and Vibration*, 33(2):223–236, March 1974.
- [13] R. M. Orris and M. Petyt. Random response of periodic structures by a finite element technique. *Journal of Sound and Vibration*, 43(1):1–8, November 1975.
- [14] D. J. Mead. Free wave propagation in periodically supported, infinite beams. *Journal of Sound and Vibration*, 11(2):181–197, February 1970.
- [15] D. J. Mead. Vibration Response and Wave Propagation in Periodic Structures. *Journal of Engineering for Industry*, 93(3):783–792, August 1971.
- [16] D. J. Mead. A general theory of harmonic wave propagation in linear periodic systems with multiple coupling. *Journal of Sound and Vibration*, 27(2):235–260, March 1973.
- [17] D. J. Mead. Wave propagation and natural modes in periodic systems: II. Multi-coupled systems, with and without damping. *Journal of Sound and Vibration*, 40(1):19–39, May 1975.
- [18] D. J. Mead. A new method of analyzing wave propagation in periodic structures; Applications to periodic timoshenko beams and stiffened plates. *Journal of Sound and Vibration*, 104(1):9–27, January 1986.
- [19] B. R. Mace, D. Duhamel, M. J. Brennan, and L. Hinke. Finite element prediction of wave motion in structural waveguides. *The Journal of the Acoustical Society of America*, 117(5):2835–2843, May 2005. Publisher: Acoustical Society of America.

- [20] B. R. Mace and E. Manconi. Modelling wave propagation in two-dimensional structures using finite element analysis. *Journal of Sound and Vibration*, 318(4):884–902, December 2008.
- [21] J. M. Mencik and M. N. Ichchou. Multi-mode propagation and diffusion in structures through finite elements. *European Journal of Mechanics - A/Solids*, 24(5):877–898, September 2005.
- [22] J. M. Mencik. On the low- and mid-frequency forced response of elastic structures using wave finite elements with one-dimensional propagation. *Computers & Structures*, 88(11):674–689, June 2010.
- [23] J.-M. Mencik. New advances in the forced response computation of periodic structures using the wave finite element (WFE) method. *Computational Mechanics*, 54(3):789–801, September 2014.
- [24] D. Duhamel, B. R. Mace, and M. J. Brennan. Finite element analysis of the vibrations of waveguides and periodic structures. *Journal of Sound and Vibration*, 294(1):205–220, June 2006.
- [25] W. X. Zhong and F. W. Williams. Wave Problems for Repetitive Structures and Symplectic Mathematics. *Proceedings of the Institution of Mechanical Engineers, Part C: Journal of Mechanical Engineering Science*, 206(6):371–379, November 1992. Publisher: IMECHE.
- [26] J. M. Mencik and M. N. Ichchou. A substructuring technique for finite element wave propagation in multi-layered systems. *Computer Methods in Applied Mechanics and Engineering*, 197(6):505–523, January 2008.
- [27] C. Droz, J. P. Lainé, M. N. Ichchou, and G. Inquiétude. A reduced formulation for the free-wave propagation analysis in composite structures. *Composite Structures*, 113:134–144, July 2014.
- [28] P. B. Silva, J.-M. Mencik, and J. R. F. de Arruda. Wave finite element-based superelements for forced response analysis of coupled systems via dynamic substructuring. *International Journal for Numerical Methods in Engineering*, 107(6):453–476, 2016.
- [29] V. Denis and J.-M. Mencik. A wave-based optimization approach of curved joints for improved defect detection in waveguide assemblies. *Journal of Sound and Vibration*, 465:115003, January 2020.
- [30] D. S. Claro, V. Denis, and J. M. Mencik. Defect localization in waveguide assemblies with curved joints via wave finite elements and time of flight analysis. *European Journal of Mechanics - A/Solids*, 97:104814, January 2023.

- [31] N. Aimakov, G. Tanner, and D. Chronopoulos. A wave finite element approach for modelling wave transmission through laminated plate junctions. *Scientific Reports*, 12(1):1852, February 2022. Number: 1 Publisher: Nature Publishing Group.
- [32] J. M. Mencik and M. N. Ichchou. Wave finite elements in guided elastodynamics with internal fluid. *International Journal of Solids and Structures*, 44(7):2148–2167, April 2007.
- [33] J. M. Renno and B. R. Mace. Calculating the forced response of cylinders and cylindrical shells using the wave and finite element method. *Journal of Sound and Vibration*, 333(21):5340–5355, October 2014.
- [34] A. Bhuddi, M.-L. Gobert, and J.-M. Mencik. On the Acoustic Radiation of Axisymmetric Fluid-Filled Pipes Using the Wave Finite Element (WFE) Method. *Journal of Computational Acoustics*, 23(03):1550011, September 2015. Publisher: World Scientific Publishing Co.
- [35] Y. Fan, M. Collet, M. Ichchou, L. Li, O. Bareille, and Z. Dimitrijevic. Energy flow prediction in built-up structures through a hybrid finite element/wave and finite element approach. *Mechanical Systems and Signal Processing*, 66-67:137–158, January 2016.
- [36] Y. Fan, C. W. Zhou, J. P. Laine, M. Ichchou, and L. Li. Model reduction schemes for the wave and finite element method using the free modes of a unit cell. *Computers & Structures*, 197:42–57, February 2018.
- [37] J.-M. Mencik. A wave finite element approach for the analysis of periodic structures with cyclic symmetry in dynamic substructuring. *Journal of Sound and Vibration*, 431:441–457, September 2018.
- [38] D. Beli, J.-M. Mencik, P. B. Silva, and J. R. F. Arruda. A projection-based model reduction strategy for the wave and vibration analysis of rotating periodic structures. *Computational Mechanics*, 62(6):1511–1528, December 2018.
- [39] F. Treyssède and J. Cesbron. Waveguide finite element modelling for broadband vibration analysis of rotating and prestressed circular structures: Application to tyres. *Journal of Sound and Vibration*, 543:117361, January 2023.
- [40] S. Sorokin, E. Manconi, L. Ledet, and R. Garziera. Wave propagation in helically orthotropic elastic cylindrical shells and lattices. *International Journal of Solids and Structures*, 170:11–21,

- October 2019.
- [41] D. Chronopoulos, M. Ichchou, B. Troclet, and O. Bareille. Computing the broadband vibroacoustic response of arbitrarily thick layered panels by a wave finite element approach. *Applied Acoustics*, 77:89–98, March 2014.
- [42] E. Manconi, S. V. Sorokin, R. Garziera, and M. M. Quartaroli. Free and Forced Wave Motion in a Two-Dimensional Plate with Radial Periodicity. *Applied Sciences*, 11(22):10948, January 2021. Number: 22 Publisher: Multidisciplinary Digital Publishing Institute.
- [43] B. E. Takiuti, E. Manconi, M. J. Brennan, and V. Lopes. Wave scattering from discontinuities related to corrosion-like damage in one-dimensional waveguides. *Journal of the Brazilian Society of Mechanical Sciences and Engineering*, 42(10):521, October 2020.
- [44] C. Aristégui, M. J. S. Lowe, and P. Cawley. Guided waves in fluid-filled pipes surrounded by different fluids. *Ultrasonics*, 39(5):367–375, 2001.
- [45] B. Vogelaar and M. Golombok. Simplified ultrasonic damage detection in fluid-filled pipes. *Journal of Nondestructive Evaluation*, 36(4):63, 2017.
- [46] E. Leinov, M. J. S. Lowe, and P. Cawley. Investigation of guided wave propagation and attenuation in pipe buried in sand. *Journal of Sound and Vibration*, 347:96–114, July 2015.
- [47] E. Leinov, M. J. S. Lowe, and P. Cawley. Ultrasonic isolation of buried pipes. *Journal of Sound and Vibration*, 363:225–239, February 2016.
- [48] Y. Gao, Y. Liu, and J. M. Muggleton. Axisymmetric fluid-dominated wave in fluid-filled plastic pipes: Loading effects of surrounding elastic medium. *Applied Acoustics*, 116:43–49, January 2017.
- [49] Q. Huan, M. Chen, and F. Li. Long-distance structural health monitoring of buried pipes using pitch-catch T(0,1) wave piezoelectric ring array transducers. *Ultrasonics*, 106:106162, August 2020.
- [50] C. R. Fuller and F. J. Fahy. Characteristics of wave propagation and energy distributions in cylindrical elastic shells filled with fluid. *Journal of Sound and Vibration*, 81(4):501–518, 1982.
- [51] H. Sato and H. Ogiso. Analytical method for guided waves propagating in a fluid-filled pipe with attenuation. *Japanese Journal of Applied Physics*, 52(7S):07HC07, jul 2013.

- [52] M. J. Kingan, Y. Yang, and B. R. Mace. Sound transmission through cylindrical structures using a wave and finite element method. *Wave Motion*, 87:58–74, 2019. Innovations in Wave Modelling II.
- [53] E. Manconi, B. R. Mace, and R. Garziera. Wave Propagation in Laminated Cylinders with Internal Fluid and Residual Stress. *Applied Sciences*, 13(9):5227, January 2023. Number: 9 Publisher: Multidisciplinary Digital Publishing Institute.
- [54] M. Maess, N. Wagner, and L. Gaul. Dispersion curves of fluid filled elastic pipes by standard FE models and eigenpath analysis. *Journal of Sound and Vibration*, 296(1):264–276, 2006.
- [55] M. Maess, J. Herrmann, and L. Gaul. Finite element analysis of guided waves in fluid-filled corrugated pipes. *The Journal of the Acoustical Society of America*, 121(3):1313–1323, 2007.
- [56] M. Maess and L. Gaul. Substructuring and model reduction of pipe components interacting with acoustic fluids. *Mechanical Systems and Signal Processing*, 20(1):45–64, January 2006.
- [57] J. Herrmann, M. Maess, and L. Gaul. Substructuring including interface reduction for the efficient vibro-acoustic simulation of fluid-filled piping systems. *Mechanical Systems and Signal Processing*, 24(1):153–163, 2010.
- [58] S. M. Kim, J.-G. Kim, S.-W. Chae, and K.C. Park. A strongly coupled model reduction of vibro-acoustic interaction. *Computer Methods in Applied Mechanics and Engineering*, 347:495–516, 2019.
- [59] M. Tournour and N. Atalla. Pseudostatic corrections for the forced vibroacoustic response of a structure-cavity system. *The Journal of the Acoustical Society of America*, 107(5):2379–2386, 05 2000.
- [60] Q. H. Tran, M. Ouisse, and N. Bouhaddi. A robust component mode synthesis method for stochastic damped vibroacoustics. *Mechanical Systems and Signal Processing*, 24(1):164–181, January 2010.
- [61] D. Duhamel and J.-M. Mencik. Time response analysis of periodic structures via wave-based absorbing boundary conditions. *European Journal of Mechanics - A/Solids*, 91:104418, 2022.
- [62] B.A. Auld. *Acoustic Fields and Waves in Solids*. Krieger Publishing Company, 1990.
- [63] J. L. Rose, J. J. Ditri, A. Pilarski, K. Rajana, and F. Carr. A guided wave inspection technique

- for nuclear steam generator tubing. *NDT & E International*, 27(6):307–310, December 1994.
- [64] J. L. Davis. *Wave Propagation in Solids and Fluids*. Springer, New York, NY, 1988.
- [65] Z. A. B. Ahmad and U. Gabbert. Simulation of Lamb wave reflections at plate edges using the semi-analytical finite element method. *Ultrasonics*, 52(7):815–820, September 2012.
- [66] Z. A. B. Ahmad, J. M. Vivar-Perez, and U. Gabbert. Semi-analytical finite element method for modeling of lamb wave propagation. *CEAS Aeronaut J*, 4(1):21–33, April 2013.
- [67] T. Hayashi and D. Inoue. Calculation of leaky Lamb waves with a semi-analytical finite element method. *Ultrasonics*, 54(6):1460–1469, August 2014.
- [68] M. N. Ichchou, S. Akrouf, and J. M. Mencik. Guided waves group and energy velocities via finite elements. *Journal of Sound and Vibration*, 305(4):931–944, September 2007.
- [69] J. F. Doyle. *Wave Propagation in Structures*. Mechanical Engineering Series. Springer International Publishing, Cham, 2021.
- [70] B. C. Lee and W. J. Staszewski. Modelling of Lamb waves for damage detection in metallic structures: Part II. Wave interactions with damage. *Smart Mater. Struct.*, 12(5):815, September 2003.
- [71] Z. Su, L. Ye, and Y. Lu. Guided Lamb waves for identification of damage in composite structures: A review. *Journal of Sound and Vibration*, 295(3):753–780, August 2006.
- [72] I. A. Viktorov. *Rayleigh and Lamb Waves: Physical Theory and Applications: Translated from Russian*. Plenum press, 1967.
- [73] L. W. Schmerr. *Propagation of Surface and Plate Waves*. Springer US, Boston, MA, 1998.
- [74] D. C. Gazis. Three-Dimensional Investigation of the Propagation of Waves in Hollow Circular Cylinders. I. Analytical Foundation. *The Journal of the Acoustical Society of America*, 31(5):568–573, July 2005.
- [75] D. C. Gazis. Three-Dimensional Investigation of the Propagation of Waves in Hollow Circular Cylinders. II. Numerical Results. *The Journal of the Acoustical Society of America*, 31(5):573–578, July 2005.
- [76] J. Li and J. L. Rose. Excitation and propagation of non-axisymmetric guided waves in a hollow cylinder. *The Journal of the Acoustical Society of America*, 109(2):457–464, February 2001.

- [77] D. Dai and Q. He. Structure damage localization with ultrasonic guided waves based on a time–frequency method. *Signal Processing*, 96:21–28, March 2014.
- [78] A. Perelli, L. De Marchi, A. Marzani, and N. Speciale. Frequency warped cross-wavelet multiresolution analysis of guided waves for impact localization. *Signal Processing*, 96:51–62, March 2014.
- [79] V. Serey, N. Quaegebeur, M. Renier, P. Micheau, P. Masson, and M. Castaings. Selective generation of ultrasonic guided waves for damage detection in rectangular bars. *Structural Health Monitoring*, 20(3):1156–1168, May 2021. Publisher: SAGE Publications.
- [80] W. Mohr and P. Holler. On Inspection of Thin-Walled Tubes for Transverse and Longitudinal Flaws by Guided Ultrasonic Waves. *IEEE Transactions on Sonics and Ultrasonics*, 23(5):369–373, October 1976. Conference Name: IEEE Transactions on Sonics and Ultrasonics.
- [81] M. G. Silk and K. F. Bainton. The propagation in metal tubing of ultrasonic wave modes equivalent to Lamb waves. *Ultrasonics*, 17(1):11–19, January 1979.
- [82] W. Zhuang, A. H. Shah, and S. K. Datta. Axisymmetric Guided Wave Scattering by Cracks in Welded Steel Pipes. *Journal of Pressure Vessel Technology*, 119(4):401–406, November 1997.
- [83] D. N. Alleyne, P. Cawley, A. M. Lank, and P. J. Mudge. The Lamb Wave Inspection of Chemical Plant Pipework. In Donald O. Thompson and Dale E. Chimenti, editors, *Review of Progress in Quantitative Nondestructive Evaluation: Volume 16A*, Review of Progress in Quantitative Nondestructive Evaluation, pages 1269–1276. Springer US, Boston, MA, 1997.
- [84] Y. Cho. Estimation of ultrasonic guided wave mode conversion in plate with thickness variation. *Ultrasonics, Ferroelectrics and Frequency Control, IEEE Transactions on*, 47:591 – 603, 06 2000.
- [85] B. Takiuti, E. Manconi, M. Brennan, and V. Lopes. Wave scattering from discontinuities related to corrosion-like damage in one-dimensional waveguides. *Journal of the Brazilian Society of Mechanical Sciences and Engineering*, 42:1–17, 2020.
- [86] A. C. Kubrusly, J. P. von der Weid, and S. Dixon. Experimental and numerical investigation of the interaction of the first four SH guided wave modes with symmetric and non-symmetric discontinuities in plates. *NDT & E International*, 108:102175, December 2019.
- [87] K. W. Lopes, C. G. Gonzalez-Bueno, and D. D. Bueno. On the Frequencies for Structural Health

- Monitoring in Plates with Symmetrical Damage: An Analytical Approach. *J Nondestruct Eval*, 41(1):29, March 2022.
- [88] K. W. Lopes, C. G. Gonzalez-Bueno, D. J. Inman, and D. D. Bueno. On the modeling of circular piezoelectric transducers for wave propagation-based structural health monitoring applications. *Journal of Intelligent Material Systems and Structures*, page 1045389X221147668, February 2023. Publisher: SAGE Publications Ltd STM.
- [89] M. J. S. Lowe, D. N. Alleyne, and P. Cawley. The Mode Conversion of a Guided Wave by a Part-Circumferential Notch in a Pipe. *Journal of Applied Mechanics*, 65(3):649–656, September 1998.
- [90] H. Bai, A. H. Shah, N. Popplewell, and S. K. Datta. Scattering of guided waves by circumferential cracks in composite cylinders. *International Journal of Solids and Structures*, 39(17):4583–4603, August 2002.
- [91] P. Cawley, M. J. S. Lowe, F. Simonetti, C. Chevalier, and A. G. Roosenbrand. The variation of the reflection coefficient of extensional guided waves in pipes from defects as a function of defect depth, axial extent, circumferential extent and frequency. *Proceedings of the Institution of Mechanical Engineers, Part C: Journal of Mechanical Engineering Science*, 216(11):1131–1143, November 2002. Publisher: IMECHE.
- [92] A. Demma, P. Cawley, M. Lowe, and A. G. Roosenbrand. The reflection of the fundamental torsional mode from cracks and notches in pipes. *The Journal of the Acoustical Society of America*, 114(2):611–625, July 2003.
- [93] Z. Liu, C. He, B. Wu, X. Wang, and S. Yang. Circumferential and longitudinal defect detection using T(0,1) mode excited by thickness shear mode piezoelectric elements. *Ultrasonics*, 44:e1135–e1138, December 2006.
- [94] M. Ratassepp, S. Fletcher, and M. J. S. Lowe. Scattering of the fundamental torsional mode at an axial crack in a pipe. *The Journal of the Acoustical Society of America*, 127(2):730–740, February 2010.
- [95] X. Wang, H. Gao, K. Zhao, and C. Wang. Time-frequency characteristics of longitudinal modes in symmetric mode conversion for defect characterization in guided waves-based pipeline inspection.

- NDT & E International*, 122:102490, September 2021.
- [96] Y.-W. Kim and K.-J. Park. The interaction of fundamental torsional guided waves from axial and oblique defects in pipes. *Insight - Non-Destructive Testing and Condition Monitoring*, 63(6):334–340, June 2021.
- [97] E. C. Rodgers, S. Mariani, and P. Cawley. The use of circumferential guided waves to monitor axial cracks in pipes. *Structural Health Monitoring*, page 14759217221130939, November 2022. Publisher: SAGE Publications.
- [98] T. C. Yung, J. S. Pang, M. N. Abdul Hamid, L. E. Ooi, and W. H. Tan. Ultrasonic guided wave testing on pipeline corrosion detection using torsional T(0,1) guided waves. *Journal of Mechanical Engineering and Sciences*, pages 9157–9166, December 2022.
- [99] A. Demma, P. Cawley, and M. J. S. Lowe. Mode conversion of longitudinal and torsional guided modes due to pipe bends. *AIP Conference Proceedings*, 557(1):172–179, April 2001. Publisher: American Institute of Physics.
- [100] B. Verma, T. K. Mishra, K. Balasubramaniam, and P. Rajagopal. Interaction of low-frequency axisymmetric ultrasonic guided waves with bends in pipes of arbitrary bend angle and general bend radius. *Ultrasonics*, 54(3):801–808, March 2014.
- [101] Y. Wang and X. Li. Propagation Characteristics and Defect Sensitivity Analysis of Guided Wave From Single Excitation Source in Elbows. *IEEE Access*, 7:75542–75549, 2019. Conference Name: IEEE Access.
- [102] M. Qi, S. Zhou, J. Ni, and Y. Li. Investigation on ultrasonic guided waves propagation in elbow pipe. *International Journal of Pressure Vessels and Piping*, 139-140:250–255, March 2016.
- [103] R. M. Sanderson, D. A. Hutchins, D. R. Billson, and P. J. Mudge. The investigation of guided wave propagation around a pipe bend using an analytical modeling approach. *The Journal of the Acoustical Society of America*, 133(3):1404–1414, March 2013.
- [104] S. Heinlein, P. Cawley, and T. K. Vogt. Reflection of torsional T(0,1) guided waves from defects in pipe bends. *NDT & E International*, 93:57–63, January 2018.
- [105] J. Ni, S. Zhou, P. Zhang, and Y. Li. Effect of Pipe Bend Configuration on Guided Waves-Based Defects Detection: An Experimental Study. *Journal of Pressure Vessel Technology*, 138(2),

- October 2015.
- [106] W. Duan. Time domain numerical modelling of guided wave excitation in fluid-filled pipes. *Finite Elements in Analysis and Design*, 210:103813, November 2022.
- [107] W. Duan and R. Kirby. Guided wave propagation in buried and immersed fluid-filled pipes: Application of the semi analytic finite element method. *Computers & Structures*, 212:236–247, February 2019.
- [108] M. Gallezot, F. Treyssède, and L. Laguerre. A numerical method for the scattering by defects in axisymmetrical open elastic waveguides. *Procedia Engineering*, 199:1527–1532, January 2017.
- [109] M. Mitra and S. Gopalakrishnan. Guided wave based structural health monitoring: A review. *Smart Mater. Struct.*, 25(5):053001, March 2016. Publisher: IOP Publishing.
- [110] B. R. Mace. Wave reflection and transmission in beams. *Journal of Sound and Vibration*, 97(2):237–246, November 1984.
- [111] K.-J. Bathe. Finite element procedures for solids and structures linear analysis. *Finite Element Procedures*, pages 148–214, 1982.
- [112] E. Deckers, O. Atak, L. Coox, R. D’Amico, H. Devriendt, S. Jonckheere, K. Koo, B. Pluymers, D. Vandepitte, and W. Desmet. The wave based method: An overview of 15 years of research. *Wave Motion*, 51(4):550–565, June 2014.
- [113] C. Willberg, S. Duczek, J. M. Vivar-Perez, and Z. A. B. Ahmad. Simulation Methods for Guided Wave-Based Structural Health Monitoring: A Review. *Applied Mechanics Reviews*, 67(010803), January 2015.
- [114] I. Bartoli, A. Marzani, F. Lanza di Scalea, and E. Viola. Modeling wave propagation in damped waveguides of arbitrary cross-section. *Journal of Sound and Vibration*, 295(3):685–707, August 2006.
- [115] L. Gavrić. Computation of propagative waves in free rail using a finite element technique. *Journal of Sound and Vibration*, 185(3):531–543, August 1995.
- [116] N. Rattanawangcharoen, W. Zhuang, A. H. Shah, and S. K. Datta. Axisymmetric Guided Waves in Jointed Laminated Cylinders. *Journal of Engineering Mechanics*, 123(10):1020–1026, October 1997. Publisher: American Society of Civil Engineers.

- [117] A. Marzani. Time–transient response for ultrasonic guided waves propagating in damped cylinders. *International Journal of Solids and Structures*, 45(25):6347–6368, December 2008.
- [118] F. Treyssède. Elastic waves in helical waveguides. *Wave Motion*, 45(4):457–470, March 2008.
- [119] J. M. Mencik and D. Duhamel. A wave-based model reduction technique for the description of the dynamic behavior of periodic structures involving arbitrary-shaped substructures and large-sized finite element models. *Finite Elements in Analysis and Design*, 101:1–14, September 2015.
- [120] Y. Waki, B. R. Mace, and M. J. Brennan. Numerical issues concerning the wave and finite element method for free and forced vibrations of waveguides. *Journal of Sound and Vibration*, 327(1):92–108, October 2009.
- [121] R. J. Allemang. The Modal Assurance Criterion – Twenty Years of Use and Abuse. *Sound & Vibration*, 37(8):14–21, 2003.
- [122] M. Pastor, M. Binda, and T. Harčarik. Modal Assurance Criterion. *Procedia Engineering*, 48:543–548, January 2012.
- [123] R. S. Langley. A transfer matrix analysis of the energetics of structural wave motion and harmonic vibration. *Proceedings of the Royal Society of London. Series A: Mathematical, Physical and Engineering Sciences*, 452(1950):1631–1648, January 1997. Publisher: Royal Society.
- [124] R. S. Langley. Wave evolution, reflection, and transmission along inhomogeneous waveguides. *Journal of Sound and Vibration*, 227(1):131–158, October 1999.
- [125] X.Q. Wang and R.M.C. So. Timoshenko beam theory: A perspective based on the wave-mechanics approach. *Wave Motion*, 57:64–87, 2015.
- [126] J. B. Kosmatka. An improved two-node finite element for stability and natural frequencies of axial-loaded Timoshenko beams. *Computers & Structures*, 57(1):141–149, October 1995.
- [127] J. M. Mencik. Model reduction and perturbation analysis of wave finite element formulations for computing the forced response of coupled elastic systems involving junctions with uncertain eigenfrequencies. *Computer Methods in Applied Mechanics and Engineering*, 200(45):3051–3065, October 2011.
- [128] M. N. Ichchou, J. M. Mencik, and W. Zhou. Wave finite elements for low and mid-frequency

- description of coupled structures with damage. *Computer Methods in Applied Mechanics and Engineering*, 198(15):1311–1326, March 2009.
- [129] R. R. Craig and M. C. C. Bampton. Coupling of substructures for dynamic analyses. *AIAA Journal*, 6(7):1313–1319, 1968.
- [130] P.-O. Persson and G. Strang. A Simple Mesh Generator in MATLAB. *SIAM Rev.*, 46:329–345, 2004.
- [131] D. S. Claro, V. Denis, and J. M. Mencik. A wave finite element strategy based on time of flight analysis to localize defects in networks of pipes. In *International Conference on Noise and Vibration Engineering (ISMA 2022)*, Leuven, Belgium, September 2022.
- [132] C. Schaal, S. Bischoff, and L. Gaul. Damage detection in multi-wire cables using guided ultrasonic waves. *Structural Health Monitoring: An International Journal*, 15(3):279–288, 2016.
- [133] W. Wang, Y. Fan, and L. Li. Extending Zhong-Williams scheme to solve repeated-root wave modes. *Journal of Sound and Vibration*, 519:116584, February 2022.
- [134] V. Serey, N. Quaegebeur, M. Renier, P. Micheau, P. Masson, and M. Castaings. Selective generation of ultrasonic guided waves for damage detection in rectangular bars. *Structural Health Monitoring*, 20(3):1156–1168, 2021.
- [135] H.J.P. Morand and R. Ohayon. *Fluid-Structure Interaction: Applied Numerical Methods*. Wiley-Masson Series Research in Applied Mathematics. Wiley, 1995.

List of Figures

1.1	Group velocity as the function of frequency for a steel pipe with an internal radius of 50 mm and wall thickness of 2.5 mm. Longitudinal modes are plotted in red, the torsional mode in green, and the flexural modes in blue, pink, and orange.	26
1.2	Wave modes for a steel pipe with an internal radius of 50 mm and wall thickness of 2.5 mm at 40 kHz: (a) L(0, 1), (b) L(0, 2), (c) T(0, 1), (d) F(1, 1), (e) F(1, 2), and (f) F(1, 3). Colors are in accordance with Fig. 1.1.	27
1.3	Comparison between (a) ultrasonic and (b) guided wave inspections. Adapted from [6].	28
1.4	Examples of real engineering application of guided waves in NDT : (a) example of a pipeline and the accelerators and detector, (b) and (c) technicians performing the NDT in pipelines.	29
1.5	Examples of commercial detectors/sources by “ <i>Guided Ultrasonics Ltd.</i> ” used for: (a) inspection of large diameter pipe, (b) subsea inspections, and (c) rail inspections	30
1.6	(a) Waveguide model for SAFE method (b) Waveguide model for WFE method, where the periodic length of a unit cell is denoted by d. Figure adapted from Ref. [113].	34
2.1	(a) Schematic of linear periodic elastic structure (periodic mesh); (b) Substructure mesh.	39

2.2	Schematics of substructures.	41
2.3	Schematics of the wave amplitudes along a periodic structure. As an example of boundary conditions, a force vector is applied at the left end and a displacement vector at the right end.	47
2.4	(a) FE mesh for the Timoshenko beam. A force is applied at $x = 0$, and the system is clamped at $x = L$. (b) Mesh of a substructure of length d , with displacement w and rotation θ DoFs.	53
2.5	Comparison of the (a) dispersion curves and (b) group velocity curves as a function of frequency between the theoretical approach and the WFE method for the Timoshenko beam.	54
2.6	(a) Comparison between the magnitude of the vertical displacement obtained using the theoretical and WFE method for the Timoshenko beam. (b) Relative error between the approaches, see Eq. (2.42).	55
2.7	Schematics of a 2D plane-stress beam and the FE mesh of the substructure. The beam is subject to a force on the left side and a clamped boundary condition on the right side.	56
2.8	(a) Dispersion curves (real part and imaginary parts of the wavenumbers β_j are plotted in continuous and dashed lines, respectively) and (b) group velocities, (i) using Eq. (2.33) and (ii) using Eq. (2.32), for the flexural (red), longitudinal (yellow), shearing (light green), and higher-order (green, pink and purple, respectively) modes.	57
2.9	Spatial representation of different wave mode shapes for the 2D beam at (a) 40 kHz and (b) 50 kHz for flexural (red), longitudinal (yellow), shearing (green), and a high-order (blue) modes.	58
2.10	(a) Comparison between the magnitude of the vertical displacement obtained with the FE and WFE methods for the 2D plane stress beam. (b) Relative error between the approaches computed by means of Eq. (2.42).	59

2.11 (a) Pulse excitation in the time domain and (b) absolute value of the Fourier transform.	60
2.12 Comparison between FE and WFE solutions for measured displacements as a function of time for a 2D plane stress beam when a Gaussian pulse centered at 25 kHz is applied: (a) longitudinal displacement (q_x) and (b) vertical displacement (q_y) at the excitation point.	61
2.13 Schematic of two waveguides 1 and 2 connected by a coupling element. Waveguide 1 is subjected to a force at the left boundary, and waveguide 2 is clamped at the right boundary. Here, $(\mathbf{Q}_1, \mathbf{Q}_1^*)$ and $(\mathbf{Q}_2, \mathbf{Q}_2^*)$ denote wave amplitude vectors for waveguides 1 and 2, respectively.	62
2.14 FE mesh of 2D coupling element. The left and right boundary nodes are highlighted in red, while interior nodes are highlighted in blue.	65
2.15 Schematics of two waveguides coupled by a coupling element representing a square with a hole. The system is subjected to a vector force at the left boundary and it is clamped on the right boundary.	69
2.16 Measured displacement obtained with the FE (black curve), and WFE (colored curves) methods when (a) 5, (b) 20, and (c) 300 fixed-interface modes are retained in the Craig-Bampton reduction; (d) shows the relative error between the FE and WFE results for each case.	70
2.17 Absolute value of the transmission coefficients (dashed line) from waveguide 1 to waveguide 2, and reflection coefficients (continuous line) from waveguide 1 to itself.	72
3.1 Schematic of a waveguide assembly with a curved joint and a defect. Input (I) and output (O) signals are recorded as functions of time (the red cross represents the measurement point).	77
3.2 Schematic of a waveguide assembly with three waveguides 1, 2 and 3, a curved joint and a defect. $(\mathbf{Q}_1, \mathbf{Q}_1^*)$, $(\mathbf{Q}_2, \mathbf{Q}_2^*)$ and $(\mathbf{Q}_3, \mathbf{Q}_3^*)$ are wave amplitude vectors.	80

3.3	Schematic of two waveguides 1 and 2 connected with an arbitrary coupling element (curved joint or defect). Q_{1q} and Q_{1p}^* are wave amplitudes for two waves q and p in waveguide 1.	84
3.4	Waveguide assemblies: (a) two waveguides with a defect; (b) three waveguides with a curved joint and a defect. The red cross highlights the measurement point.	86
3.5	FE meshes of (a) a waveguide substructure, (b) the defect, and (c) the curved joint.	89
3.6	(a) Dispersion curves (real part and imaginary parts of the wave numbers β_j are plotted in continuous and dashed lines, respectively) and (b) group velocities for the flexural (blue), longitudinal (red), shearing (orange), and higher-order (green, pink and purple waves).	90
3.7	Time signals at measurement point for a waveguide assembly without joint: (a) input signal (flexural waves), (b) total reflected signal, (c) reflected flexural wave packet, (d) reflected longitudinal wave packet and (e) reflected shearing wave packet. Red crosses highlight tips (highest magnitudes) of reflected wave packets.	93
3.8	Frequency-time map of the reflected signals for a waveguide assembly without joint. Measured times of flight are highlighted by yellow spots. Estimated times of flight represent the crossing points between the curves and the white dashed line: (a) total signal, (b) flexural wave packet (blue), (c) longitudinal wave packet (red) and (d) shearing wave packet (orange).	94
3.9	Times of flight τ_{ij} as functions of l_1 , for different pathways (blue, red and orange curves are pathways associated with the wave packets shown in Fig. 3.7); measured times of flight are highlighted by horizontal dashed lines.	96
3.10	Amplitudes of the (a) reflected flexural wave packet and (b) reflected shearing wave packet as functions of the central frequency (input flexural pulse) and the radius of the hole R_h (defect).	97

3.11 Time signals at measurement point for a waveguide assembly with a joint: (a) input signal (flexural waves), (b) total reflected signal, (c) reflected flexural wave packet, (d) reflected longitudinal wave packet and (e) reflected shearing wave packet. Red crosses highlight tips (highest magnitudes) of reflected wave packets. 98

3.12 Frequency-time map of the reflected signal for a waveguide assembly with a joint. Measured times of flight are highlighted by yellow spots. Estimated times of flight represent the crossing points between the continuous curves and the white dashed line: (a) total signal, (b) flexural wave packet (blue), (c) longitudinal wave packet (red) and (d) shearing wave packet (orange). The first reflections from the joint and extra reflections from the defect are represented by dashed lines. 100

3.13 Times of flight τ_{ijkl} as functions of l_2 , for different pathways (blue, red and orange curves are pathways associated to the wave packets shown in Fig. 3.11); measured times of flight are highlighted by horizontal dashed lines. 101

3.14 Measured time signals for an input flexural wave packet at 16.1 kHz (black) and 27.3 kHz (blue): (a) reflected flexural wave packet, (b) reflected longitudinal wave packet and (c) reflected shearing wave packet. 104

3.15 Amplitudes of the (a) reflected flexural wave packet, (b) reflected longitudinal wave packet and (c) reflected shearing wave packet as functions of the central frequency (input flexural pulse) and the angle of curvature of the joint. Red cross highlights values initially considered to obtain Fig. 3.11 105

3.16 Incident and reflected time signals for a waveguide assembly with a joint (total signal (a), reflected signals from the joint (b) and reflected signals from the defect (c)): (black) FE solution; (blue) WFE solution for the reflected flexural wave packet; (yellow) WFE solution for the reflected shearing wave packet. 107

3.17 Schematic of a pipe described from identical substructures on an elastic foundation (periodic mesh). 108

3.18 (a) Real and imaginary parts of $\beta_j d$ and (b) group velocities c_{gj} : (green line) torsional mode T(0, 1), (orange line) flexural mode F(1, 2); (black line) flexural mode F(1, 3); (red line) flexural mode F(2, 2); (blue, yellow and purple lines) longitudinal modes.	110
3.19 (a) Schematic of a pipe described from identical substructures on an elastic foundation; mesh for (b) joint and (c) coupling element with a defect; (d) representation of the angular extent of the defect θ_a	111
3.20 (a) Pulse excitation in the time domain and (b) absolute value of the related Fourier transform.	112
3.21 Reflected wave packets T(0, 1) at the measurement point: (1) wave packet reflected by the joint; (2)-(5) wavepackets issued from the defect. Dark crosses highlight the tips of the wave packets.	113
3.22 (a) Transmission coefficients for the incident wave T(0, 1) through the joint; highest coefficients at 30 kHz are highlighted by colored curves. (b) Times of flight τ_{ijkl} as functions of the length l_2 , for different pathways; measured times of flight are plotted using horizontal dashed lines.	114
3.23 Frequency-time map of the reflected waves issued from the defect. Measured times of flight are highlighted by yellow spots. Estimated times of flight represent the crossing points between the black curves and the white dashed line.	116
4.1 FE mesh of an elasto-acoustic waveguide and FE mesh of a substructure of length d . The elastic part is plotted in gray, and the acoustic part is plotted in blue. . .	122
4.2 (a) Dispersion curves (real and imaginary parts of $\beta_j d$ are plotted in continuous and dashed lines, respectively) and (b) group velocities for modes: T(0, 1) (in blue), SF(0, 1) (in magenta), SF(0, 2) (in red), SF(0, 3) (in orange), and FS(0, 1) (in green). Other modes are plotted in gray lines.	129
4.3 Ratios (a) $P^E/(P^E + P^A)$ and (b) $P^A/(P^E + P^A)$ for the modes: T(0, 1) in blue, SF(0, 1) in magenta, SF(0, 2) in red, SF(0, 3) in orange, and FS(0, 1) in green. . .	130

4.4	Wave shapes at 20 kHz for modes: (a) $T(0, 1)$, (b) $SF(0, 1)$, (c) and (d) flexural. The pressure is plotted using colored scale, the in-plane displacement (x and y directions) is plotted using red arrows, and the out-plane displacement (z-direction) is plotted in grayscale.	131
4.5	(a) Comparison between the displacement obtained via FE method, in black continuous line, and WFE method, in blue dot lines, for the fluid-filled pipe case. (b) Relative error between the two solutions.	132
4.6	(a) Comparison between the acoustic pressure obtained via FE method, in black continuous line, and WFE method, in blue dot lines, for the fluid-filled pipe case. (b) Relative error between the two solutions.	133
4.7	Two fluid-filled pipes connected by a curved joint.	134
4.8	Comparison between the displacement obtained uses the FE method (black continuous line), and the WFE method for fluid-filled networks: (a) without reduction and (b) with reduction for the joint.	143
4.9	Relative error between the FE method and the WFE method for fluid-filled pipes networks: without reduction (blue) and with reduction (red).	143
4.10	FE and WFE time response (displacement) for fluid-filled networks connected with a joint when a force given by a Gaussian pulse centered at 5 kHz is applied.	144
4.11	Relative error between the FE method and the WFE method with CB reduction for the joint when considering different \tilde{m}_E of \tilde{m}_A	145
4.12	Schematics of the coupling elements: (a) defect and (b) joint.	147
4.13	Power scattering coefficients for the defect: (a) $T(0, 1) \rightarrow T(0, 1)$ and (b) $SF(0, 1) \rightarrow SF(0, 1)$. Transmission and reflection coefficients are plotted in continuous and dashed lines, respectively.	148
4.14	Power scattering coefficients for the joint: (a) transmission and (b) reflection $T(0, 1) \rightarrow T(0, 1)$. Fluid-filled pipe in blue lines, and empty pipe in black lines.	148

4.15	Power coefficients for the joint: (a) transmission and (b) reflection from $T(0, 1)$ to flexural modes (in gray) and to $T(0, 1)$ (in blue) for fluid-filled pipes.	149
4.16	Power coefficients for the joint: (a) transmission and (b) reflection from $SF(0, 1)$ to other modes.	150
4.17	Power coefficients using different radii for the joint: (a) transmission and (b) reflection from $T(0, 1)$ to itself.	151
4.18	Time of flight in: (a) transmission and (b) reflection for the joint considering the mode $T(0, 1)$. Results for fluid-filled and empty pipes are plotted in blue and black lines, respectively.	152
4.19	Tangential displacement at the measurement point: (1) input wavepacket; (2) reflected wavepacket at the joint, and (3) reflected wavepacket issued from the defect. The dark cross highlights the tip of the wave packets. The incident pulse is a Gaussian " $T(0, 1)$ " at 10 kHz.	153

List of Tables

2.1	Elapsed times for FE method and WFE method + CB reduction. The number of retained fixed-interface modes analyzed is 5, 20, and 300. For comparison purposes, the time associated with the computation of the wave modes $\{\mu_j, \phi_j\}_{j=1,\dots,n}$ and $\{\mu_j^*, \phi_j^*\}_{j=1,\dots,n}$ is also shown. f_{max} is the maximum frequency of the frequency band.	71
3.1	Estimated position of the defect obtained from Eq. (3.28) and relative error (reference is $l_1 = 10$ m).	95
3.2	Estimated position of the defect obtained from Eq. (3.30) and relative error (reference is $l_2 = 5$ m).	102
3.3	Estimated position of the defect issued from analyzing extra reflected wave packets, and relative error (reference is $l_2 = 5$ m).	103
3.4	Estimated position of the defect from Eq. (3.30), and relative error (reference is $l_2 = 10$ m).	115
4.1	Elapsed times for FE and WFE methods for a straight fluid-filled pipe.	133
4.2	Elapsed times to compute the solutions using the FE method, the full WFE, and the WFE method with CB reduction for the joint.	144
4.3	Total elapsed time for different values of \tilde{m}_E and \tilde{m}_A . The reduction of the computational time and the maximum error compared to the FE method are also displayed. The errors as a function of the frequency can be seen in Fig. 4.11.	146

- 4.4 Estimated position of the defect from Eq. (3.30), and relative error (reference is $l_2 = 10$ m). 153
- 4.5 Estimated position of the defect from Eq. (3.30), and relative error (reference is $l_2 = 10$ m). 155

Diego SALAM CLARO

Approches numériques basées sur les ondes pour le contrôle non destructif des assemblages composés de guides d'ondes élastiques rectilignes connectés pas des jonctions coudées

Résumé :

Cette thèse étudie la détection et la localisation des défauts dans les assemblages de guides d'ondes, en explorant l'interaction entre les ondes se propageant dans des assemblages de guides d'ondes droits contenant des jonctions coudées et des défauts. A cet effet, la méthode Wave Finite Element (WFE) est utilisée. Des expériences numériques valident la robustesse et la précision de la méthode WFE à partir de comparaisons avec des solutions analytiques et éléments finis, en se concentrant particulièrement sur les courbes de dispersion et les réponses forcées. En élargissant l'étude aux assemblages comportant des éléments de couplage, tels que des joints et des défauts, l'étude met en évidence l'efficacité de la méthode WFE dans des scénarios impliquant de tels assemblages. Une nouvelle stratégie utilisant un formalisme en matrices de diffusion est proposée pour la localisation des défauts, qui met l'accent sur les structures contenant des jonctions coudées. L'approche repose sur le calcul du temps de vol de paquets d'ondes transmis ou réfléchis au niveau d'un élément de couplage. La stratégie est validée par des simulations numériques, démontrant la précision de la localisation des défauts pour divers scénarios, notamment des poutres 2D en contraintes planes et des tuyaux avec une jonction coudée et un défaut. Les structures élasto-acoustiques sont également traitées. Une stratégie de réduction basée sur la méthode de Craig-Brampton avec des vecteurs d'enrichissement est proposée pour améliorer le coût de calcul de la modélisation des éléments de couplage. L'analyse des coefficients de transmission et de réflexion en puissance des ondes dans des structures présentant des défauts et des jonctions met en évidence la pertinence du mode de torsion dans les contrôles non destructifs par ondes guidées dans ce type de système. Ces travaux de recherche contribuent non seulement à la compréhension de la propagation des ondes dans les assemblages de guides d'ondes, mais proposent également des stratégies pratiques pour une détection et une localisation précise des défauts, avec des applications potentielles dans divers contextes d'ingénierie.

Mots clés: méthode Wave Finite Element, propagation d'onde, jonctions coudées, détection de défauts, temps de vol

Wave-based numerical approaches for non-destructive testing of structural assemblies involving straight waveguides and curved joints

Summary :

This thesis investigates defect detection and localization in waveguide assemblies, exploring the interaction between waves in straight waveguides with curved joints and defects. For this purpose, the Wave Finite Element (WFE) method is used. Numerical experiments validate the robustness and accuracy of the WFE method through comparisons with analytical and Finite Element solutions, particularly focusing on dispersion curves and forced responses. By extending the investigation to assemblies with coupling elements, such as joints and defects, the study highlights the efficiency of the WFE method in scenarios involving waveguides. A novel strategy is proposed within the scattering matrix formalism for defect localization, with a specific emphasis on structures containing curved joints. The approach relies on computing the time of flight of narrow wavepackets transmitted or reflected at a coupling element. The strategy is validated through numerical simulations, showcasing precision in defect localization for diverse scenarios, including 2D plane-stress beams and pipes, with a curved joint and a defect. Elasto-acoustic structures are also treated. A reduction strategy based on Craig-Brampton reduction with enrichment vectors is proposed for computational efficiency to model coupling elements. Analysis of power transmission and reflection of waves in structures with defects and joints highlights the significance of the torsional mode in guided wave-based non-destructive testing in this type of system. This research work contributes not only to the understanding of wave propagation in waveguide assemblies but also offers practical strategies for accurate defect detection and localization, with potential applications in diverse engineering contexts.

Keywords : Wave finite element method, wave propagation, curved joints, defect detection, time of flight



INSTITUT NATIONAL
DES SCIENCES
APPLIQUÉES
CENTRE VAL DE LOIRE

Laboratoire de Mécanique Gabriel LaMé,
UR 7494
3 Rue de la Chocolaterie, 41000 Blois,
France